Karlsruher Institut für Technologie

IEKP-KA/2016-1

Entwicklung von strahlenharten n-in-p Silizium-Teilchendetektoren und Studien von Triggermodulen für den CMS Detektor am LHC

Martin Printz

Zur Erlangung des akademischen Grades eines
DOKTORS DER NATURWISSENSCHAFTEN
von der Fakultät für Physik des
Karlsruher Institut für Technologie (KIT)

genehmigte

DISSERTATION

von

Dipl.-Phys. Martin Printz (geb. Strelzyk)
aus Gleiwitz

Tag der mündlichen Prüfung: 22. Januar 2016

Referent: Prof. Dr. Thomas Müller, Institut für Experimentelle Kernphysik
Korreferent: Prof. Dr. Willem de Boer, Institut für Experimentelle Kernphysik

Karlsruhe Institute of Technology

IEKP-KA/2016-1

Development of radiation-hard n-in-p type silicon detectors and studies on modules with transverse momentum discrimination for the CMS detector at the LHC

Martin Printz

Zur Erlangung des akademischen Grades eines
DOKTORS DER NATURWISSENSCHAFTEN
von der Fakultät für Physik des
Karlsruher Institut für Technologie (KIT)

genehmigte

DISSERTATION

von

Dipl.-Phys. Martin Printz (geb. Strelzyk)
aus Gleiwitz

Tag der mündlichen Prüfung: 22. Januar 2016

Referent: Prof. Dr. Thomas Müller, Institut für Experimentelle Kernphysik
Korreferent: Prof. Dr. Willem de Boer, Institut für Experimentelle Kernphysik

AUTHOR'S DECLARATION

I declare that the work in this dissertation was carried out in accordance with the requirements of the University's Regulations and Code of Practice for Research Degree Programmes and that it has not been submitted for any other academic award. Except where indicated by specific reference in the text, the work is the candidate's own work. Work done in collaboration with, or with the assistance of others is indicated as such. Any views expressed in the dissertation are those of the author.

SIGNED: .... DATE: ....

DEUTSCHE ZUSAMMENFASSUNG

Der Large Hadron Collider LHC am CERN in Genf ist mit einem Umfang von 27 km und einer aktuellen Schwerpunktsenergie von 13 TeV der leistungsstärkste Teilchenbeschleuniger der Welt. Hierbei werden zwei gegenläufig beschleunigte Protonstrahlen unter anderen im Zentrum von dem Compact Muon Solenoid Experiment (CMS) mit einer Rate von 40 MHz zur Kollision gebracht. Die Kollisionsprodukte bzw. deren Zerfälle werden durch Messung von Sekundärteilchen detektiert und analysiert, wobei das Physikprogramm sowohl Untersuchungen zur Vervollständigung des Standard Models der Teilchenphysik als auch neue Phänomene der Natur umfasst.

Im Zuge einer sequentiellen Erhöhung der instantanen Luminosität von bis zu 5×10^{34} $\mathrm{cm^{-2}s^{-1}}$ sowie der Protonstrahlenergie zu 7 TeV steigen die Anforderungen an die Detektoren enorm. Die erwartete höhere Teilchendichte führt sowohl zu einer erhöhten Strahlenbelastung der Detektoren als auch zu einer größeren Datenmenge. Um diesen Anforderungen während der Hochluminositätsphase des LHC gerecht zu werden, werden die Subdetektoren ebenfalls verbessert beziehungsweise weiterentwickelt. Der CMS Teilchenspurdetektor wird konzeptionell völlig überarbeitet und während einer langen Umbauphase, geplant für die Jahre 2024 bis 2026, komplett ersetzt.

Der CMS Spurdetektor besteht aus Siliziumsensoren, worin die Ionisationsladung von durchgehenden geladenen Teilchen an Elektroden gesammelt wird. Aktuell sind die Elektroden als p-Typ Streifen implantiert in einem n-Typ Substrat. Die Siliziumsensoren des zukünftigen Spurdetektors werden, im Gegensatz zum aktuellen Detektor, aus p-Typ Substrat sein. Diese Entscheidung wurde auf Grund von umfangreichen kollaborativen Messkampagnen und Untersuchen der Strahlenhärte von Siliziumsensorn in Abhängigkeit der Polarität getroffen. Die in dieser Arbeit untersuchten p-Typ Sensoren weisen nach Bestrahlungen bis zu einer Fluenz von $\Phi = 1 \times 10^{15}$ $\mathrm{n_{eq}cm^{-2}}$, welche gegen Ende der Hochluminositätsphase erwartet werden, eine höhere Ladungssammlungseffizienz im Vergleich zur Löchersammlung im n-Substrat auf. Jedoch tretet bei dieser Technologie auf Grund eines positiven Potentials an der Oberfläche auch eine Akkumulation von Elektronen auf, welche die Auslesestreifen ohne zusätzlicher Maßnahmen kurzschließen würde.

Die Optimierung der Technologie, welche eine Unterbrechung dieser Anhäufung von negativer Ladung zwischen den Sammelelektroden unabhängig von der Strahlenbelastung gewährleistet, war ein wichtiger Bestandteil dieser Arbeit. Die Isolationstechnologie der p-Typ Sensoren hat einen signifikanten Einfluss auf das Durchbruchsverhalten der Sensoren. Darüberhinaus wurde innerhalb dieser Arbeit herausgefunden, dass eine zu hohe Dotierkonzentration der Isolationschicht zu zufällig verteilten Ladungsanhäufungen führt, welche von der Detektierlogik als Teilchendurchgänge interpretiert werden. Andererseits sinkt bei einer zu niedrig kalkulierten Dotierkonzentration der Isolationsschicht der Zwischenstreifenwiderstand mit Bestrahlung als direkte Folge der Akkumulationsschicht. Als Resultat sinkt die Auflösung der Sensoren auf Grund von Ladungsteilung auf viele Streifen, sodass der Suchalgorithmus für Teilchendurchgänge keine genauen Werte mehr liefern kann und eine zuverlässige Positionsbestimmung der Teilchenspuren unmöglich macht. Daher wurden drei verschiedene Produktionen mit unterschiedlichen Herstellern der Halbleiterindustrie durchgeführt, wobei Testsensoren mit unterschiedlichen Isolationscharakteristika auf den jeweiligen Wafern platziert wurden. Ein Vergleich vor und nach Bestrahlung wurde durchgeführt, wobei jeweils eine elektrische Qualifizierung als auch Ladunssammlungseffizienzen gemessen und verglichen wurden. Darüberhinaus konnten T-CAD Simulationsstudien Messdaten reproduzieren und die Leistung von Sensoren in Abhängigkeit wichtiger Parameter wie Dotierkonzentration und Dotiertiefe der Isolatiosschicht vorhersagen. Die Kombination der experimentell bestimmten Daten sowie der Ergebnisse aus den Simulationen erlauben die Charakteristika der Streifenisolierung, welche der herausfordernden Umgebung des HL-LHC standhalten kann, vorherzusagen.

Die Funktionalität eines neuen Modulkonzepts ist ein weiterer Schwerpunkt dieser Arbeit. Um die erwartet höhere Teilchendichte auflösen zu können, werden im zukünftigen Spurdetektor die Streifenlänge als auch der Streifenabstand im Vergleich zum aktuellen Spurdetektor verkleinert. Dies resultiert in einer erhöhten Anzahl an Kanälen, wobei auch die Datenmenge, welche aus dem Detektor ausgelesen werden muss, ebenfalls steigt. Daher werden die Signalhöhen im Analogteil des neuen Auslesechips mit einem Schwellenwert auf Modulebene verglichen und in binäre Werte konvertiert. Informationen wie Pulshöhe werden nicht mehr aus dem Detektorvolumen transferiert, was schließlich zu einer Datenreduktion führt.

Darüberhinaus wird der Spurdetektor erstmals auch zur globalen Triggerentscheidung beitragen. Dies wird ebenfalls mit Hilfe des neuen binären Auslesechips CBC realisiert. Dabei korreliert eine Auslesechiplogik Treffer in zwei Sensoren, welche planparallel zu einander mit wenigen Millimetern Abstand in einem Modul angeordnet sind. Auf Grund der Spurkrümmung von geladenen Teilchen in dem 3.8 T starken Magnetfeld des CMS Experiments wird der Versatz von Treffern der beiden Sensoren je Modul gemessen. Der Versatz ist auf Grund der Lorenzkraft direkt mit dem Transversalimpuls korreliert. Übersteigt der Transversalimpuls einen Wert von 2 GeV/c, so wird im CBC Datenstrom ein zusätzlicher Bit (Stub Bit) auf level high gesetzt. Diese Stub Information wird mit der Kollisionsrate von 40 MHz ausgelesen und zur globalen Triggerentscheidung genutzt.

Innerhalb dieser Arbeit wurde ein Auslesesystem basierend auf dem CBC aufgebaut, wobei sowohl der Chip als auch die binären Daten qualifiziert wurden. Hierfür wurden die Chips und Sensoren zu den erwarten Fluenzen bestrahlt und mit Messungen vor Bestrahlung verglichen. Der Chip zeigt sowohl vor als auch nach Bestrahlung eine verlässliche Funktionalität, wobei sich die Korrelationslogik wie erwartet verhaltet. Um dieses auch während realen Konditionen zu beweisen, wurde ein Triggermodul, bestehend aus zwei Testsensoren mit je 254 Streifen und zwei CBCs, konstruiert. Wie zuvor wurden die Sensoren und Auslesechips bis zu den erwarteten Fluenzen bestrahlt und am SPS Beschleuniger am CERN in einem hochenergetischen Teststrahl vermessen. Die Ergebnisse des Experiments mit dem Prototypmodul stimmen mit den Erwartungen überein. Die Korrelationslogik des CBC generiert ein Stub Bit high, wenn der Strahl im Suchfenster der Logik trifft (äquivalent zu einem Teilchendurchgang mit einem hohen Transversalimpuls). Letzteres wurde durch ein Drehen des Moduls im Teststrahl simuliert. Somit konnte das Triggermodulkonzept verifiziert werden, wobei weitere Teststrahlexperimente bereits in Vorbereitung sind.

Die Arbeit gliedert sich in drei Teile. Im ersten werden der Large Hadron Collider und das CMS Experiment vorgestellt. Des Weiteren wird das Phase II Upgrade diskutiert, wobei insbesondere auf den Teilchenspurdetektor von CMS eingegangen wird. Das Verständnis eines Siliziumsensors und dessen Eigenschaften in Anhängigkeit der Bestrahlung werden behandelt sowie die Wechselwirkung von Teilchen mit Materie.

Im zweiten Teil werden experimentelle Ergebnisse hinsichtlich der Strahlenhärte und des Modulkonzepts diskutiert. Zuerst wird die Strahlenhärte der Silziumsensoren in Abhängigkeit der Isolationsschicht sowohl mit Hilfe von T-CAD Simulationen als auch anhand von Messungen behandelt. Dabei wird neben den elektrischen Eigenschaften auch auf die Ladungssammlungseffizienz und die Auswirkung der Strahlenschäden eingegangen. Zusätzlich wird ein neues Sensorkonzept, welches eine weitere Erhöhung der Anzahl der Auslesekanäle auf Sensorlevel erlaubt, vorgestellt. Anschließend werden der CBC und die CBC Messstation thematisiert. Hierbei wird die Stahlenhärte des CBC nach Röntgenbestrahlung erläutert. Im letzten Abschnitt des zweiten Teils wird das Teststrahlexperiment am SPS sowie die ersten Analysen der gewonnen Daten mit unbestrahlten und bestrahlten Triggermodulen vorgestellt.

Im dritten Teil wird eine Zusammenfassung der wichtigsten Erkenntnisse in dieser Arbeit gegeben. Ein Ausblick über bestehende offene Fragestellungen hinsichtlich der Simulation und Triggermodule sowie Vorschläge für ergänzende Messungen und Simulationen schließen den letzten Teil ab.

TABLE OF CONTENTS

Page

I Introduction and Theory

II Analysis

III Appendix

Part I

Introduction and Theory

CHAPTER 1

INTRODUCTION

The Large Hadron Collider at CERN is the most powerful particle accelerator ever built. The collision of high intensity proton beams at a center of mass energy of up to 14 TeV allows the exploration of the undiscovered territory at the TeV scale with great detail. The high energy physics frontier covers detailed Standard Model (SM) physics like the search for the SM Higgs boson, which has been found in July 2012, but also physics beyond the SM like the Supersymmetry or studies of the quark-gluon plasma.

The production rate of certain events is correlated to the instantaneous luminosity which is a measure for the number of detected events within a certain time with respect to the interaction cross-section. In order to increase the statistics by collecting more data, the integrated luminosity is maximized as far as possible. Simultaneously, an increase of the particle energy and the luminosity reveals challenging experimental requirements for the trigger and detector systems present at the LHC.

After a successful Run 1 of the machine between 2010 and 2013, the energy and the instantaneous luminosity of the machine are sequentially increased up to the last, so called Phase II Upgrade planned for the years 2024 and 2025. The high luminosity LHC will provide particle beams with the final 14 TeV center of mass energy at an instantaneous luminosity of 5×10^{34} cm^{-2}s^{-1}, which is five to seven times the nominal design luminosity. In the course of the Upgrade, the experiments will face extraordinary radiation environments and particle densities and will also have to be upgraded in order to cope with the challenging demands.

The Compact Muon Solenoid (CMS) at CERN is a general purpose experiment with a diverse physics measurement program. It is built of several subdetectors. The innermost part consists of the pixel detector and the silicon strip tracker. The latter will be replaced completely during the Phase II Upgrade by a new layout in which a different silicon sensor technology and module design will be deployed.

Silicon strip and macro-pixel sensors in the future CMS experiment will face a fluence of up to $\Phi = 1 \times 10^{15}\ \mathrm{n_{eq}cm^{-2}s^{-1}}$ after an integrated luminosity of 3000 $\mathrm{fb^{-1}}$ and 10 years of operation in HL-LHC conditions. Therefore, the radiation hardness of the sensors must guarantee high charge collection efficiency which degrades with increasing radiation damage. Extensive radiation damage and charge collection studies have been exercised in order to find the most suitable sensor material and layout which will withstand the harsh operation environment. The key technology has been decided to be p-type substrate in which electrons with a high mobility and less trapping effects are collected by the readout electrodes. However, this technology requires detailed investigations of the necessary isolation layer which prevents a build-up of an accumulation layer below the sensor surface which would directly lead to a lower resolution of the tracker.

Furthermore, an elevated particle or track density requires a higher granularity. Hence the strip length of the sensors and the strip pitch will be reduced resulting in more channels and as a direct consequence more data which has to be transmitted out of the tracker volume. In contrast to the current tracker, the signal level will be compared to a threshold by the new binary readout chip CBC and just the binary hit information will be processed to the next instance.

In addition, the tracker will contribute to the global Level-1 trigger decision. The contribution will be achieved by the correlation logic of the binary readout chip which detects hits on two stacked sensors in one module. Depending on the particle curvature in the CMS 3.8 T magnetic field, the transverse momentum p_T of the traversing particles is estimated on-chip and compared to a programable threshold. Simulations indicate that rejecting hits from low momentum particles in the range below 2 GeV/c reduces the data amount by several orders of magnitude.

The radiation hardness of silicon strip sensors for the Phase II Upgrade was investigated with respect to the breakdown voltage and charge collection efficiency. Furthermore, the concept of the transverse momentum discriminating trigger modules was studied.

In chapter 2, the Large Hadron Collider at CERN and the CMS experiment will be introduced in more detail. Especially the different readout options (analogue vs. binary) of the current and the future tracker are discussed. Chapter 3 covers the Phase II Upgrade plans of the CMS Tracker. Here, the new current baseline of the future tracker layout is described as well as the concept of the trigger modules, both with the background of the fluence and dose which is estimated with the help of FLUKA simulations. Chapters 4 and 5 deal with the concept of particle tracking detectors equipped with silicon sensors. In particular, the radiation damage as well as the impact on the sensor performance are discussed. A brief summary of extensive measurement campaigns within the CMS Tracker and RD50 collaborations leading to the decision on the future sensor substrate polarity is presented.

The analysis and results part starts with T-CAD simulation studies. Main interest of the simulations was, firstly, to reproduce data of measured sensors before and after irradiation. Secondly, predictions of the breakdown and charge collection efficiency were performed with the help of validated radiation damage models which allow accurate simulation studies of irradiated samples up to a fluence of $\Phi = 1.5 \times 10^{15}\ \mathrm{n_{eq}cm^{-2}s^{-1}}$. In this study, several wafers with different sensor layouts and test structures were designed. The workflow and the most important sensor layouts are covered in chapter 7. After the production of the most promising sensor layouts following the simulation studies, irradiation studies were conducted. Chapter 8, deals in particular, with the results with respect to the p-type isolation which significantly affects the overall sensor performance. A recommendation on the isolation technique as a consequence of the simulation and irradiation studies is presented.

In chapter 9, the CMS binary chip CBC will be introduced in more detail. A setup was built in order to investigate both the CBC and the performance of a small scale readout system based on the CBC connected to non-irradiated and irradiated silicon strip sensors. In order to prove the concept of the low p_T discrimination, 2S mini modules were built and tested in test beam conditions. The layout of the mini modules, the test beam setup and goals as well as the results showing the efficiency of the p_T discrimination are summarized in chapter 10. A conclusion on the presented studies and an outlook are given in chapter 11.

CHAPTER 2

LHC AND CMS

The Large Hadron Collider (LHC) at the European Organization for Nuclear Research (CERN) [CER] near Geneva/Suisse is the world's largest and most powerful particle accelerator and has been designed to collide counterotating high-intensity proton beams with a center of mass energy $\sqrt{s}$ of up to 14 TeV at a frequency of up to 40 MHz. The proton bunches collide in the center of the Compact Muon Solenoid (CMS) [The08] experiment and the products of the collisions are detected in several sub-detectors of CMS.
In this chapter, the LHC and the CMS experiment will be briefly introduced.

2.1 The Large Hadron Collider

The LHC is the last accelerator of a complex of machines with increasingly higher energies, see figure 2.1. It is filled with protons from pre-accelerators and accelerates the particle bunches to an energy of each beam up to about 7 TeV, resulting in a center of mass energy of $\sqrt{s}$ of 14 TeV. In order to achieve these high beam energies, the LHC has a circumference of approximately 27 km, since the maximum energy is a function of the radius and the magnetic field of the superconducting magnets. It is roughly 100 m below ground level due to geological considerations and situated between Lake Geneva and the Jura mountains.
In table 2.1, the kinetic energy and speed of the particles after each accelerator in the chain are presented. This high energy and speed in a circular accelerator allows collisions of hadrons only because the about 2000 times lighter electrons would lose to much energy per circulation due to synchrotron radiation. The most important parameters of the LHC are listed in table2.2.

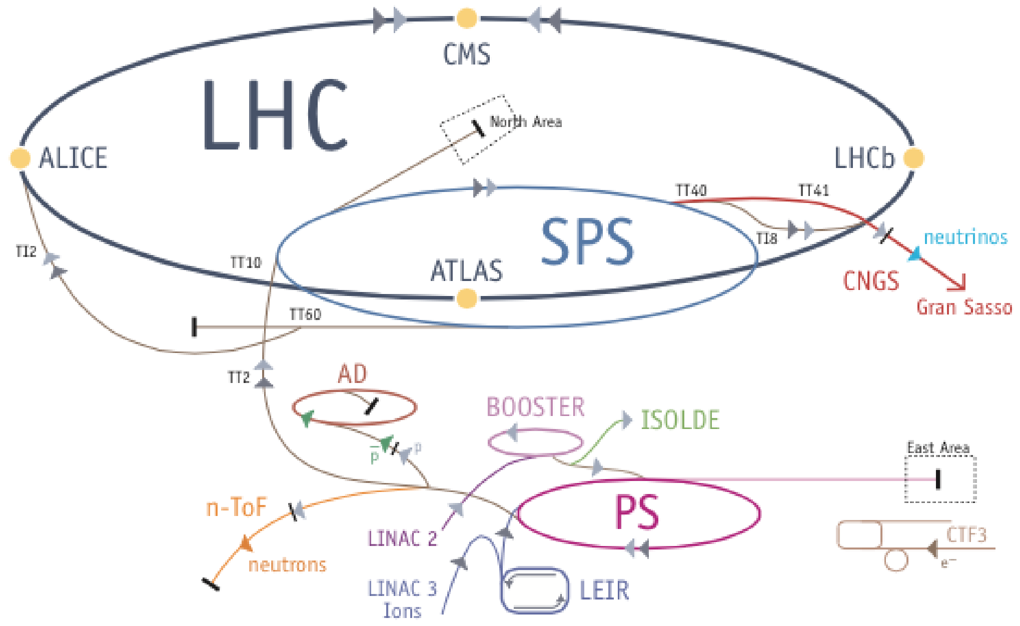

Figure 2.1: The LHC complex at CERN. First, decoupled protons from hydrogen atoms are accelerated in the Linac2 and than injected into the PS Booster to be further accelerated in the PS and SPS machines. After that, the particles have a kinetic energy of about 450 MeV and a speed of 99.9998 % of light speed. At this energy, the particle bunches can be injected into the LHC where they reach their nominal energy and speed, [CER09].

Table 2.1: Kinetic energy and speed of a proton after each accelerator, [CER09].

Kinetic energy of a proton	Speed (%c)	Accelerator
50 MeV	31.4	Linac 2
1.4 GeV	91.6	PS Booster
25 GeV	99.93	PS
450 GeV	99.9998	SPS
7 TeV	99.9999991	LHC

2.1.1 Definition of luminosity $\mathscr{L}$

One important quantity in table 2.2 in respect to statistics for data analysis of very rare events is the luminosity which, after the energy, is the second most important qualification of a beam collider. The luminosity is the proportionality between the number of events per second dR/dt and the cross section σ_p of an event, which is a measure of the probability that an event occurs, [HM06]:

$$\frac{dR}{dt} = \mathscr{L} \cdot \sigma_p. \tag{2.1}$$

The unit of the luminosity is $\mathrm{cm}^{-2}\mathrm{s}^{-1}$.

Table 2.2: Importamt parameters of the LHC, [CER09]

Quantity	number
Circumference	26659 m
Dipole operating temperature	1.9 K
Number of magnets	9593
Number of main dipoles	1232
Number of main quadrupoles	392
Number of RF cavities	8 per beam
Nominal energy for protons	7 TeV
Peak magnetic dipole field	8.33 T
Min. distance between bunches	7 m
Design luminosity	10^{34} cm^{-2}s^{-1}
No. of bunches per proton beam	2808
No. of protons per bunch	1.1×10^{11}

2.1.2 Definition of integrated luminosity $\mathscr{L}_{\text{int}}$

In order to define a measure for the real observed events, the integrated luminosity has to be taken into account after [HM06] which is:

$$\mathscr{L}_{int} = \int_0^T \mathscr{L}(t')dt', \tag{2.2}$$

and hence can be related to:

$$\mathscr{L}_{int} \cdot \sigma_p = \text{number for events of interest.} \tag{2.3}$$

The aim of the operation of a collider must be to optimize the integrated luminosity.

2.2 The Compact Muon Solenoid

In figure 2.1 one can see that the machine provides collisions in several experiments at CERN. The four most prominent experiments indicated in the figure are: The Compact Muon Solenoid (CMS), the Toroidal LHC Apparatus (ATLAS) [ATL], the LHC-b experiment [LHC] and A Large Ion Collider Experiment (ALICE) [ALI]. CMS and ATLAS are the two general purpose experiments with a congruent measurement program. Both complex experiments collect data and thousands of scientists search with these data for new particles, like the Higgs boson, new phenomenology in physics as well as for supersymmetry or extra dimensions. The asymmetric design of the LHC-b detector allows the study of B mesons which most likely traverse the detector in forward direction. B mesons are interesting due to their behavior which is linked to a range of quantum phenomena. ALICE studies the conditions shortly after the big bang with the quark gluon plasma, the very early state of material in the universe.

A detailed overview of the physics program of the experiments at the LHC is given in [Gia04].

2.2.1 Requirements for the CMS detector

In order to face the tremendous physics program at the LHC, the CMS detector has to fulfill several requirements. A short summary of the requirements has been extracted from [The08]:

- A robust, precise and efficient reconstruction of trajectories of charged particles
- Radiation hard detectors and electronics due to the harsh radiation environment
- Sufficient muon identification and momentum resolution as well as the determination of the muon charge
- Efficient track reconstruction, especially for the inner tracker (pixel detector) and sufficient trigger capability
- Good electromagnetic energy resolution and a wide range coverage
- High missing transverse energy resolution

These requirements were driving the layout and construction of the CMS experiment leading to an onion-like assembly of sub-detectors, each with a dedicated task in order to determine all necessary parameters of the traversing particles for further physics analysis. A short description of the layout and the sub-detectors is given in the next subsection.

2.2.2 General design of the experiment

Figure 2.2 indicates the CMS detector from perspective view where all sub-detectors are visible. The experiment is about 21 m long, 15 m wide and 15 m high. The overall weight is roughly 14000 tonnes in which 12000 tonnes are ascribed to the iron/steel return yoke in order to guide and form the 4 Tesla strong CMS magnetic field. The magnetic field allows the determination of a traversing particle's momentum by tracking its bent path through the detector. The size of the experiment is entitled to accurate calculations of the particle momentum by taking several measurements along its path. Furthermore, the partially very high energies of traversing particles have to be absorbed by a huge amount of material, again leading to the actual size of the experiment. Describing the detector from the outer to the inner sub-detectors one can divide the experiment as follows:

- The muon system [Tey10]: Besides the detection of muons, the muon system also triggers and measures the transverse momentum. In order to achieve the requirements, the system has been designed with three different technologies. It consists of drift tubes (DT), cathode strip chambers (CSC) and resistive plate chambers (RPC). All three technologies have in common that traversing particles ionize the gas contained in the tubes and plates. The knocked off electrons and positive ions drift along the electric field inside the detectors leading to a position determination and trigger capability due to closely spaced wires.

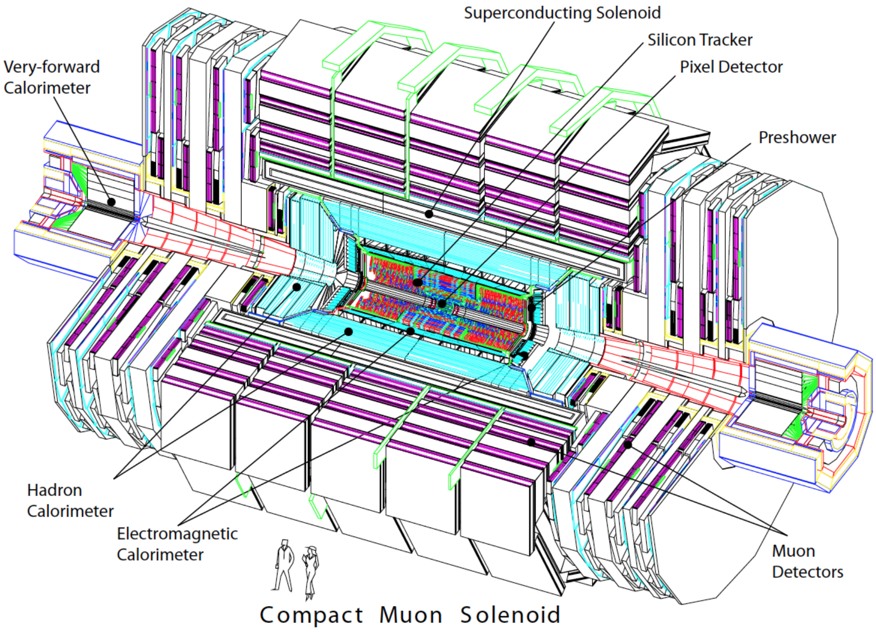

Figure 2.2: The CMS detector from perspective view [The08].

- The solenoid magnet and iron return yoke [The10]: An important key role of the CMS experiment is its superconducting magnet enclosed inside a 12,000 tonnes iron return yoke. The yoke ensures the homogeneity of the magnetic field in the tracker volume and the return of the magnetic flux to the solenoid, thereby reducing the stray field. With the 3.8 Tesla strong magnetic field, the determination of particles' momenta due to their bent paths inside the detector is implemented.

- The hadron calorimeter [CMS10b]: Consisting of sampled massive absorbers and plastic scintillators which produce a blue-violett light pulse in repeated layers, the hadronic calorimeter measures the energy of hadrons like protons, neutrons, kaons and pions.

- The electromagentic calorimeter [CMS10a]: Electromagnetically interacting particles like electrons and photons deposit their energy in the electromagnetic calorimeter producing showers. The requirement for high energy resolution is stringent in oder to be sensitive on the Higgs boson decay into two photons. Therefore, lead tungstate crystal scintillators are used in which electrons and photons deposit energy. The produced scintillation light is proportional to the particle energy.

- Tracking detector [ftC14]: About 206 m^2 of silicon sensors divided into a pixel detector in the inner part and a strip detector surrounding the pixel modules represent the tracker of CMS. Positioned within the solenoid magnetic field, the tracker is able to provide momentum

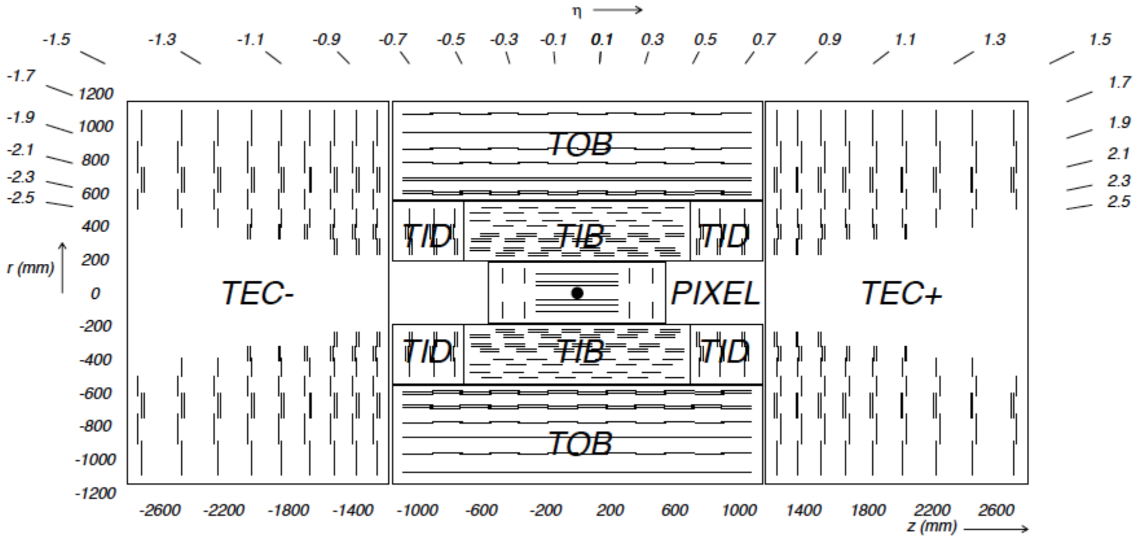

Figure 2.3: Schematic cross section through the CMS tracker. Each line represents a detector module.

information of passing charged particles by reconstruction of their bent paths due to the Lorenz force. A more detailed description of the tracker is given in the next section.

2.2.3 The inner tracking system

Informations presented in this section are mainly derived from [The08], if not stated otherwise. In order to reliably distinguish between the high density of particle paths, the tracker provides position measurements with an accuracy of about 10 μm. Such high track resolution requires a dense arrangement of thousands of silicon sensors at which the distance between the readout channels per sensor is in the range of a few tens to hundreds of micrometers, depending on the module position in the tracker. Simultaneously, the construction is conditioned to be as lightweight as possible for the purpose of minimizing multiple scattering, bremsstrahlung and nuclear interactions. On average, approximately 1000 charged particle tracks out of 20 proton-proton events per bunch crossing (pile-up) at up to 40 MHz occur. Therefore, the tracker must feature high granularity and fast response. These constraints have been implemented in a 5.8 m long tracker with a diameter of 2.5 m surrounding the center of the interaction point.
At the design luminosity of $10^{34}\text{cm}^{-2}\text{s}^{-1}$, a hit rate of 1 MHz/mm^2 at a radius of 4 cm from the collision point falling to 3 kHz/mm^2 at the radius of 115 cm was expected. Therefore, the tracker layout is comprised of a high resolution pixel detector with three cylindrical layers at 4.4 cm, 7.3 cm and 10.2 cm from the interaction point. In order to cover the forward region as well, two disks equipped with pixelated sensors complement the vertex detector.
With falling particle hit density, the need for high granularity decreases slightly, hence the pixel detector is surrounded by a silicon strip tracker with lower but sufficient resolution with the

advantage of the need for less electronics. The strip tracker is divided into inner barrel layers (TIB) with inner end caps (TID) where both TIB and TID are surrounded by the tracker outer barrel layers (TOB). Comparable to the pixel detector, the strip tracker is also complemented by so called end cap disks (TEC). As the strip modules arrangement varies a lot in thickness, pitch and layout of the sensors, the details are not further discussed for simplicity but can be looked up in chapters 3.1 and 3.2 in [CMS98]. A schematic cross section of the CMS tracker is shown in figure 2.3. The choice for the tracking system layout keeps the occupancy at or below 1% in order to ensure reliable distinction of particle paths. Additionally, the TID/TEC cover the pseudorapidity $\eta = -\ln\tan(\theta/2)$ up to $|\eta| < 2.5$, where the polar angle θ is measured from the z-axis. This range is required by the LHC physics program in order to achieve precise reconstruction of trajectories of charged particles which also fly in the very forward direction [CMS].

2.2.4 Analogue pipeline ASIC APV25

The silicon strip sensors generate signals which are amplified and shaped by the analogue APV25 read-out chip with 128 channels fabricated in 0.25μm CMOS technology [ea00], [FJM$^+$01]. In combination with thin gate oxide and layout adjustments, this technology ensures radiation hardness and low noise with a high circuit density. Detected signals from the sensors are integrally amplified. The information of the pulse height of signals on the strips is important and used too. A comparison of the signal heights with the charge center-of-gravity method improves the position resolution to sub-strip range. On the example of two strips one can calculate the resolution σ_{x} to:

$$\sigma_x \propto \frac{p}{SNR} \quad \text{with} \quad x = x_1 + \frac{h_1^2}{h_1 + h_2}(x_2 - x_1). \tag{2.4}$$

X_1 and x_2 denote the positions of the first and the second strip, where h_1 and h_2 stand for the signal heights on the corresponding strip. P is the strip pitch and SNR is the signal to noise ratio. Hence, a low strip pitch and a high SNR result in a higher resolution of the hit detection.

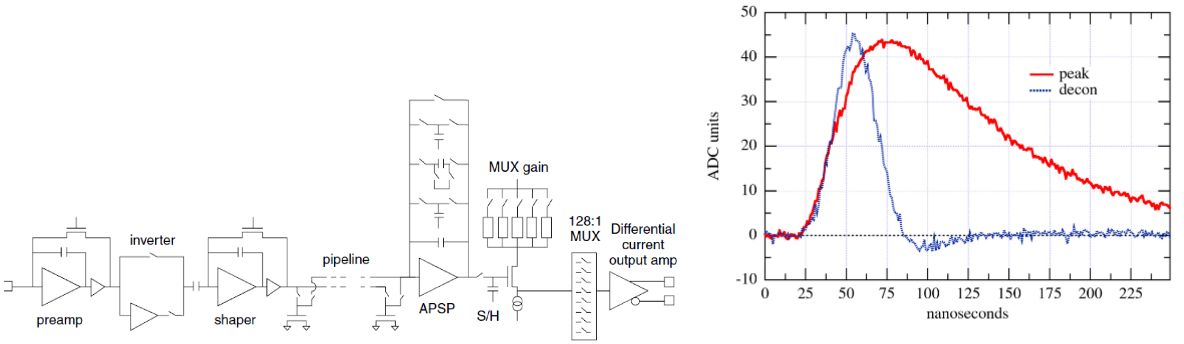

(a) Schematics for one APV25 channel

(b) Pulse shapes for peaking and deconvolution modes.

Figure 2.4: The APV25 logic and pulse shapes for two different modi operandi [FJM$^+$01]

The resulting pulses are formed by a CR-RC shaper with a peaking time of 50 ns. The APV25 contains a 192 column analogue memory into which data is stored with the LHC 40 MHz frequency and read out after the trigger decision. Two modi operandi have been implemented in the chip, the peaking and the deconvolution mode. In the first mode, each cell is read out separately with a peaking time of 50 ns which is too slow for accurate time distinction of events at the LHC frequency. In the deconvolution mode, the APSP[1] reads tree channels sequentially and a weighted sum is the output, see figure 2.4(b). This re-shaping results in a 25 ns peaking time which is suitable to the collision rate at LHC experiments. The output is then sampled and held and directly fed into the 128:1 Multiplexer with one resulting differential current output which is then transferred out of the detector by optical fibers.

2.2.5 The CMS trigger system

At the current full LHC luminosity, the CMS experiment records more than 1000 particle tracks within about 20 pile-up events with 25 ns bunch crossing time. As the typical event size is 1-2 MByte, the data throughput would be around 1TByte/s for 10^9 events per second [Jei14]. This amount of data cannot be read out with the LHC frequency and successfully processed. Therefore, a two stages trigger system for the CMS Experiment has been designed and implemented. The main task is the selection of high interest events while suppression of events of less interest has to be given.

The first level in the trigger decision is the Level-1 (L1) trigger which is implemented in ASICs[2] and programmable FPGAs[3]. L1 reduces the data stored in 3.2 μs deep front-end pipelines from the 40 MHz LHC frequency to 100 kHz. After a positive L1 decision (L1 Accept), data corresponding to a certain bunch crossing is fully read out and processed by the High-Level Trigger (HLT). The latter is a completely software based trigger system where full reconstruction of the events and data storage are executed with an overall event selection of about 100 Hz.

The existing L1 Trigger uses just a part of the full detector information for the decision provided by the muon sub-detector and the calorimeters. Data from the tracker is only available for the HLT after a positive L1 decision.

---

[1] Analogue Pulse Shape Processor

[2] Application-Specific Integrated Circuit

[3] Field Programmable Gate Array

CHAPTER 3

THE PHASE II UPGRADE

The Large Hadron Collider (LHC) accelerator is being upgraded in several steps. In the next step, the machine will increase the energy of accelerated protons from 6.5 TeV to 7 TeV and the delivered luminosity which was introduced in 2.1.1. Higher energy and collision rate ensure an extended physics program for the experiments situated at CERN. In particular, very rare events with small cross sections and physics beyond the standard model of particles need higher statistics ensured by the increased luminosity. In order to fully profit from the high luminosity LHC (HL-LHC), the CMS experiment undergoes a step-by-step upgrade too. This includes the sub-detectors as well as the trigger system. The following sections shortly describe the upgrade plans of LHC and CMS with respect to the Phase II Tracker upgrade.

3.1 LHC upgrade in a nutshell

The LHC ramped up its energy up to 8 TeV during its first four years of operation. The design peak luminosity of 10^{34} cm^{-2}s^{-1} has almost been reached with 7.7×10^{33} cm^{-2}s^{-1} at the end of November 2012. The first long shutdown called LS1 started in February 2013 with the aim of increasing the LHC energy of pp collisions to $\sqrt{s} = 13 - 14$ TeV and the peak luminosity to the design value. A further long shutdown is scheduled for 2019 (LS2) where the injector and the LHC will upgrade to twice the design luminosity of 2×10^{34} cm^{-2}s^{-1} at a center of mass energy of $\sqrt{s} = 14$ TeV with a 25 ns bunch spacing. At this point, the luminosity will already reach values beyond the design luminosity. In the subsequent run, the machine will deliver about 300 fb^{-1} of pp collisions [RR14]. Due to its interesting discoveries, high potential for precise measurements as well as new physics frontiers, the LHC physics program will be prolonged for an additional 10 years after the last planned long shutdown during the LS3 scheduled for 2024. During this

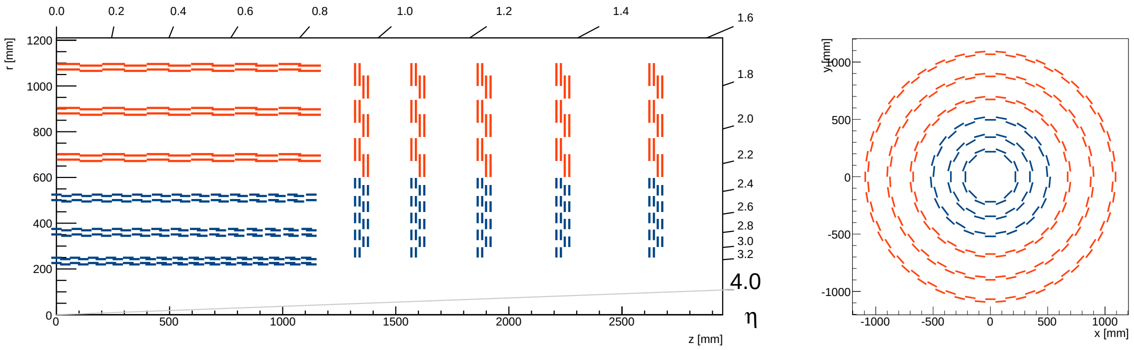

(a) Quarter section of the new tracker layout - cut at $\Phi = 0$

(b) Cut at Z= 0

Figure 3.1: The sketches show the current CMS tracker upgrade baseline layout. Blue lines indicate the positions of the PS modules whereas the red lines represent the 2S modules [Mer14].

future run, the aim is to collect 3000 fb^{-1} of data.

3.2 Upgrade of the CMS Tracker

As a consequence of this long physics run with high luminosity, the CMS detector has to be upgraded as well in order to manage the increasing demand for radiation tolerant subdetectors. In particular, the whole CMS tracker, including the pixel detector and strip detector, will be replaced completely (but some services) during the long shutdown in 2024 because the current tracker would suffer from thermal runaway of the silicon detectors due to the steadily increasing leakage current as a consequence of the radiation damage. For years now, the CMS tracker collaboration has been investigating several material technologies for silicon detectors which have to be able to withstand the harsh expected radiation environment. Besides the radiation tolerance of the silicon detectors, the tracker layout has to be redesigned in order to assure sufficient reconstruction of particle tracks despite the increasing track density with the overall aim of material reduction to achieve a low radiation length. Thus, the channel granularity must be increased to keep the overall occupancy of the detector below 1%. Moreover, information for the trigger system of the CMS experiment have to be processed already at tracker level in order to achieve a Level-1 trigger rate of a few hundreds kHz. This fact requires, in comparison to the trigger system described in 2.2.5, a completely new detector module layout and readout ASICs (see section 3.2.3).
Some of the demands mentioned in this section were investigated and will be described in more detail in the following chapters.

3.2.1 Tracker layout for HL-LHC with trigger contribution

In comparison to the tracker layout shown in figure 2.3, the new design will cover the pseudorapidity up to $|\eta| < 4.0$, hence the capabilities of CMS to cover a wider physics program will be

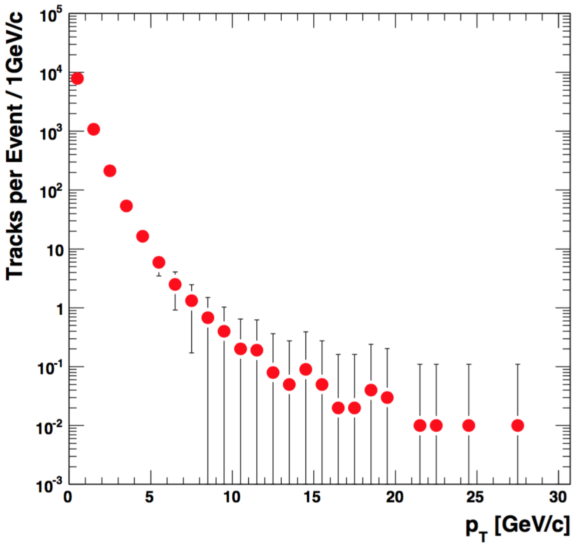

Figure 3.2: The p_T spectrum (averaged per event) for all minimum bias particles that generate stubs in a stacked layer under HL-LHC pileup conditions. Results are for a stacked layer at 25 cm with a sensor separation of 1 mm and a row correlation window of 3 strips [PH10].

enhanced. Furthermore, the modules will be double-sided, meaning that two stacked sensors with a separation of several millimeters depending on the module placement in the tracker will be connected to common hybrids equipped with the readout electronics. Two options for these modules will be implemented. The “PS module“ will be built of two stacked sensors in which one sensor will be a pixelated and the other one a microstrip sensor. PS modules will cover the range of the tracker between R~20 cm and R~60 cm . The “2S module“ will consist of two stacked microstrip sensors and will be mounted in the outer regions of the tracker at ~R > 60 cm .

The baseline tracker layout for the HL-LHC era is sketched in figure 3.1. Figure 3.1(a) shows the quarter section of the tracker. Point (0,0) is the interaction point of the proton beams in the very center of the experiment. Figure 3.1(b) is the front view of the future tracker. This layout is the result of extensive simulations using Monte-Carlo methods and a special software package [G. 14]. Further studies on the most promising geometrical position of the modules are ongoing as well as the search for the optimal pixel detector geometry. The latter will not be discussed any further.

3.2.2 Concept of p_T trigger modules

The L1 trigger will be upgraded to a rate of ~750 kHz and a latency of 12.8 μs. The new tracker layout takes the L1 trigger into account and allows the addition of track information to the L1 decision. The data from the modules is read out with 40 MHz rate which would result in a huge bandwidth. In order to achieve the goal of track information at L1, the p_T trigger modules concept has been chosen.

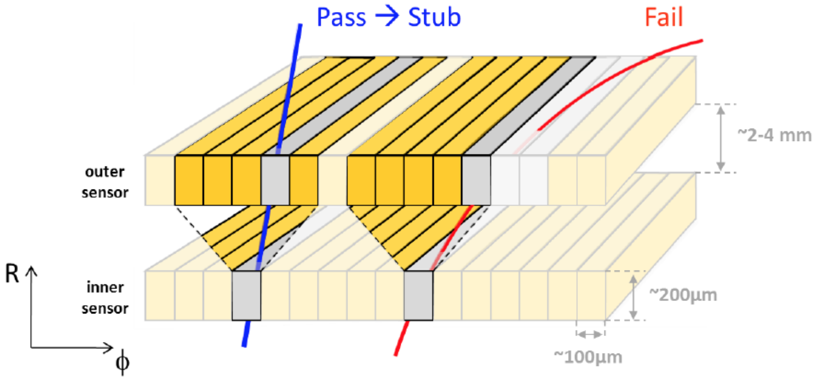

Figure 3.3: The sketch illustrates the trigger module concept described in 3.2.2. The blue track of a particle passes the searching window in the outer tracker and a stub is generated. The red track fails due to low particle momentum [ea14a].

Charged particles are bent on their track in the 3.8 T magnetic field depending on their transverse momentum following the Lorentz law. With two stacked sensors and common readout ASICs with hit correlation logic, the data throughput can be reduced by one order of magnitude if a threshold of 2 GeV is applied [AM12] by rejecting particles with transversal momentum below 2 GeV at module level.

The rejection itself is achieved by correlating hits of two closely-spaced sensors. The spacing will be 1.6, 2.6 and 4.0 mm for the PS and 1.8 respectively 4.0 mm for the 2S modules. In this scope, the module position in the tracker is the decisive factor. The front-end electronics at the edges of the modules are capable of detecting the signals from both sensors in the module. After a hit of the inner sensor from the interaction point of view, the correlation logic of the ASICs searches for a hit in a programable searching window in the outer sensor. The window size is programable in ±1 strip pitches up to ±8 times the pitch. If the hits in both sensors are within the window, a stub is generated which implies a particle with high momentum and of interest. In case of a hit outside the searching window due to a low p_T particle and hence strong bending, the track will be rejected. As for the sensor spacing within one module, the size of the searching window depends on the module position. The stub data is processed at bunch crossing rate while the hit data is stored in the up to 12.8 μs (512 × 25 ns bunch crossing rate) deep front-end pipeline which will be read out after the trigger L1 accept. The stub finding logic is illustrated in figure 3.3.

3.2.3 CMS Binary Chip (CBC) - ASIC for 2S p_T modules

The new ASICs for the 2S trigger module will be the CMS binary chip (CBC). After a first successful submission of the CBC1 and several tests of it, the CBC2 which is the current version of the ASIC has been designed in 130 nm CMOS process and delivered in early 2013. The CBC2 is a 254-channel binary readout front-end with correlation logic and optimized for the application in 2S modules. The analogue front-end consists of a preamplifier, a gain amplifier and a comparator,

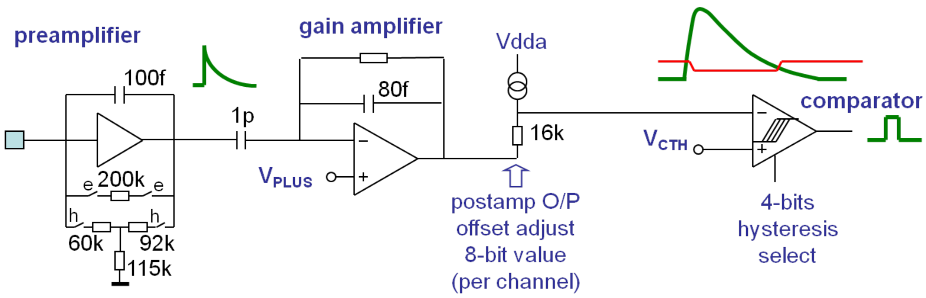

Figure 3.4: Analogue front-end scheme of the CBC for one channel [Bra13].

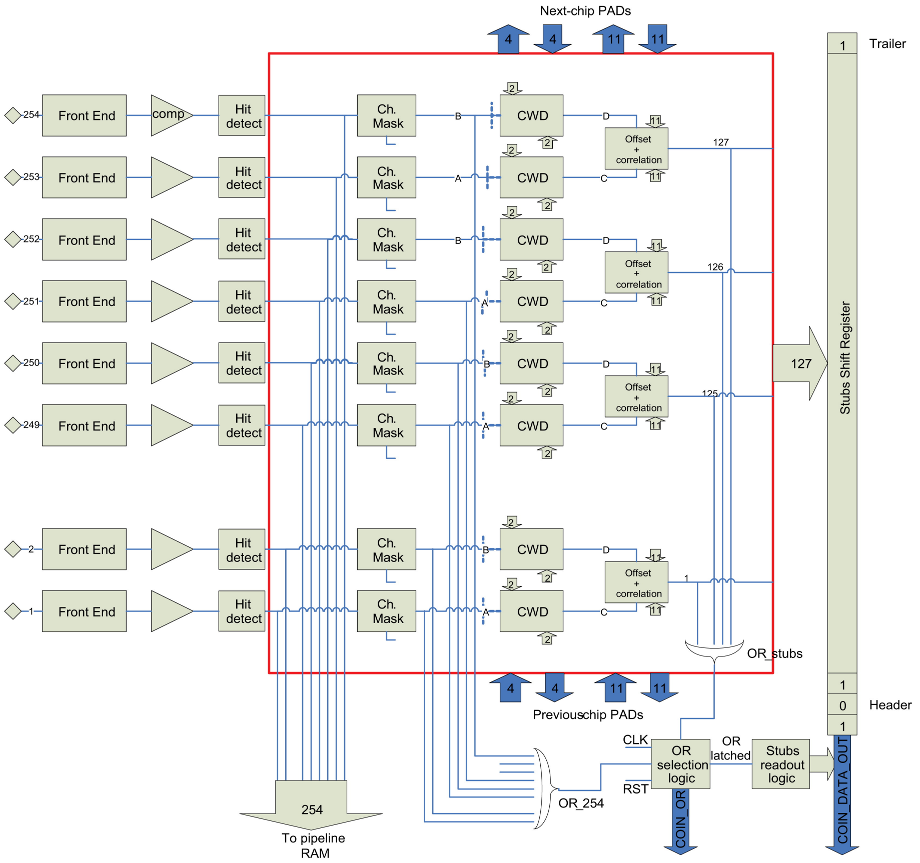

Figure 3.5: The CBC stub finding logic for correlation of hits [ea14b].

see figure 3.4. The channels of the chips are bonded alternately to the inner and outer sensor, allowing the correlation of hits in both sensor levels. After detection of the signal, the output voltage of the preamplifier is again amplified by the capacitive gain respectively post-amplifier. The following pulse is detected by the comparator if the pulse height exceeds the programmable comparator threshold (vcth). A binary “1“ indicating a hit and a “0“for no hit will be produced for

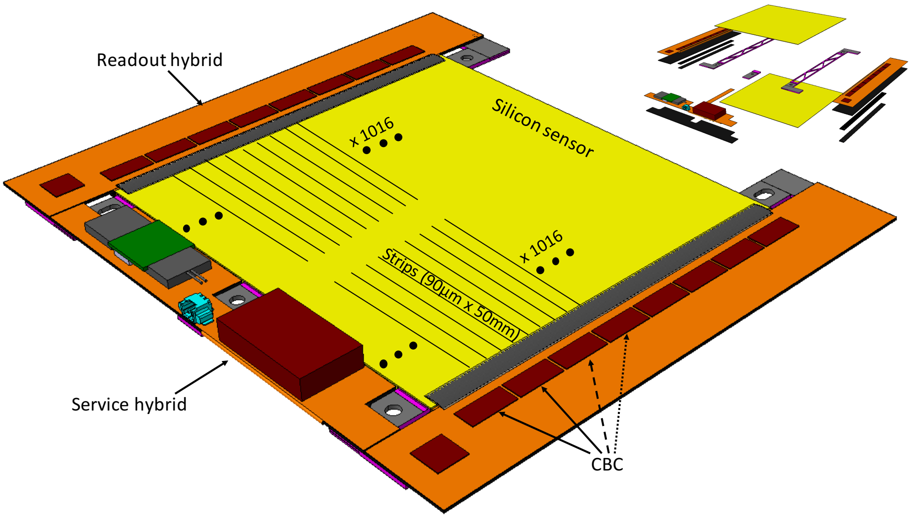

Figure 3.6: The 2S trigger module from perspective view and an in picture exploded view to visualize the arrangement of two sensors [Ros15].

each channel at bunch crossing rate and sampled into the pipeline RAM.

The stub finding logic is shown in figure 3.5. After hit detection, the cluster width discrimination (CWD) rejects huge cluster widths[1] depending on the CBC setting. The CWD can be varied between one and three strips. Clusters bigger than 3 strips are always discarded as they are attributed to low momentum particles. The center strip of the CWD output is than the reference position of the inner sensor and the correlation logic checks for valid clusters (within the searching window) in the outer sensor. After validation, the strip of the inner sensor is considered as a valid stub [ea14b]. The outputs for all channels of the coincidence logic are ORed and latched into the stub shift register if a stub is found. This is a test feature of the current chip version and a full stub readout will be implemented in the next and probably last version (CBC3, scheduled for 2016).

3.2.4 2S p_T modules

The 2S trigger modules will consist of two approximately 10 cm × 10 cm silicon strip sensors. A CAD drawing of the current module design is shown in figure 3.6. The strips of the sensors (each 2×1016 strips) are parallel to each other in order to assure the stub finding logic. A feature of the sensors is the segmentation of the strips into 90 μm × 5 cm strips. This increases the granularity accounting for the high track density. The 16 CBC ASICs are bump-bonded to two flexible readout hybrids. The readout hybrids feature routing lines to wire bond pads. This arrangement assures the connectivity of the inner and outer sensor to one hybrid or rather one chip row. Therefore, two hybrids with each 8 CBCs at the opposite ends of the sensors are necessary. In addition, a

---

[1] Number of simultaneously firing adjacent strips

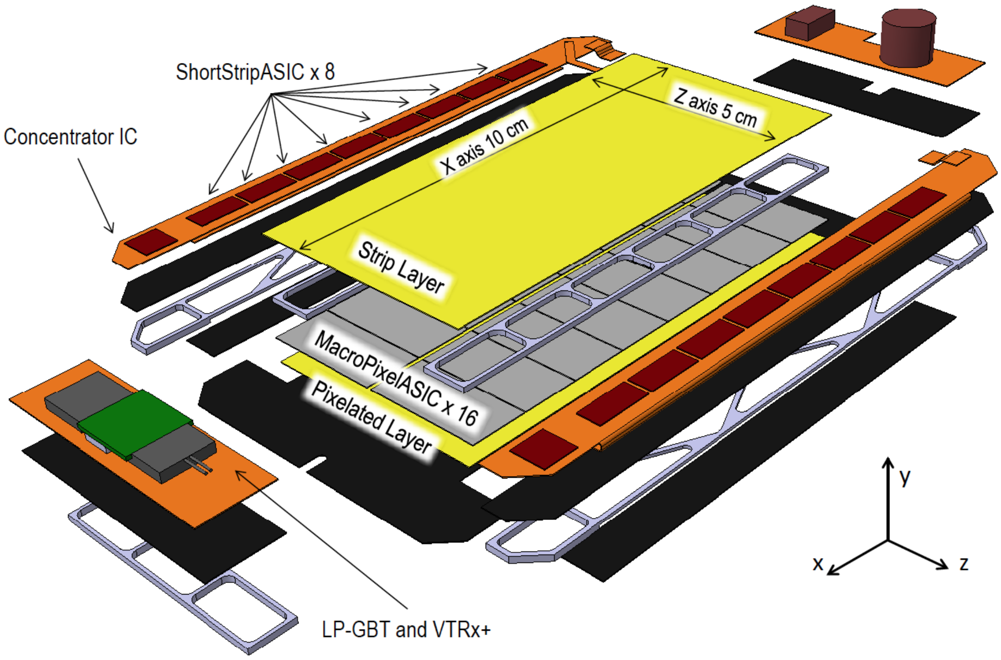

Figure 3.7: Exploded view of the current PS module baseline [CMK+14].

service hybrid holding the powering, optical converter and a 5 Gbs link is mounted. The design is driven by several needs concerning heat transfer, low mass to keep the radiation length minimal and a reproducible production. Optimization using finite element analysis is ongoing.

Considering the 2S module, within this thesis radiation tolerant sensor technologies have been optimized and studied. Furthermore, a setup with a dedicated CBC readout chain has been build[2] and the prove of principle of such trigger modules has been investigated during test beam conditions. The results are discussed in the later chapters.

3.2.5 PS p_T modules

Comparably to the 2S module concept, the PS module provides high p_T particle information by correlation of hits on two sensors. In the case of the PS module however, the inner sensor is a macro-pixel sensor with a cell size of 100 μm × 1.4 mm. The choice for PS modules for the inner three layers of the outer tracker barrel is due to the higher density of tracks next to the interaction point where a higher granularity and information along the y coordinate is necessary. This concept requires additional readout ASICs for both, the pixelated sensor and the strip sensor. 16 Macro Pixel ASICs (MPA) will be directly bump-bonded to the 5 cm × 10 cm pixelated sensors. The strip sensor ASICs (SSA) are not yet defined. The strip sensor will be segmented in 100 μm

---

[2] within the CMS tracker collaboration

× 23 mm and wire-bonded to the readout hybrid. The cross section of a possible layout of the PS module is illustrated in figure 3.7.

High particle density at increased luminosity requires radiation tolerant sensors. In addition to the strip sensors, for the first time the pixelated sensors for the PS module application have been designed, produced and investigated on the electrical properties and signal quality before and after irradiation.

3.3 Radiation environment

In the previous sections the upgrades of the LHC and the CMS have been described shortly. The increased instantaneous luminosity after 2024 is equivalent to a higher particle hit density per area in the detector. FLUKA studies allow the simulation and estimation of the expected particle fluence for the HL-LHC era. With the help of this tool, the radiation level of the CMS cavern can be visualized. The following presented studies on radiation tolerant sensor and ASICs refer to the estimations from the FLUKA plots. The Monte Carlo estimation of the expected fluence for proton beam energies of 7 TeV with the new tracker layout is shown in figure 3.8 [FLU15]. Like in figure 3.1, the interaction point of the proton beams is at point (0,0). The fluence is given in 1 MeV neutron equivalent damage in silicon. This unit is taken in order to compare different particle energies and interaction mechanisms following the NIEL[3] damage law. Hadrons, neutrons, photons and electrons are implemented depending on their spectra. The maximum fluence on the sensors depends on their position in the tracker. Clearly, the innermost and very

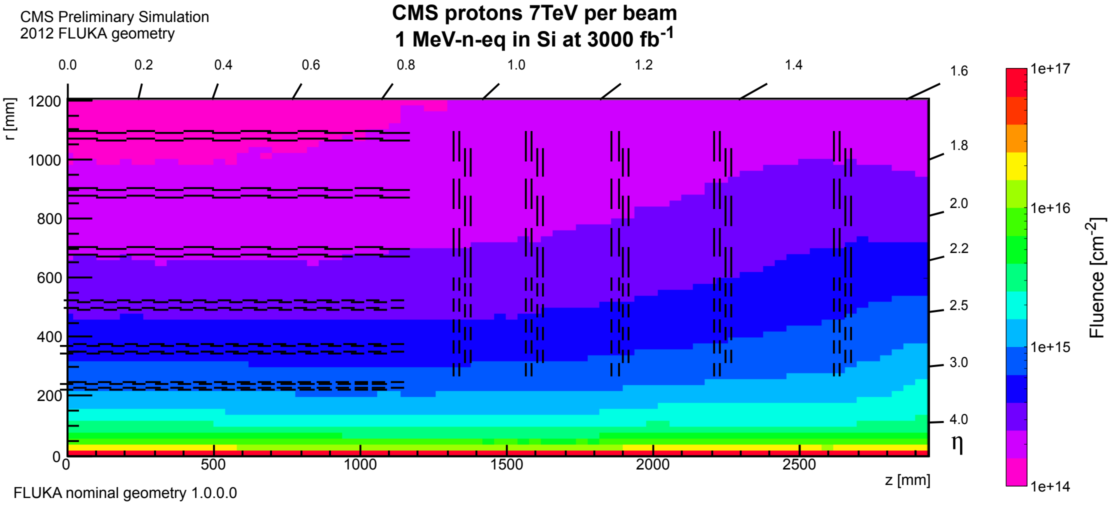

Figure 3.8: FLUKA simulation - expected fluence after 3000 fb^{-1} in silicon [FLU15].

---

[3] Non Ionizing Energy Loss

forward regions are exposed to the highest radiation levels. The plot represents the expected exposure after 10 years of operation equivalent to 3000 fb^{-1}.

From the plot one can see, that the innermost layer of the future outer tracker will suffer from $\Phi = 1 \times 10^{15}\ \mathrm{n_{eq}cm^{-2}}$. As a consequence, the new silicon detectors for the HL-LHC era have to withstand this harsh radiation level and provide reliably signals even after 10 years of operation. Therefore the sensors under test which have been designed and produced within this thesis have been irradiated with protons and neutrons up to $\Phi = 2 \times 10^{15}$ 1MeV $\mathrm{n_{eq}cm^{-2}}$. The safety margin of about 100% should guarantee sufficient sensor performance if for instance by chance the FLUKA simulations underestimate the particle fluence.

Not only bulk damage affects the overall sensor performance but also the surface damage especially during the HL-LHC lifetime. Here FLUKA simulations predict a dose higher than 1×10^{5} Gy after 3000 fb^{-1}. Therefore a detailed studies in the sensor surface damage as well as the radiation hardness of the future readout chips have to be executed.

A more detailed description of the irradiation will follow in the corresponding chapters.

CHAPTER 4

SENSORS BASED ON SILICON

Silicon tracking detectors have been successfully used in high energy physics experiments for decades now. While the first experiments during the 1970s used some mm^2 area of silicon sensors, the current biggest ever built silicon detector of the CMS experiment consists of more than 200 m^2 . The reasons for using silicon for tracking applications in high energy experiments are manifold. First of all, the element silicon is available in huge amounts and can be easily obtained from the upper earth crust at relatively low costs. Secondly, silicon has revolutionized the electronics industry and is therefore well known, both in industry and research. Furthermore, passing ionizing particles deposit their energy while interacting with the silicon lattice respectively the electrons. Thereby, ~75-80 free electron-hole pairs are generated per μm distance in silicon, hence the amount of generated charges in 100-500 μm thick detectors is relatively high and due to fast carrier mobilities, the charges can be collected within a few nanoseconds. These characteristics are the main decisive facts leading to large area applications of silicon for tracking devices.

In the following chapter, some of the silicon properties will be introduced in more detail. After understanding silicon as a semiconductor and its properties for silicon tracking detectors, the silicon strip sensors for HEP experiments will be introduced. As the sensors are used in harsh radiation environments, lattice and surface damage must be considered and discussed.

4.1 Silicon properties

Silicon is a tetravalent metalloid with the atomic number 14. The silicon lattice has a diamond structure and is visualized in figure 4.2. Tetravalent means that each silicon atom has four neighboring silicon atoms. The covalent bonding is due to sharing eight electrons between five silicon atoms, forming the crystal lattice. Silicon is a semiconductor, hence the electrical

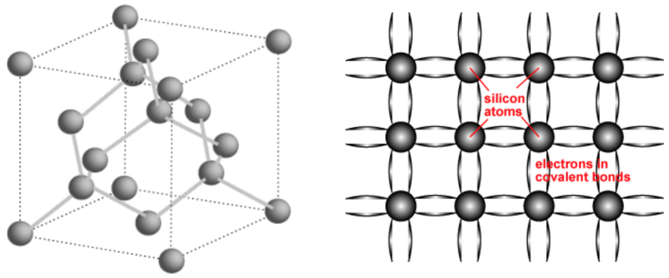

(a) (b)

Figure 4.1: Silicon tetravalent lattice with diamond structure. (a) 3D orientation and (b) two-dimensional representation after [Kit96].

conductance is somewhere between the conductivity of a metal and an isolator. Semiconductors vary in the specific resistivity between 10^{-4} Ωm and 10^{7} Ωm [Hun07]. At 0 K of the absolute temperature, semiconductors behave like isolators. In this state, all electrons are arranged in the valence band, the top most band filled with charge carriers. The conduction band on the contrary, is completely unoccupied. The energy needed to overcome the barrier between the valence band $\mathrm{E_V}$ and conduction band $\mathrm{E_C}$ is called the bandgap energy $\mathrm{E_G}$:

$$\mathrm{E_G} = \mathrm{E_C} - \mathrm{E_V} \qquad \text{(=1.12 eV at 300 K for Silicon)}. \tag{4.1}$$

With increasing temperature for instance, charge carriers may overcome the bandgap, occupy one of the next higher energy levels and contribute to conductance as free charge carriers in the conduction band[1]. This bandgap is responsible for the electronic properties of semiconductors and in case of silicon, the bandgap energy of 1.12 eV at T = 300 K is particularly useful for tracking detectors.

Intrinsic case

In semiconductors, electrons and holes contribute to the conductivity. Hence, the conductance can be expressed as [Hun07]:

$$\sigma = e \times (n\mu_\mathrm{n} + p\mu_\mathrm{p}), \tag{4.2}$$

in which n and p are the densities of free electrons and holes, accordingly $\mu_\mathrm{n} = 1350\ \mathrm{cm^2V^{-1}s^{-1}}$ and $\mu_\mathrm{p} = 450\ \mathrm{cm^2V^{-1}s^{-1}}$ are the electron and hole mobilities [Har09]. In order to obtain the electron density in the conduction band, one integrates the product of the density of state $\mathrm{D_C(E)}$ and the Fermi-Dirac function f(E, T). In a similar way, the hole density can be calculated where the occupation probability of an energy band for the holes is $(1 - \mathrm{f(E,T)})$:

$$n = \int_{E_C}^{\infty} D_C(E) f(E,T)\, dE \qquad \text{and} \qquad p = \int_{-\infty}^{E_V} D_V(E)[1 - f(E,T)]\, dE. \tag{4.3}$$

---

[1] definition of “semiconduction“

For the integration limit, it is allowed to take infinity because just the lowest states in the conduction band are of interest due to the quickly decreasing fermi function with increasing energy, where the fermi function is defined as:

$$f(E,T) = \frac{1}{e^{\frac{E-E_F}{k_B T}} + 1} \qquad \text{for } E > E_F \tag{4.4}$$

and

$$1 - f(E,T) = \frac{1}{e^{\frac{E_F-E}{k_B T}} + 1} \qquad \text{for } E < E_F. \tag{4.5}$$

E_F is the energy at which the occupancy probability for the electronic states is 50%. The density states in equation (4.3) is given by:

$$D_C(E) = \frac{(2m_n^*)^{\frac{3}{2}}}{2\pi^2\hbar^3}\sqrt{E - E_C} \qquad \text{for } E > E_C \tag{4.6}$$

and

$$D_V(E) = \frac{(2m_p^*)^{\frac{3}{2}}}{2\pi^2\hbar^3}\sqrt{E_V - E} \qquad \text{for } E < E_V. \tag{4.7}$$

The energy range $E_V < E < E_C$ does not allow any electronic states. The effective masses $m_n = 0.32m_e$ and $m_p = 0.26m_e$ depend on the crystal orientation [Kit96].
In the intrinsic case and in thermal equilibrium state, the density for free charge carriers can be simplified to:

$$n_i = p_i = \sqrt{N_C N_V}\, e^{\frac{-E_G}{2k_B T}}. \tag{4.8}$$

Here, the “i“ indicates the intrinsic case, N_C and N_V are the effective densities of states. The intrinsic charge carrier density for silicon is $n_i = 1.1 \times 10^{16}\ m^{-3}$.

Extrinsic case - doping of semiconductors

Semiconductors without any impurities are intrinsic and the electrical properties can be calculated as shown in the section before. Extrinsic semiconductors are intentionally doped semiconductors. This means that atoms in the lattice are replaced by foreign atoms (“impurities“), which introduce further energy levels. In general, electrical properties can be tuned by doping. One of the effects is that the conductivity of semiconductors can increase by several orders of magnitude in comparison to the intrinsic case. Silicon is a group IV element with 4 electrons in the outer shell. By doping silicon with group III elements like boron, one introduces one electron less than expected by the lattice resulting in a *p-type acceptor* level E_A. From now on, we will call this type of silicon p-type. As a consequence, additional energy level above the valence band are generated. Taking group V elements like phosphorus for the doping, energy levels E_D below the conduction

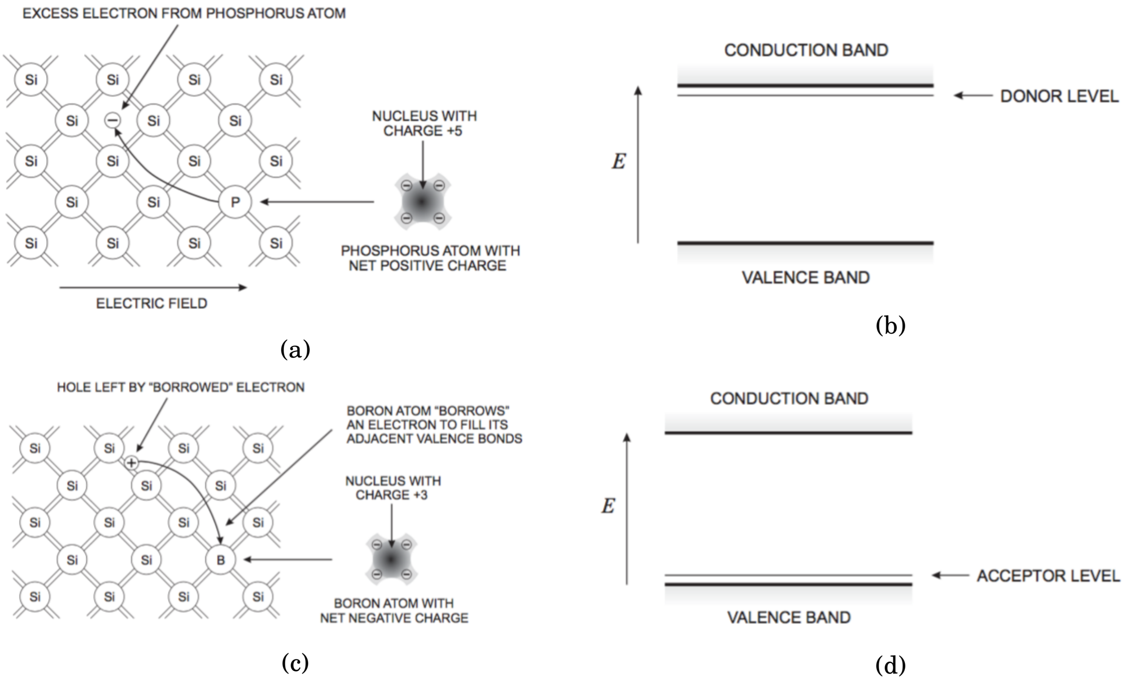

(a) (b)

(c) (d)

Figure 4.2: Introduction of group V elements: (a) lattice with impurities and (b) additional shallow donor level. For group III elements holes are left over shown in (c) with a resulting shallow acceptor level shown in (d) [Spi05].

band are introduced and the semiconductor is called *n-type donator*, or simply N-type, due to the additional negative free charge. In figure 4.2, one can see that impurities depending on their outer shell number of electrons introduce additional shallow energy levels in the bandgap.

Usually, the doping concentration is several orders of magnitude higher than the intrinsic case, therefore n in (4.8) can be expressed by N_D for N-type silicon. For P-type silicon p is replaced by N_A. Now the effective charge carrier density can be calculated according to [Hun07]:

$$n = \sqrt{\frac{N_C N_D}{2}}\, e^{\frac{-E_d}{2k_B T}}, \tag{4.9}$$

with $E_d = E_C - E_D$.

Doping of semiconductors is realized by implantation or diffusion processes at high temperatures exceeding 1000°C and up to hundreds of keV Energy for the dopants.

4.2 pn-junction

The CMS tracking detector with more than 200 m^2 of silicon sensors is based on the electrical properties of a pn-junction, also well known as a diode. Here, p-type doped material is in direct contact with n-type doped material and vice versa. Initially, n- and p-doped materials are electrically neutral because the number of existing positive ionized atoms and free negative charge carriers is equal. Due to the contact of oppositely doped regions and the resulting concentration gradient, electrons diffuse from the n-doped region to the p-type region until the fermi level is equalized and recombine. The holes drift from the p-type to the n-type region. The positive dopants in the n-side and negative acceptors in the p-side however remain due to the crystal lattice boundary. Thus, a net positive charge arises in the n-type region and a negative one in the p region, creating an electrical field which counteracts the diffusion process due to the concentration gradient. As a consequence, a region free of mobile charges is formed, also called the space charge region (SCR).

Width of the space charge region

The width w of the SCR is one of the crucial properties of a pn-junction, which are used in the silicon detectors, therefore a quick derivation of the space charge region following [LR09] is executed. Starting from the Poisson equation, the electrostatic potential Ψ, the electric field E and the width of the space charge region can be derived:

$$\frac{d^2\Psi}{dx^2} = -\frac{\rho(x)}{\epsilon}, \tag{4.10}$$

where $\epsilon = 1.054$ pFcm is the silicon electric permittivity. The charge density $\rho(x)$ is given by

$$\rho(x) = \begin{cases} qN_d, & \text{for } \; 0 \le x \le x_n \\ -qN_a, & \text{for } -x_p \le x \le 0 \end{cases}, \tag{4.11}$$

assuming an abrupt junction. N_d and N_p are the donor respectively the acceptor concentrations, x_n and x_p the widths of the depletion in the specific n and p regions. Now the Poisson equation can be integrated with the boundary conditions $E(x_n) = E(-x_p) = 0$ resulting in the electric field of the pn junction:

$$E(x) = -\frac{d\Psi}{dx} = \begin{cases} E_n(x) = q(N_d/\epsilon)(x - x_n), & \text{for } \; 0 \le x \le x_n. \\ E_p(x) = -q(N_a/\epsilon)(x + x_p), & \text{for } -x_p \le x \le 0. \end{cases} \tag{4.12}$$

The space charge region free of mobile charges can now already act as a silicon detector. An energy of at least $E = 3.67$ eV [B⁺12] for the ionizing particle is needed to create an electron hole pair. This excited energy compared to the silicon bandgap energy of $E_g = 1.12$ eV is due to the conservation of energy and momentum as of silicon lattice excitations as silicon is an indirect semiconductor. The generated charges now drift in the electric field, in dependence on their charge, towards the electrodes and the signal is fed into the readout front-end for further processing.

The electrostatic potential is derived from the integration of equation (4.12):

$$\Psi(x) = \begin{cases} \Psi_n(x) = \Psi_n - q(N_d/(2\epsilon))(x - x_n)^2, & \text{for } \; 0 \le x \le x_n. \\ \Psi_p(x) = \Psi_p - q(N_a/(2\epsilon))(x + x_p)^2, & \text{for } -x_p \le x \le 0. \end{cases} \tag{4.13}$$

The contact potential V_0 of the pn-junction in silicon is about $0.3-0.6$ eV at 300 K. With the contact voltage, the width w of the depletion region can be calculated to:

$$w = x_n + x_p = \sqrt{\frac{2\epsilon V_0}{q}\left(\frac{1}{N_d} + \frac{1}{N_a}\right)}. \tag{4.14}$$

The width of the SCR without any applied voltage depends on the doping concentrations or rather the concentration gradient. Therefore, silicon detectors are used by applying a reverse bias voltage to the pn-junction, which results in an extension of the SRC by increasing the reverse bias. As a direct consequence, the active region where electron hole pairs are generated grows, leading to a larger signal and hence better signal-to-noise ratio. With this, the total width of the SCR is calculated to:

$$w = x_n + x_p = \sqrt{\frac{2\epsilon(V_0 + V_{bias})}{q}\left(\frac{1}{N_a} + \frac{1}{N_d}\right)}. \tag{4.15}$$

The contact voltage was replaced by $(V_0 + V_{bias})$ where V_{bias} stands for the outer reverse bias voltage. The current CMS outer tracker is built of $\mathrm{p}^+ - \mathrm{in} - \mathrm{n}$ type sensors. This means that the bulk substrate is of low n doping of about 1×10^{12} cm^{-3}, and below the collecting electrode highly doped p^+ regions with concentrations of about 1×10^{19} cm^{-3} are implanted. Hence, $x_p << x_n$ and therefore the equation (4.15) can be simplified to:

$$w \approx x_n \approx \sqrt{\frac{2\epsilon}{qN_d}(V_0 + V_{bias})}. \tag{4.16}$$

The voltage needed to fully extend the SCR region over the bulk is the depletion voltage V_{fd}:

$$V_{fd} \approx \frac{w^2}{2\epsilon\mu\rho}. \tag{4.17}$$

This means high resistivity sensors need a low full depletion voltage and vice versa. The range is about 500 V - 250 V, depending on the bulk doping concentration $|N_{eff}| = |N_a - N_d|$. N_{eff} can be determined by capacitance over voltage measurements because a silicon detector can be considered a parallel plate capacitor.

4.3 Position sensitive silicon detectors

Silicon sensors vary in geometry and coupling of the signal to the electrode. The simplest silicon sensor is a diode with reverse bias voltage. However, tracking detectors like the CMS tracker with hundreds of particles crossing within 25 ns need high resolution of the tracks for precise physics analysis. Therefore, the sensors are segmented in several pn-junctions. Depending on the radius in the tracker, pixelated sensors with small cells and high electronics density are necessary in the innermost layers in order to sufficiently distinguish between the dense particle tracks. The outer

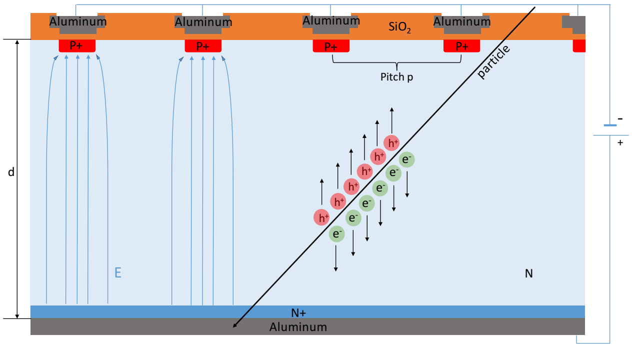

Figure 4.3: Working principle of a $p^+ - in - n$ silicon strip sensor.

Table 4.1: Sensor parameters

Quantity	number
Thickness d	100-500μm
Strip pitch	20-250μm
Resolution	5-70μm ($p/\sqrt{12}$)
Bulk doping	~1×10^{12} cm^{-3}
Strip doping	~1×10^{19} cm^{-3}
Back doping	~1×10^{19} cm^{-3}
Charge (MIP)	75-80 e/h pairs per μm
Charge collection	a few ns

layers of the tracker are equipped with silicon strip sensors. Figure 4.3 illustrates the working principle of a $p^+ - in - n$ silicon strip sensor.

The substrate or bulk of the sensor in figure 4.3 is n doped and of relatively low concentration of about 1×10^{12} cm^{-3}. This results for a exemplary 300 μm thick sensor in a full depletion voltage of about 150 V, depending on the wafer resistivity. The HV is applied to the backplane whereas the AC coupled aluminum strips are on ground potential (an alternative biasing option via the sensor periphery in order to cope with the mechanical challenges in the p_T modules described in section 3.2.4 is presented in appendix C). In order to achieve an ohmic contact, a high backplane implantation is present. The strip implants (p^+) are highly doped as well to about 1×10^{19} cm^{-3} and a few μm deep. The strip pitch p defines the distance between adjacent strips and directly influences the resolution. With reverse bias, the depletion region extends through the whole bulk[2]. Between the strip implants and the aluminum electrodes a coupling oxide[3] (mostly SiO_2) is grown. The generated charge is read out capacitively be the ASICs. Furthermore, the silicon oxide has safety functions and prevents damage to the sensor surface. Due to the outer voltage, an electric field is present and in case of a $p^+ - in - n$ detector, holes drift along the electric field towards the electrodes and induce a signal. This signal is than amplified and processed by the front-end electronics.

Interaction of particles with matter

The collected charge of a sensor is generated by passing charged particles through ionization processes where mainly elastic collisions with the shell electrons dominate. The mechanism of the energy deposition is described by the Bethe-Bloch formula [Bet30] and [Blo33]:

$$\frac{dE}{dx} = 2\pi N_L r_e^2 m_e c^2 \rho \frac{Zz^2}{A\beta^2} \left[ln \left(\frac{2m_e\gamma^2 v^2 W_{max}}{I^2} \right) - 2\beta^2 - \delta - 2\frac{C}{Z} \right], \tag{4.18}$$

---

[2] before irradiation; after irradiation this may change, see section 4.4

[3] Pixel sensors are DC coupled with direct contact of the electrode and the implant

with

- x is the path length ($\frac{\mathrm{g}}{\mathrm{cm}^2}$)
- $2\pi N_L r_e^2 m_e c^2 = 0.1535\ \frac{\mathrm{MeVc}^2}{\mathrm{g}}$
- the electron radius $\mathrm{r_e} = 2.817 \times 10^{-13}$ cm
- the electron mass $\mathrm{m_e}$
- the Avogadro number $\mathrm{N_L}$
- I the effective ionization potential
- Z, the atomic number of the medium
- A, the atom ic weight
- ρ, the medium density
- z, representing the charge of the crossing particle
- $\beta = \frac{\mathrm{v}}{\mathrm{c}}$, the velocity of the crossing particle
- $\gamma = \frac{1}{\sqrt{1-\beta^2}}$
- δ is the density correction
- C represents the shell correction
- $\mathrm{W_{max}}$ is the maximum energy transferred in a single collicion

Due to the electric field and depleted bulk, the generated electron hole pairs do not recombine, but are separated and drift parallel to the electric field to opposite electrodes due to the electrostatic force [Lut99]:

$$\vec{F} = q\vec{E} + m_e \frac{v}{\tau}, \tag{4.19}$$

with the average drift velocities for electrons and holes given by:

$$v_n = \mu_n E \qquad \text{and} \qquad v_p = \mu_p E. \tag{4.20}$$

The amount of the collected charge in an unirradiated sensor is directly proportional to the deposited energy. In the Bethe-Bloch formula, a region at about $\beta\gamma \approx 3-4$ can be identified as the minimal deposited energy corresponding to about 300 eV per μm distance. Taking the ionization energy of 3.6 eV for one electron hole pair, an average charge generation of about 80 electron hole pairs per μm is expected as the most probable value. A particle with energy this low is called a minimal ionizing particle (MIP) and would generate the minimal charge of 24000 electron hole pairs in a 300 μm thick sensor. The charge distribution itself follows a Landau distribution due to energy fluctuations in the energy transfer. The Bethe-Bloch relation describes the gaussian mean energy deposition E_0 in material. In addition, a long tail towards high energies due to knock-on electrons (δ-electrons) is present. This means that the most probable value of the energy deposition is about 30% lower than the mean deposited energy. Later, when comparing results from signal measurements, the MPV is considered.

Photon absorption

In order to generate signal in the test sensors during laboratory measurements, a Sr90 source was taken. The β-decay electrons interact with the silicon material. Some of the studies, especially when looking into the substrip resolution, were done by using a 1060 nm laser. The photons interact by the inner photoelectric effect, which means that the photon is absorbed, leading to an excitation of an electron from the valence band to the conduction band.

4.4 Radiation damage

The upgrade of the CMS tracker detector discussed in chapter 3 is a consequence of the harsh radiation environment. The particles additionally interact with the atoms via Coulomb interactions and nucleus-nucleus scattering. Atoms can be displaced from their lattice position leaving a vacancy and the knocked-on atoms (PKA) can act as interstitial atoms. The threshold of the recoil energy for such a displacement is $E_R \approx 21$ eV [ABC$^+$01]. These defects appear as additional energy levels within the bandgap, thus changing the electrical properties of the detector.

When considering radiation damage, one can distinguish between bulk damage and surface damage. Bulk damage mechanisms directly influence the charge collection efficiency by adding trapping centers, increase leakage currents and depletion voltage through build-up of space charge. Furthermore, ionization processes in the silicon dioxide can influence the sensor performance severely. The surface damage can significantly influence the electric field distribution. Additional increasing surface currents might decrease the breakdown voltage and lead to lower position resolution, depending on the substrate type due to effects on the strip isolation. The damage depends on the energy of the penetrating particle as well as the charge. Protons introduce more likely point-like defects and with increasing energy also cluster defects [Huh02], while neutrons mainly create cluster defects. Cluster defects are initiated by recoil atoms, which can displace further atoms.

4.4.1 NIEL scaling

In order to compare damage introduced by different irradiation energies and particle type (charge), the non-ionizing energy loss hypothesis is used with the assumption that the damage scales linearly with the deposited displacement energy. In this scope, neutrons with an energy of

1 MeV are taken as reference. The following irradiations of the sensors performed within this thesis include proton and neutron irradiations. A scaling factor $\kappa = 2$ is used for irradiations with 23 MeV protons at the Zyklotron AG at KIT in Germany [Zyk15]. The factor has been defined in [Die03]. The Proton Synchrotron (PS) at CERN has been used in order to perform proton irradiations with an energy of 23 GeV. Here the hardness factor of $\kappa = 0.62$ is used for scaling [G. 10]. For the neutron irradiation at the TRIGA Mark II reactor in Ljubljana [TRI15], a hardness factor of 0.90 ± 0.03 is applied [Zon98].
Taking the hardness factors, the fluence equivalent to a 1 MeV neutron can be calculated by:

$$\Phi_{eq} = \kappa \times \Phi = \kappa \times \int \Phi(E)dE. \tag{4.21}$$

All results and irradiation levels presented later in this study refer to the 1 MeV neutron equivalent fluence $\Phi_{\mathrm{eq}} = \mathrm{n_{eq}cm^{-2}}$.

4.4.2 Impact on the sensor performance

Defects, which are either created during the manufacturing process or after irradiation, change the sensor performance. Vacancies or interstitials can further react to new defect complexes and clusters, each with specific impact on the electronic behavior of silicon. In fact, depending on the defect formation, additional energy levels in the bandgap are introduced. A detailed study of the defect formation and measurements of the energy levels are investigated within the RD50 group [RD5] and [Jun11].

Bulk defects

Main bulk defect effects visualized in figure 4.4 are:

- The creation of shallow levels next to the valance and conduction band which mainly affect the effective doping concentration $\mathrm{N_{eff}}$ as these defects can be easily ionized resulting in a change of the space charge. Additional donors and acceptors are created where the ratio of both depends on the particle energy and the type. For the sensors in this study, which are $\mathrm{n^+ - in - p}$ type only, an increase of the depletion voltage is the consequence. Hence, with increasing radiation dose or sensor lifetime, a higher voltage up to 900 V depending on the sensor thickness is necessary in order to fully deplete the detector. Therefore the capability of the power system of the experiment has to be taken into account during the search for radiation hard detectors. Moreover with increasing sensor power P= U·I, the cooling power has to be increased too.

- The introduction of deep levels which mainly increase the leakage or dark current. Energy levels in the middle of the bandgap act as generation and recombination centers for electrons

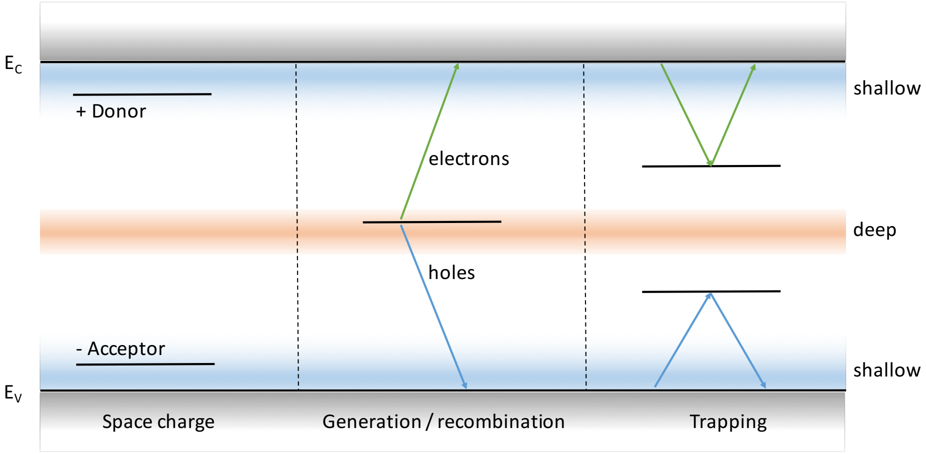

Figure 4.4: Effects of defect levels in the silicon bandgap.

and holes. In measurements of different sensor materials and types it has been found that the leakage current increases linearly with fluence and can be calculated by

$$\frac{\Delta I}{V} = \alpha \times \Phi_{eq} \tag{4.22}$$

with the proportionality factor α as the current related damage rate [Mol99]. Typically, the leakage current in reverse bias is in the order of pA per cubic centimeter before irradiation. The leakage current increases until the depletion of the bulk is reached and than saturates. By further increasing the HV, the sensor becomes conductive, leading to an electrical breakdown. After irradiation, the current increases to the order of $\mathcal{O}(\mu\mathrm{A/cm^{-3}})$ at 293 Kelvin.

- Trapping of drifting charges. Intermediate and deep level states with a large emission time compared to the readout time capture the charges and emit them with some delay. This signal is not detected within the collection time and does not contribute. The charge collection with respect to the unirradiated case decreases significantly with fluence. At high fluence, signal cannot be distinguished from noise sufficiently.

Surface defects

Surface defects are categorized as the defects appearing in the silicon dioxide at the sensor surface at the transition region $\mathrm{Si-SiO_2}$. Main defect mechanism is ionization and not atomic displacement like in the bulk. After electron hole generation, the charges separate due to the fact that the electron mobility in $\mathrm{SiO_2}$ is several orders of magnitude higher than the mobility of the holes ($\mu_{\mathrm{e,SiO_2}} \approx 20\,\frac{\mathrm{cm^2}}{\mathrm{Vs}}$, $\mu_{\mathrm{h,SiO_2}} \approx 2\times10^{-5}\,\frac{\mathrm{cm^2}}{\mathrm{Vs}}$) [Wun92]. Electrons drift to the positive metal electrode and are removed while the holes slowly drift towards the $\mathrm{Si-SiO_2}$ interface where they get trapped in deep levels ($\mathrm{E_{g,SiO_2}} = 8.8$ eV). As a consequence, a positively charged layer arises which represents an attractive potential for drifting electrons in the bulk. This leads to a slight increase of the interstrip capacitance due to additional charges and hence the input noise. Furthermore, the interstrip resistance decreases, leading to increasing charge-sharing of adjacent readout strips. In particular, $n^+ - in - p$ type sensors suffer from lower resolution. In this type of substrate, electrons are collected at the electrodes and the additional accumulation layer of electrons below the surface short-circuits the strips. Due to the fact that the buildup of positive charge in the SiO_2 is unavoidable (without any special treatment or SiO_2 grown technique like slow dry growing), additional production processes in form of further p^+ implantation steps between the strips are necessary. The latter forms an isolation layer in order to prevent a short-circuit of the strips. The most promising doping characteristics and pattern of such p^+ isolation layer are one of the main interests in this thesis and will be discussed in more detail in the coming chapters.

The interplay of bulk and surface damage is under study. Clearly, surface damage affects the overall sensor performance either considering the sensor current through additional surface currents, electrical breakdown due to influence on the electric field strength in the bulk or the resolution. Therefore, both damage regions (bulk and surface) will be discussed later.

4.4.3 Annealing

Table 4.2: Annealing steps used for the measurements in this study

Step	Temperature [°C]	Time [min]
1	60	10
2	60	10
3	60	20
4	60	76
5	80	15
6	80	30
7	80	60

The defects in silicon and silicon dioxide are not stable and can recombine or form new defects. This effect is called annealing. It is strongly related to the temperature. Whereas at $-20°$ C the annealing effect is almost frozen, the velocity of the defect kinetics increases rapidly with increasing temperature. Moll [Mol99] parametrized the anneling behavior of the current and the effective doping concentration in the Hamburg model.

The impact of increased temperature at the sensors for a certain period of time after irradiation needs to be understood because the CMS tracker might be heated up for maintenance during yearly shut downs up to room temperature[4].

A detailed description of the annealing behavior of the current and the effective doping con-

---

[4] currently, the tracker operates at $-10°$ C, the aim for the Phase II Upgrade is $-20°$ C

centration is given in [Mol99] and [Har09]. The temperature steps and the time of increased temperature in this study were chosen isothermally and are listed in table 4.2. Normally, after each step, the leakage current, depletion voltage and charge collection of the sensors under study were measured and scaled to an equivalent time at room temperature (20° C). The following relation after [Chi11] is valid (see section 6.4 for more detail):

$$I(T = 20^{\circ}C) = I(T) \times \left(\frac{293\,K}{T}\right)^{2} exp\left(\frac{-1.21\,eV}{k_B T}\left[\frac{1}{293\,K} - \frac{1}{T}\right]\right). \tag{4.23}$$

CHAPTER 5

SILICON SENSORS FOR HL-LHC

The RD50 collaboration searches for radiation hard silicon devices for high luminosity colliders. Several participating groups have been investigating for years now which type (n^+-in-p, p^+-in-n or n^+-in-n) is most promising to deal with increasing demands to sustain an overall sufficient performance even after the expected 3000 fb^{-1} during HL-LHC. Moreover, detectors built of wafers from different silicon ingot growth technics (Magnetic Czochralski "MCz" [Czo17] and Float Zone "FZ" [CW00]), which mainly differ in the initial oxygen concentration, are under study. Precise measurements of the particle track also require a low mass tracker concept to avoid influence on the track by multiple scattering, for example. Hence, the thickness is varied and has to be balanced in order to achieve sufficient charge collection and low power always keeping the mass production in mind[1].

In the following chapter, a brief summary of the current status of theses studies is presented. The summary plots leading to the decision for using n^+-in-p type sensors for the CMS Tracker Phase II upgrade are extracted from [Die13].

5.1 N-type vs. P-type sensors

Within the CMS Tracker Collaboration, a huge measurement campaign [Hof11] was carried out with the aim to identify the most radiation hard single-sided sensors which will face the high luminosity environment. The processed wafers were delivered by Hamamatsu Photonics K.K, a manufacturer who had already delivered the sensors for the current CMS Outer Tracker in high quality. The wafers differed in the substrate type (n- and p-type), the growth process (MCz and FZ) and active thickness (300 μm, 200 μm and 120 μm). An overview of the sensors, to which the

---

[1] very thin sensors may be more expensive due to special handling and thinning processes

Table 5.1: Overview of the sensor labels and characteristic

Sensor label	physical thickness [μm]	active thickness [μm]
FZ320N/P/Y	320	300
FZ200N/P/Y	200	200
dd-FZ200N/P/Y	320	200
MCz200N/P/Y	200	200

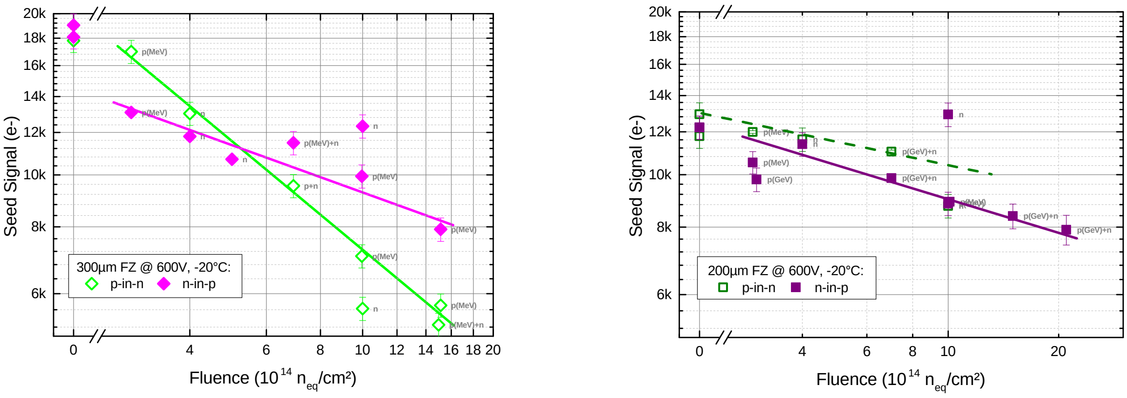

(a)

(b)

Figure 5.1: Signal measurements of (a) 300 μm and (b) 200 μm thick sensors with different substrate types as a function of the fluence. The measurements were performed at $\mathrm{T} = -20°C$ and $\mathrm{V_{bias}} = 600\ V$.

following plots refer, is listed in table 5.1.

The labels indicate the substrate growth technique, the physical thickness and the substrate type. The latter is expresses by N for n-type, P for p-type with p-stop isolation and Y for p-type with p-spray isolation. Within this study, no significant difference of the sensor performance in dependence on the isolation layer was observed. Therefore, the different techniques will be explained later when necessary.

One photolithographic mask set was used to produce 144 wafers in 6 inch size. The sensors were distributed amongst the participating institutes and electrically qualified before and after irradiation. The samples were irradiated with mixed particles (neutrons and protons) to $\Phi = 7 \times 10^{14}$ 1MeV $\mathrm{n_{eq}cm^{-2}}$, corresponding to a radius of ≈40 cm and $\Phi = 1.5 \times 10^{15}$ 1MeV $\mathrm{n_{eq}cm^{-2}}$, according to ≈20 cm radial distance from the interaction point in the CMS experiment. Compared to the FLUKA predictions, the fluence was chosen with a safety margin of about 50%. Before and after irradiation, the charge collection of the sensors was measured with β-electrons from the Sr90 decay. Sensors with the 20 cm irradiation were also investigated on their properties after several annealing steps.

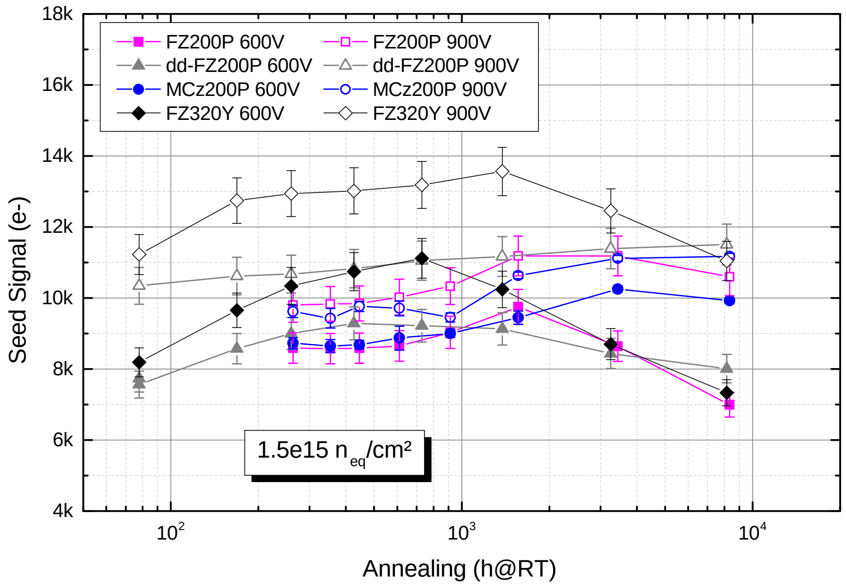

Figure 5.2: Annealing of the seed signal. The signal is more or less constant over a period of 20 weeks (3360 hours) at room temperature. The signal in MCz material seems to stay constant or even increases for longer annealing times. The annealing is scaled to room temperature according to the annealing behavior of the leakage current.

In figure 5.1, the collected seed[2] charge as a function of the fluence in logarithmic scale is plotted. Here, 300 μm thick FZ sensors of both substrate types are shown. All samples were measured at T = −20°C. This temperature is envisaged to be the future sensor temperature during operation in order to keep the leakage currents and accordingly the cooling power as low as possible. At each measurement point, the particle type (neutron or proton) and the energy (if not labeled 23 GeV p) are indicated. Clearly, and in agreement with several studies [Man13] [Wei13], the p^+−in−n sensors suffer earlier high charge loss due to trapping. After a fluence of $\Phi = 7 \times 10^{14}$ 1MeV $n_{eq}cm^{-2}$, the p-type sensors collect significantly more charge.

5.2 Thin vs. thick sensors

Thick sensors collect more charge before irradiation compared to thin sensors due to the simple relation deduced in section 4.3 where it was calculated that a MIP generates about 80 electron hole pairs per μm distance in silicon. However, after high irradiation of about $\Phi = 7 \times 10^{14}$ 1MeV $n_{eq}cm^{-2}$, thin sensors collect a comparable charge amount like the thick ones. The reason is the slightly higher electric field strengths and hence higher drift velocities in thin sensors and shorter drift distances. Therefore, drifting charges are less prone to be trapped. Furthermore, the annealing behavior of the charge collection is plotted in figure 5.2 for the

---

[2] strip with the highest signal in a cluster

different substrate material, n^+−in−p polarity and thickness. Thin sensors show a more constant annealing behavior, considering the charge collection efficiency up to 20 weeks during room temperature. This could be beneficial during operation, as explicitly increasing the temperature of the tracker could decrease the leakage current and hence noise, but the signal would stay unchanged.

5.3 Consequence and motivation for this study

As a consequence of the results briefly shown in the previous sections, the following study concentrates only on the n^+−in−p type technology of silicon sensors for the CMS Outer Tracker. Due to the tremendous demands on the sensor reliability, the p-type technology has to be studied in more detail. Besides the most promising thickness which affects leakage current, charge collection, radiation length and annealing, general aspects like the pattern of the strips and detector periphery are of interest. In particular, in section 4.4.2 the influence of the silicon dioxide on the p-type bulk sensor was introduced and the need for additional strip isolation layers was mentioned.

Hamamatsu Photonics K.K (HPK) has proven to deliver silicon sensors with high quality for HEP experiments. This fact was one reason why this manufacturer produced the silicon sensors for the current CMS Tracker. The sensors were developed in collaboration with the Hamamatsu Photonics process engineers. The manufacturer was allowed to change the provided data files for the production of the photolithographic masks to ensure high voltage stability and stable operations. In addition, process details on the implantations were developed within HPK and are a corporate secret. Hence, any important values which affect the sensor performance like implantation dose, energy and temperatures (which define also the doping depth) are not provided by HPK but are assumed from experience. When considering n^+−in−p type technology, in particular the p^+ isolation layer although at floating potential is critical and difficult to calculate in order to preserve good strip isolation independent of the fluence and keep the electric field strengths as low as possible to avoid electrical breakdown. Clearly, R&D studies are also conducted with other vendors. In this study, sensors from five different vendors were investigated. The main point is that some of the vendors, for instance, process silicon sensors for HEP experiments for the first time. This means that doping concentrations and further sensor characteristics should be provided to the manufacturer.
Therefore, the presented R&D studies were used to scan critical parameter of the p^+ isolation. Sensors with comparable specifications but different doping concentrations and depths of the p^+ layer were produced and will be discussed in detail in the following chapters.

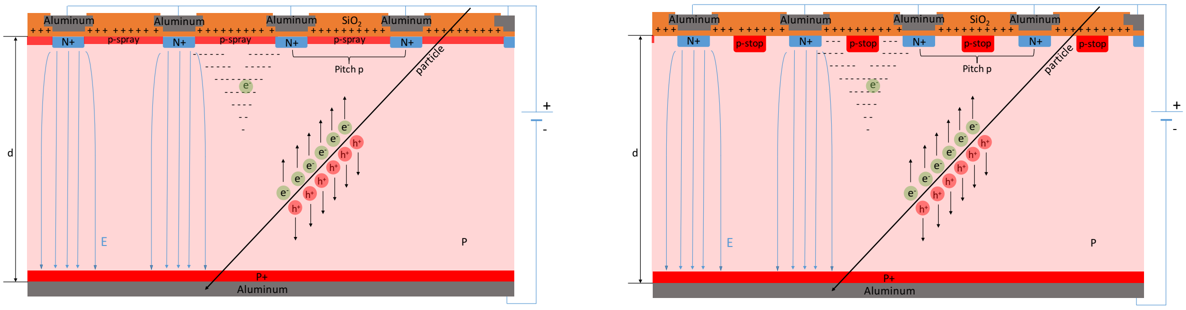

(a) (b)

Figure 5.3: Visualization of the p isolation techniques of n$^+$–in–p detectors, (a) p-spray covering the whole wafer with no additional implantation mask and (b) p-stop, which is an individual pattern between the strips due to an additional photolithographic step.

5.4 N$^+$–in–p **technology**

Basically, the n$^+$–in–p technology is the vice versa version of the p$^+$–in–n. The bulk is of low p (boron) doping concentration of around $\mathrm{p_{conc.}} \approx 1 \times 10^{12}$ cm^{-3}, which gives a bulk resistivity $\rho = \frac{1}{e(\mu N_d)} \approx 4 - 10\mathrm{k\Omega cm}$. The strip implants are of high peak concentration n$^+$ with values of around $\mathrm{n_{conc.}} \approx 1 \times 10^{19}$ cm^{-3} and around 1 to 2 μm deep. In most cases, the group V element phosphorus is used. In order to avoid a Schottky contact, the backside is also highly doped with boron to $\mathrm{p_{conc.}} \approx 1 \times 10^{19}$ cm^{-3}. While the backside of the detector is fully covered with aluminum for the HV supply, the grounded aluminum readout strips on top of the coupling SiO$_2$ are segmented and exhibit the so-called “metal overhang“ of a few μm, extending the width of the n$^+$ strip implants. This overhang, which is around 6 μm to each side, results in lower high electric field densities at the strip implants through attracting the fields towards the overhang edges. This actually increases the breakdown voltage. As mentioned previously, the positively charged SiO$_2$ attracts the drifting negative charges towards the surface. An accumulation layer of electrons short-circuiting the strips appears. In order to prevent such buildup of an electron layer, additional implantations of a group III element between the strips are necessary.

P$^+$ **isolation techniques**

Three different technologies are currently available and two of them are visualized in figure 5.3. The p-spray technology in figure 5.3(a) is a p$^+$ layer which covers the whole wafer. An advantage of this technology is that for the production one less mask is needed, as the p-spray does not hold any specific pattern. Due to the fact that the p-spray layer is in direct contact with the highly doped n strip implants, lateral pn junctions are created. Here, the development of the lateral space charge region influences the electric field density at the n$^+$ strip edges, which can be critical for the operation. As a consequence, the doping concentration and in particular the doping depth

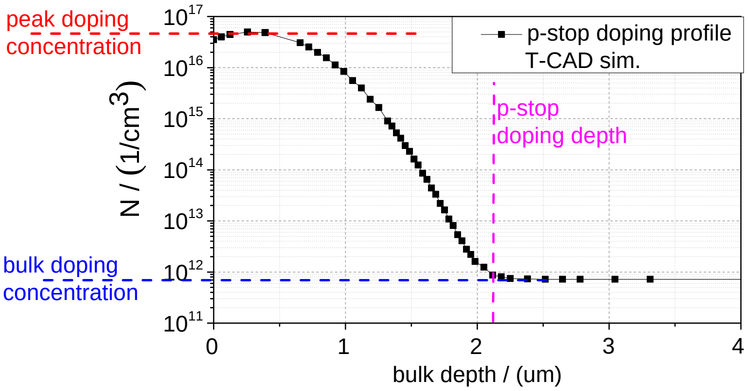

Figure 5.4: Definition of the implantation depth used for the T-CAD simulation studies showing a gaussian shape with the peak doping concentration at a depth of 300 nm. Here, the exemplary p-stop parameters are shown.

have to be calculated carefully. A rough estimate on the p-spray characteristics are the following: the peak doping concentration of boron is in the range of $n_{\text{conc.}} \approx 5 \times 10^{15}$ cm^{-3} with a relatively shallow depth of 200 nm to 500 nm. Here, the ratio of the doping depths for the strips and the p-spray are crucial. In order to keep the electric field densities at the strip implant edges as low as possible, the n^+ strips should be implanted significantly deeper to around 2 μm, see later in chapter 6.4.

The doping depth of the implants is defined as the depth at which the additional implantations reach the value of the bulk doping and is visualized exemplary for the p-stop solution in figure 5.4. The curve is of gaussian shape and was defined and used in the T-CAD simulation studies (see chapter 6).

A second option for the p^+ isolation is implanting a certain pattern for each individual strip, indicated in figure 5.3(b). Here, the multiplicity of the p-stops is one and called “common p-stop“. But also two p-stops between the strips are possible. This arrangement is called “p-stop atoll“in which the strip is surrounded by an individual p-stop. While preparing the data files (GDS format) for the mask production, an additional mask for the p-stop pattern is needed. This increases the costs however, the costs for a photolithographic mask, considering a mass production, are negligible. As a matter of fact, no significant cost deviation for p-spray or p-stop wafers was asserted but might be dependent on the vendor as the number of process steps might change between the two different techniques. The advantage of the p-stop technology in comparison to the p-spray technique is obviously the prevention of the lateral pn junction formation at the strip implant edges. Figures 5.3(a) and 5.3(b) indicate that the implantation depth of the p-stop is higher than for p-spray. It is assumed to be around 2 μm, like the strip implants. The doping concentration also needs to be calculated carefully, as in the p-spray case. Low doping concentrations might be not sufficient enough for good strip isolation, whereas high doping concentrations might lead to high electric field strengths and low breakdown voltages. The concentration of boron acting as p-stop is in the range of $n_{\mathrm{conc.}} \approx 5 \times 10^{15}$ cm^{-3} and $n_{\mathrm{conc.}} \approx 1 \times 10^{17}$ cm^{-3}. The determination of the most promising p-stop doping depth and concentration is one of the topics covered in this thesis and will be discussed in more detail in chapter 6.

The third option, which is currently under study amongst different institutes, is the combination of both techniques. A moderate p-spray is used and additional p-stops with moderate concentration are present. The combination might be advantageous for the pixel detector due to the expected higher fluence of $\Phi \approx 1 \times 10^{16}$ 1MeV n_{eq}cm^{-2}, leading to even higher electric field strength in the sensors. This technique is therefore not covered here.

In any of the three cases, the boron implants are neutral acceptors after implantation or diffusion. Then, electrons from the bulk are captured by the acceptors and a negative space charge (acceptor$^-$) forms at the regions of the boron implants. Now, electrons drifting towards the electrodes are repelled due to Coulomb's law from the negative space charge and as a result the accumulation layer is interrupted.

Part II

Analysis

CHAPTER 6

SIMULATION STUDIES OF SILICON STRIP SENSORS

In this study, the combination of both measurements and simulation was used in order to investigate the most promising sensor layout and process characteristics for the future CMS Tracker. Technology Computer-Aided Design (T-CAD) is a powerful tool to develop and optimize semiconductor applications like silicon detectors. The commercial Synopsys Sentaurus [Syn] simulation package offers a variety of industrial leading tools which are able to simulate and analyze different devices based on semiconductors. Simulations were tuned to reproduce measurements of existing silicon detectors as well as for the performance predictions of new detector layouts and process characteristics. After successful reproduction of data, the developed radiation damage models within the CMS Tracker Collaboration [Ebe13, Eic12, Pel14] were used and applied to new sensor layouts. Subsequently, the most promising layouts were produced with several vendors from the semiconductor industry. For this purpose, the files for the production of the photolithographic masks were prepared with agreement to the technical constraints of the vendors.

In this chapter, the simulation tool Sentaurus T-CAD and the workflow will be briefly introduced. After that, the dedicated characteristics of n^+-in-p technology sensors under study will be discussed and the performance before and after irradiation in dependence on the isolation technique introduced in section 5.4 will be shown. As the results from the simulation were directly driving the layout of the new sensors, the design of the masks for the photolithographic steps during production will be briefly described afterwards.

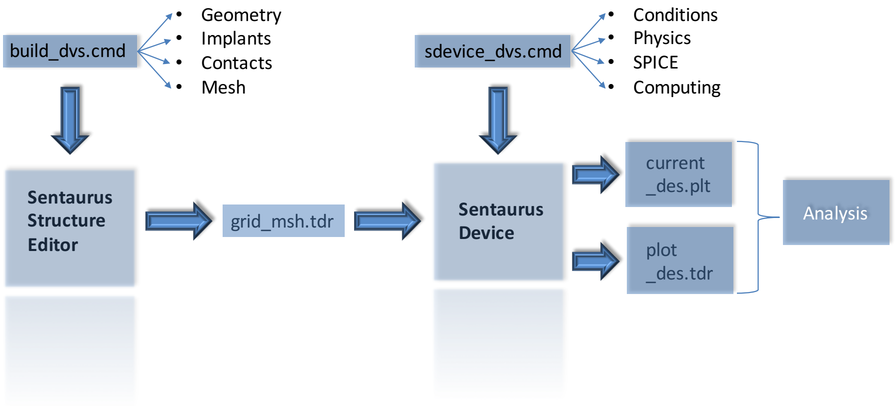

Figure 6.1: T-CAD simulation workflow with the Synopsys Sentaurus software package.

6.1 Technology Computer-Aided Design

Simulation studies were performed due to two important facts. First, the costs are low in comparison to wafer production and processing. The following results were computed on a 8 core machine with 16 GB RAM memory. Secondly, simulations help to understand physical details of some measured sensor features like the electrical behavior and the charge collection efficiency as a function of the fluence, for instance.

In figure 6.1, the workflow of a T-CAD simulation is sketched. First of all, the geometry of the device is built, and the resulting file *build_dvs.cmd* contains all relevant geometry and process informations. A significant advantage of simulations is the quick production of different layouts using variables. In particular, the strip implant width, the p-stop atoll width and the p-stop to strip distance (PS) were varied and studied in detail. Furthermore, the doping concentrations and doping depths of the strip implants as well as for the p-stop were varied. In particular, the latter is of high interest regarding the radiation hardness. The resulting geometry file can be viewed with the Sentaurus Structure Editor. This tool allows a quick check, if all parameters and the definitions of the electrical contacts are set correctly. As a last step of the geometry build, the mesh is generated and stored into the *grid_mesh.tdr* file. The number of mesh points or rather the size of the mesh cells defines the accuracy of the simulation. For the latter, a simple correlation is valid: the more mesh points, the higher the accuracy of the simulation but also higher demands for computing power. Therefore, a custom mesh was used in which the mesh size is small in regions of interest (strip implant, p-stop, silicon dioxide) and is coarse in regions of less importance for accurate physics (for instance deep bulk along y).

The *build_dvs.cmd* and *grid_mesh.tdr* files are direct input files into the Sentaurus Device tool. This is the actual simulation tool in which all physics models, starting conditions of the simulation as well as the SPICE[1] network and computing steps are defined. The simulation results are then

---

[1] Simulation Program with Integrated Circuits Emphasis

stored into the *_des.plt* and *_des.tdr* files and can be analyzed either with additional Synopsys tools or exported into any readable files.
The simulator itself is based on the calculation of the Poisson equation in order to resolve the electrostatic potential:

$$\nabla \cdot \left(\epsilon \nabla \phi + \vec{P}\right) = -q\,(p - n + N_D - N_A) - \rho_{trap}, \tag{6.1}$$

where ϵ is the electrical permittivity and $\vec{\mathrm{P}}$ is the ferroelectric polarization. Moreover, q is the elementary electron charge and $\mathrm{N_D}$ is the concentration of ionized donors respectively $\mathrm{N_A}$ is the concentration of ionized acceptors. ρ_{trap} is the charge density contributed by traps and fixed charges. The electron and hole densities n and p are calculated with Boltzmann-statistics to:

$$n = N_C exp\left(\frac{E_{F,n} - E_C}{k_B T}\right) \quad \text{and} \quad p = N_V exp\left(\frac{E_V - E_{F,p}}{k_B T}\right). \tag{6.2}$$

The constituents are:

- N_C and N_V, the effective density-of-states
- $E_{F,n} = -q\phi_n$ and $E_{F,p} = -q\phi_p$, the quasi-Fermi energies for electrons and holes
- ϕ_n and ϕ_p, the electron and hole quasi-Fermi potentials

In addition, the charge conservation must be assured and calculated at each mesh point. The continuity equations read as follows:

$$\nabla \vec{J_n} = qR_{net} + q\frac{\partial n}{\partial t} \qquad -\nabla \vec{J_p} = qR_{net} + q\frac{\partial p}{\partial t}, \tag{6.3}$$

with $\mathrm{R_{net}}$ as the net recombination rate and $\mathrm{J_n}$ and $\mathrm{J_p}$ as the electron current density and hole current density.
Physics models have to be applied by stating specific headwords. The definition of the models as well as the equations are described in the Sentaurus manual in detail. Exemplary simulation configuration files with different physics model and the description of the most important ones can be found in the appendix.

6.2 Electric fields in silicon detectors

The electric field strength which mainly affects the sensor performance or rather the breakdown voltage, especially after irradiation, can be simulated in detail. Several studies have already been executed in which the comparison between $\mathrm{n^+}$–in–p and $\mathrm{p^+}$–in–n type sensors considering the electric field strength was extracted [Ebe13, EBD⁺14b, Eic12]. These studies have in common that the data, to which the studies refer, was recorded within a huge measurement campaign, the HPK campaign [Hof11] briefly described in section 5.1. Hence, the simulations were mainly performed in order to reproduce the data for both substrate polarities. The simulated geometries were taken from the GDS files of the campaign without any layout variations of the sensors.

Table 6.1: Effective two-defect damage model for proton irradiation of silicon sensors for T = 253 K. E_C and E_V are the edge energies of the conduction and valence band. σ_e and σ_h are the capture cross sections for electrons and holes. Φ is the fluence.

Defect	Energy (eV)	σ_e (cm^{-2})	σ_h (cm^{-2})	Concentration (cm^{-3})
Acceptor	$E_C - 0.525$	1.0×10^{-14}	1.0×10^{-14}	$1.189\ \text{cm}^{-1} \times \Phi + 6.454 \times 10^{13}$
Donor	$E_V + 0.48$	1.0×10^{-14}	1.0×10^{-14}	$5.598\ \text{cm}^{-1} \times \Phi - 3.949 \times 10^{14}$

Table 6.2: Effective two-defect damage model for neutron irradiation of silicon sensors for T = 253 K.

Defect	Energy (eV)	σ_e (cm^{-2})	σ_h (cm^{-2})	Concentration (cm^{-3})
Acceptor	$E_C - 0.525$	1.2×10^{-14}	1.2×10^{-14}	$1.55 \times \Phi$
Donor	$E_V + 0.48$	1.2×10^{-14}	1.2×10^{-14}	$1.395 \times \Phi$

Radiation damage model

A second main task during the campaign was to develop a radiation damage model for T-CAD simulations which should be able to reproduce the data after irradiation. This means that additional energy levels in the silicon bandgap have to be parameterized. Different models were developed, ranging from two-effective defects [Ebe13] to five-effective defects [EBD$^+$14a]. All damage and energy levels are compressed into two to five effective defects. Development of a model means that the additional inter bandgap levels are configured such that the current, depletion voltage and electric fields of the simulation match the measurements.

In this thesis, the two-effective defect model for proton and neutron irradiations was used. The models for both particle types are listed in table 6.1 and 6.2.

In the model valid for neutron irradiation, the concentration of the defects is directly proportional to the fluence. In order to match the full depletion voltage, the cross sections for electron and holes are set to 1.2×10^{-14} cm^2. The concentration for the donor is 90% of the concentration of the acceptor. In the proton model, the cross sections are 1.0×10^{-14} cm^2 for both electron and holes. The probability of a drifting charge carrier to be captured by a defect is dependent on the cross section, the bulk defect concentration N_i and the probability P_i which describes whether a defect is already occupied or not:

$$\frac{1}{\tau_{eff}} = \sum N_i \left(1 - P_i^{e,h}\right) \sigma_{e,h} v_{drift_{e,h}}, \tag{6.4}$$

where τ_{eff} is the effective trapping time, which is correlated with the mean free path of the charge carrier. The concentration of defects has additional correction values. Without the correction a reproduction of the charge collection would not be possible. This effect is related to the different defects in dependence on the charge of the incoming particle. Both models are valid in the range

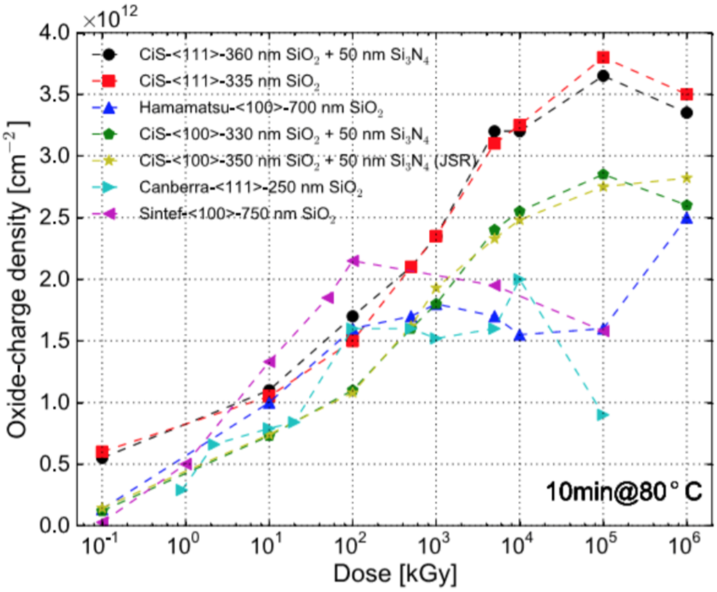

Figure 6.2: Fixed oxide charge as a function of the ionizing dose. Here different oxide thicknesses as well as different crystal orientations have been studied [Zha13].

between $\Phi = 1 \times 10^{14}$ 1MeV $n_{eq}cm^{-2}$ and $\Phi = 1.5 \times 10^{15}$ 1MeV $n_{eq}cm^{-2}$. This range of the fluence is exactly the range for the sensors which are investigated in this study. In order to simulate higher fluence of the pixel detector region, new damage models have to be developed.

Role of the surface damage

During irradiation of detectors, not only bulk defects but also surface defects which affect the sensor performance are introduced. Basically, the surface damage should be also parametrized, as the bulk damage shown above. The surface damage is complex and can be divided into the *fixed oxide charge* as deep level defects, the *oxide trapped charge* and *interface traps* at the $Si - SiO_2$ interface. The interplay of these defect types has been studied in detail in [Zha13] for the European XFEL facility in Hamburg, Germany. The defects are created by ionization and may increase the current due to additional surface currents. Especially in the case of n^+–in–p type detectors, the formation of the accumulation layer of electrons is a direct consequence of the positively charged oxide defects. The dependence of the fixed oxide charge on the dose after an annealing of 10 min at 80°C is show in figure 6.2. Before irradiation, the positive oxide charge is in the range of 1×10^{10} cm^{-2} to 1×10^{11} cm^{-2}, depending on the growing method during the processing. After irradiation it increases and saturates at about 3×10^{12} cm^{-2}. At the HL-LHC, a dose of about 10^5 kGy is expected. However, the bulk damage models shown in tables 6.1 and 6.2 were developed for a fixed value of fixed oxide charge and a beneficial annealing of 10 min at 60°C. This means, independent of the fluence or rather the dose, the proton model is valid in the range of $\Phi = 1 \times 10^{14}$ 1MeV $n_{eq}cm^{-2}$ and $\Phi = 1.5 \times 10^{15}$ 1MeV $n_{eq}cm^{-2}$ and a fixed oxide charge of

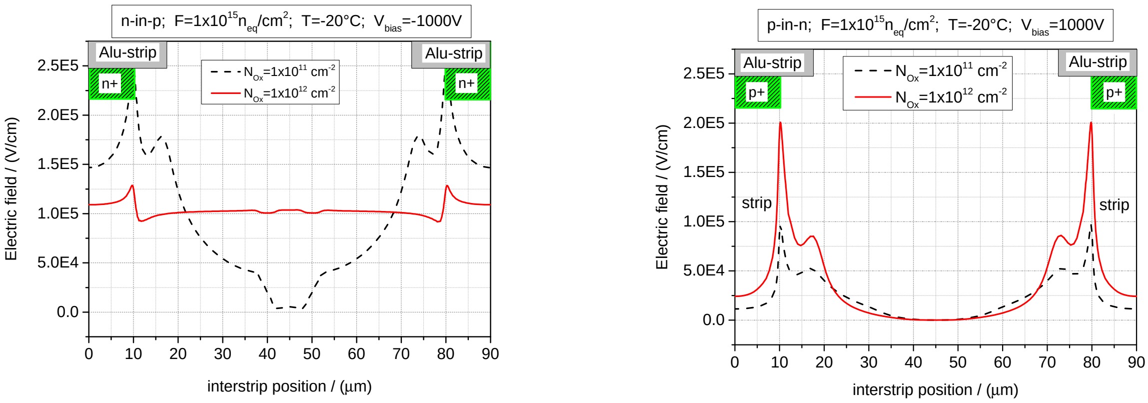

(a)

(b)

Figure 6.3: Electric field strength in dependence on the oxide charge.

1×10^{12} cm^{-2} at $T = -20^{\circ}\mathrm{C}$. The neutron model reproduces data for a surface defect concentration of 7×10^{11} cm^{-2}. The latter is due to the fact that neutrons in general ionize the SiO_2 less. A detailed parameterization of the surface damage is currently ongoing within the CMS Tracker Collaboration. Within this study, the fixed values for the simulations were used.

6.3 Electric field strength as a function of the oxide charge

Simulations calculate the electric field strength in the bulk although due to model uncertainties the values should be interpreted qualitatively in order to understand the coherences. Figure 6.10 shows the electric field distribution 1.3 μm below the sensor surface for $n^{+}-in-p$ type in 6.3(a) and $p^{+}-in-n$ type in 6.3(b). At this depth, the pn junction for this geometry starts.
In this simulation, the pitch and the width-to-pitch-ratio are chosen corresponding to the current Tracker Phase II Upgrade baseline with 2S modules ($p = 90\ \mu\mathrm{m}, w/p = 0.22$). The proton model was taken and the conditions are $V_{\mathrm{bias}} = -1000$ V at $T = -20^{\circ}\mathrm{C}$ for a fluence of $\Phi = 1.0 \times 10^{15}$ 1MeV $n_{\mathrm{eq}}\mathrm{cm}^{-2}$. It is obvious that for p-type detectors the increasing oxide charge is advantageous with respect to the electric field strength, whereas in n-type detectors, increasing oxide charge results in higher electric field strength. In case of n-type sensors, the electric field density at the strip implant edges is high where local avalanche effects may occur. Hence, p-type detectors are less prone to local microdischarges or electrical break down due to the flat electric field distribution between the strips which is due to the conductive electron layer below the surface. This observation led, amongst others, to the decision to use p-type detectors for the upgrade. Besides, the secondary peaks of the distributions just below the Alu-strip are the effect of the metal overhang of 6 μm which for both polarities attracts the field towards the Alu-strip edges leading to lower maximum electric fields in the bulk.

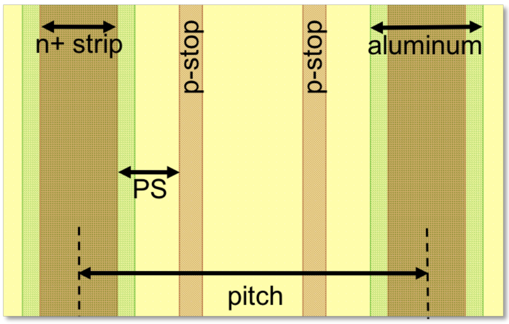

Figure 6.4: Section from a GDS file showing the definition of the strip to p-stop distance.

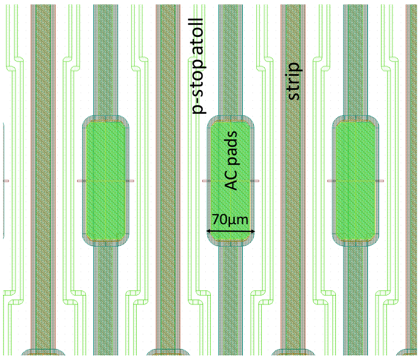

Figure 6.5: P-stop atoll pattern in the AC pad region for the sensors in the HPK campaign.

6.4 Electric fields in dependence on the p-stop characterstics

The p-stop atoll is a pattern where each individual strip posseses its own individual p-stop implantation surrounding itself. Accordingly, the question arises of what the pattern should look like. The p-stop should not affect the sensor's leakage current and charge collection but at the same time ensure a sufficient strip isolation. Furthermore, in dependence on the strip to p-stop distance PS shown in figure 6.4, the design of the p-stop is much simpler compared to the example shown in figure 6.5. Here, one can see that due to a close spacing of the p-stop to the strip implant, the p-stop has to be designed around the AC pads. The AC pads are the connecting pads for the readout chip and are around 50 μm to 70 μm wide. The width of the AC pads should ensure wire bonding with high yield and also the placement of probing needles for the electrical qualification. Therefore, (although technically possible and without any known impact on electrical properties) the p-stop should not be implanted below the pads as this leads to a non-uniform metal surface. In order to ensure good connectivity during measurements or bonding, the metal surface should be as even as possible.

Before the design of the sensors for this study, simulations were carried out in which the p-stop pattern was varied. A script extracts the maximum electric field strength in the silicon bulk from the simulation results. For this study, the proton model for simulations of irradiated devices was used. In order to get reliable results from the simulations, the parameters of the HPK campaign sensors were used due to the fact that the damage model was developed on HPK data. The sensor characteristics are listed in table 6.3. The pitch was varied to p= 90 μm compared with p= 80 μm for the HPK sensors as this pitch was decided to be used for the 2S p_T modules.

As during the qualification of sensors in an electrical probe station, the simulations were performed at T= 20°C for unirradiated and T= −20°C for irradiated sensors. The latter temperature is the target temperature at sensor level for the HL-LHC conditions. Lowering the temperature at the sensor decreases the leakage current and improves the noise behavior. The relation between

Table 6.3: Parameters used for the simulation of the p-stop effects on electric field strength

Quantity	Value
Substrate thickness	300 μm
Strip pitch	90 μm
Bulk doping	3×10^{12} cm^{-3}
Strip implant doping	1×10^{19} cm^{-3}
Strip doping depth	1.5 μm
Strip doping width	25 μm
Backside doping	5×10^{18} cm^{-3}
Backside doping depth	5 μm
p-stop implant doping	varied from 1×10^{16} to 9×10^{16} cm^{-3}
p-stop width	varied to $4, 6, 8$ μm

temperature and leakage current for a diode was described in [Chi11]:

$$I(T) \propto T^2 exp\left(\frac{-1.21\ eV}{k_B T}\right). \tag{6.5}$$

It is possible to normalize the measured current at lower temperatures to the equivalent current at room temperature T= 20°C with the following formula:

$$I(T = 20°C) = I(T) \times \left(\frac{293\ K}{T}\right)^2 exp\left(\frac{-1.21\ eV}{k_B T}\left[\frac{1}{293\ K} - \frac{1}{T}\right]\right). \tag{6.6}$$

Before irradiation, the sensors are fully depleted at around $\mathrm{V_{FD}} = 220$ V. Within the sensor community, it has been decided to measure all relevant parameters at $V > 1.2 \times \mathrm{V_{FD}}$. For the simulation study, a voltage of $\mathrm{V} = -300$ V in the unirradiated case was used. Not only the leakage current increases but also the full depletion voltage because it is directly proportional to the effective doping concentration $|\mathrm{N_{eff}}| = \mathrm{N_D} - \mathrm{N_A}$ which changes with ionizing irradiation, too. $\mathrm{N_D}$ and $\mathrm{N_A}$ are the concentrations of donors and acceptors. When more donors than acceptors are created, the positive space charge increases and as a consequence the full depletion as well, due to the simple relation:

$$V_{FD} = \frac{qd^2|N_{eff}|}{2\epsilon_{Si}}, \tag{6.7}$$

where d is the sensor thickness. The absolute value of charges is represented by q. In order to collect as much generated charge as possible, the sensors have to be powered with higher voltages compared to unirradiated sensors. For the future Tracker, different scenarios have been calculated. Currently, it is under study if a high voltage of up to around 900 V could be applied to the sensors during Run 3 with the existing services. A high voltage of around 600 V is the baseline. Therefore, the simulation results after irradiation were performed at 600 V and 900 V.

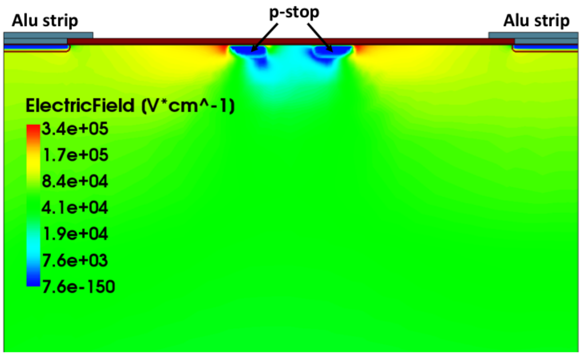

(a) Exemplary 2d simulation of the electric field between two half strips with the HPK parameters (here after irradiation in order to visualize the gradient).

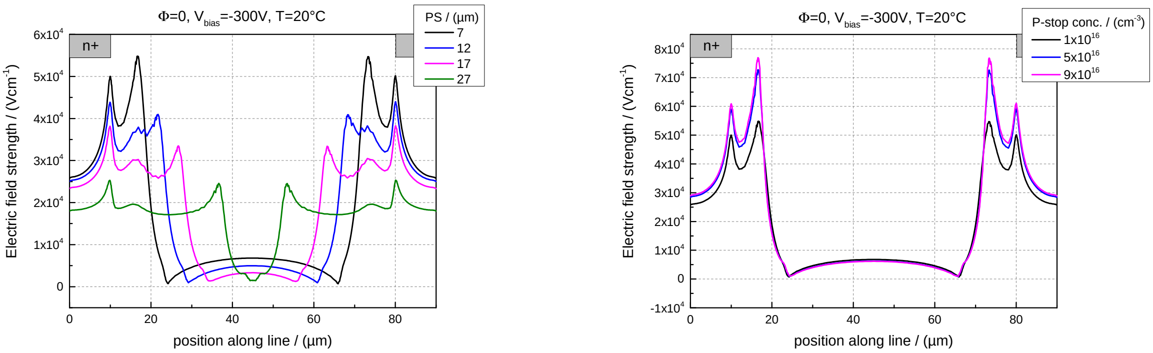

(b) $p_{conc} = 1 \times 10^{16}$ cm^{-3}, width= 6 μm

(c) PS= 7 μm

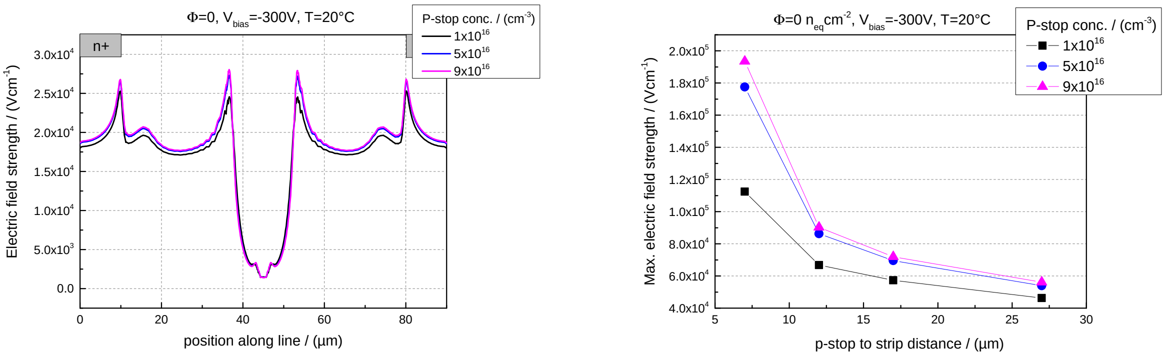

(d) PS= 27 μm

(e) max. electric field strength

Figure 6.6: Figure 6.6(a) visualizes the electric field in the simulation. From these results, different informations are extracted. In 6.6(b) the max. electric field is plotted as a function of the PS before irradiation. 6.6(c) shows a cut line through the electric field 1.5 μm below the Si-SiO$_2$ interface for PS= 7 μm and 6.6(d) for PS= 27 μm in dependence on the p-stop doping concentration. In 6.6(e), the max. electric field strength in the bulk is plotted as a function of PS.

Results - unirradiated case

The following information and results are derived from the 2d simulation. Figure 6.6(a) exemplarily visualizes such a 2d electric field plot. In order to keep the computing time low, the symmetric geometry of two half strips with a pitch of 90 μm was used. Due to the fact that this structure periodically recurs up to several hundreds times in a real sensor, the Neumann boundary conditions are applied implicitly to all boundaries which are not set as contacts (in this case, to the left and right of the shown 2d plot).

In figure 6.6(b), one can see the effect of the p-stop to strip distance in the unirradiated sensor at a bias voltage of -300 V and room temperature. Clearly, the lower the PS value, the higher the electric field strength. Here, the electric field density is higher at the strips due to the influence of the p-stop on the potential. The p-stop doping depth is kept constant to 2 μm and the strip implants to 1.5 μm. Also, the effect of the metal overhang (MO) is recognizable, which is the second peak in the electric field cut line 1.5 μm below the Si-SiO$_2$ interface next to the first peak just under the n+ implant. Figures 6.6(c) and 6.6(d) show, at the same conditions as in 6.6(a), cut lines for PS= 7 μm and PS= 27 μm for three different p-stop doping concentrations respectively. It seems that before irradiation, the doping concentration of the p-stop does not influence the electric field strength in a significant way. From this point of view, a relatively high p-stop peak doping concentration of about 9×10^{16} cm^{-3} is good before irradiation as the interstrip resistance is assured (see the measurements chapter 8.1). Taking a closer look at figure 6.6(a), it can be seen that the maximum electric field strength is some tens of nanometers below the Si-SiO$_2$ interface. Therefore figure 6.6(e) shows the maximum electric field strength which was extracted from the silicon bulk independent of the high field position. As a consequence, the values are slightly higher compared to the values plotted in 6.6(b). Nevertheless, as a further consequence of the simulations of unirradiated silicon n$^+$−in−p strip sensors with different p-stop atoll pattern, clearly the implantation of the p-stop should be placed just in the center between two adjacent strips. This lowers the maximum electric field and hence the breakdown voltage increases.

The p-stop common technique has been investigated in [VBF$^+$12] with the result that the p-common negatively influences the signal to noise ratio of the sensors. Therefore, the study presented concentrates on the p-stop atoll only. Nevertheless, samples with the p-stop common layout were also produced in order to check against the results shown in [VBF$^+$12] and comparable investigations were started.

Results - irradiated case

For the irradiated case, the simulation with the damage models described in tables 6.1 and 6.2 changes the picture in dependence on the applied isolation parameter. First of all, in figure 6.7(a) the significance of the cut line below the surface is shown. Here, one can see that a wrong interpretation of the electric field strength could happen if the cut line is not set properly. This is of importance in particular after irradiation to $\Phi = 1 \times 10^{15}$ n$_{\mathrm{eq}}$cm^{-2}, indicated by the

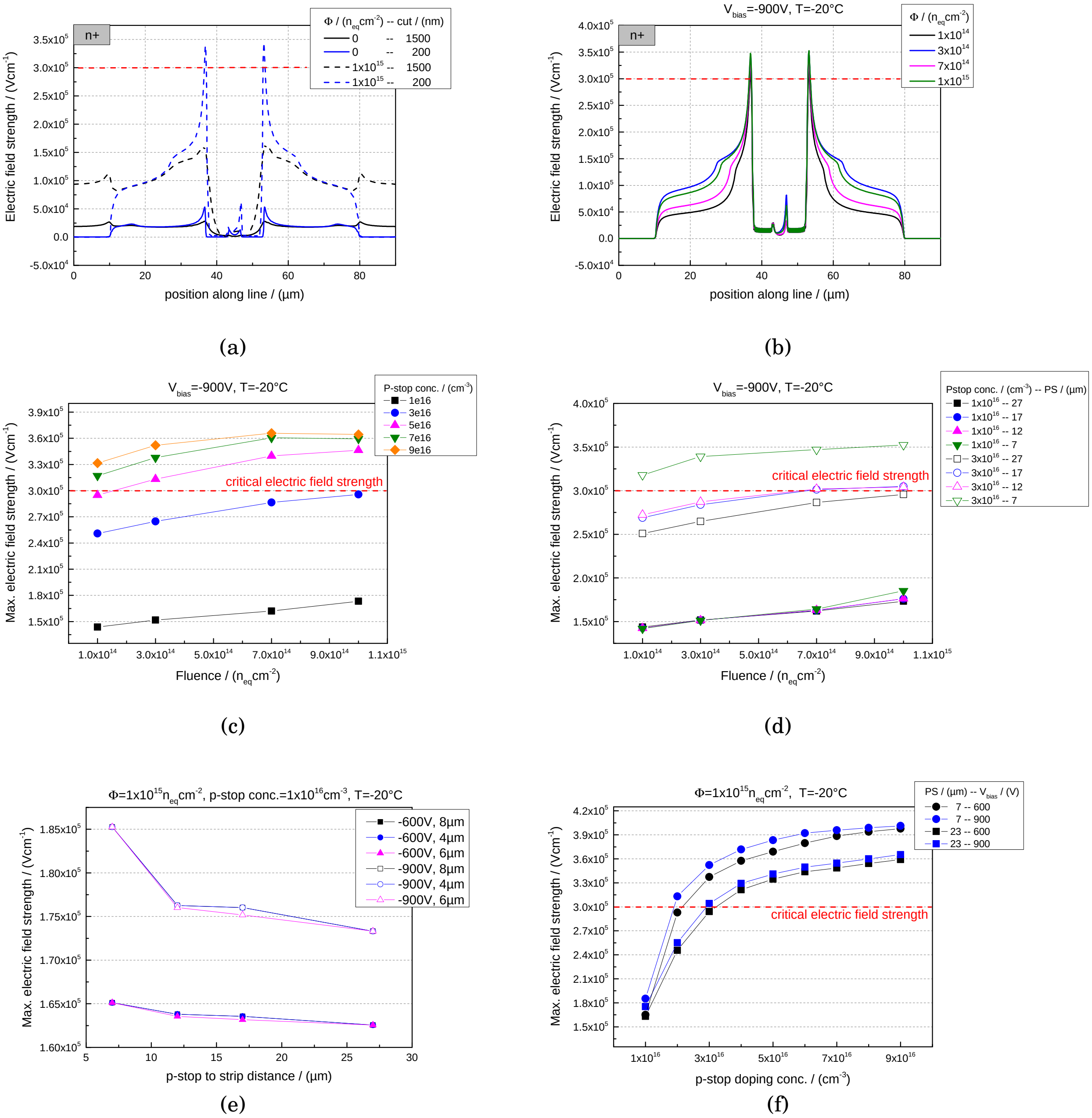

(a) (b)

(c) (d)

(e) (f)

Figure 6.7: Figure 6.7(a) indicates the significance of the correct cut line. In 6.7(b), the max. electric field is plotted as a function of the fluence for a p-stop doping concentration of 9×10^{16} cm^{-3}. 6.7(c) and 6.7(d) show the maximum electric field independent of the appearance for different p-stop doping concentrations and positions. In 6.7(e), the max. electric field strength in the bulk for three different p-stop widths is shown, assuming a doping concentration of 1×10^{16} cm^{-3}. Figure 6.7(f) shows the extracted maximum electric field strength as a function of the doping concentration after a fluence of 1×10^{15} n$_{\text{eq}}$cm^{-2}.

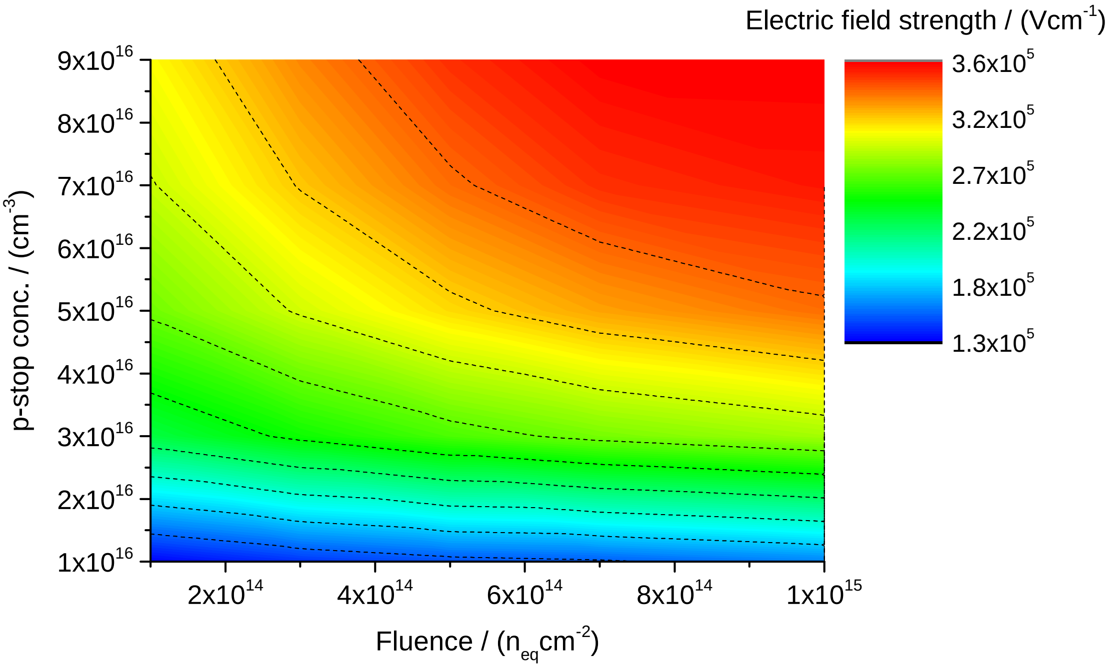

Figure 6.8: Scan of the electric field strength as a function of the p-stop peak doping concentration and particle fluence. Proton model and sensor parameters as in table 6.3, T= 253 K, $V_{\text{bias}} = -600$ V, $N_{\text{Ox}} = 1 \times 10^{12}$ cm^{-2}.

dashed lines when high electric fields in the region of $\approx 10^5$ Vcm^{-1} are expected. In figure 6.7(b), one can see such high fields at the p-stop curvatures already after a relatively low fluence of $\Phi = 1 \times 10^{14}$ n$_{\text{eq}}$cm^{-2}. Especially after a proton fluence of $\Phi = 1 \times 10^{15}$ n$_{\text{eq}}$cm^{-2}, the electrical breakdown voltage of a pn-junction in silicon with 3×10^5 Vcm^{-1} is reached. Hence, a scan of the p-stop peak doping concentration was performed for the same fluence. From figure 6.7(c) one can derive that for the nominal doping depth of the boron of around 2 μm, a peak doping concentration of 3×10^{16} cm^{-3} should not be exceeded to stay below critical field strengths. Here, the positioning of the p-stops was already optimized taking the value for the p-stop to strip distance PS of 27 μm.

Figure 6.7(d) now concentrates on the p-stop doping concentrations of 1×10^{16} cm^{-3} and 3×10^{16} cm^{-3}. According to the simulations, these values seem to assure high breakdown voltages. But when using this values with the different p-stop doping positions one can see that the electric field strengths for the lower p-stop concentration are not affected at all while the higher p-stop doping concentration of 3×10^{16} cm^{-3} also shows high electric fields when the p-stop to strip distance was chosen to be smaller and towards the end of the sensor lifetime. Consequently, the upper range for the p-stop doping concentration is limited and so far the interstrip resistance R_{int} has not been considered at all. R_{int} will be discussed in the coming sections.

So far, the doping width of the p-stop was been considered. The constraints for the width are the effect on the electric field, the interstrip resistance and the production feasibility for the vendor. This means that an implantation of a few μm is not trivial and some vendors require at least 4 μm wide pattern. In addition to the physical implantation width, the lateral diffusion has to be taken into account. In general, after implantation, diffusion processes are applied in which the wafers are heated up to several hundreds degrees. This thermal diffusion also spreads laterally. A value of about 80% of the depth can result in lateral diffusion. The lowest value for almost all vendors is 4 μm. After the diffusion process, a p-stop width of about 5 μm is expected[2]. The electric field strength for the p-stop doping concentration of 1×10^{16} cm^{-3} and a fluence of 1×10^{15} n$_{\text{eq}}$cm^{-2} for three different p-stop doping widths of 4, 6 and 8 μm is plotted in figure 6.7(e). Here the bias voltages of 600 V and 900 V are shown. For both high voltages, the electric field strengths are within a safe range although for higher voltages also the electric field strength increases. From this point of view, the width of the p-stop does not affect the breakdown voltages but it has to be mentioned that although the width was varied, the PS distance was kept the same. This means that the electric field density between the strip edge and the p-stop edge is the same. The relatively small range for the p-stop doping concentration is shown in figure 6.7(f). One can see, how the critical range for the electric field strength is quickly reached even for a low boron doping concentration of 2×10^{16} cm^{-3} when the position of the implant is close to the strip, for both 600 V and 900 V. Here, again the end of the lifetime after an integrated luminosity of 3000 fb^{-1} was considered for inner strip sensors of the PS modules. The default simulation settings are such that although the electric field strength lowers the breakdown voltage, the simulator does not stop as long as the calculations converge.

The maximum electric field strength as a function of the proton fluence and the p-stop doping concentration was simulated for the HPK sensor characteristics listed in table 6.3 and is plotted in figure 6.8. Independent of the appearance in the bulk, the maximum electric field strength in the sensor was extracted for a bias voltage of -600 V and T= 253 K. Obviously, with increasing fluence and p-stop doping concentration, the maximum electric field strength increases too.

The measurements for different sensor suppliers and boron doping concentrations will cover the range shown in this plot in order to make a comparison and to verify the damage model and in general the simulation predictions.

Besides the doping concentration and position of the p-stop isolation structure, also the depth of the implant has to be balanced. As in figure 6.8, a scan of the p^{+} and n^{+} doping depths was performed as well. In figure 6.9, the results are shown for two different p-stop doping concentrations of 1×10^{16} cm^{-3} and 5×10^{16} cm^{-3} for the fluence of $\Phi = 1 \times 10^{14}$ n$_{\text{eq}}$cm^{-2} and $\Phi = 1 \times 10^{15}$ n$_{\text{eq}}$cm^{-2} respectively. It seems that an increasing p-stop doping depth influences the electric fields negatively whereas the strip implant concentration does not effect the field strength at all. Furthermore, for the concentration of 1×10^{16} cm^{-3}, the electric field strength stays in a low range even for deep diffusion to 3 μm. Simulation of the interstrip resistance has

---

[2] depending on the vendor and the chosen process sequence

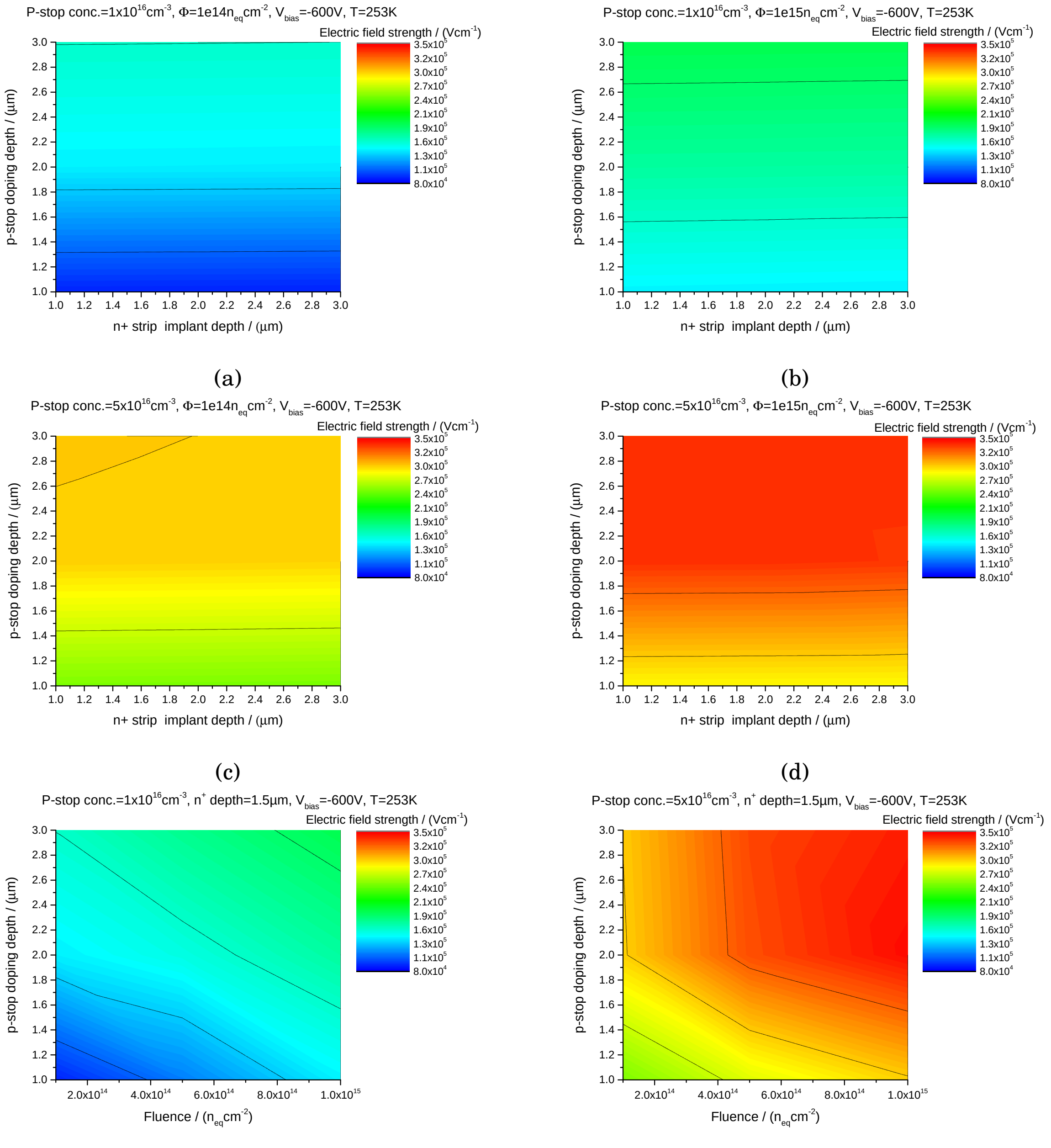

(a) (b)

(c) (d)

(e) (f)

Figure 6.9: Electric field strength in dependence on the n^+ and p^+ doping depths. Two different p-stop concentrations and fluence are shown. Colored legend shows the maximum electric field in bulk.

now to be executed in order to study if a shallow doping and the maximum boron concentration for the isolation leads to a satisfying interstrip resistance.

The effects of the various p-stop isolation characteristics on the electric fields E_{max} with respect to simulation studies in particular after irradiation is summarized in table 6.4:

Table 6.4: Effects on the maximum electric field E_{max} in dependence on the p-stop characteristics

Value: Quantity:	low	high
p-stop-strip distance	$E_{max} \Uparrow$	$E_{max} \Downarrow$
p-stop width	$E_{max} \Leftrightarrow$	$E_{max} \Leftrightarrow$
p-stop doping conc.	$E_{max} \Downarrow$	$E_{max} \Uparrow$
p-stop depth	$E_{max} \Downarrow$	$E_{max} \Uparrow$

6.5 Interstrip resistance R_{int}

The interstrip resistance is a crucial parameter for silicon detectors as it directly influences the resolution of a sensor. A high interstrip resistance must be achieved independent of the irradiation level in order to isolate adjacent strips and distinguish successfully between hit strips. R_{int} is measured between two adjacent strips on their DC pads. The DC pads hold the feature that the pads are, with the help of vias, directly contacted to the strip implant and the direct current can be measured. These DC pads are not mandatory for the operation but are used for the qualification of sensor parameters like the interstrip resistance. While the whole sensor is biased via the bias ring with high voltage, an additional low voltage (LV) is applied to two neighboring strips and a voltage ramp in 0.2 V steps up to 2 V is conducted. The Ohmic law describes the relation between current, voltage and resistance. Hence, the interstrip resistance is obtained from the current measurement driven by the LV. A measurement setup is shown in figure 6.10(a).

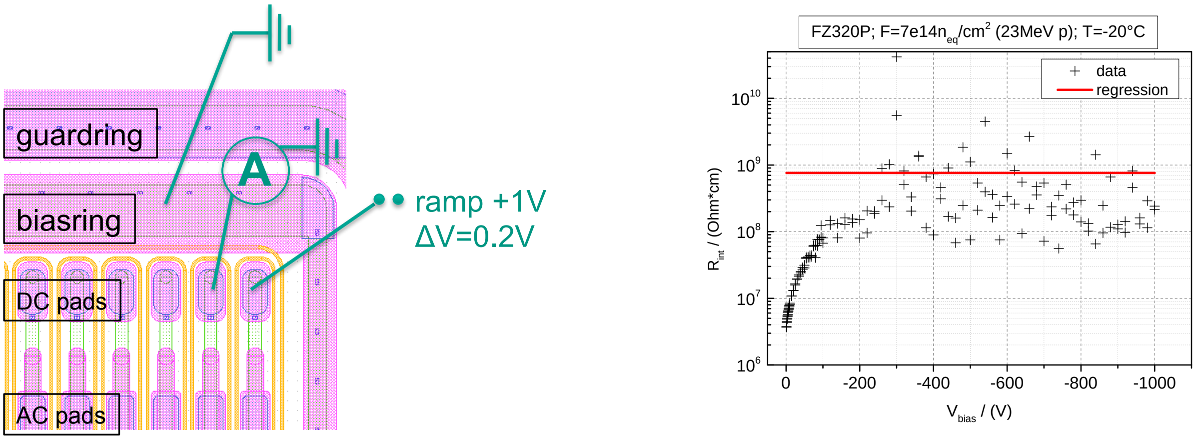

(a) R_{int} measurement network

(b) Definition of the R_{int} value

Figure 6.10: Definition and measurement setup of the interstrip resistance R_{int}. In (a), the measurement network is shown where an additional LV is applied between two adjacent strips, and in (b), the determination of R_{int} for a float-zone 320 μm thick sensor after a proton irradiation to 7×10^{14} $n_{eq}cm^{-2}$ is shown.

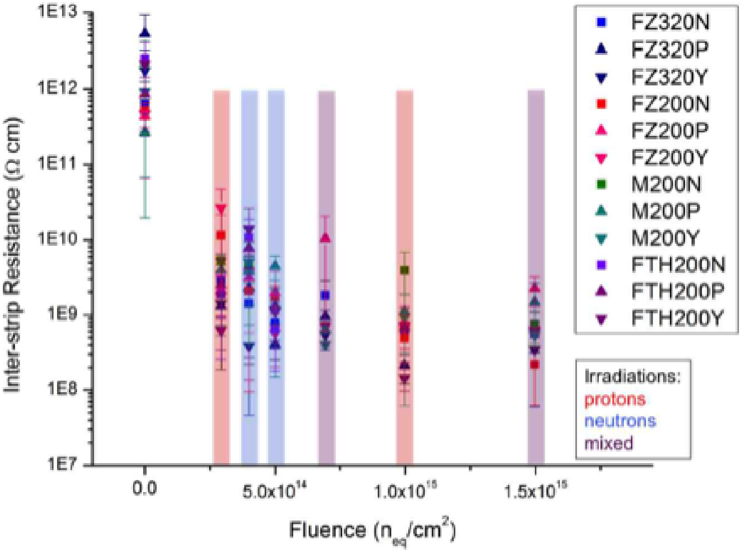

Figure 6.11: Interstrip resistance for different substrate material, thickness and polarity for the HPK samples as a function of the fluence [Hof13].

Constraints of the measurement are the strip leakage current, noise and the current range of the measurement device. In the following chapter, in which the results from the measurements will be shown, the interstrip resistance is determined in a bias voltage ramp shown in figure 6.10(b). In general, all strips of a sensor are scanned for high statistics and in order to absorb fluctuations. As R_{int} increases and saturates with the HV, a linear fit with a slope of 0 is fitted to the values in the range between 400 V and 900 V, as this is the bias range after high irradiation level.

During the large HPK measurement campaign, the interstrip resistance was also measured for all kinds of sensors [Hof13]. Here, the substrate materials, thickness and polarity were varied and the sensors were irradiated to a high fluence. Within this study, it was found that the interstrip resistance is the only parameter for the electrical measurements which significantly changes after irradiation. While R_{int} starts in the range of tens of GΩ before irradiation, the value decreases by at least three orders of magnitude for the HPK samples, see figure 6.11. Unfortunately, the parameters for the boron isolation are not known from the vendor, due to its corporate secret. Nevertheless, even after degradation, the value of about $> 10^8$ GΩcm still fulfills the specification of $R_{int} > 20 \times R_{poly}$. R_{poly} is the poly silicon bias resistor for each individual strip and is in the range from 2 MΩ to 4 MΩ, where the range has been specified by the CMS tracker community.

For the simulation, the SPICE network was adapted in order to mirror the measurement setup. This means, as during the electrical qualification, an LV ramp between two adjacent strips was added in order to be as close to the measurement setup as possible. Than again, the p-stop doping concentration as well as the p-stop depth was varied. The result is plotted in figure 6.12. Several conclusions can be drawn: First of all, one can see that a sufficient interstrip resistance in the simulation can be achieved first for a minimum p-stop doping concentration of

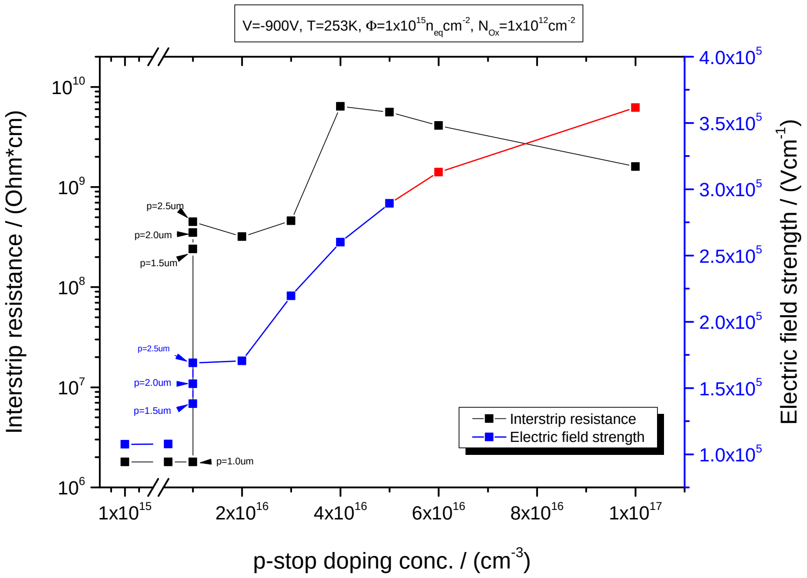

Figure 6.12: Simulated interstrip resistance as a function of the p-stop doping concentration and depth after a fluence of $\Phi = 1 \times 10^{15}$ $n_{eq}cm^{-2}$ at -900 V and T= 253 K. The strip implant depth is 2 μm.

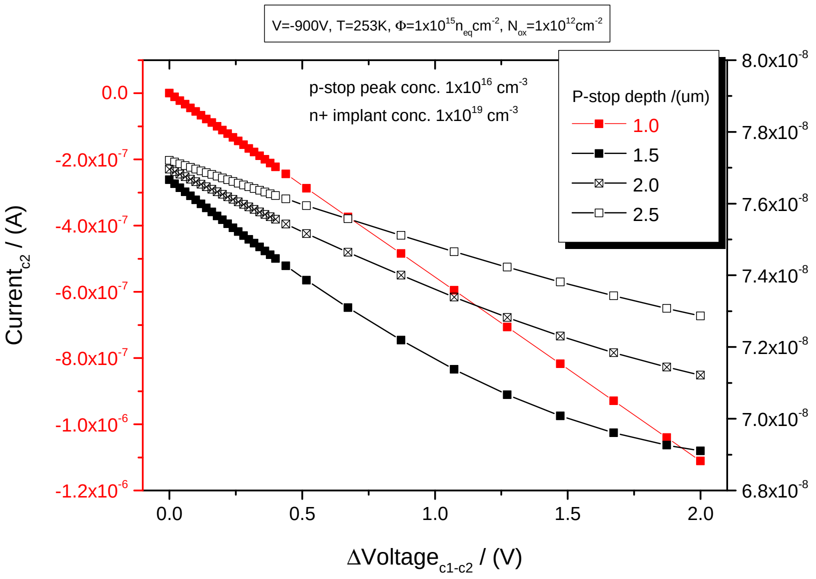

Figure 6.13: Simulated interstrip resistance as a function of the p-stop doping depth after a fluence of $\Phi = 1 \times 10^{15}$ $n_{eq}cm^{-2}$ at -900 V and T= 253 K. The strip implant depth is 2 μm and the p-stop doping concentration is kept constant to 1×10^{16} cm^{-3}.

1×10^{16} cm^{-3} and more importantly, the p-stop doping depth should be at least 1.5 μm. This is valid if the strip implant doping depth is 2 μm, which was used for this simulation. Moreover, the simulated interstrip resistance is combarable with the measured interstrip resistance after

$\Phi = 1 \times 10^{15}$ $n_{eq}cm^{-2}$, shown in figure 6.11. With increasing p-stop doping depth, R_{int} increases as expected and the electric field strength, too. But the latter is, for the moderate boron concentration of 1×10^{16} cm^{-3}, still in a healthy range and in agreement with the results shown in figure 6.9 in the previous section. The red line emphasizes the range of the high electric field strength above 3×10^5 Vcm^{-1}. The value for R_{int} of 1 MΩcm for low doping concentrations is due to the fact, that if the R_{int} is too low, the measured or simulated value for the R_{int} corresponds to the resistance of the measured R_{poly} bias resistors in parallel mode. As here two strips, each with a R_{poly} = 2 MΩcm was simulated, a resistance of 1 MΩcm is expected when no strip isolation is given.

Figure 6.13 visualizes the point in figure 6.12 where the R_{int} starts to be satisfactory (p-stop conc.= 1×10^{16} cm^{-3}). C1 and C2 are the electrodes at which the LV is applied. The inverse of the curve's slope is the interstrip resistance. The red curve is related to a low interstrip resistance and behaves linearly in this range. An interesting fact is that like in the measurement, the fit to the LV ramp points is linear by default. But in measurements as in the simulated case, a non-linear curve is observed after irradiation. This is related to the leakage current of the bulk and also in agreement with the simulation.

As for the maximum electric field strength in the previous section, the effects on the interstrip resistance in dependence on the p-stop characteristics are listed in table 6.5:

Table 6.5: Effects on the interstrip resistance R_{int} in dependence on the p-stop characteristics. (The last points have not been shown implicitly).

Value: / Quantity:	low	high
p-stop doping conc.	$R_{int} \Downarrow$	$R_{int} \Uparrow$
p-stop depth	$R_{int} \Downarrow$	$R_{int} \Uparrow$
p-stop width	$R_{int} \Leftrightarrow$	$R_{int} \Leftrightarrow$
p-stop position	$R_{int} \Leftrightarrow$	$R_{int} \Leftrightarrow$

Drawbacks of present radiation damage models

In general, tens of different point defects and clusters depending on the irradiation particle type and energy are present. Clearly, the phase space for the implementation of all known defects into the simulation is too large. Therefore, defect damage models with a couple of defects (in this thesis, the 2-effective defect model) are developed which can describe the measurements in a certain region with good agreement. The main goal was to reproduce the data from the technical point of view. A physical approach should include more, or in best case, all defects. The damage model used in this thesis is the 2-defect damage model, as described in one of the previous sections. This model is valid for the fluence range of $\Phi = 1 \times 10^{14}$ $n_{eq}cm^{-2}$ to $\Phi = 1.5 \times 10^{15}$ $n_{eq}cm^{-2}$. More important is that the model is only valid when a constant number

of positive oxide charges ($N_{\text{Ox}} = 1 \times 10^{12}$ cm^{-2} for the proton model) is used. But the study of Zhang, shown in figure 6.2, clearly indicates that the oxide charge after such high fluence exceeds the value of $N_{\text{Ox}} = 1 \times 10^{12}$ cm^{-2} for proton irradiation. As soon as the oxide charge is slightly increased in the simulation using the 2-defect model, the interstrip resistance vanishes also for a p-stop doping concentration of $= 1 \times 10^{16}$ cm^{-3} and higher which, at a first glance, seems to be a suitable value corresponding to the results gained during the HPK campaign[3]. Hence, some further defects at the $Si - SiO_2$ interface and oxide have to be implemented. One approach has been presented by [Pel14], where a third trap in form of shallow acceptor levels just 1 μm under the $Si - SiO_2$ interface was implemented (the work was done within the CMS silicon sensor simulation working group). This model also reproduces data with good agreement and also allows higher values for the oxide charge ($N_{\text{Ox}} = 2 \times 10^{12}$ cm^{-2}). A further model was developed within the simulation working group and published in [JBD^{+}15]. Here in particular, the interface and oxide damage, which has significant influence on p-type sensors, was extended by two additional surface acceptor levels. With this model it is also possible to reproduce data for a even higher fluence (important for the pixel detector region), but in contrast it is only valid for a second software, the Silvaco software simulation package [Sil]. Actually, the different simulation software packages (Synopsys and Silvaco) differ slightly in some of the implemented physics models due to different values for physical paramters. Hence, a direct comparison of results obtained from different packages is difficult.
Nevertheless, simulations are a powerful tool for sensor development and should be taken into account, especially in order to save time and costs, but clearly the production and measurements of silicon sensors for such harsh radiation environment like at the HL-LHC are unavoidable.

This brings us now to the next chapter in which the design of different wafers and sensors based on simulation results will be discussed.

---

[3] The concentration and depth of the HPK samples have been measured with the spreading resistance method [Tre12]

CHAPTER 7

DESIGN OF SILICON STRIP SENSORS

Development of radiation hard silicon detectors includes several aspects, ranging from the choice of the substrate material and thickness to the design or rather the surface layout of the components, like the strips and the isolation structure. As shown in the previous chapter, simulation studies support the development and understanding of detector characteristics. Nevertheless, the design and production with subsequent measurements and irradiation studies are required. The combination of simulations and data should converge to the choice of the silicon detectors for the CMS Tracker Phase II Upgrade.

The most promising design aspects from the T-CAD studies as well as some of the less promising ones, in order to prove the simulation predictions, were realized on three different wafers of three different vendors. Sensor design aspects like the close PS distance were also included in the wafer design in order to qualify and check the simulation predictions. In this chapter, the design of the silicon strip detectors used for the p-stop isolation study will be shown.

7.1 Design of photolithographic masks

The layouts for the photolithographic masks for the production of the wafers were designed within this study. In total, three different wafers were realized and produced. The final wafer layouts and a short description of wafer processing at ITE Warsaw[1] are in the appendix B.

The mask design itself was done with the LayoutEditor software [LE] which is a graphical design software for IC structures. The output files are in the GDS format, which can be directly taken for the mask production at the producing company. The layouts were designed using macro scripts programmed in C++ like code which allows a fast redrawing of structures. This is important due

---

[1] Institute of Electron Technology Warsaw

to many changes during the layout process and additional constraints by the vendor which are propagated during the iterations before the final production.
For the p-type wafers with p-stop isolation pattern, at least seven masks are necessary in order to process a silicon strip detector. At this juncture, masks for the different implantations are required as well as masks for the metal layer and passivation openings. Furthermore, additional masks for the DC contacts are needed. Depending on the run and vendor, an additional mask is necessary if a shallow nitride layer below the coupling oxide is required. This layer should ensure radiation hardness in form of stable coupling capacitances and hence a stable channel noise input. In this study, this technique was not used and will not be discussed any further. Then, an additional mask may be required if the periphery of the sensor shall be implanted with a higher dose in order to achieve a higher doping concentration in the order of 1×10^{19} cm^{-3}. The higher concentration in the periphery is applied in order to prevent an influence of additional currents which are generated at the sensor edges due to the dicing. The latter destroys the single crystal lattice of the silicon bulk and introduces undesired currents. This technique was used for the ITE and CNM[2] runs whereas for the CiS[3] run it has been discarded. Here, the periphery concentration is equal to the p-stop doping concentration ($\approx 1 \times 10^{16}$ cm^{-3}), hence one photolithographic mask for both implantation regions was used.

7.2 Sensor layout for the p-stop isolation study

All three wafer layouts contain one specific test strip sensor design. The parameters of the design correspond to the 2S module design aspects, like a fix pitch of 90 μm and a strip width of 25 μm. Furthermore, variations of this standard layout with varying p-stop pattern, for instance, were placed on the wafers too. Hence, each wafer contains a number of several silicon strip detectors which differ in layout but have the same process parameters. This fact should ensure the comparison of data for the different layouts. The sensors are on average the size of $1x2$ cm^2 with 64 strips. Basically, the results of the electrical qualifications are normalized to 1 cm long strips and can be scaled to a real size sensor ($\approx 10x10$ cm^2).
A global zoom into the GDS file of a test sensor for the p-stop study is shown in figure 7.1. This standard design was placed on each wafer submission. The most important design constituents are labeled. The picture shows one edge of a sensor, hence the size of the periphery in relation to the strip pitch can be extracted. Currently, studies are being done in which the sensor periphery is scaled down [F$^+$13] in order to increase the active region as far as possible. This topic will not be discussed any further. The periphery itself contains, besides the strip numbering, also additional alignment marks. These are, especially for the trigger modules, of high importance because the two stacked sensors in one module have to be aligned with high precision. Going from the periphery to the inner parts, the guard ring can be seen. It is in operation basically on

---

[2] Centro Nacional de Microelectronica (IMB-CNM-CSIC) Barcelona

[3] CiS Forschungsinstitut fuer Mikrosensorik GmbH Dresden

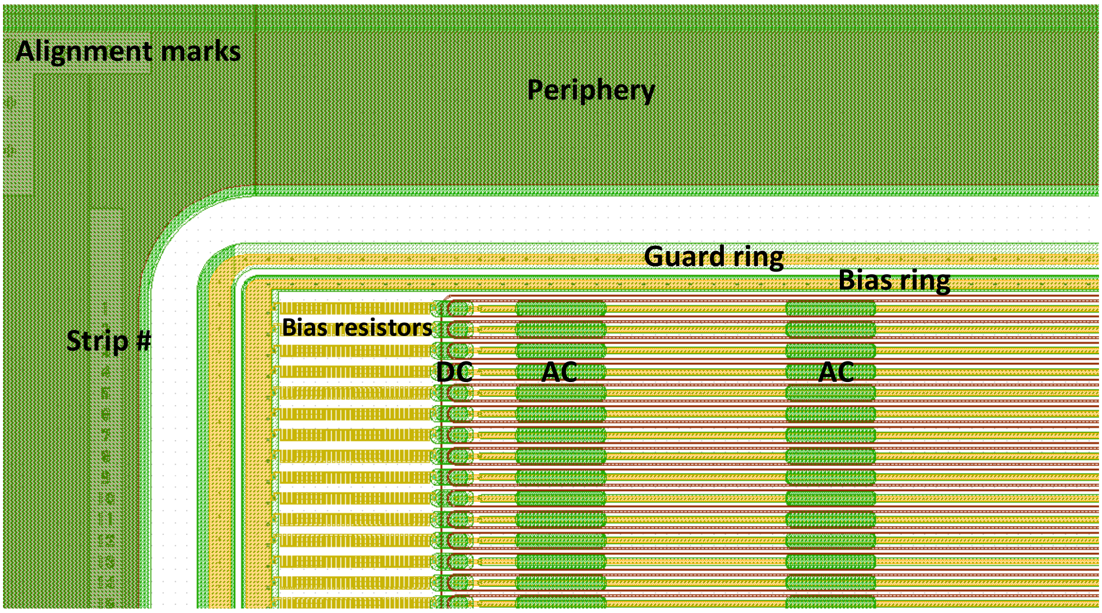

Figure 7.1: GDS section showing an edge of a silicon strip sensor designed and used in this thesis.

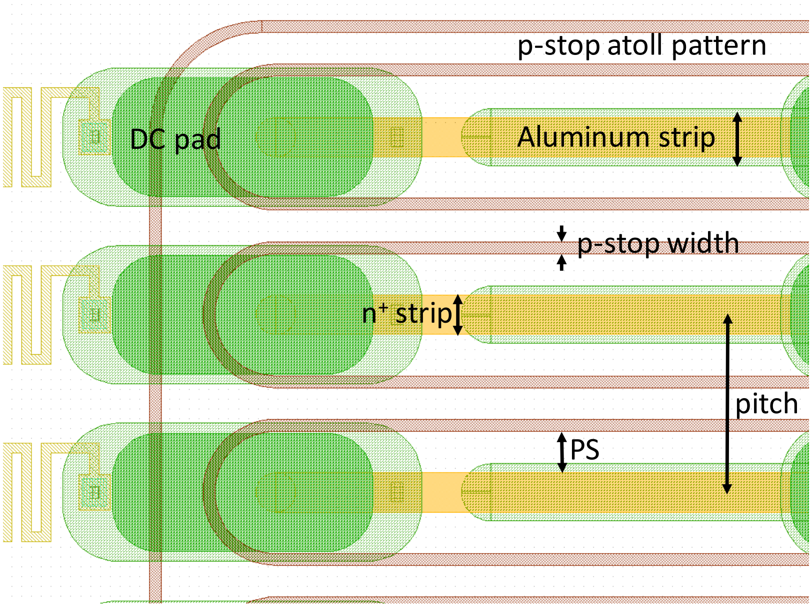

Figure 7.2: Zoom into the sensor shown in the figure above.

floating potential and shapes the electric field inside the active region in order to minimize any effects from the sensor edges. For this purpose, the same material as for the strips is used as an implant. The bias ring is implemented in the same way as the guard ring but during operation at ground potential. The R_{poly} bias resistors connect the ground potential of the bias ring with the individual strips which are connected to the readout chip via the AC pads.

In figure 7.2, the most important quantities for the p-stop isolation study are labeled correspond-

Table 7.1: P-stop doping profile parameters of the sensors in this study.

Vendor /Variant	peak conc. (cm^{-3})	doping depth (μm)	projected surface conc. (cm^{-2})
HPK	1×10^{16}	2.2	9×10^{11}
CNM	9×10^{16}	2.7	8×10^{12}
ITE	$<< 1 \times 10^{16}$	< 2.0	$<< 1 \times 10^{11}$
CiS / V1	1×10^{16}	1.5	7×10^{11}
CiS / V2	1×10^{16}	2.5	9×10^{11}
CiS / V3	1×10^{17}	2.5	8×10^{12}

ing to the simulation studies. Here, the p-stop width, the strip implant to p-stop distance PS and the strip implant width are of importance.

7.3 P-stop characteristics of the different submissions

In order to cover the whole phase space for the different p-stop parameters, p-type sensors from four different submissions and four different manufacturers were investigated. In addition to the wafers designed within this study, the sensor results from the HPK campaign were taken into account too.

For all submissions, the specifications were the same. The wafer substrate material is float-zone and high resistive (4 kΩcm to 10 kΩcm) p-type. The crystal lattice orientation is < 100 > and the sensors should withstand a bias voltage up to 500 V before irradiation. At this voltage, the leakage current should not exceed 5 nA/mm^3 (< 0.1 μA/cm^2). The physical thickness varies between 200 μm and 320 μm, which mainly has an effect on the leakage current and charge collection efficiency. For the p-stop study, the thickness is not important. The values for the p-stop doping concentration and doping depth for the different submissions are listed in table 7.1. One can see that the range for doping concentrations is between $<< 1 \times 10^{16}$ cm^{-3} and 1×10^{17} cm^{-3}. The p-stop doping depths vary between 1.5 μm and 2.7 μm. For both quantities, the values are mainly derived from process simulations by the manufacturers. In case of the HPK variant, the concentration and depth have been measured with the spreading resistance method. In case of the CNM submission, the choice on the p-stop parameters was done by the manufacturer, as this was a joint R&D submission with collaborators. The CiS samples were ordered as the last submission at which the specifications for the p-stop parameters were propagated by the author. The purpose for the latter was to check against the simulation results and measurements of the previous submissions with HPK, ITE and CNM.

Furthermore, on the ITE and the CNM wafer standard test sensors with different p-stop positions were placed in order to check whether any differences as a function of strip to p-stop distance PS can be observed.

The surface implant dose in table 7.1 was calculated assuming a gaussian shape of the doping profiles. Then, the simulated profile was integrated. It is worth mentioning that the magnitude of the dose is approximately the surface concentration of oxide charges after irradiation. For the high p-stop concentration and depth a value of 8×10^{12} cm^{-2} for the surface implantation dose was calculated. This is quite high in comparison to the positive oxide charge of $1-3 \times 10^{12}$ cm^{-2} and may be related to the high electric field strength in the bulk for high boron concentrations.

CHAPTER 8

SILICON SENSORS - IRRADIATION STUDIES

In general, test sensors are electrically qualified in a semi-automatic probe-station before and after irradiation. By placing probe needles to the bias ring and pads, several sensor parameters can be qualified. In this particular case, the interstrip resistance in dependence on the p-stop characteristics is of high interest. Besides the electrical qualification, also the noise and the charge collection of the samples are measured with an analogue readout chip. Both the interstrip resistance and the charge collection degrade with increasing radiation level, whereas the noise, mainly generated by leakage current, increases. As shown in chapter 6, the interstrip isolation significantly affects the electric field strength and distribution respectively and is directly related to the charge collection and noise of the sensor.
In order to investigate the relation between the radiation hardness of a sensor and the isolation technique, irradiations in several steps were done. The subsequent qualification of the sensors considering the p-stop influence is summarized in the following chapter. Furthermore, studies on different sensor designs for PS and 2S modules will be discussed as well as a new sensor layout developed at KIT.

8.1 Interstrip resistance before and after irradiation

All samples with the different p-stop characteristics from table 7.1 were irradiated with protons and/or neutrons. The range of the fluence was chosen from $\Phi = 1 \times 10^{14}$ $\mathrm{n_{eq}cm^{-2}}$ to $\Phi = 1.6 \times 10^{15}$ $\mathrm{n_{eq}cm^{-2}}$ in order to cover the expected radiation level after 3000 $\mathrm{fb^{-1}}$. The highest chosen fluence is approximately two times the maximum expected fluence for safety reasons.
In figure 8.1, again the simulated interstrip resistance and electric fields are plotted for $\Phi = 1 \times 10^{15}$ $\mathrm{n_{eq}cm^{-2}}$ and 900 V. In addition, the different submissions from the four vendors are

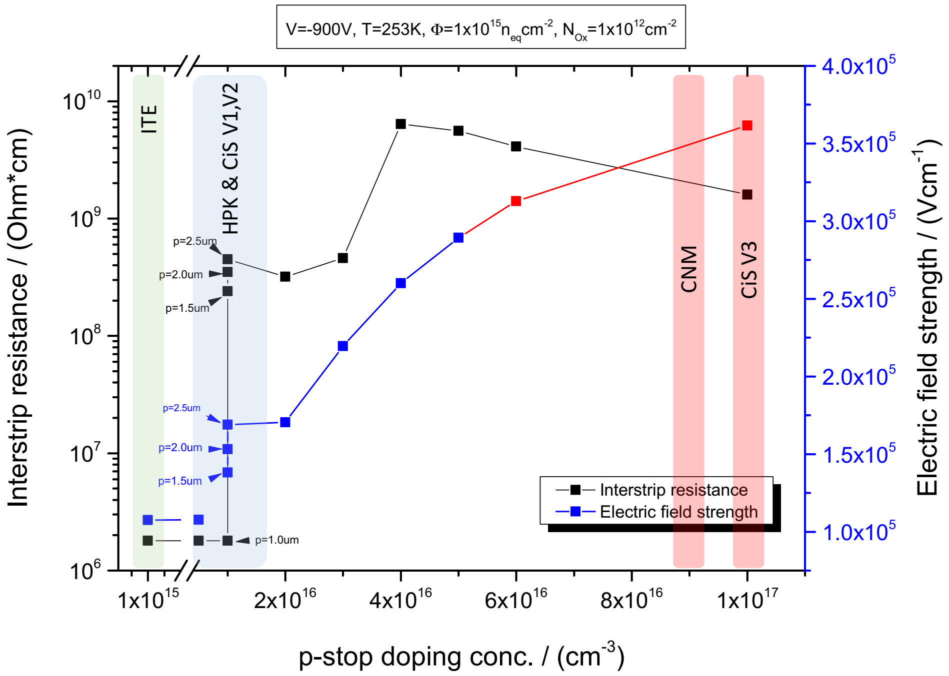

Figure 8.1: Simulated interstrip resistance and electric fields and the expectations for the different vendors.

indicated by colored areas corresponding to the p-stop doping concentration of the individual run. For the ITE samples (greenish), it is expected that the interstrip resistance is far too low as the doping concentration is significantly below 1×10^{16} cm^{-3} due to some process problems during production. The HPK and the CiS V1 and V2 (blueish) are expected to behave well with respect to a good strip isolation and simultaneously low electric field strength. The latter can be derived from noise measurements and will be discussed later. Finally, for the CNM as well as for the CiS V3 samples (reddish), though the interstrip resistance is expected to be sufficient due to high doping concentrations of the p-stop isolation, the electric field strength is expected to be in the critical region at around 3×10^5 Vcm^{-1}.

Measurements

The samples were measured before irradiation at T= 20°C. Although p-type detectors deplete from the sensor surface to the backside, the bias voltage was at least $V_{bias} = 1.2 \times V_{FD}$ for scans in which several strips were measured. Furthermore, bias scans have been performed too. After irradiation, the measurements have been performed at T= −20°C due to the increased leakage current as a consequence of the radiation damage. A bias voltage of up to 900 V was applied.
The results from these measurements are plotted on figure 8.2 as a function of the fluence. For the irradiation either just protons and neutrons or mixed particle were used. The latter is realized by

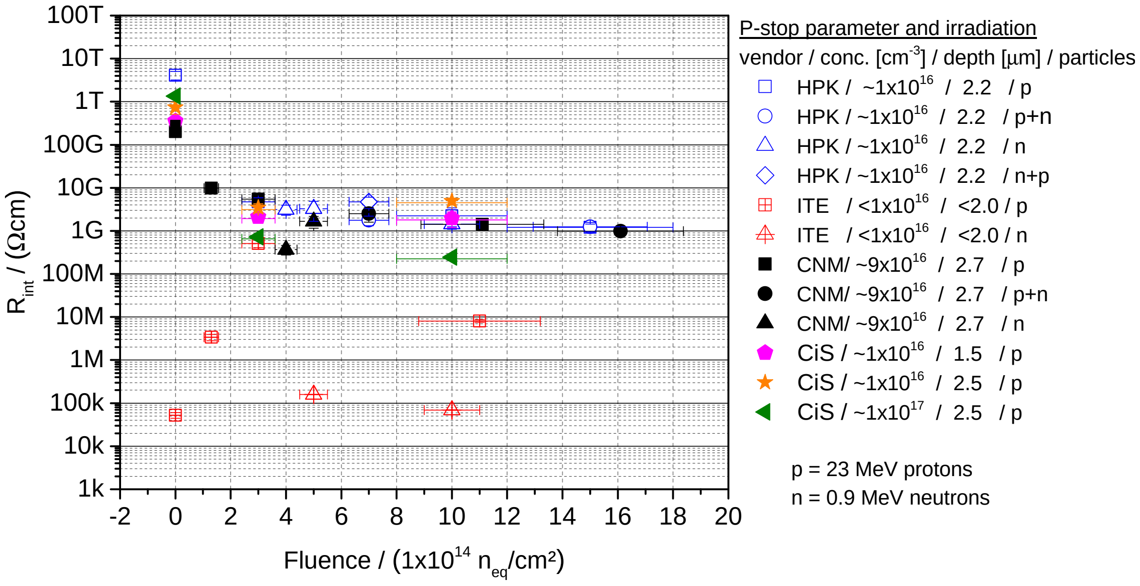

Figure 8.2: Measured interstrip resistance for the different vendors and variants respectively before and after irradiation. The CiS samples were processed with different p-stop characteristics.

subsequent irradiations. The estimated errors for the fluence are 20% for the protons and 10% for the reactor neutrons. The errors on the interstrip measurement are derived from a linear fit with a slope of 0 to the several measured samples and strips where the mean error was extracted.

All samples but the ITE with low p-stop doping concentration show a sufficient interstrip resistance, even after a fluence of $\Phi = 1.6 \times 10^{15}$ $\mathrm{n_{eq}cm^{-2}}$. The lowest measured value was for the CiS V3 samples after a fluence of $\Phi = 1 \times 10^{15}$ $\mathrm{n_{eq}cm^{-2}}$, although still above 100 MΩcm, whereas 50 MΩcm are required. In particular, the CiS samples of version 1 with the relatively shallow doping depth of 1.5 μm and a doping concentration of 1×10^{16} $\mathrm{cm^{-3}}$ for the p-stop behave well. This range for the p-stop characteristics is corresponding to the simulation studies advantageous with respect to low electric field strength. In general, at the high fluence level all samples but the ITE sensors hold an interstrip resistance of about 1GΩ which is sufficient and correspond to the values predicted in the simulations, which is shown in figure 8.1. The plot shows measurements for samples with different p-stop doping positions (CNM). No difference related to the position PS regarding the interstrip resistance was observed .

Figure 8.3 shows a comparison between T-CAD simulation and measurement of an irradiated sample, in this case a CiS V3 sensor. Here, the bias voltage was ramped and at each ramping point the interstrip resistance was measured. While during the measurement the interstrip resistance slowly increases depending on the bias voltage up to around 200 V until the final value, the $\mathrm{R_{int}}$ increases in the simulation, too, but much faster. At a bias voltage of around

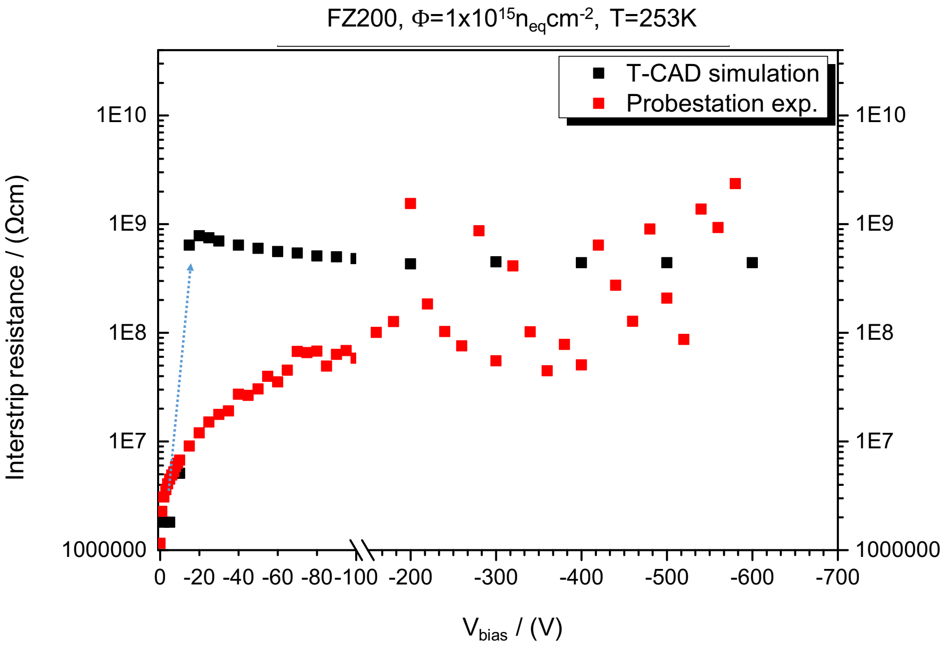

Figure 8.3: Measured and simulated interstrip resistance for a bias voltage scan.

20 V, the simulation reaches the final value for the interstrip resistance. This effect has not been understood so far and has to be investigated further. After around 200 V in both simulation and measurement, the values match well and a sufficient strip isolation is given in both measurement and simulation. Hence, simulations can reliably predict the sensors' performance when the model and radiation level range used are comparable, but on the other hand some discrepancy is observed and has to be resolved.

Role of the space charge

The ITE samples with a low p-stop doping concentration result in no sufficient strip isolation before irradiation. Here, a value of some tens of kΩ was measured. This is expected as these sensors feature 64 strips, each contacted via a bias resistor of about 2 MΩ to the bias ring. With a low interstrip resistance, these 64 strips are measured in parallel and an interstrip resistance of ≈ 30 kΩ is the result.

After irradiation, an increase of the interstrip resistance is observed for the proton irradiated samples, whereas the neutron irradiation does not change the R_{int} in a significant way. This effect in dependence on the charge of the hadrons during the irradiation can be explained by considering the space charge. This theoretical idea was first developed within the CMS silicon sensor simulation working group. For the 23 MeV proton irradiation, more acceptor-like point defects are introduced which are homogeneously distributed through the silicon bulk [Neu13]. As a further consequence, the effective bulk doping increases and the full depletion voltage as well.

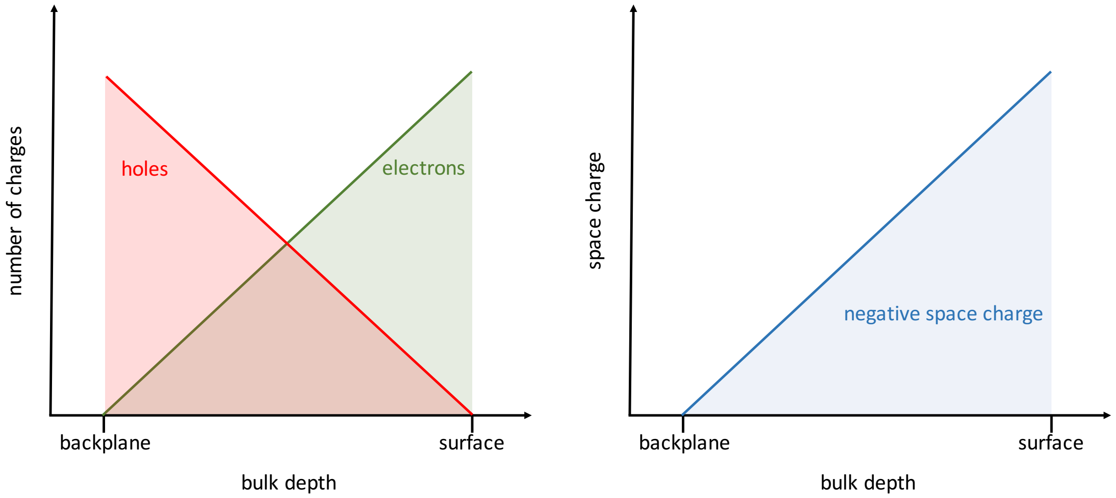

Figure 8.4: Relative proportion of charges in the bulk in dependence on the polarity and the resulting space charge density as a function of the bulk depth.

Now in case of a n^+−in−p detector, the electrons are collected at the electrodes, whereas the holes drift to the backplane. Hence, the neutral acceptor like defects capture the electrons which drift towards the collecting electrodes. As the proportional density of the electrons is higher at the surface, also the number of negatively charged acceptor defects at the surface increases. In turn, a negative space charge region at and between the strips arises and acts in principle in the same way like the p-stop or rather the p-spray isolation, see figure 8.4. The electrons are repelled by the negatively charged acceptor defects and no accumulation layer builds up. In case of the ITE samples, the interstrip resistance increased after a proton fluence of $\Phi = 3 \times 10^{14}\ \mathrm{n_{eq}cm^{-2}}$ from the initial $\approx 30\ \mathrm{k\Omega}$ to almost $1\ \mathrm{G\Omega}$. This value again fulfills the specifications. For the neutron irradiation, more donors than acceptors are created, which increases the positive space charge instead of the negative and hence no increase of the interstrip resistance is expected.

In order to check whether the space charge mechanism is responsible for the raise of the interstrip resistance, the ITE sensors were irradiated in the x-ray tube at EKP. The 23 MeV protons at KIT create in addition to bulk damage also surface damage, where a dose of about 150 kGy per $1 \times 10^{14}\ \mathrm{n_{eq}cm^{-2}}$ was calculated. In contrast, a dose of just about $1\ \mathrm{kGy}/1 \times 10^{14}\ \mathrm{n_{eq}cm^{-2}}$ for the 0.91 MeV neutrons is introduced. X-rays in general introduce damage in the oxide whereas no bulk damage is created. Hence, a buildup of an accumulation layer due to additional fixed positive surface charge is expected. The result is plotted in figure 8.5. For the low irradiation to 10 kGy an increase in the interstrip resistance was measured and is probably related to any additional surface charge-up which affects the bulk current but it is not understood completely.

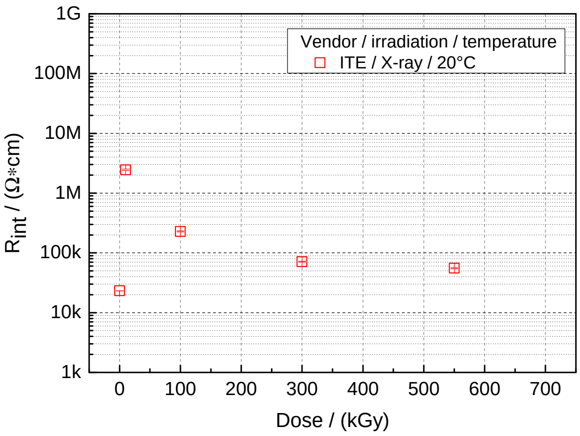

Figure 8.5: X-ray irradiation of the ITE samples with low initial interstrip resistance.

For the further x-ray irradiations, the interstrip resistance stays low and as expected. The result confirms the space charge effect.

Unfortunately, the effect of increasing interstrip resistance after proton irradiation cannot be reproduced with the damage model by simulations. Here, basically a p-type sensor without any isolation structure was simulated and damage corresponding to a fluence of $\Phi = 1 \times 10^{15}\ n_{eq}cm^{-2}$ was set. But the simulator results in no or very low interstrip resistance and the charge is distributed equally amongst the simulated strips. Clearly, the model has to be either adapted or more likely to be extended by further additional defect levels in order to reproduce the observation. Some first approaches are currently ongoing within the simulation working group.

An example of how the charge collection and cluster size behave for the different samples will be drawn in the next sections.

8.2 Signal measurements

Besides the electrical quantities and the necessity for low leakage currents, the charge collection of silicon detectors is the most important parameter. A traversing particle (especially a MIP) should be detected reliably even after the expected fluence of $\Phi = 1 \times 10^{15}\ n_{eq}cm^{-2}$ for the outer tracker silicon strip sensors. In order to measure the generated charge by a particle, the ALiBaVa[1] readout system was used [MH08]. The readout system is based on the Beetle chip with 128 readout channels which is used by the LHC-b experiment at CERN. It is an analogue chip with about 25 ns peaking time and allows a detailed analysis of the detector signal (information are the pulse shape and height). The sensors are bonded to the Beetle chip and analyzed with scripts using the ROOT software framework [ROO]. Charge carriers are generated by traversing

---

[1] A Liverpool Barcelona Valencia

β-electrons from the Sr90 decay on top of the sensor and triggered by a scintillator. The samples can be cooled down during the measurement to T= -30°C and also annealing studies at elevated temperatures (> 80°C) can be performed within the ALiBaVa setup.

In order to determine the noise of a sample, a pedestal run prior to the measurement is performed where randomly triggered events are recorded. From this, a mean pedestal P_s for each strip is calculated by

$$P_s = \frac{1}{N}\sum_{i=1}^{N} ADC_{s,i}, \tag{8.1}$$

where N is the number of triggers taken and ADC the signal of an individual strip. The noise itself is the variance of the the pedestal and can be calculated to:

$$N_s = \sqrt{\frac{1}{N}\sum_{i=1}^{N}(ADC_{s,i} - P_s)^2}\,. \tag{8.2}$$

After the calculation of the pedestal and the noise, the particle hits can be identified.

The signal measured by the analogue chip is algorithmically calculated to the cluster signal. Cluster is a measure for the multiplicity of adjacent strips which detect signals generated by one hit. The strip with the highest signal within a cluster is called the seed strip and must be at least 5 times higher than the calculated noise. Furthermore, any adjacent strips which detect signals higher than 2 times the noise contribute to the cluster charge (5/2σ-cut). The cluster signal of several triggers is of an asymmetric Landau-Gauss distribution due to energy deposition fluctuations, see figure 8.6. Therefore, the mean is always higher than the most probable value (MPV).

In figure 8.6(c) the combination of the noise and the signal can be seen. Due to the 5σ-cut for the seed strip, in this case the part of the tail exceeding $5\sigma = 5 \times 3.783 = 18.915$ is interpreted as signal and corresponds to a hit.

Results - signal measurements for the different submissions

As in the simulation studies, the expected fluence range for the PS p_T modules with the highest fluence in the outer tracker was covered in the irradiation studies for the different submissions. All samples were measured before irradiation, too, in order to study the signal degradation with increasing damage. Due to increasing leakage current after irradiation, the sensors were cooled down to T= -20°C, independent of the fluence. In addition, the bias voltage was chosen to 600 V in this plot in order to keep the noise as low as possible[2]. The results are summarized in figure 8.7 where the MPV value of the Landau-Gauss fit is plotted as a function of the fluence for the seed signal. The seed signal is of particular importance due to the change of the future readout ASICs to binary readout. In this case, the signal of each strip is compared to a threshold in the

---

[2] due to the fact, that CNM and CiS V3 samples show high noise, see later

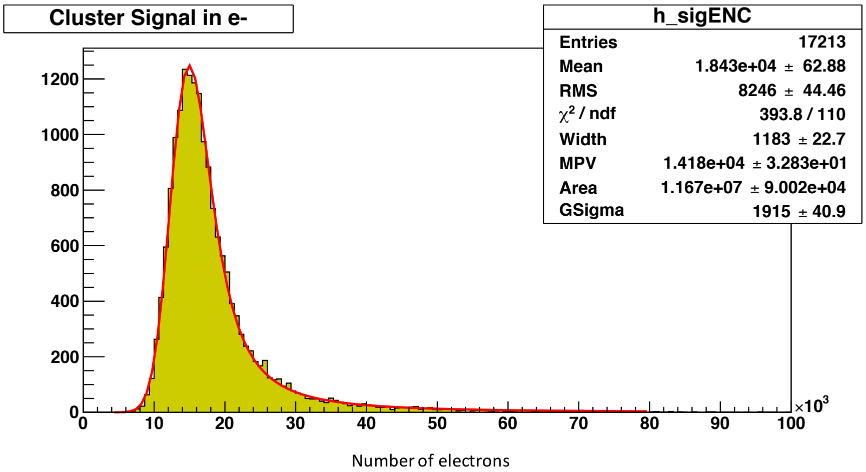

(a) Landau-Gauss fit to the signal distribution. In this measurement, the MPV of the CiS V1 200 μm thick sensor before irradiation leads to a collected charge of $\approx$14200 electrons.

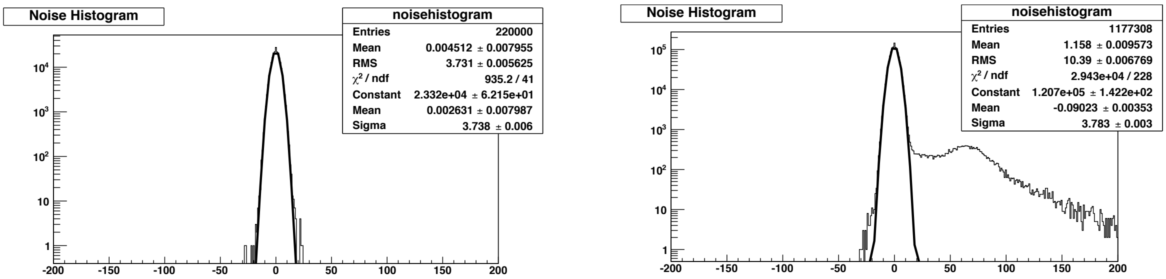

(b) pedestal run

(c) source run

Figure 8.6: Exemplary signal measurements in the ALiBaVa readout system of a CiS V1 sample. 8.6(b) shows the noise from the pedestal run which is of gaussian shape. In 8.6(c) one can see the pedestal subtracted signal distribution.

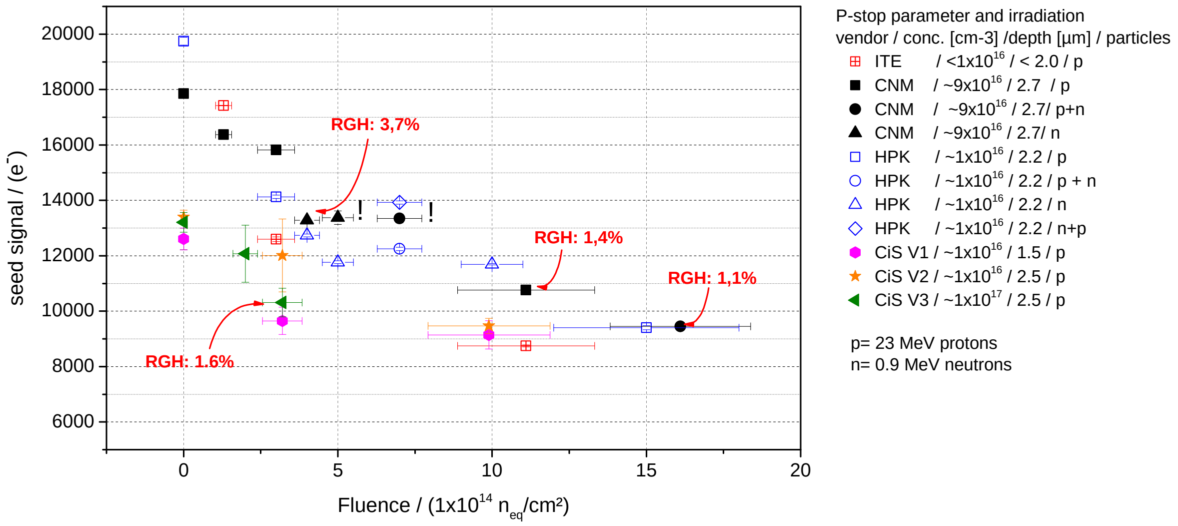

Figure 8.7: Summary plot for the charge collection as a function of the fluence for the different submissions. Measurements were performed at 600 V and T= −20°C after irradiation. The MPV of the cluster charge is plotted.

comparator. Hence, not the higher cluster but the seed signals should be considered. All samples independent of the irradiation collect sufficiently high charge confirming existing studies which were briefly introduced in chapter 5. The CiS samples show lower charge collection compared to the other samples because the substrate material is 200 μm thick, compared to about 300 μm for the other submissions. As shown in the plots in chapter 5, after a high fluence the difference in charge collection is less pronounced for both substrate thicknesses as before irradiation. The ITE sensors are included as well due to an improved interstrip resistance after irradiation, as expected from the electrical qualification.

The CNM and CiS V3 samples with the high p-stop doping concentrations of 9×10^{16} cm^{-3} and 1×10^{17} cm^{-3} and relatively high doping depth are labeled with “RGH“. The acronym stands for “random ghost hits“ and will be discussed in detail in the following section.

Random ghost hits

During the HPK measurement campaign, a non-gaussian noise for n-type detectors after high irradiation has been observed [Die12]. Figure 8.8 shows pedestal noise runs, one for a p-type sensor from this campaign in (a) and one for a n-type substrate, where a non-gaussian noise contribution is observed in (b). This effect has been observed for 200 μm and 320 μm thick n-type sensors for both silicon growth techniques, Float-Zone and Magnetic-Czochralski. The p-type sensors of HPK did not show this effect at all. This non-gaussian noise results in fake particle hits in n-bulk sensors as the fake signal is comparably high as a signal generated by a MIP. The

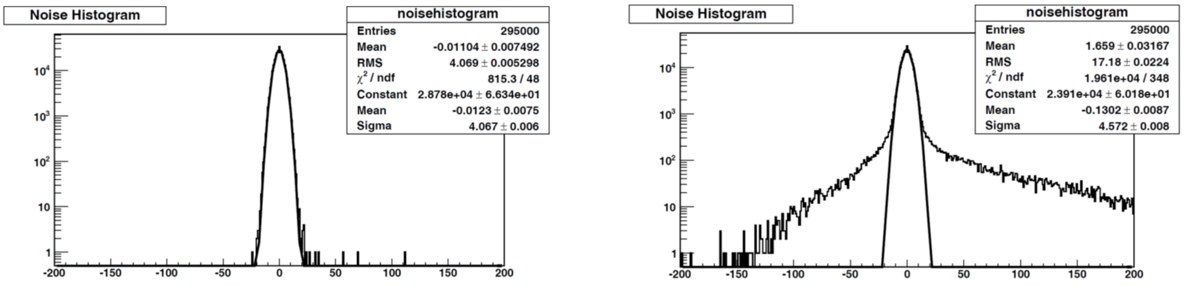

(a) (b)

Figure 8.8: Noise contributions for (a) p-type and (b) n-type sensors in the HPK campaign for a fluence of $\Phi = 1.5 \times 10^{15}$ $\mathrm{n_{eq}cm^{-2}}$ measured at $T = -20°C$ and $V_{\mathrm{bias}} = 900\ V$.

effect was quantified and defined as the number of strips with a signal above 5 times the noise divided by the number of triggered events and connected strips on the sensor. In this study, if the RGH occupancy is higher than 1%, the sensor is discarded as bad.

Now, in this thesis, a non-gaussian noise contribution was also observed for p-type detectors, in particular only for the CNM and the CiS V3 samples. Both of them have the relatively high p-stop doping concentration in common. The signal measurements of samples which show RGH above 1% are labeled as such in figure 8.7. On each wafer several sensors have been irradiated for statistical reasons and here, the sensors showing the least RGH occupancy are shown. The CiS V3 sensors for a fluence higher than $\Phi = 3 \times 10^{14}$ $\mathrm{n_{eq}cm^{-2}}$ are not plotted due to extremely high noise where no distinction between noise and signal was possible. On the other hand and of high importance is the fact that the CiS V1 and V2 samples with a moderate p-stop doping concentration of 1×10^{16} $\mathrm{cm^{-3}}$ do not show any measurable non-gaussian noise. Simultaneously, a good interstrip resistance is present, hence the moderate boron concentration for strip isolation seems to be suitable with respect to low noise and sufficient interstrip resistance.

Combination of simulations and measurements

The effects observed after irradiation, particularly the appearance of the random ghost hits, can now be explained by taking the simulations into account which were discussed in chapter 6. There, it was found that with increasing p-stop doping concentration, the electric field strength in the sensors increases, too. In figure 8.9, the simulated electric field strength for the CNM sample is plotted. The red line indicates the critical breakdown region of the electric field, whereas the blue line indicates the start of the avalanche model. This means that a multiplication of charges by electrons in high electric fields first appears if the electric field strength exceeds the value of 1.75×10^5 $\mathrm{Vcm^{-1}}$.

Here, the electron-hole production is due to the impact ionization which requires a threshold in the electric field strength. The Van Overstraeten and De Man model [vOdM70] from 1970 has been used which is applicable in the range of 1.75×10^5 $\mathrm{Vcm^{-1}}$ to 6×10^5 $\mathrm{Vcm^{-1}}$. Here, the

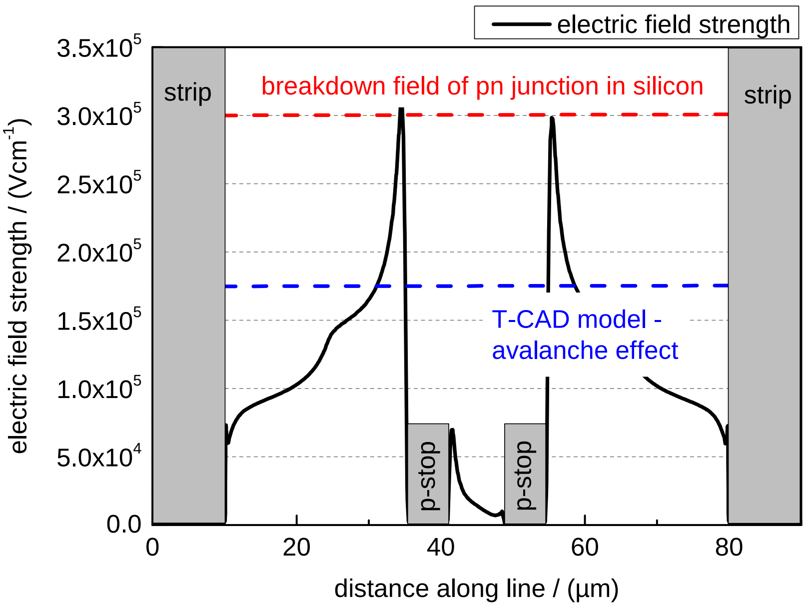

Figure 8.9: Electric field line cut just below the sensor surface. Here, the CNM sample was simulated after a fluence of $\Phi = 1\times10^{15}$ $\mathrm{n_{eq}cm^{-2}}$ at 600 V and T= -20°C. The asymmetry between the p-stops is due to the chosen individual mesh.

impact coefficients for the electrons are the same in the lower and higher electric field regions 7.03×10^{5} $\mathrm{cm^{-1}}$.

This means that in the local regions at the p-stop curvatures with electric fields higher than 1.75×10^{5} $\mathrm{Vcm^{-1}}$, avalanche electrons can be created which may contribute to the non-gaussian noise and be interpreted as hits by traversing particles. In particular, this range of high fields is first reached in the simulation when the p-stop doping concentration exceeds 3×10^{16} $\mathrm{cm^{-3}}$ at 600 V for a doping depth of 2 μm. Hence, the upper limit for the doping concentration of boron atoms for isolation layers seems to be low in the range of $1-3\times10^{16}$ $\mathrm{cm^{-3}}$.

For the CiS V1 and V2 samples, which just differ in the p-stop doping depth, no significant difference was observed. This fact is also just as predicted by the simulations shown in 6.12, where the electric field strength stays below 1.5×10^{5} $\mathrm{Vcm^{-1}}$ for the 1×10^{16} $\mathrm{cm^{-3}}$ concentration, even after the relativly high fluence in the innermost layers of the outer tracker. As a conclusion, it seems that the vendor produced the sensors corresponding with the specified p-stop isolation characteristics.

Considering the p-stop to strip distance PS, the CNM samples were measured, too, and the results are shown in figure 8.10. Here, the charge collection of the Sr90 measurement as well as the expectations from the simulations are plotted. The PS is either 16 μm or 25 μm. In this plot, the RGH are not labeled in order to keep the plot less crowded but all samples after irradiation show undesired fake hits.

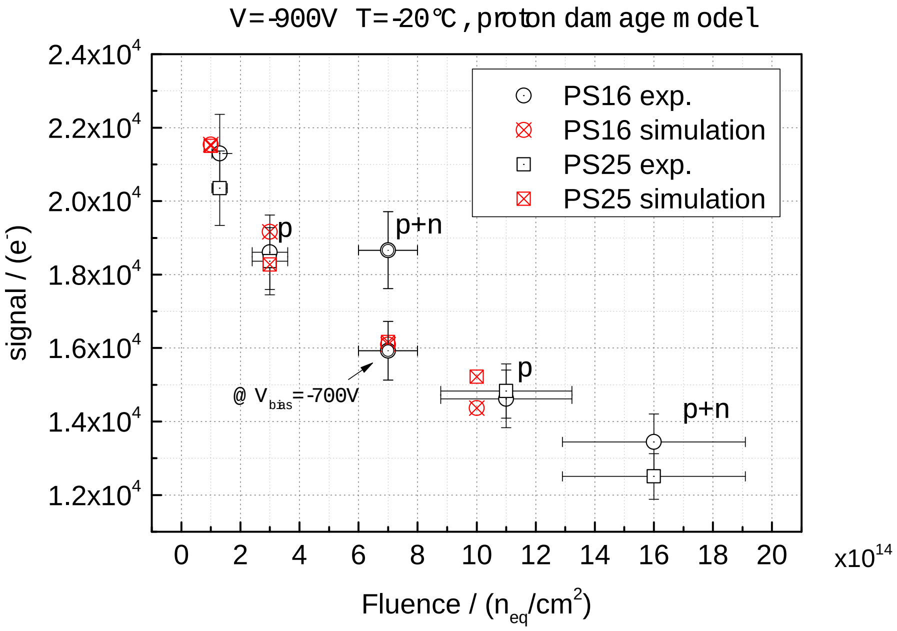

Figure 8.10: Simulated and measured charge collection (cluster signal) for the CNM samples and different PS up to a fluence of $\Phi = 1.6 \times 10^{15}$ $n_{eq}cm^{-2}$ at 900 V and T= −20°C.

For the proton irradiations only, the data and simulation match well, which confirms the proton 2-defect damage model for T-CAD. The irradiations of $\Phi = 7 \times 10^{14}$ $n_{eq}cm^{-2}$ and $\Phi = 1.6 \times 10^{15}$ $n_{eq}cm^{-2}$ are of mixed particles. In the first case, after an initial proton irradiation of $\Phi = 3 \times 10^{14}$ $n_{eq}cm^{-2}$, an additional neutron irradiation of $\Phi = 4 \times 10^{14}$ $n_{eq}cm^{-2}$ was performed. For the higher irradiation, the samples were first irradiated with protons to $\Phi = 1.1 \times 10^{15}$ $n_{eq}cm^{-2}$ and subsequently with neutrons to additional $\Phi = 5 \times 10^{14}$ $n_{eq}cm^{-2}$. An additional drawback of the damage model is that in principle a simulation of a mixed irradiation is not possible so far. Here, too many variables diverge, like the fact that for the neutron model a fixed oxide charge of 7×10^{11} cm^{-2} is assumed. But the mixed samples in case of the highest irradiation first received a proton irradiation of $\Phi = 1.1 \times 10^{15}$ $n_{eq}cm^{-2}$ which probably already resulted in a fixed oxide charge higher than 1×10^{12} cm^{-2}. The measurements of the samples with a mixed fluence of $\Phi = 7 \times 10^{14}$ $n_{eq}cm^{-2}$ show higher values than expected. This is probably due to the starting avalanche effect. In this case namely, the part of the neutron irradiation is higher than the proton part which means that the oxide charge might not be saturated so far. As shown in figure 6.10, this could lead to even higher electric fields at lower radiation level, as in p-type detectors an increasing oxide charge is advantageous. At this fluence, the measurement at a bias voltage of 700 V matches the expectations only. The 900 V data is around 2500 electrons higher than expected. This is valid for both p-stop-to-strip distances of 16 respectively 25 μm.

For the proton irradiations only, no significant difference in the charge collection in dependence on the p-stop-to-strip distance for both measurement and simulations was observed. This means

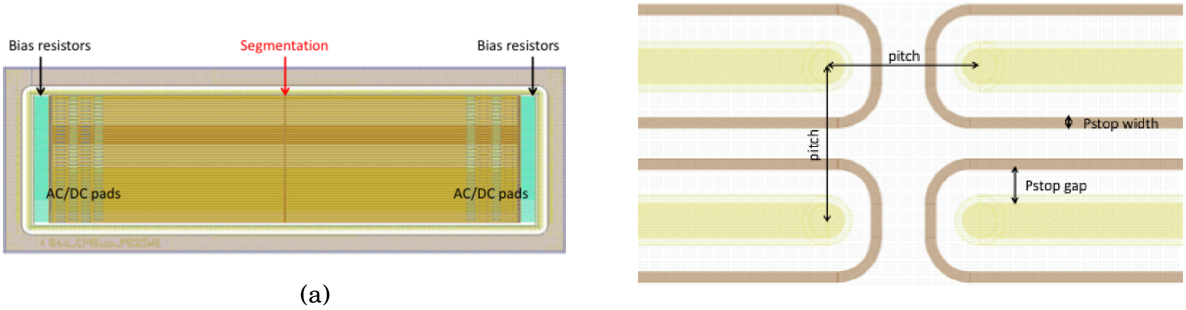

(a)

(b)

Figure 8.11: Layout of a test 2S module sensor from the GDS file with 64 strips on each side. (b) shows the zoom into the segmentation region where the strips meet.

from this point of view, the PS can be chosen to be high and accordingly implanted in the center between two strips in order to keep the electric field strength as low as possible.

8.3 Sensor layouts for high particle track density

In addition to the p-stop isolation study, all wafers also included other sensor layouts in order to study the different needs for the future tracker sensor technology. One of the main goals and needs is an increased granularity due to an increasing particle track density as a consequence of the higher luminosity. Several approaches were investigated and will be shown in the following sections.

8.3.1 Sensors for the 2S module

In chapter 3.2.4, the concept of the 2S trigger module was introduced. One main feature of the sensors is that by dividing the strips in the center and adding AC pads to both ends of the sensor, the granularity is increased by a factor of two. The layout of a small scale 2S strip sensor is shown in figure 8.11. Here, the strips are segmented symmetrically in the center of the sensor. The readout chips will be wire-bonded to the pads in this picture on the left and right side respectively. A zoom into the segmentation region is shown in figure 8.11(b). These kind of test sensors were implemented in all wafer layouts which have been discussed so far.
As this kind of sensor for the 2S module was designed for the first time, the question arose how much the strips have to be separated in the center. Basically, the active region should be as big as possible. As charge sharing between strips due to the interstrip capacitance is present, the layout shown in figure 8.11(b) was chosen in which the segmentation is equal to the strip pitch. Variations of the segmentation gap were implemented on a current run with HPK and will not be discussed here. For the ALiBaVa setup a dedicated board was designed on which the Beetle readout chips are facing each other, as in the future 2S module. The drawings of the 2-end board

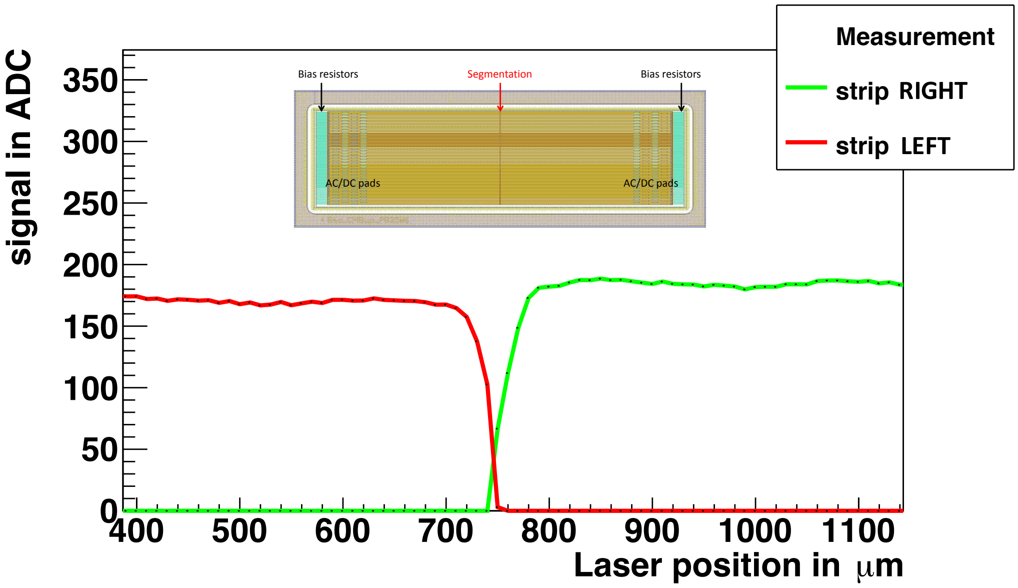

Figure 8.12: Laserscan of the segmentation region in a 2S test sensor at 300 V and T= 20°C. A 1060 nm laser has been used on a xy-stage with 1 μm step size.

are in the appendix D.1. With this, a sensor can be bonded from both sides simultaneously and the segmentation region can be studied as well.
Figure 8.12 shows a scan with a 1060 nm laser in the ALiBaVa setup which was placed on a x-y-stage with 1 μm step size accuracy. The laser was moved with 10 μm step size along the strips. The global laser position on the x axis is arbitrary but the scale is correct. The laser was positioned such that it is about 10 μm next to the aluminum strip. With this, a significant charge sharing with the adjacent strip is suppressed. When the laser is in the left part of the sensor, the right part does not see any signal by capacitive coupling at all. As soon as the laser position with a focus of about 7-8 μm reaches the segmentation region, the signal vanishes and appears on the right side (in this example) of the sensor. At the global value of $x = 750 \pm 10$ μm, the signal is shared between the two facing strips. After irradiation, this picture does not change at all. Hence, it seems that a strip segmentation in the order of the strip pitch seems to be appropriate and no inactive regions (though very small) appear. On the other hand, the signal in the exact center decreases to around 30%which might be too low after irradiation for the CBC threshold of around 6000 electrons. Therefore, in a current submission, samples with different separation values were included and a detailed study of this region in dependence on the fluence will be performed.

8.3.2 Sensors for the PS module

The PS module concept was introduced in chapter 3.2.5. While the trigger concept is the same as for the 2S modules, the design of the PS modules differs significantly. This is due to the increased requirement on higher granularity in the tracker regions at about R~20 cm to R~60 cm. In

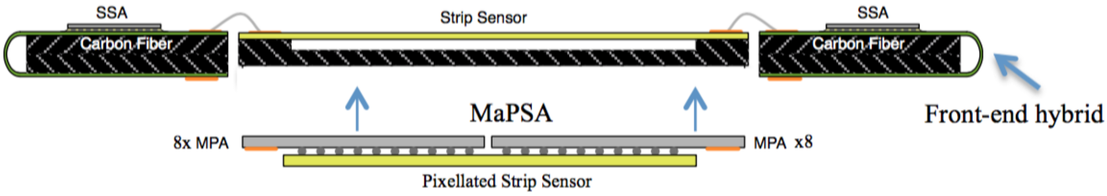

Figure 8.13: Cross section of the PS module [Ros15].

order to fulfill this demand, the PS module consists of a strip sensor and a pixelated sensor in the bottom layer. The strip sensor will be read out with a distinct chip (SSA=strip sensor asic), connected via wire bonds to the AC pads. Due to the high channel density of the macro pixel sensor, the readout chip (MPA=macro pixel asic [CMK+14]) has to be directly bump-bonded to the sensor pads. The macro pixel sensor itself will be around 5 cm × 10 cm huge and 16 MPA chips will be required per module to connect all 30720 bump pads respectively macro pixel strips of the sensor.

While the strip sensors for the PS module hold the same features as for the 2S module, no additional R&D on this type of sensor is necessary[3]. Besides the strip pitch of 100 μm and the overall size of 5 cm × 10 cm nothing else changes in comparison to the 2S strip sensor design. As such kind of macro pixel sensor had not existed, a collaborative R&D study between the CERN CMS electronics group and the CMS sensor community on the Macro Pixel Sub Assembly (MaPSA) was carried out and is ongoing. This subassembly is shown in figure 8.13 and consists of the macro pixel sensor and the MPAs. As a first iteration, the MaPSA concept was checked in a MaPSA light subassembly in which the ASICs as well as the macro pixel sensors are test devices and smaller compared to the final layout. The chip is of the size of 6.5 mm × 1.6 mm and contains 48 bump pads. Following the demands and compatibility with the ASIC (see appendix E), the sensors were designed within this study and produced at CiS in Erfurt. They contain overall 288 channels with 100 μm × 1446 μm cell size and the same bump pad pattern as the MPA. In total, the test sensors are 8 mm × 12 mm huge and are equipped with each 6 MPAs in the MaPSA light subassembly.

Standard design of the MaPSA light sensor

Several aspects for the DC coupled macro pixel sensor for PS modules need to be investigated in order to achieve the most compatible design with respect to high efficiency and radiation tolerance. The physical and active thickness of the sensors is 200 μm. Besides the fixed pixel cell size, the width-to-pitch ratio and in particular the region on the sensor where the MPA chips meet need to be studied. In figure 8.14, one of the six cell rows of the MaPSA light standard sensor is shown.

---

[3] besides the thickness which is also under investigation for the 2S sensors

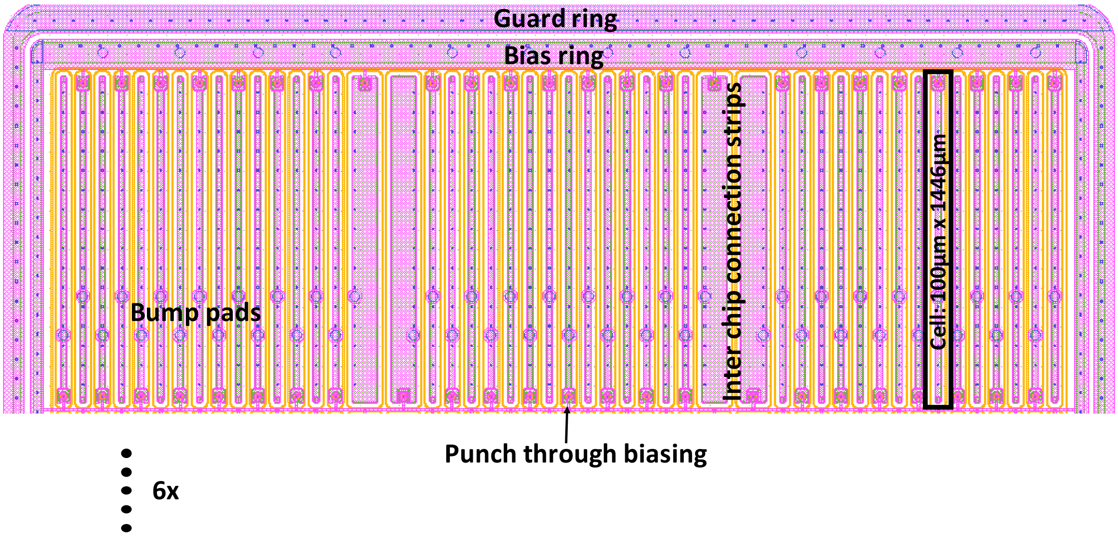

Figure 8.14: Extract from the GDS file of the standard MaPSA light sensor.

The width-to-pitch ratio is w/p = 0.25 and a p-stop isolation pattern and characteristics following the results discussed in sections 6.5 and 8.1 was used. In the region where the MPAs meet, the strips are 125 μm wide. The reason for this choice is that in this configuration, the strip-to-strip distance in the interconnection region of the chips stays the same just as throughout the whole sensor. This is necessary due to the inactive periphery of the chip. The interstrip capacitance and hence charge sharing by traversing particles between the strips is equal to the w/p = 0.25 regions, although the overall input capacitance to these individual chip channels is higher as a consequence of the wider strip [Har09]:

$$C_{n-side}[\text{pF/cm}] \approx 2 \times \left(1.5 + \frac{w}{p}\right), \tag{8.3}$$

where w stands for the strip width and p defines the strip pitch.

Furthermore, all sensors are biased via punch through (PT) structures which basically are npn transistors. During the operation in the tracker, the sensors are biased with high voltage. The ground potential at the strips is provided by the MPA chips which are at ground potential, too. For the purpose of electrical qualification in a probe station, a bias grid had to be implemented in order to allow strip measurements but also a homogeneous depletion. Moreover, the PT structure was able to contribute to the safety of the readout ASIC if a higher current from the sensor concentrated at a few or one channel would appear. This scenario is possible during a beam splash or significant damage of a channel on the sensor. The feasibility and performance of such PT structures needs to be studied in detail and will not be discussed any further. The layout of the PT structure design used works well and was designed following the layout used during the

Table 8.1: Overview of the sensor layout variations for the MaPSA light sensor. In all cases the strip pitch is 100 μm.

Sensor label	edge [μm]	pixel width [μm]	gap pixel [μm]
std (wp025)	850	25	125
wp03	850	30	125
wp04	850	40	125
wp04gap40	850	40	40
wp025gap50	850	25	50
edge500	500	25	125
edge350	350	25	125

HPK campaign for some of the pixel test sensors.

The variations of the standard macro pixel sensor layout placed on the wafer are summarized in table 8.1. The variations can be divided into two main parts: variations of the pixel active region and variations of the periphery. The former includes alternatives for the width to pitch ratio as well as options for the chip-to-chop gap region while the latter concentrates on the ratio between active and inactive region of a sensor. Here, the width of the periphery was scaled down from nominal 850 μm to 350 μm.

Electrical qualification

The samples were received in three batches and qualified in the probe station. In this study, the samples from batch number 3 are discussed as these show the best electrical properties. Process variations of the wafers differed in the p-stop isolation characteristics with the same values used for the CiS strip sensor study. This is due to the simple fact that the discussed strip sensors and MaPSA light sensors were placed on the same wafer at which the former are AC coupled and the latter DC coupled. Such realization was possible due to the CiS DC process in which for the DC contacts an additional mask is required. This means, after the oxide growing, the via mask is used to etch the oxide away in the regions where the DC contacts need to be placed. As a consequence, AC coupled detectors can be designed and placed on the same wafer by discarding these oxide openings for the DC contacts.

The first parameter under study is the current over voltage relation due to the completely new sensor layout. The IV characteristics of a standard MaPSA light sensor design are shown in figure 8.15 in dependence on the humidity inside the probe station. The breakdown voltage of the sensor before irradiation and in dependence on the humidity was extracted and plotted in figure 8.16.

From this, one can see that specifications for the currents and breakdown voltage which are

$$\text{I@}500V < 5\ \text{nA/mm}^3 \longrightarrow \text{measured} \approx 1\ \text{nA/mm}^3 \tag{8.4}$$

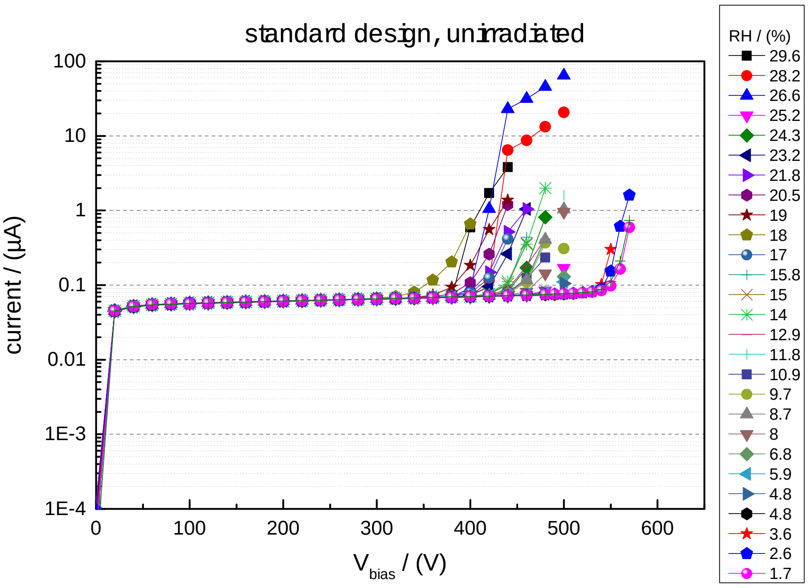

Figure 8.15: IV characteristics for the standard MaPSA light sensor of variant 2 (p-stop conc.= 1×10^{16} cm^{-3} and 2.5 μm deep) in dependence on the humidity RH.

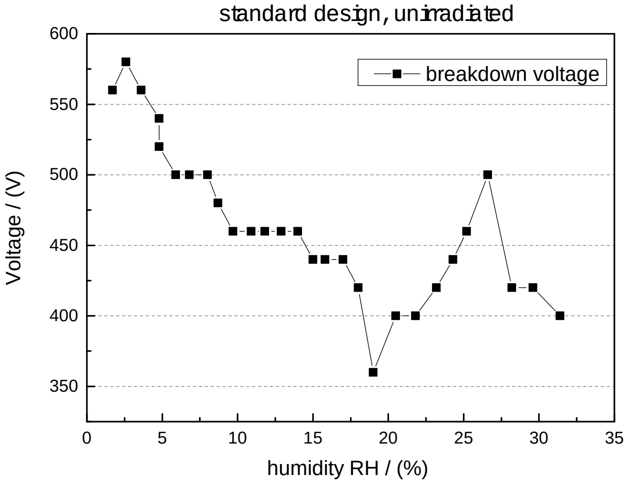

Figure 8.16: Breakdown voltage for the standard MaPSA light sensor as a function of the RH.

are reached for variants 1 and 2 though, but this is strongly related to the environmental conditions of the measurement. The dependence of the currents on the humidity is still under study and in discussion with the vendor.

In order to check whether the variant of the p-stop isolation technique affects the currents of the sensors, the standard sensors of each wafer always at the same position in the wafer center were measured as a function of the voltage. Several observations were made. First, the process

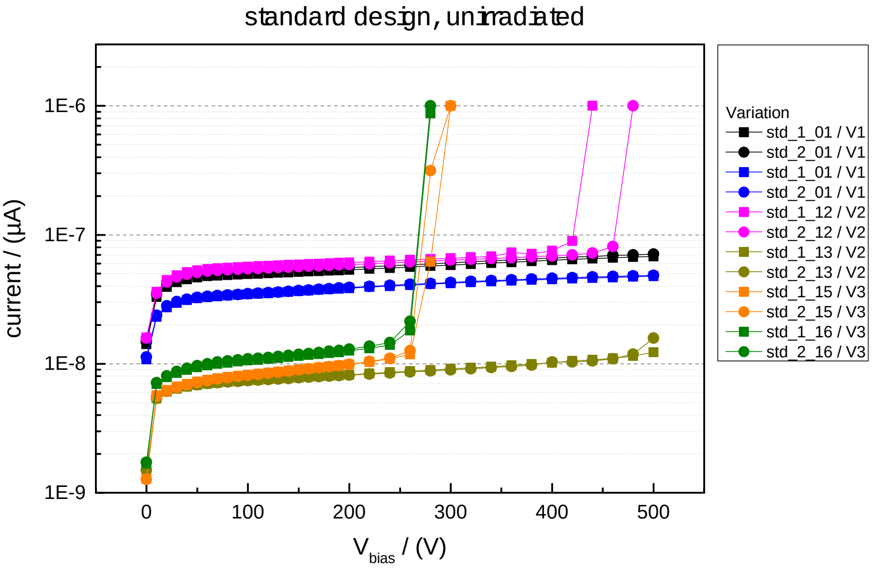

Figure 8.17: Breakdown voltage for the standard MaPSA light sensor for the different p-stop isolation techniques.

stability for variant 1 (p-stop conc.= 1×10^{16} cm^{-3} and 1.5 μm deep) is most pronounced. Variant 2 (p-stop conc.= 1×10^{16} cm^{-3} and 2.5 μm deep) shows for one wafer breakdown voltages below 500 V inconsistent with the specifications, whereas the second wafer with same specifications shows currents one order of magnitude lower and without a breakdown. Lastly, variant 3 (p-stop conc.= 1×10^{17} cm^{-3} and 2.5 μm deep) always shows early breakdown in the range of about 250 V. This observation is valid for all sensors of variant 3.

Clearly, the breakdown voltage is affected by the process. For the implantation of all three variants an ion energy of 130 keV was used and the surface projected ion concentration varied from $= 6.5 \times 10^{11}$ cm^{-2} for variant 1 to $= 8.6 \times 10^{11}$ cm^{-2} for variant 2 and $= 8.2 \times 10^{12}$ cm^{-2} for variant 3. From the measurements it seems that the high p-stop concentration and depth increase the electric field strength in the CiS samples, even before irradiation, to a critical value, leading to early breakdown voltages, although such low breakdown voltages had not necessarily been expected.

The different gap pixel sizes and width-to-pitch ratio variations of the standard design do not show any measurable differences in the current over voltage characteristics.

The interstrip resistance was measured too, see figure 8.18. Here, no deviation from the strip sensors were expected and observed, even after an irradiation of $\Phi = 2 \times 10^{15}$ n$_{\mathrm{eq}}$cm^{-2} with 23 MeV protons. In the plot example, the three different width-to-pitch ratios of variants 1, 2 and 3 are shown. A sufficient strip isolation is always present, independent on the variant.

The sensors with the different periphery size are investigated at the HEPHY[4] institute in Vienna

---

[4] High Energy Physics

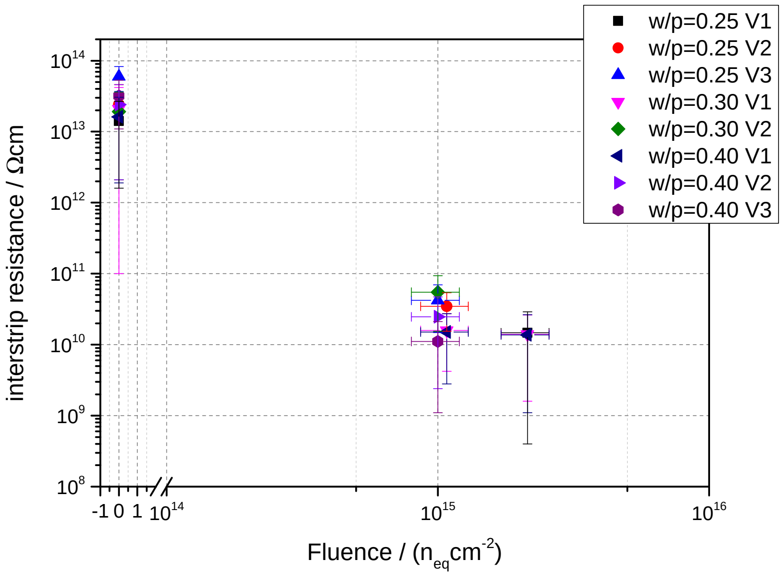

Figure 8.18: Interstrip resistance for variants 1, 2 and 3 sensors with different width to pitch ratios before and after irradiation. No difference has been observed.

and will not be discussed here.

Signal measurements

Meanwhile, the MPA is existing and has been qualified intensively within the electronics community and also subassemblies consisting of 6 chips on one MaPSA light sensor have been produced. At the time of writing this thesis, no dedicated MaPSA readout system was available, meaning that a system qualification based on the readout of a macro pixel sensor via the MPA was not possible. Fortunately, the Beetle chip of the ALiBaVa system is capable of dealing with AC and DC coupled sensors. Hence, in order to study the sensor's charge collection and fake hit rates, the PS-p light sensors were connected to the Beetle chip. The clustering algorithm was kept the same as for strip sensors and accordingly just one row of the macro pixel sensor strips was wire-bonded to the Beetle. For the measurements, again β-electrons from the Sr90 decay were used to generate MIP signal. Furthermore, the environmental conditions were chosen to be compatible with the tracker conditions. This means that the sensors were qualified at T= 20°C before and at T= −20°C after irradiation, independent on the fluence. The ALiBaVa setup was flooded constantly with dry air: the humidity during the measurements was always below 10% and the temperatures were set to T= 20°C for unirradiated and T= −20°C for irradiated samples. In figure 8.19, the MPV of the cluster charge at bias voltages of 600 V and 900 V is plotted. The values in the brackets indicate the number of samples measured so far as the irradiation had just taken place. Before irradiation, the MPV signal is above 15000 electrons, which is in agreement

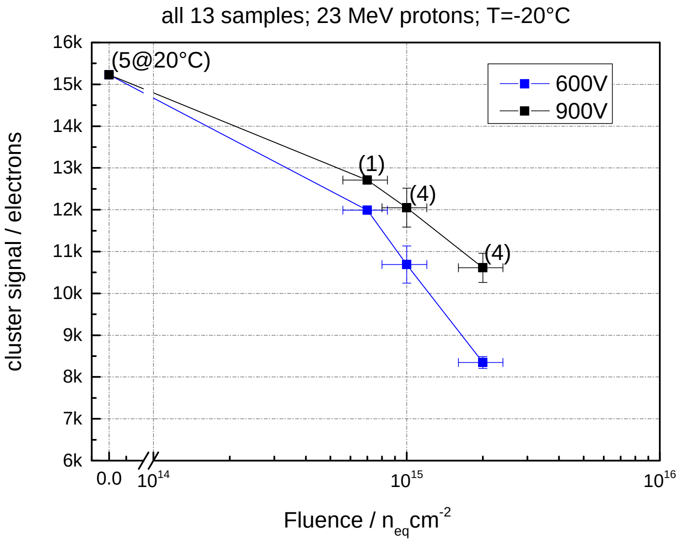

Figure 8.19: MPV cluster charge for the MaPSA light sensors of variant 1 & 2 before and after irradiation with protons.

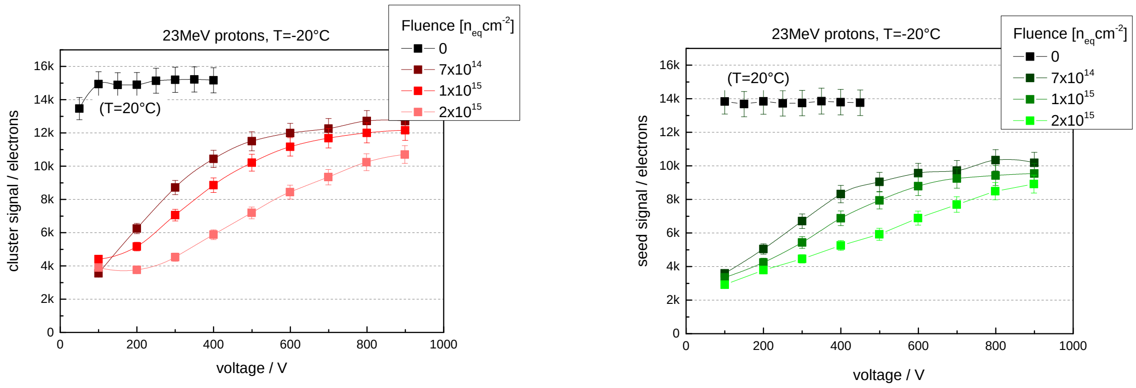

(a) Cluster signal

(b) Seed signal

Figure 8.20: Charge collection of MaPSA light sensors as a function of the voltage.

with the expectations for substrates 200 μm thick. After irradiation, the signal degrades and ends up in:

$$\text{Cluster signal: } 10.7\ \text{ke}^{-}@-600\ V\ \ \&\ \ 12.1\ \text{ke}^{-}@-900\ V\ \ (\text{F} = 1\times10^{15}\text{n}_{\text{eq}}\text{cm}^{-2}). \tag{8.5}$$

For the three different irradiations to $\Phi = 7\times10^{14}$ $\text{n}_{\text{eq}}\text{cm}^{-2}$, $\Phi = 1\times10^{15}$ $\text{n}_{\text{eq}}\text{cm}^{-2}$ and $\Phi = 2\times10^{15}$ $\text{n}_{\text{eq}}\text{cm}^{-2}$, the cluster and the seed signals were plotted as a function of the bias voltage in 8.20. The seed signal is of interest due to the fact that as in the 2S modules, the sensors will be read out by a binary chip. In the analogue IC of the binary chip, a comparator compares the incoming signal height with a threshold. If the signal exceeds this threshold, a hit of the corresponding channel is detected but no pulse height informations are stored. Comparing

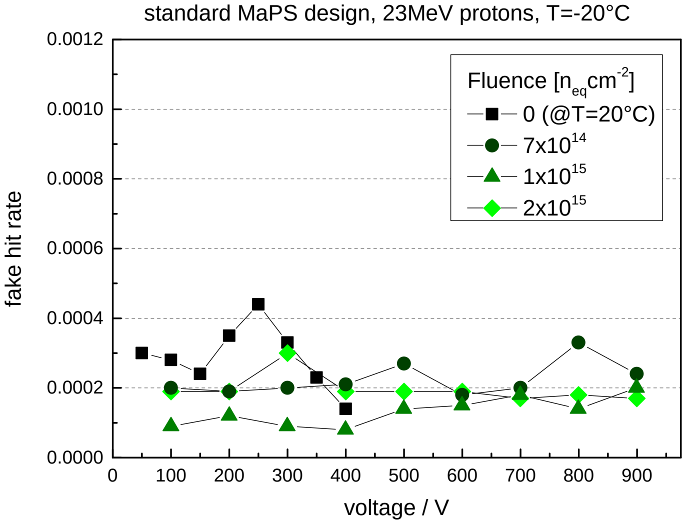

Figure 8.21: Random ghost hit rate for the standard MaPSA light sensor of variant 1 before and after irradiation.

the cluster signal in figure 8.20(a) with the seed signal in 8.20(b), one can see that the seed signal is lower. Before irradiation, the difference is about 1500 to 2000 electrons. After an irradiation to $\Phi = 1 \times 10^{15}$ $n_{eq}cm^{-2}$, the seed signal at 600 V is about 8400 electrons, compared to 9500 electrons at 900 V. The threshold in the binary chip will be below 3000 electrons and is currently studied by the chip designers. This means that either the sensor thickness has to be increased in order to gain more charge or the bias voltage has to be increased to 900 V in order to reliably distinguish the signal from the noise.

Figure 8.21 shows the RGH rate exemplary for a standard layout MaPSA light sensor for different irradiation fluence, plotted over the bias voltage. For this irradiation study, variant 3 with the high p-stop concentration and doping depth was not investigated due to the low breakdown voltages before irradiation of about 250 V. Variant 2 has to be measured. On the other hand, the variant 1 with the moderate p-stop doping concentration of 1×10^{16} cm^{-3} shown in figures 8.19 behave well even after a high proton fluence of $\Phi = 2 \times 10^{15}$ $n_{eq}cm^{-2}$. In particular, the noise and fake hit rate and the RGH rate respectively were studied too. Here, both variants with a moderate p-stop doping concentration are included at which the curve for the highest fluence is extracted from the measurements of variant 2. Clearly, both variants show neither high noise nor a too low interstrip resistance, which can be seen in the cluster width distribution shown in figure 8.22. In this plot, in addition to the standard layout, also the sensors with different width to pitch ratios are included up to a fluence of $\Phi = 2 \times 10^{15}$ $n_{eq}cm^{-2}$. The cluster size of around 1.5 at 600 V and 1.6 at 900 V are as expected and comparable to strip sensor cluster widths in the HPK campaign. The increase if the cluster width is related to the lower interstrip resistance

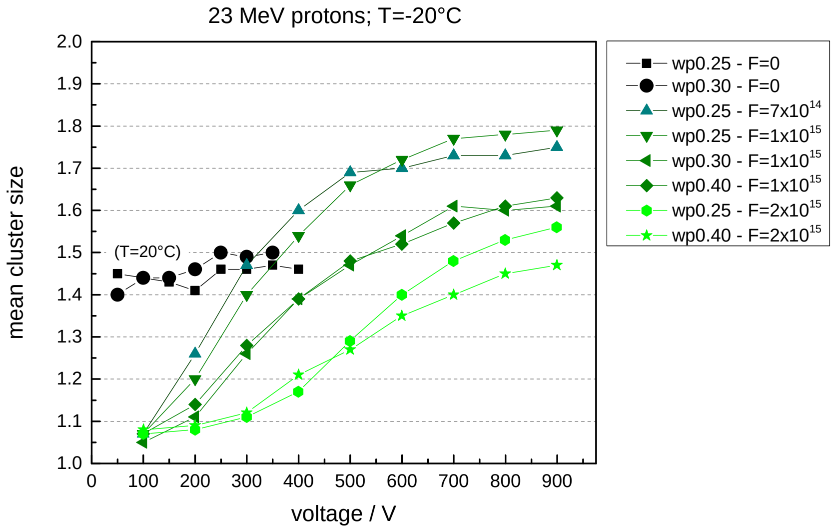

Figure 8.22: Cluster size for the standard MaPSA light sensor of variants 1 & 2 before and after irradiation.

after irradiation and hence a more pronounced charge sharing between the strips. Nevertheless, the effect is within the expectations.

Conclusion on the first MaPSA light sensor design for PS modules

The first attempt of the small test sensors with PS module demands is, with respect to the irradiation studies, very promising. This means that both charge collection and noise behavior were tested up to the fluence of $\Phi = 2 \times 10^{15}\ \mathrm{n_{eq}cm^{-2}}$. This fluence is two times higher than the expected fluence for the inner PS modules.
In the ALiBaVa setup, no significant differences in the performance depending on the layout of the MaPSA sensor were observed. In order to check whether a certain layout is some percent more efficient compared to other ones, more detailed studies with substrip resolution are necessary. For this purpose, the sensors need to be qualified during beam test conditions. The latter will be introduced and discussed in more detail in chapter 10.

8.3.3 FOSTER

The increase in luminosity after the LHC Phase II Upgrade will also increase the density of particle tracks in the detector. In order to sufficiently distinguish between several thousands of tracks per trigger event, the granularity of the detector needs to be increased too. A basic requirement of each tracking detector is also to keep the material budget as low as possible in order to suppress multiple scattering. For the future CMS outer tracker, the concept of PS and 2S modules with two stacked sensors is the current baseline with the aim of coping with the

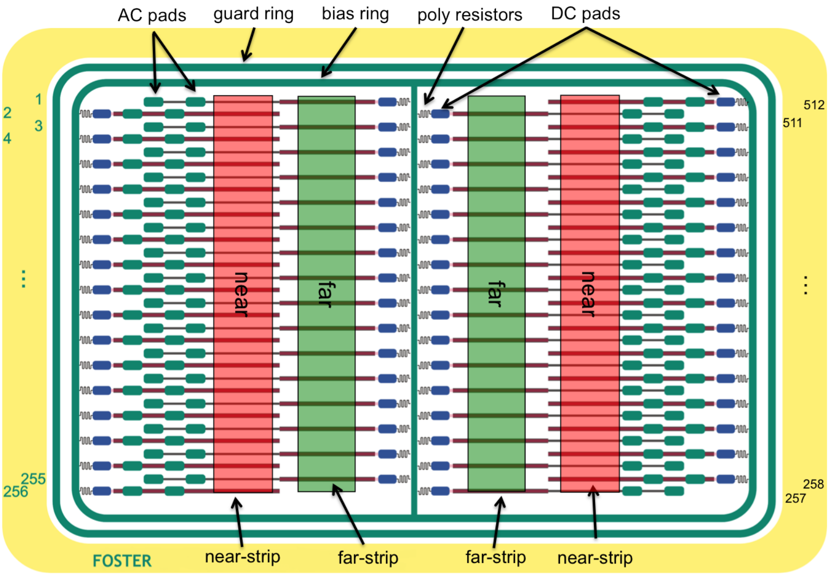

Figure 8.23: Schematic view of the FOSTER layout.

increasing demands and track density. As the occupancy of the channels should be as low as possible to allow reliable discrimination of particle tracks, the granularity of the future strip sensors were increased by a factor of two by dividing the strips into two half strips. Both halves will be connected at the opposite edges of the sensors to the readout ASICs via wire bonds. The wire bond technology is well known and of high yield.
Within the EKP hardware working group at KIT, a new layout of a strip sensor for high track density experiments was developed and proposed. The new layout increases the granularity by a factor of four compared to common strip sensors but simultaneously, the layout allows the usage of the wire bonding technology at the edges of the sensor, and hybrids do not have to be mounted on the sensor. The sensor is called FOSTER (**FO**urfold segmented **ST**rip sensor with **E**dge **R**eadout).

The following sections will describe the chronological development of the FOSTER. The first layout had already been implemented in the HPK campaign wafer. The first prototype showed undesired behavior [Kor11]. In a second submission with ITE, though the sensor showed some improved performance, the undesired behavior was still present [Hof13, gS12]. In a further submission with CNM and an addition of layout improvements, the auspicious performance was proved. The results in the following sections were published in [dBDH$^+$15].

Sensor layout

The design of the FOSTER is schematically shown in figure 8.23. The sensor is divided in two identical halves, separated by a bias line connected to the bias ring in the center of the sensor.

Furthermore, each half is again divided into two regions. There is the “near“ strip region which is next to the sensor edge and the “far“region with strips which are connected via thin aluminum routing lines running between the near strips to the AC pads for wire bonding at the edges. In order to allow such routing, the near strips are displaced by a half pitch in comparison to the far strips and vice versa.

First prototypes with HPK

The first prototypes were implemented within the HPK campaign on different substrate material and thickness. The sensors held 4×128 strips of about 7 mm length with a pitch of 100 μm. The electrical qualification was promising as the sensors fulfilled the specifications of low currents and strip parameters like strip isolation and interstrip capacitance [Hof13].

The charge collection measurements were performed in the ALiBaVa setup either with a Sr90 source or with a 1060 nm laser. Regarding the FOSTER design, it is crucial for the signal generated in the near strip region to be not coupled to the routing line of the far region strips because this would lead to a wrong hit position assignment. In order to prove if a coupling is present or not, the laser with a 15 μm beam spot was moved in 1 μm steps above the far and near region respectively. The result is shown in figure 8.24.

The FOSTER in this case is a p-type sensor with p-spray isolation. Corresponding to the colors indicated in the sketch of the far and near regions, the signal of the contributing strips was plotted. The scan of the far region in figure 8.24(a) shows an expected behavior, where the signal is first seen on the left far strip (blue) and then by moving the laser it vanishes and appears on the next far strip (green). The corresponding near strip does not see any signal at all as desired. After repeating the same measurement in the near region of the FOSTER, a signal coupling to the corresponding far strip was observed. One can see in figure 8.24(b) a red curve belonging to the far strip. Here, the generated charge in the near region coupled to the routing line of the far strip. In such a scenario, a traversing particle in the near region but next to the routing line would be wrongly interpreted by the readout electronics as a hit in the far region. The grayish bars in the signal plot indicate the position of the aluminum strips and routing line at which the laser gets reflected and as a result no signal appears at this positions. The measurements with the Sr90 source led to the same conclusion, as the cluster charge in the near region was about 5% lower than the cluster charge in the far region. In this case, it can be concluded that this missing fraction was induced to the routing line of the far strip. In particular, when placing the source above the near region, more than 31% of the seed signal positions (strip with the highest signal in the cluster finding algorithm) was attributed to the far region. In comparison, less than 1% of wrongly assigned seed signals was detected while placing the source above the far region. In both cases, a wrong assignment of about 1% can be attributed to the spread of the source which was placed in a collimator with a 0.8 mm opening 8 mm above the sensors.

The induced signals on the routing line were observed for both n-type and p-type sensors.

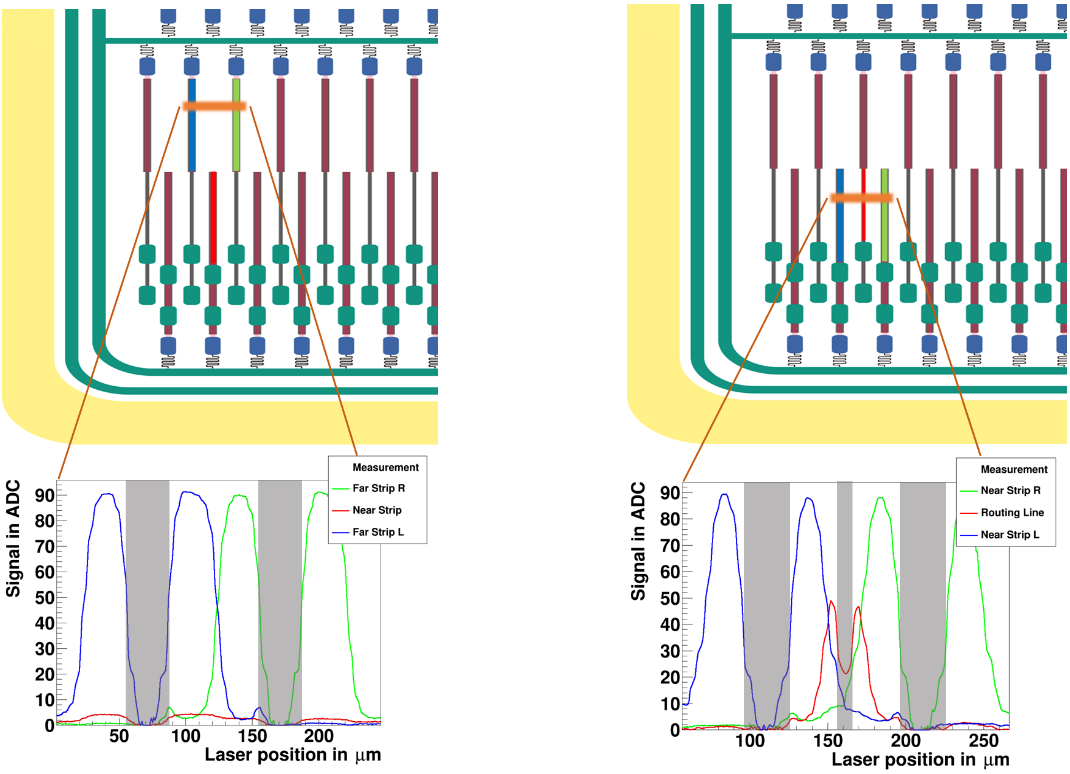

(a) Far region laser scan

(b) Near region laser scan

Figure 8.24: Laser scan of the FOSTER prototype. The orange bars indicate the laser scan position and the resulting signals on the strips are shown below.

Simulation studies

In order to understand the signal coupling to the routing line, T-CAD simulations were performed. In general, induced currents on electrodes can be calculated following the Shockley-Ramo theorem [Sho38, Ram39]. Given an electrode i, the induced current I is:

$$I_i = e\left(\vec{v}\cdot\vec{\nabla}\Phi_{wi}(\vec{x})\right), \tag{8.6}$$

with e as the electron charge and $\vec{v}$ the instantaneous electron velocity. The weighting potential Φ_{wi} is responsible for the coupling of a point charge to an electrode i. As a consequence, when a weighting potential or a weighting field $|\vec{\nabla}\Phi_{wi}|$ is present, a signal is induced to an electrode i. The weighting potential can be simulated by applying 1 V to an electrode and leaving all other electrodes at ground potential.

In figure 8.25, the weighting potential for the FOSTER p-type prototype with p-spray isolation obtained in the simulation is shown. The parameters used for the simulation are the same as for the sensor studies in chapter 6. For the purpose of simulating the weighting potential, one simulation with all electrodes at ground potential and 300 V bias voltage was performed and one additional simulation for which a potential of 1 V on the routing line was applied. The difference

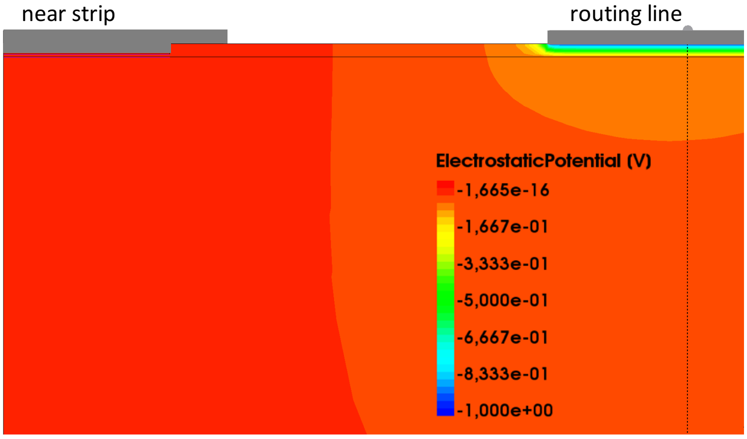

Figure 8.25: Simulated weighting potential for the prototype FOSTER.

of both simulations is the resulting weighting potential. A potential not equal to 0 is present and hence a charge at any given position in the sensor induces after Shockley-Ramo a current on the electrode proportional to the velocity and weighting field, in this case the routing line.

In this simulation, also the electric field was investigated and the result with an indicated direction of the electric field by unit vectors is shown in figure 8.26. The p-spray doping concentration was chosen to 2×10^{15} cm^{-3} and 1 μm depth. This concentration was estimated for the HPK p-spray samples. The electric field vectors are all directed from the sensor surface to the backside of the sensor. As a consequence, electrons are not just drifting towards the collecting electrodes but also to the routing line, or more precisely, in general towards the surface, and induce the undesired signal.

A possible solution to the problem should be a higher doping concentration of the p$^+$ isolation layer in order to flip the electric field just below the routing line. With this, drifting electrons will be repelled by the electric field below the routing line and no signal induction is expected any more. While investigating the FOSTER, the CNM submission was prepared. The CNM run was decided to be of p-type material with p-stop isolation. Hence, a p-stop below the routing line was simulated too and the relative induced signal on the electrode as a function of the p-stop doping concentration is plotted in figure 8.27. Besides, this effect with increasing boron concentration is, with respect to simulation results, also valid for the p-spray technology [Hof13, gS12].

One can observe that with increasing p-stop doping concentration the relative induced signal on the routing line vanishes for a p-stop peak doping concentration of 9×10^{15} cm^{-3} and 1.5 μm depth. This in fact is of high interest, as this peak doping concentration was also found to assure a good interstrip resistance and low electric fields and as a result high breakdown voltages, see chapter 6.4.

The effect of the vanishing signal on the routing line is also present in the simulation of the weighting field and electric field strength. Figure 8.28 shows the weighting potential when a

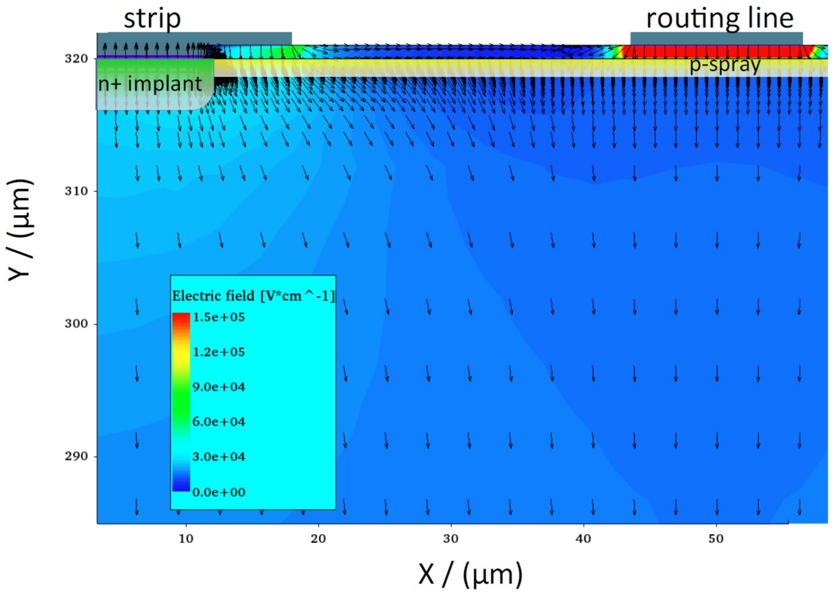

Figure 8.26: Simulated electric field for the prototype FOSTER with p-spray isolation.

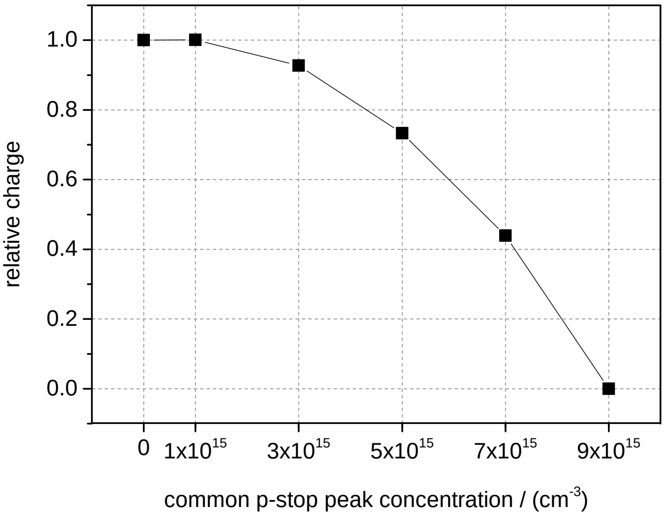

Figure 8.27: Relative induced signal on the routing line as a function of the p-stop doping concentration.

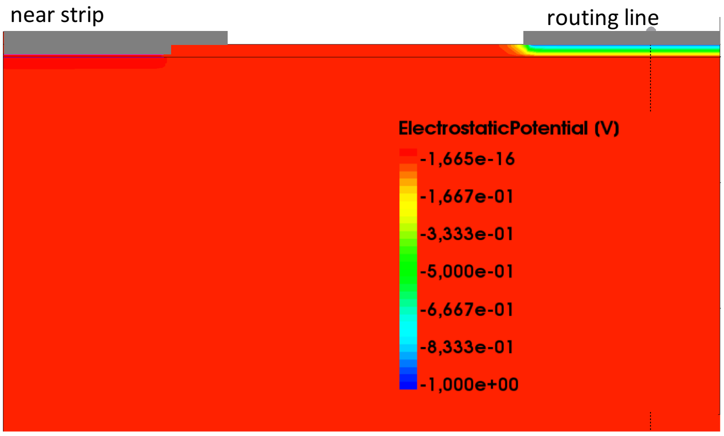

Figure 8.28: Weighting potential for a FOSTER with a p-stop below the routing line. The doping concentration in this plot is 1×10^{16} cm^{-3} and of 1.5 μm depth

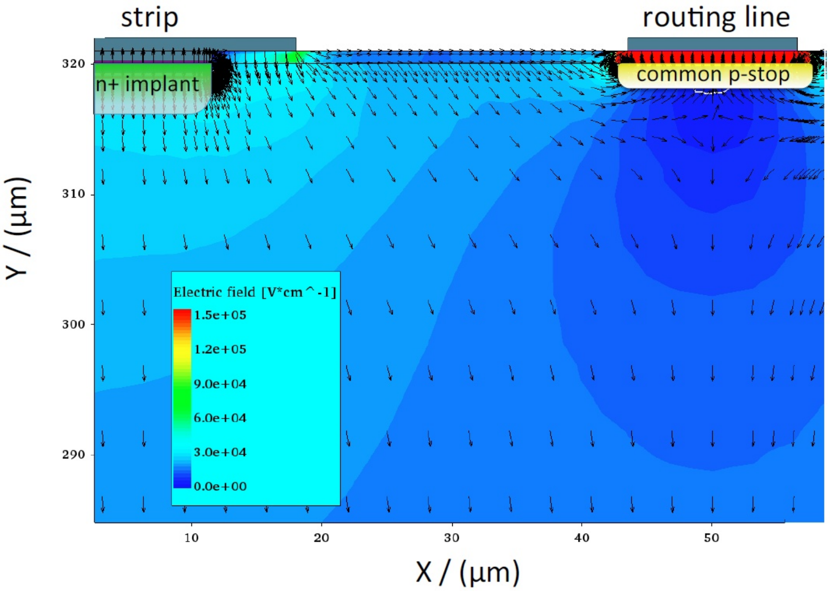

Figure 8.29: Simulated electric field for a FOSTER with a p-stop below the routing line. The doping concentration in this plot is 1×10^{16} cm^{-3} and of 1.5 μm depth.

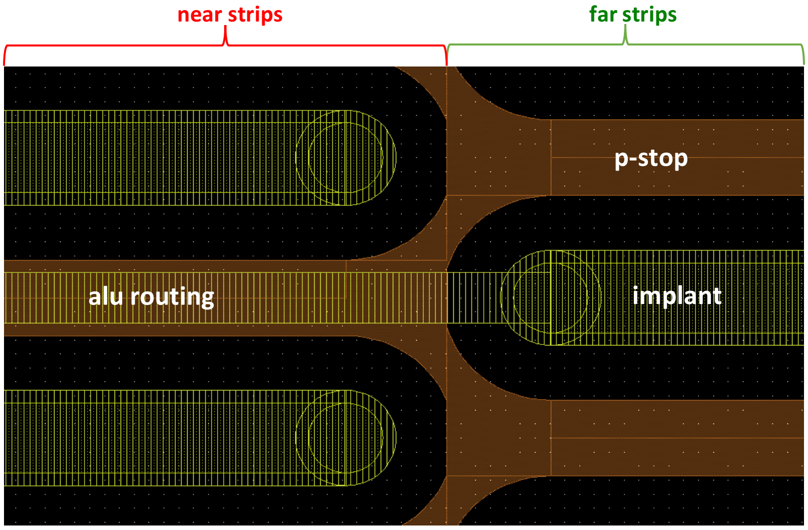

Figure 8.30: Section of the transition region of the new FOSTER design.

p-stop with a concentration of 1×10^{16} cm^{-3} and 1.5 μm depth is present below the routing line. Basically no weighting potential is there and hence, following the theory, no induction of any signals is expected.
Also, the electric field shown in figure 8.29 is flipped below the routing line due to the moderate p-stop peak doping concentration of 1×10^{16} cm^{-3} and of 1.5 μm depth. As a result, the electrons are repelled from this region and no signals are induced any more.
The finding of this effect was directly applied to a new FOSTER layout and submitted to the CNM run in 2014 together with the strip sensors discussed in the previous chapter.

Improved FOSTER design

The design did not change significantly to the HPK design due to the fact, that besides the signal coupling to the routing line, in general all strip parameters were showing reasonable values. Due to a limited available space on the CNM wafer, the new FOSTER sensor is 25 mm long and 6 mm wide with 4×32 strips. Each strip is about 4.9 mm long. The p-stop doping concentration in the CNM run is as mentioned earlier about 9×10^{16} cm^{-3} and roughly 2.7 μm deep.
Two variations of the new FOSTER were implemented. The widths of the routing line as well as of the p-stop below the latter hold different sizes and are listed in table 8.2. Although the widths have been varied, the ratio of the aluminum width to the p-stop width is the same in both cases.

Performance of the new FOSTER design

After receiving the new FOSTER, the measurements were repeated including laser scans of the far and near regions as well as Sr90 source measurements. The results from the laser scan as shown for the prototype HPK FOSTER in figure 8.24 are shown in figure 8.31 for a new FOSTER

Table 8.2: The differences of the new FOSTER layout. The routing line and the p-stop width below it were varied.

FOSTER design	p-stop width [μm]	routing line width [μm]
“narrow“	15	10
“wide“	27	18

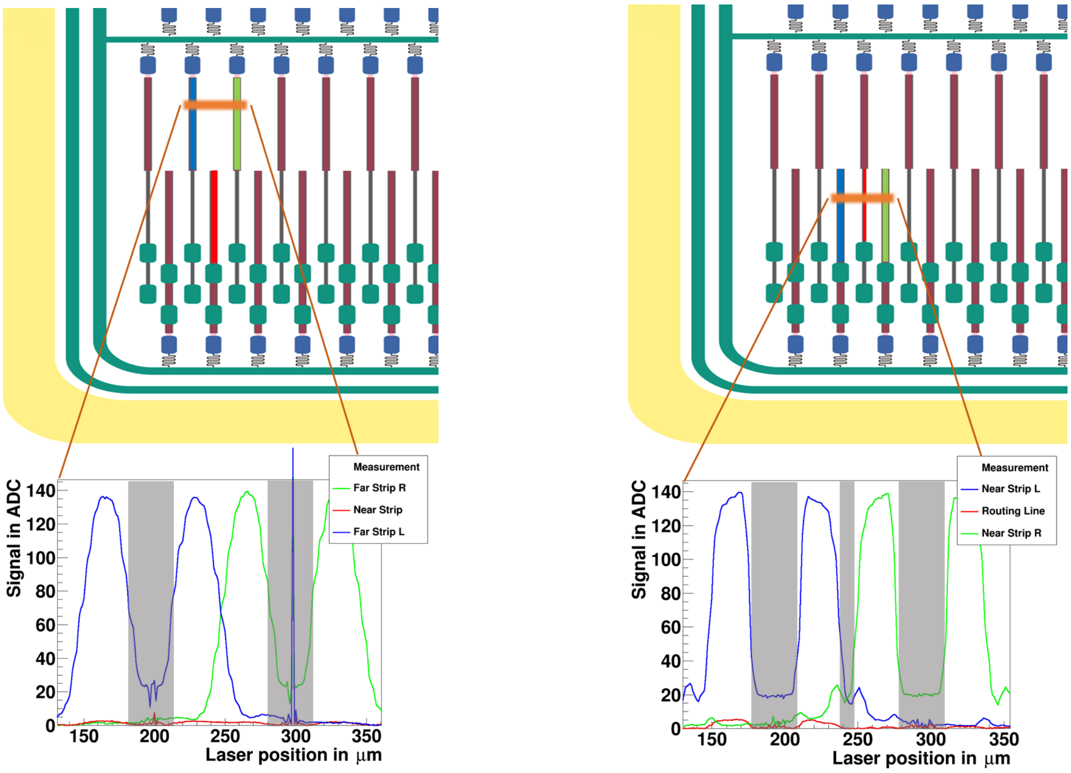

(a) Far region laser scan

(b) Near region laser scan

Figure 8.31: Laser scan of the new CNM FOSTER performed as in figure 8.24. There is no unwanted signal coupled to the routing line any more.

before irradiation. The interesting scan of the near region is shown in figure 8.31(b), where no signal on the routing line is observed any more. As predicted by the simulation studies, the additional p-stop below the routing line prevents a signal induction if the boron peak doping concentration is chosen moderate to high[5].

Complementary measurements with a Sr90 source were also performed. The source was placed either above the far region or the near region. The cluster finding algorithm searches for a strip with the highest signal and attributes this strip to the hit position (in case of the FOSTER to one of the four strip regions). The result is shown in figure 8.32. The upper two plots in the figure

---

[5] the concentration should in addition fulfill the requirements discussed in chapter 6 and 8

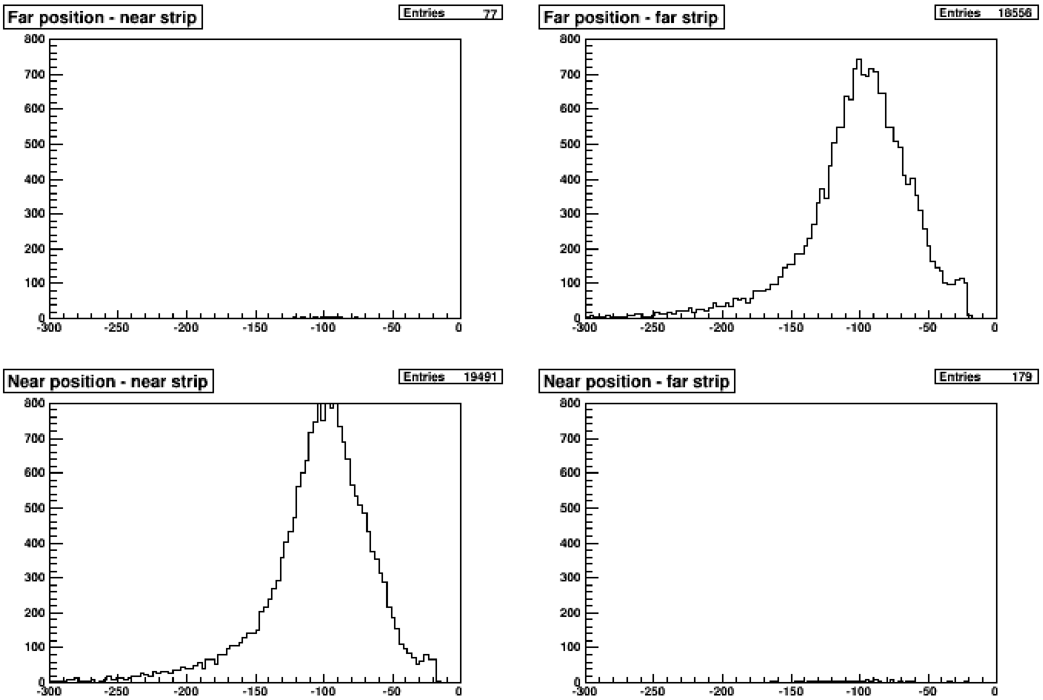

Figure 8.32: Source measurements of the different regions of the new FOSTER design. Each plot shows the position of the source at a certain region and the number of attributed seed strips to any region.

show the number of attributed seed strips when the source is placed above the far region. A negligible part of the hits is attributed to a hit in the near region although the source is above the far region and is unavoidable due to the spread of the source respectively the collimator. After placing the source above the near region, the same observation was made vice versa. This means also a negligible part of the hits was wrongly attributed to the far region. These measurements, both laser and source in combination with the simulation, proved the concept of the new FOSTER. After the initial qualification before irradiation the sensors have been irradiated with protons at KIT up to a fluence of $\Phi = 1.1 \times 10^{15}$ $n_{eq}cm^{-2}$. Again, laser measurements and Sr90 source measurements have been performed.

The laser scan of the near region of the wide FOSTER after a fluence of $\Phi = 3 \times 10^{14}$ $n_{eq}cm^{-2}$ is plotted in figure 8.33. Due to increased leakage current after radiation damage the sample was cooled down to $T = -20°C$ and the bias voltage was increased to 600 V. Also, in this figure no undesired signal coupling to the routing line is observed and the direction of the electric field towards the routing line that repels the drifting electrons is still present. But indeed, with increasing fluence more wrongly attributed seed strips are found in dependence on the routing line width and p-stop width. The ratio of wrongly assigned hits to the number of overall found clusters is shown in figure 8.34.

The wide FOSTER design shows less wrongly assigned hits in the order of about 7% after the

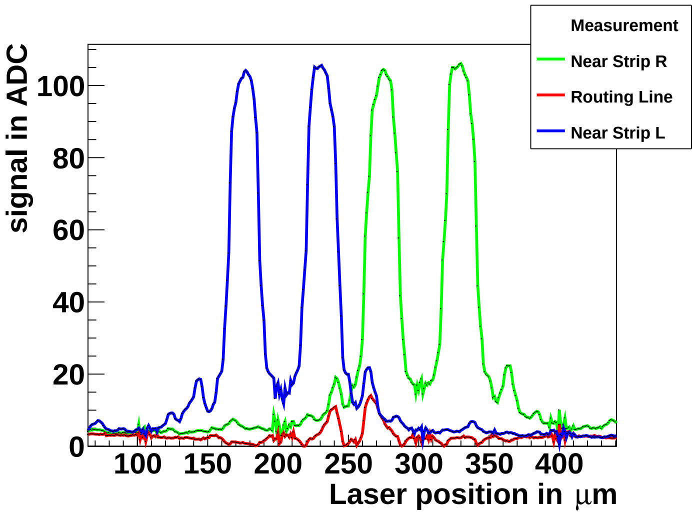

Figure 8.33: Laser scan of the near region of the new wide FOSTER design after proton irradiation to $\Phi = 3 \times 10^{14}$ $n_{eq}cm^{-2}$ at T= −20°C and 600 V.

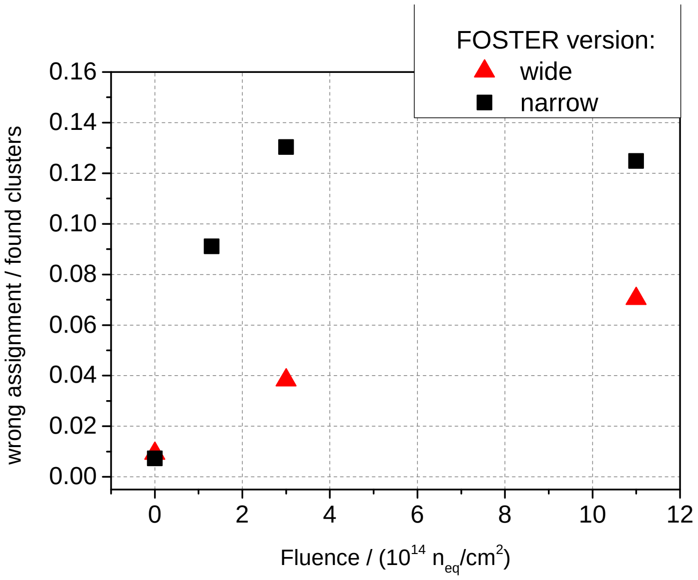

Figure 8.34: Source measurements and the ratio of wrongly assigned hits after proton irradiation up to $\Phi = 1.1 \times 10^{15}$ $n_{eq}cm^{-2}$, performed at T= −20°C and 600 V for the two different FOSTER designs.

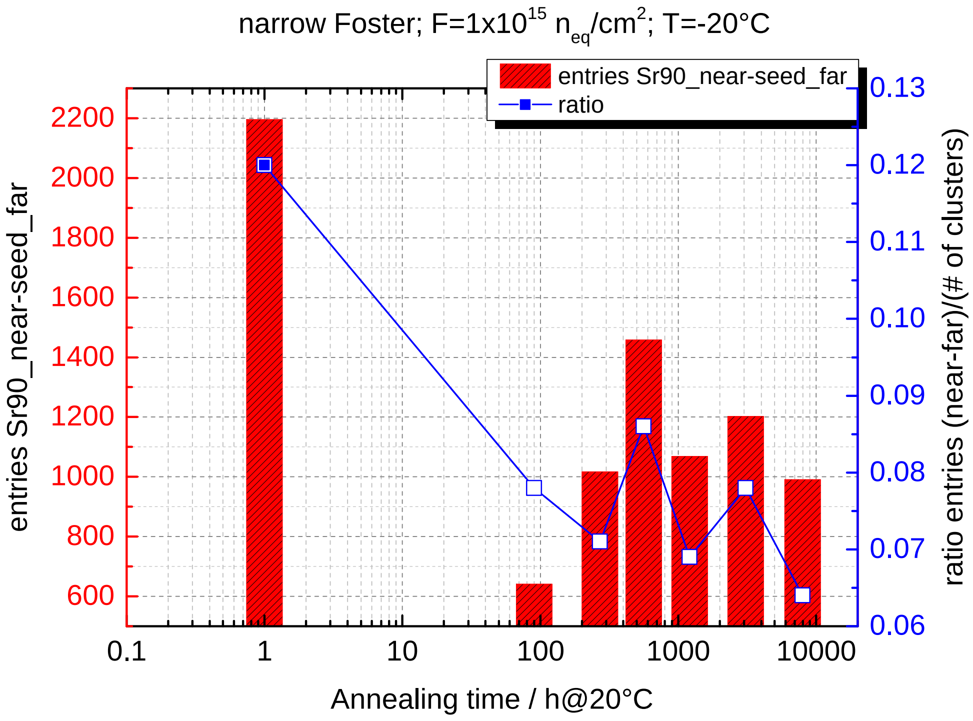

Figure 8.35: Narrow FOSTER source measurements and the ratio of wrong assigned hits after proton irradiation to $\Phi = 1 \times 10^{15}$ $n_{eq}cm^{-2}$.

highest proton irradiation. The narrow FOSTER design shows 13% wrong hits. Both numbers are in comparison to the first prototype with than 30% better but nevertheless the coupling is not negligible anymore, particularly for the narrow version of the FOSTER.

This growing effect with fluence can be explained by the increasing negative space charge below the surface after irradiation, see chapter 8.1. As a consequence, the electric field just below the routing line is affected by the space charge and a pronounced direction of the electric field towards the routing line is not given any more. Probably a wider p-stop implant might help to reduce the change after irradiation and secure a radiation hardness beyond a fluence of $\Phi = 1 \times 10^{15}$ $n_{eq}cm^{-2}$.

An annealing study for the narrow FOSTER after a fluence of $\Phi = 1 \times 10^{15}$ $n_{eq}cm^{-2}$ is presented in figure 8.35. The annealing times were chosen corresponding to the HPK campaign and as listed in table 4.2. The source has been placed on the near region and for each measurement 100000 trigger events were recorded. After the cluster finding algorithm, the number of seed strips attributed to the far region through the coupling to the routing line was analyzed and is plotted on the left y axis. The ratio of these wrongly assigned seed strips and the number of found clusters is plotted on the right y axis. The first annealing point is basically the direct measurement after receiving the sensor from irradiation and might differ to 1 hour at room temperature due to transportation time. One can see that the initial 12% of wrongly assigned seed strips decrease significantly with increasing annealing and end up at about 6%, like the wide FOSTER without annealing. But even after the first annealing step, in this measurement corresponding to 90 hours at room temperature, the ratio drops from 12% to less than 8%. Clearly, from the combination of the x-ray irradiation with the annealing study, the effect just depends on the bulk damage and is independent on the surface damage.

Conclusion on the FOSTER

Increasing demands for detectors with high particle density also require an increase in the granularity. The FOSTER design was developed at KIT and increases the granularity by a factor of four compared to standard silicon strip sensors. Furthermore, standard wire-bond techniques can be used, as the signal from the far strips regions are routed to the edge of the sensor. After studying the first prototype, an unwanted signal coupling to the routing lines was observed. Complementary simulation studies hint to a solution of this problem and a new FOSTER layout was designed and produced with CNM Barcelona. Before irradiation, the new sensors behave well and no coupling is observed anymore. After irradiation, the coupling shows up again, although significantly less compared to the prototype. The wide version on the other hand shows fewer induced signals than the narrow version, hence a wider p-stop might prevent the effect even after high irradiation fluence of $\Phi = 1 \times 10^{15}$ $\mathrm{n_{eq}cm^{-2}}$. Hence, further simulations and a new run with additional small improvements might finally lead to a radiation hard FOSTER.

CHAPTER

9

CBC - BINARY CHIP FOR THE PHASE II OUTER TRACKER UPGRADE

The new ASIC for the Outer Tracker 2S modules, the CMS binary chip (CBC) introduced in chapter 3.2.3, is a key part of the trigger contribution provided by the tracker. For this purpose, a correlation of hits within a certain searching window on the two stacked sensors in one 2S module is defined as a high p_T stub. The stub information itself will be read out at 40 MHz LHC bunch crossing rate, while the binary data of the sensors can be stored into a 12.8 μs deep buffer until the global trigger decision.
The CBC is designed and investigated in several submissions. After the first promising version (CBCv1) with restricted functionality, the CBC in version 2 is currently being investigated. The latter already holds most of the final features and the final design and functionality will just change slightly. In order to study the performance of such a sensor-chip system based on the CBCv2 chip, a test setup was build. With this, it is possible to investigate noise and efficiencies of either just the ASIC or a combined system of a sensor connected to the CBC.
In this chapter, the CBC setup will be introduced on the basis of measurements and theory. Furthermore, irradiation studies were carried out where the CBC received either x-rays doses or proton fluence equivalent to the expected dose towards the end of the HL-LHC era. The results on the radiation hardness are discussed in the last section.

9.1 Purpose of the CBC setup

The CBC needs to be investigated as a standalone hardware part as well as an integrated part within the 2S module system. Both categories include studies by the chip designers as well as by users. The latter are several international institutes. This system test group aims to proof the

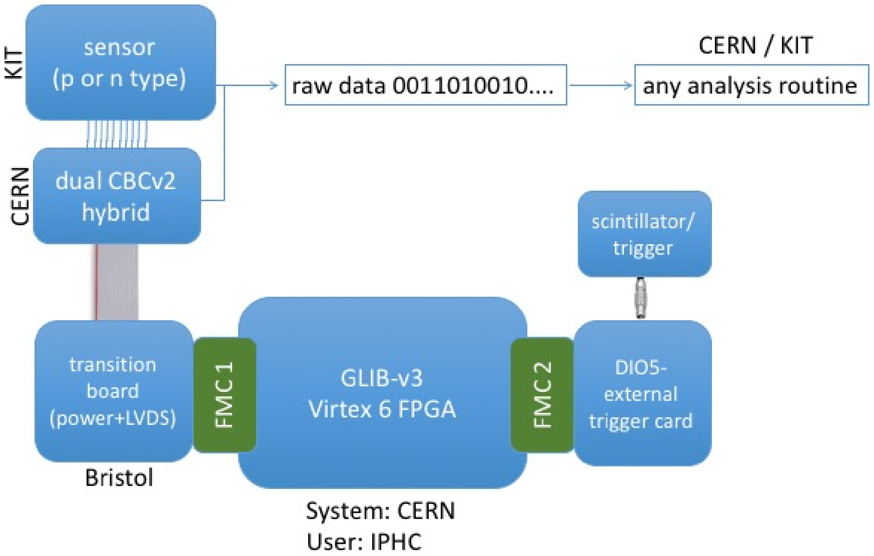

Figure 9.1: Functional diagram of the CBC bench top test system at KIT.

concept of the low transverse momentum trigger modules and the feasibility of its integration within the CMS experiment. In order to study the CBC performance, small scale systems based on a few CBCs and one or none connected sensor (instead of two) are developed. The test system is based on the GLIB AMC[1] evaluation board [MBB+13]. This project is a Virtex-6 FPGA-based evaluation platform of which the hardware, firmware and software are provided by the GLIB project community. The board handles optical links and can be used as a data aquisition system for bench-top experiments at the laboratory or in beam tests. The GLIB AMC features two additional high pin count industrial standard FPGA Mezzanine Card (FMC) sockets which assure additional I/O and clock lines.

Within this study, a setup based on the GLIB and a dual-CBCv2 hybrid [BBH+12] was built up and studies were performed in order to get used to the CBC readout system as well as to understand the functionality and evaluate the overall system and the chip respectively. Particularly the latter is of high importance as any issues found directly affect the next and close to final third version of the CBC, which is going to be submitted in early 2016.

9.2 The bench top readout system based on the CBCv2 and GLIB platform

The functional diagram of the bench top test system with 2 CBCs is shown in figure 9.1. The system consists of several hardware parts, each developed and supported by the contributing collaborators within the system test working group. The individual parts are the following:

---

[1] Gigabit Link Interface Board - Advanced Mezzanine Card

- GLIB-v3: The GLIB in version 3 is a standalone evaluation platform based on a Virtex-6 FPGA with several I/O and clock lines of different interfaces, allowing a broad connectivity. The system part of the firmware code has been developed and is supported by the CERN electronics group. The core user part is specified to the data transmission between the CBCs and the DAQ machine has been developed and is maintained by the Straßbourg IPHC group.

- Transition board: The transition board developed by the Bristol group is connected via a 32 pin flat ribbon cable to one of the FMC sockets on the GLIB. It handles both the powering of the CBCs as well as the LVDS data transmission.

- Dual-CBC2 hybrid: The custom made dual-CBC2 hybrid contains two CBCv2 ASICs bump-bonded to the hybrid. In order to allow the connectivity of two stacked sensors simultaneously, wire-bond pads on the top and the bottom of the hybrid are available. Furthermore, the high voltage to the sensors is distributed via the dual-CBC hybrid. Both sensors in a mini module can be either biased individually or via one bias voltage supply channel.

- Sensors: Considering the sensors, no restrictions are given due to the fact that the CBCv2 features a selectable feedback network which can handle both polarities (p-type or n-type respectively electron or hole readout). Each CBC holds 254 input channels. The channels of each CBC are alternatingly connected to the top and the bottom sensor in order to allow a coincidence logic of hits in both sensors. Hence, in total a maximum number of 254 strips of one sensor can be connected if two sensors are present.

- FMC-DIO5 [FMC]: The CBC produces either internal trigger signals or can be read out at a trigger receive signal. The latter is fed into the readout network via the FMC-DIO5 card. It is a 5-bit port digital I/O card with FMC connectivity. The I/Os can be individually programmed to either an input or an output channel. The trigger signal coming from the scintillator and the photo multiplier respectively is transmitted via the DIO-5 to the GLIB and processed further within the aquisition system.

- Analysis: Depending on whether the comparator of the front-end detects a signal which is higher than the defined threshold, it produces a digital 1 for a hit or a 0 for no hit per channel. A basic software to start and execute calibration and data taking is provided by CERN. The software can be downloaded at `https://gitlab.cern.ch/cmstkph2/Ph2_ACF`. Within this software framework, a C++ object-based library describes the system components (CBCs, Hybrids, Boards) and their properties (values, status). The configuration of the readout as well as of the chips can be accessed via dedicated registers in order to manipulate threshold settings and calibration procedures. Any further procedure routines are implemented by the user.

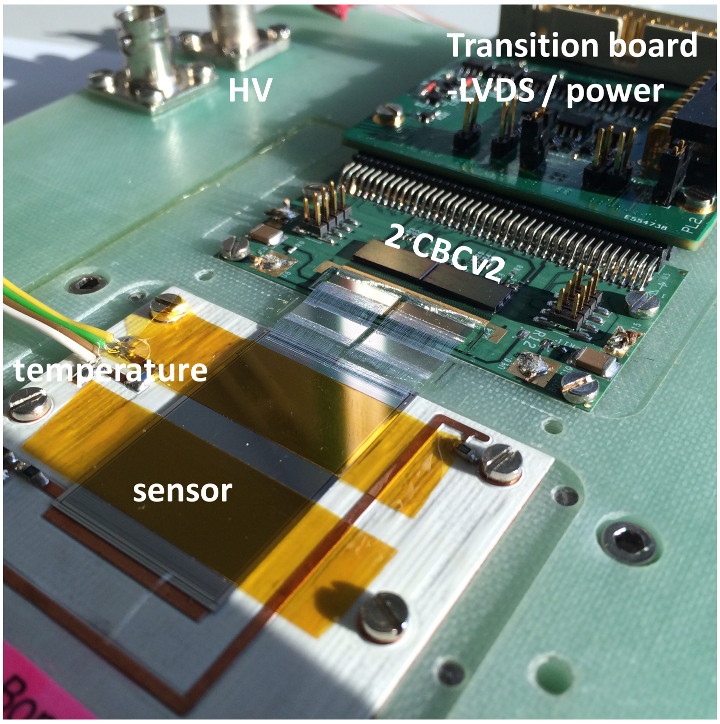

Figure 9.2: The dual-CBC2 hybrid test board as built and used at KIT.

Figure 9.2 shows the board which was designed compatible with the ALiBaVa setup box. The box contains a cooling jig precooled by water and peltier elements in order to stabilize the temperature during the measurement. A constant temperature is important as after the calibration, the threshold changes in the order of 300 electrons per 1°C. A radioactive source can be placed in a collimator above the sensor respectively module.

Calibration procedure

The creation of the binary hit information at the comparator output of the CBC depends on the threshold voltage, which can be adjusted via register manipulation. The aim for the threshold in 2S modules is about 6000 electrons. This value shall assure a high hit detection efficiency and a sufficient low noise rate but is still in optimization process.

The simplified schematic of the CBC front-end and the pulse shapes in electron mode are shown in figure 9.3. During the calibration procedure, three registers are adjusted in order to fulfill high hit efficiency. The global voltages Vcth and VPlus are set for the chip and Offset is adjusted for each channel individually. Vcth sets the global threshold of the comparator for all channels and VPlus sets the global DC signal voltage at the post-amplifier output. For a full efficiency, the DC voltage needs to be tuned for each channel via the Offset registers. Each register is of 8-bit length, hence the I^2C range is from 0 to 255, which translates to the voltages between 0 and 1.2 V. The calibration procedure reads as follows:

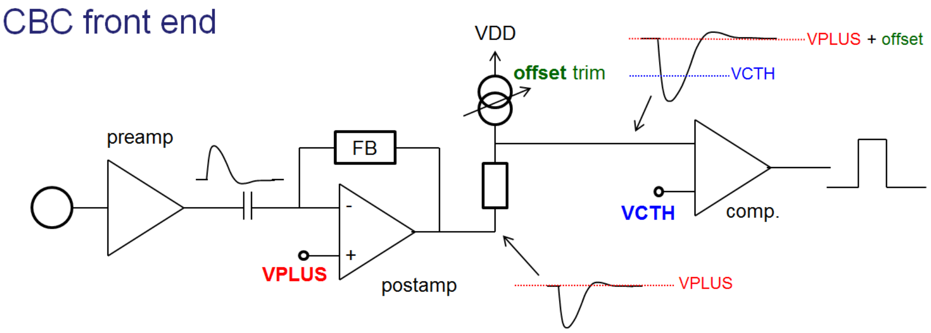

Figure 9.3: Simplified CBC front-end scheme and pulse for electron mode [BHJ+12].

- set the global Vcth threshold to a certain value (examplary Vcth= 120 I^2C units)
- the vcth scan is performed obtaining s-curves. The Offsets are set to 80 I^2C units for some different VPlus values
- the VPlus which assures a Vcth value of 120 is obtained
- s-curve calibration for the optimized VPlus value is performed again setting the indicidual offsets

After this, the calibration of the chip(s) is done and the results are stored in the configuration file(s). The latter is flashed onto the CBC(s) and the setup is ready to take data. The data output is purely binary at 40 MHz clock frequency and consists of a header with 2 logic 1 bits, 2 error bits, the 8 bit pipeline address and the data for all 254 channels.

9.3 Measurements and results

In order to gain experience with the CBC chip and the CBC setup respectively, after building the system some studies were performed. First of all, the calibration procedure and the system noise estimation were practiced with samples from the HPK campaign.

An exemplary result of a calibration is shown in figure 9.4. Here, an unirradiated float-zone p-type sensor with p-stop isolation and 320 μm thickness was calibrated to a Vcth threshold of 120 (dec.). In electron mode, a high Vcth value corresponds to a low threshold. In operation mode, the global threshold is configured after the calibration via the Vcth register, hence if the threshold value were set higher than 120 (in this example), all channels would detect hits and the fake hit rate and efficiency would jump to 100% as in this range the comparator value is within the nominal noise range.

If after calibration one or more strips show high noise, for instance due to a bad sensor strip channel, the noisy strips can be masked individually via the corresponding register. In case of electron mode, the channel offset would be set to 0 I^2C units, hence the threshold is far too high

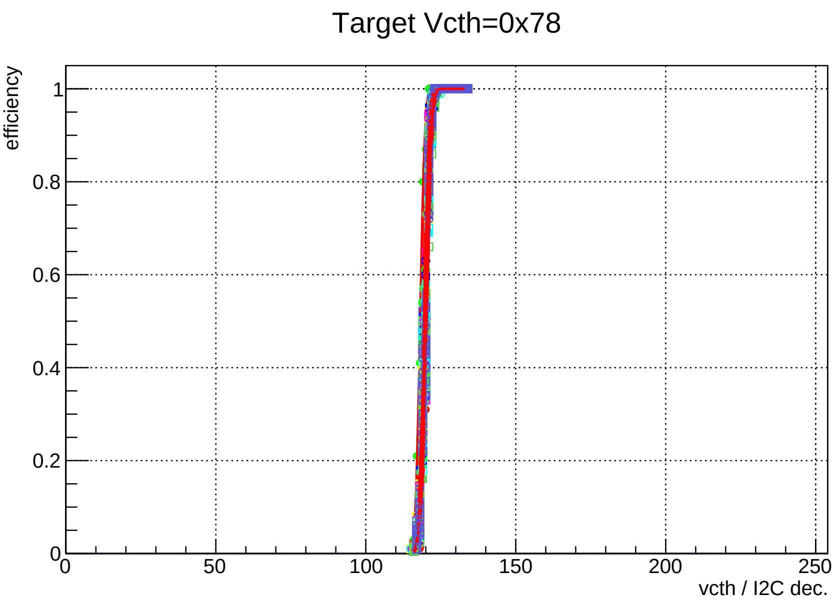

Figure 9.4: S-curves for all connected 254 channels after calibration of the CBCs with an unirradiated FZ320P sensor with 254 strips.

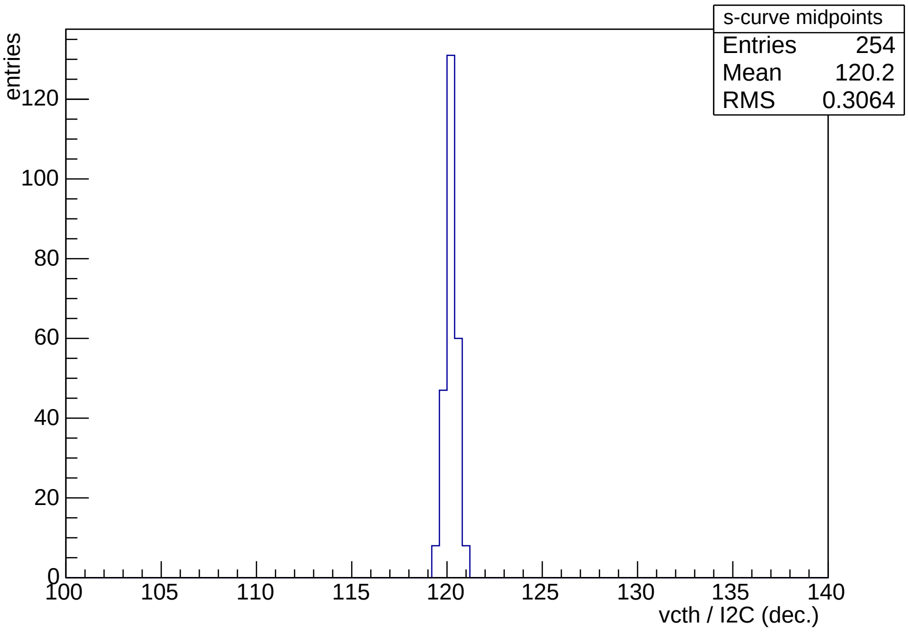

Figure 9.5: Spread of the s-curve midpints for all 254 channels after calibration of the CBC with an unirradiated FZ320P sensor. A RMS = 0.3064 corresponds in the KIT setup to about 100 electrons.

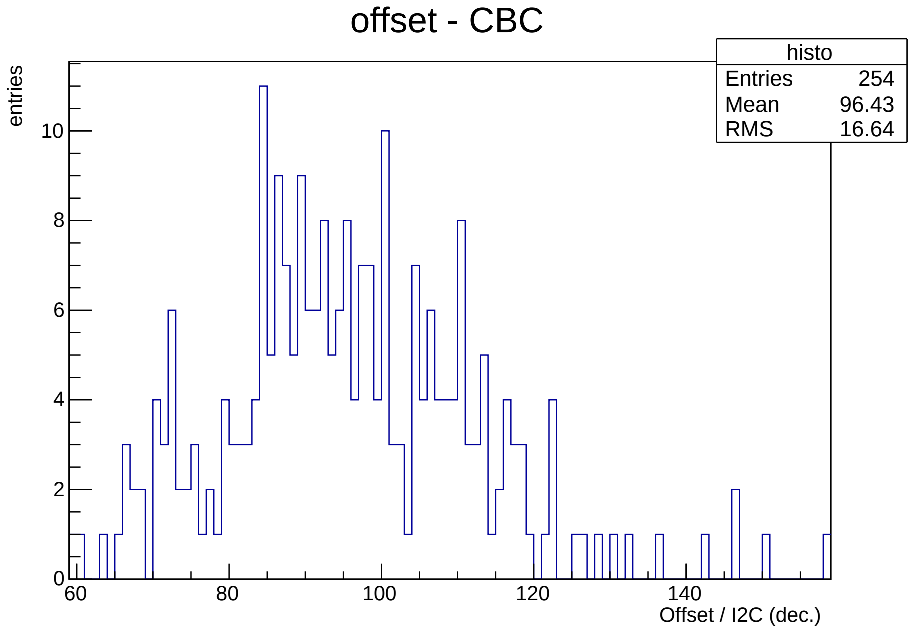

Figure 9.6: Offsets for each connected individual channel after calibration of the CBCs.

and never reached (vcth= 0 corresponds to a charge of about 40000 electrons).
The inflection points of the s-curves were extracted after calibration and plotted in figure 9.5. The mean is 120.2, showing that the calibration (in this case to 120) works reliably, while sigma of the s-curve midpoints is 0.3064. This value translates into about 100 electrons spread of the threshold value for all channels in this setup. The latter was determined with help of the on-chip test pulse (see next section).
In figure 9.6, the offsets after calibration for the 254 channels are shown. The mean value is 96.43 I^2C units with a significant root mean square of 16.64. This is directly connected to the individual strip leakage currents and noise. Due to the individual offsets for each comparator input transistor, now all channels respond equally to the global threshold Vcth.

Gain of the system

The CBC holds an analogue test pulse with programmable charge generator. The generator uses a programmable DAC in order to adjust the test pulse signal from 0 fC to 5 fC [Bra13]. A test pulse of 1 fC corresponds to 12 I^2C units and the charge step resolution is 0.04 fC with 10% accuracy. In order to determine the system noise, a test pulse of 2 fC≈ 12680 electrons was coupled into the channels and the threshold was increased from the nominal threshold sequentially in 1 I^2C unit steps until no hits in the data output appeared. The threshold for the test pulse as a function of the test pulse charge is plotted in figure 9.7.
A difference of 20 I^2C units in the global threshold Vcth increase is necessary in order to get rid of hits on the chip if the test pulse is increased by 1 fC≈ 6430 electrons. Hence, the gain of the

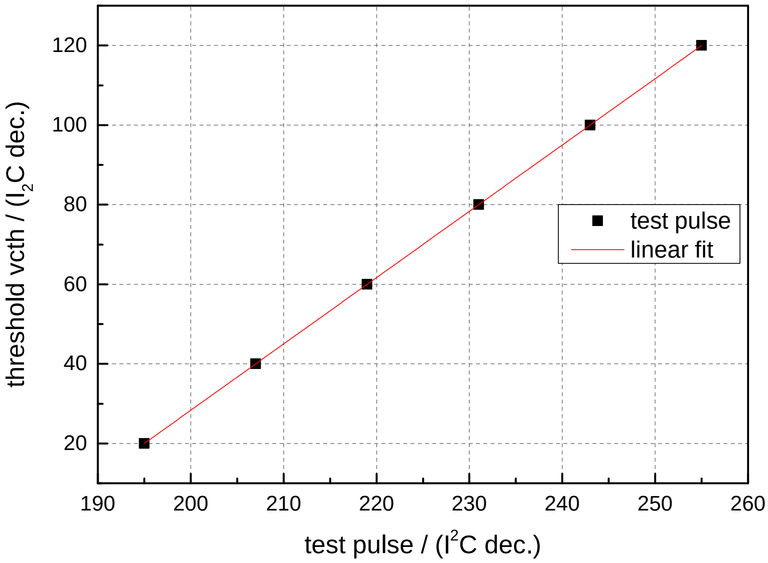

Figure 9.7: Threshold as a function of the test pulse charge coupled into the CBC channels by the on-chip generator.

setup per I^2C is about 322 electrons ± 10%.
Knowing the gain, now it is possible to set a certain global threshold corresponding to a certain amount of charge where the threshold is set via the vcth threshold register with 1 I^2C step accuracy (about 320 electrons per step).

Examples of measurements with HPK samples

A HPK float zone 320 μm thick sensor before and after irradiation was measured with the setup in order to check whether the CBC behaves well with input noise coming from a silicon sensor. In figure 9.8, one can see the result of the unirradiated sensor in dependence on the threshold, here set in hexadecimal values as in the CBC registers.
The plot contains measurements for three different Vcth values of 32, 64 and 96 decimal I^2C units. This corresponds with nominal threshold and taking the gain of 322 electrons per I^2C unit into account, to 28300, 18000 and 7800 electrons respectively[2]. The entries were fitted with a gaussian function. The shape reproduces the expected distribution of the Sr90 decay as the source was placed in a collimator in 8mm height above the sensor. With increasing threshold, the signal slowly disappears. But for the relatively high threshold of about 28000 electrons, still a small signal is visible.
In comparison to the measurement of the same sample with the analogue Beetle chip in the

---

[2] in electron mode a lower Vcth value corresponds to a higher threshold

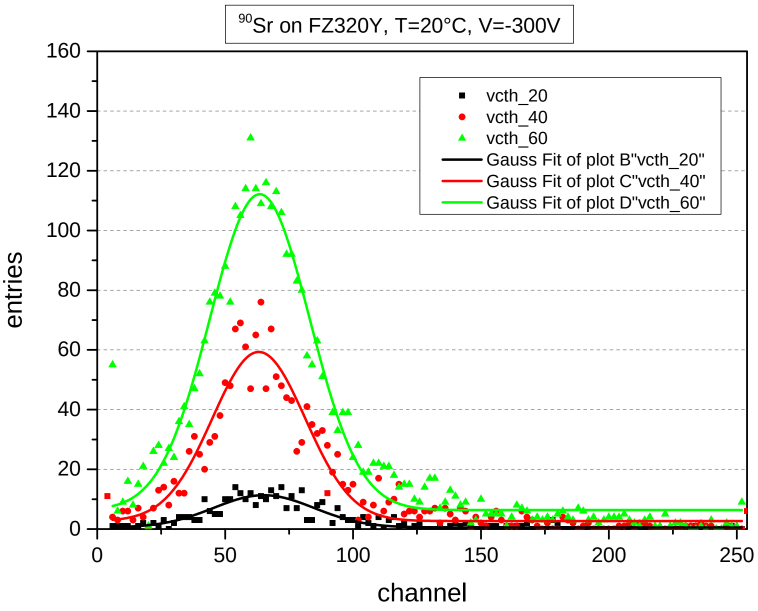

Figure 9.8: Measurement of an unirradiated FZ320 sensor with p-spray isolation with the CBC setup.

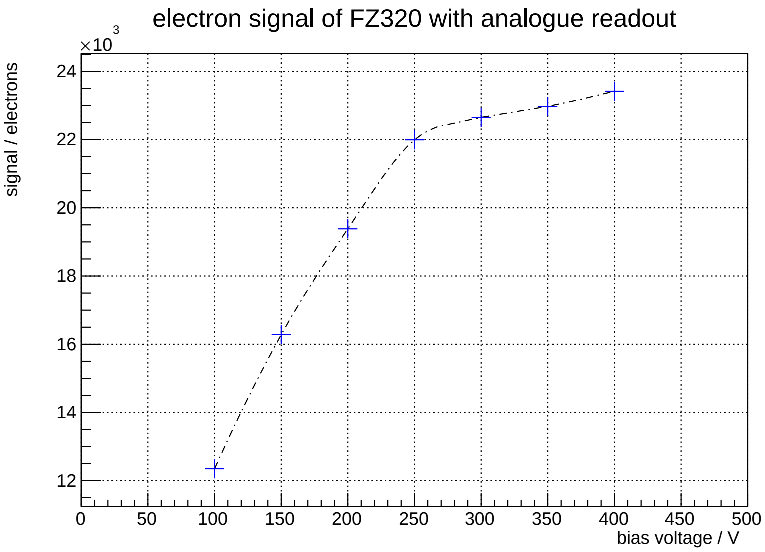

Figure 9.9: Measurement of an unirradiated FZ320Y sensor with the analogue Beetle chip in the ALiBaVa setup. The MPV of the signal distribution is plotted.

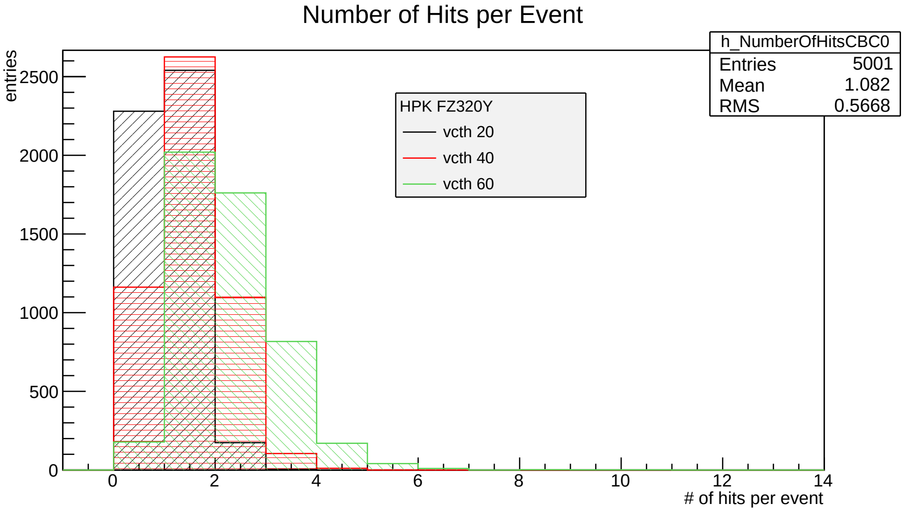

Figure 9.10: Number of hits in the unirradiated FZ320 sensor per trigger event for three different threshold values.

ALiBaVa setup, see figure 9.9, no hits are expected any more. Here, one can see that a charge of 23000 electrons at 300 V is the maximum. But as mentioned in chapter 8.2, the signal distribution is of a Landau shape. Hence, the detected hits correspond to a higher energy deposition of the MIPs and are not directly comparable to the MPV shown in figure 9.9.

The distribution of the β-electron direction due to scattering at the collimator edges and the effect of charge sharing between adjacent strips can been seen in the binary cluster size. In figure 9.10, the number of hits per trigger event are plotted for the three different threshold values. If the threshold is relatively low, in the range of 8000 electrons, several adjacent strips detect a hit. Up to 5 strips detect a signal. This is related to the low threshold, the charge sharing and a not perpendicular track direction of the MIP coming from the collimator. In this case, not just hits of adjacent strips are included but also strips which are not direct neighbors, for instance due to an increased strip noise. The CBC logic also includes a cluster width discrimination (CWD) which is programmable between one and three strips. Cluster widths higher than three strips, are in general, attributed to low momentum particles and are therefore rejected. In this case, the default state was set in which the CWD is bypassed and all hits pass to the subsequent stage. After increasing the threshold, the cluster size decreases as expected and just the strips with a high signal are detected (compared to the analogue 5/2σ-cut, where some strips do not pass the threshold).

The measurements were repeated for irradiated sensors as well. The HPK samples were irradiated with neutrons and protons to a fluence of $\Phi = 6.9 \times 10^{14}$ $n_{eq}cm^{-2}$, which exceeds the expected fluence for the inner 2S modules by about 40%. The calibration to Vcth= 120 of the chips had to be repeated as well in order to compensate for any additional noise or bad strips after irradiation. A threshold scan was performed for 600 V and 900 V and the result can be seen in figure 9.11.

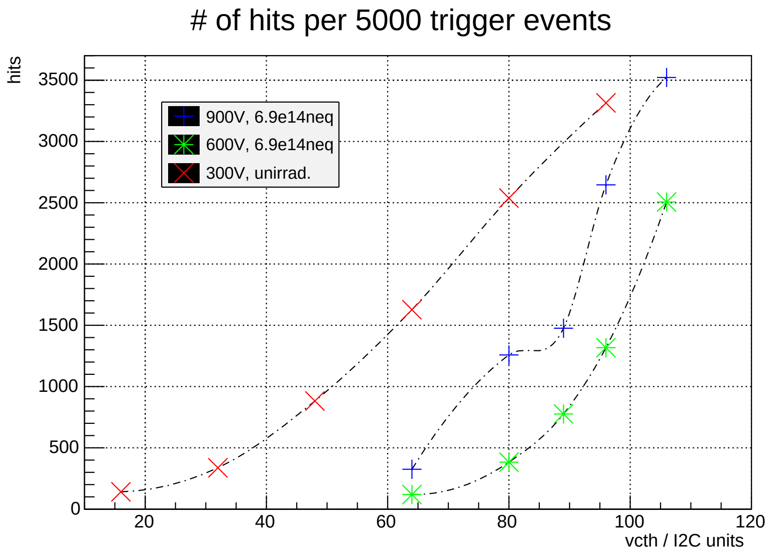

Figure 9.11: Comparison of the hit detection efficiency before and after irradiation as a function of the threshold of an irradiated FZ320 sensor. $\Phi = 6.9 \times 10^{14}$ $n_{eq}cm^{-2}$, T= −20°C after irradiation.

Clearly, after irradiation the signal decreases due to trapping effects and hence an earlier drop in the hit detection efficiency is expected if the threshold is set high. For each of the measurement, 5000 trigger in total and the resulting number of hits have been counted. One can see that already at a threshold of 106 I^2C units, which is about 5600 electrons, the efficiency drops and depends on the sensor high voltage. At this fluence and thickness of the sensor, a charge of about 11000 electrons at 600 V and 14000 electrons for 900 V is expected. Hence, a significant part of the β-electrons pass the sensor in an angle not perpendicular to the sensor surface. As a consequence, the charge is shared even more than in a perpendicular particle hit between several strips, where no strip signal exceeds the threshold of 5600 electrons. In order to study the efficiency of the CBC before and after irradiation, beam test conditions are necessary (see next chapter).

9.4 CBC - irradiation studies

A Monte Carlo estimation of the absorbed dose in CMS after an integrated luminosity of 3000 fb^{-1} for a proton energy of 7 TeV is plotted in figure 9.12. In this plot, the current tracker with 500 μm thick sensors has been simulated. From this, a dose in the order of 30 Mrad is expected for the most inner layer equipped with 2S modules. With a two times safety margin, the CBC should survive 60 Mrad without showing any negative influence. The chip designers did some studies up to an x-ray dose of 40 Mrad with the result that the CBC behaves well with respect to operation and on-chip voltages and currents. From this, no influence on the hit detection efficiency can be concluded [BR].

The availability of the x-ray source during the first irradiation test of the chip designers was lim-

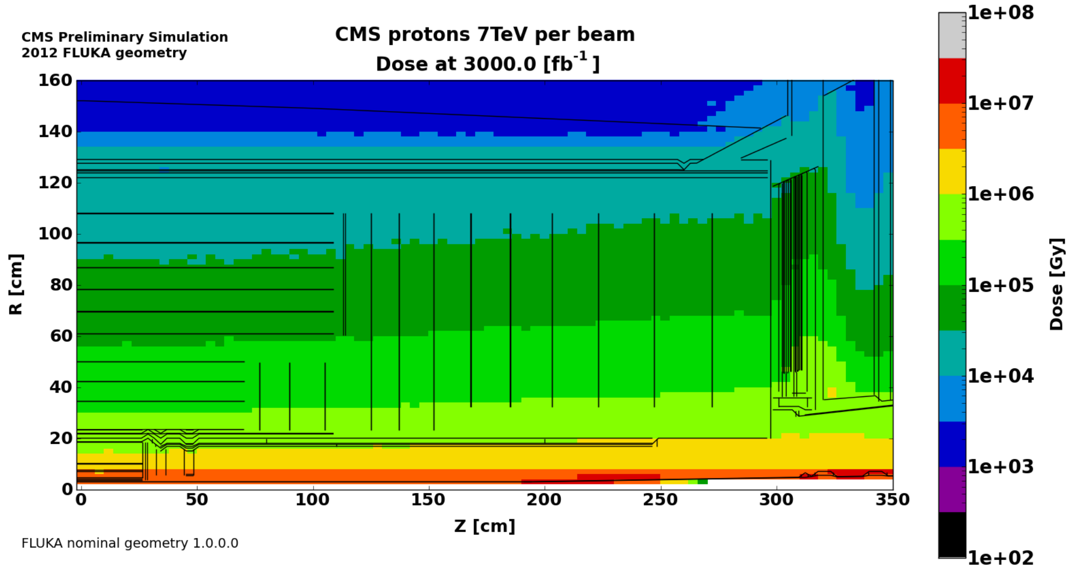

Figure 9.12: Expected dose in CMS after 3000 fb^{-1} for a proton energy of 7 TeV [FLU15]. Here, the layout of the current tracker has been simulated.

ited. As at KIT, both proton irradiation and x-ray irradiation are possible, additional irradiation studies were performed in order to complete the conclusion on the CBC radiation hardness.

X-ray irradiation

At the EKP[3], an x-ray tube with an accelerating voltage up to 60 kV is available. Depending on the height of the source, a beam diameter of up to 2 cm can be achieved. The CBC dimensions are $12 \times 6\ mm^2$, hence a full coverage during the irradiation is possible.
The measurements were performed before and after x-ray irradiation up to 180 Mrad. The highest dose was chosen in order to check the radiation hardness beyond the specifications in order to see if any changes after such high dose appear[4]. The bias voltages and bias currents are accessible via an analogue multiplexer (A-MUX) on the chip, and the CBC hybrid respectively.
The irradiations were done sequentially in steps of different size (0, 47, 60, 75, 90, 105, 120, 180 Mrad) at room temperature. Hence, a simultaneous annealing of the surface defect has to be taken into account, although according to [Zha13] it takes more than three years to anneal 50% of the fixed oxide charge. After each partial irradiation, the bias currents and bias voltages of the chip were measured. In order to cover the whole range of possible values of the different registers listed in table 9.1 (the nominal values might have to be changed during operation and in dependence on the lifetime within the radiation environment), the registers were measured as a function of the I^2C value from 0 to 255.
One can see from the figures 9.13(a) to 9.13(i) that neither the bias currents nor the bias voltages

---

[3] Institut fuer Experimentelle Kernphysik

[4] 23 MeV KIT protons are equal to 15 Mrad dose per $\Phi = 1 \times 10^{14}\ n_{eq}cm^{-2}$

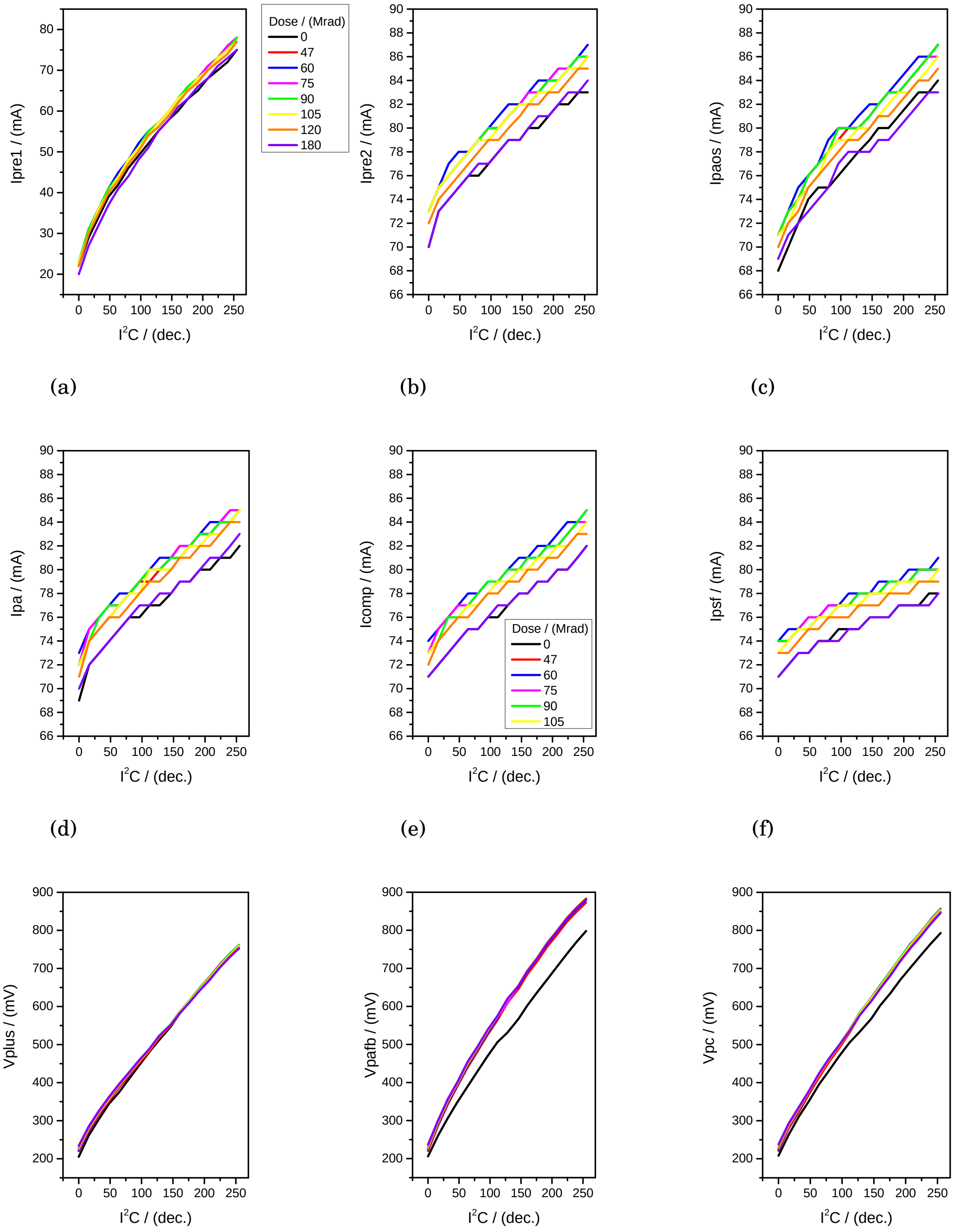

(a) (b) (c)

(d) (e) (f)

(g) (h) (i)

Figure 9.13: Current and bias voltages generated by the on-chip bias generator in dependence on the x-ray dose.

Table 9.1: The bias generator registers [Bra13].

Name	Function	Nominal	Range
Ipre1	Preamp Input Branch Bias Current	90 μA	0-255 μA
Ipre2	Preamp Cascode Branch Bias Current	10 μA	0-51 μA
Ipsf	Preamp Source Follower Bias Current	25 μA	0-51 μA
Ipa	Postamp Bias Current	20 μA	0-51 μA
Ipaos	Postamp Offset Adjust Bias Current	4 μA	0-12.7 μA
Icomp	Comparator Bias Current	2 μA	0-12.7 μA
Vpafb	Postamp Feedback Bias Current	2.5 μA	0-25.5 μA
Vpc	Preamp Cascode Bias Voltage	0.4 V	0.2-0.8 V
Vplus	Postamp Bias Voltage	0.6 V	0.2-0.8 V

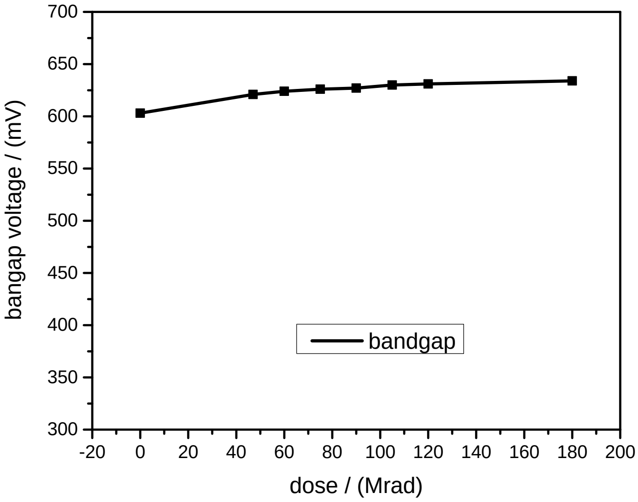

Figure 9.14: Bandgap voltage as a function of the x-ray dose.

change significantly with increasing x-ray dose which shows the radiation hardness of the CBC. The slight increase of 3-5% in the bias currents is related to the slight increase of the bandgap voltage shown in figure 9.14. The latter is the master reference for the bias generator which also changes after irradiation from 600 mV to 640 mV or by about 6-7%. The voltages are generated by applying a programmable current into a resistor, so an increase in the master current reference also leads to an increase in the voltage range. After propagating and discussing the results with the chip designers, these slight changes are within a safe range and may not affect the CBC performance although this conclusion has to be proven during operation of an irradiated module (CBC&sensor).

Conclusion on the CBCv2

The CMS Binary Chip in version 2 has been studied in detail by the chip designers and at different institutes with the aim to collect any user issues and found problems during operation. Any found issues have to be taken into account in the design and specifications of the third and close to final chip, the CBCv3 which is going to be submitted in 2016.

In a bench-top setup based on the GLIB and CBCv2, the performance of the CBC is reliable before and after irradiation of up to 180 Mrad, which is far beyond the expected dose during the HL-LHC era. Unirradiated and irradiated sensors were read out by the CBC and the results are within the expectations. Due to the fact that the CBC output is purely digital, further studies with enhanced setups are necessary, in particular if the investigation of the efficiency is of interest. These requirements can be fulfilled in a beam test setup.

The CBCv2 was used for operation in 2S mini modules during beam test conditions twice and the results will be discussed in the next chapter.

CHAPTER 10

2S MINI MODULE - BEAM TEST

Within the characterization process of the CBC or rather modules readout by the CBC, measurements and studies during conditions comparable to the future requirements in the tracker are necessary. Therefore, small scale prototype modules were built and investigated in test beam experiments before and after irradiation. 2S small scale modules were built with the dual-CBC2 hybrid which was also used for the bench-top setup as well as sensors from the CNM wafer discussed in the previous chapters.

In this chapter, a short discussion of a beam test at DESY with unirradiated modules built at CERN and the results considering the stub efficiency will be discussed. For the second test beam with irradiated modules, the prototype 2S mini modules were built and calibrated at KIT. The module production, calibration process and the analysis of the test beam data will be shown.

10.1 DESY BT 2013 - unirradiated mini module

The first beam test with 2S p_T modules was conducted at the DESY-II test beam facility [DESb] in November 2013. For this purpose, two prototype 2S mini modules were built at CERN. Each module has been equipped with two small test sensors, each with 254 strips, one module with sensors from CNM and one from Infineon. The sensor for the CNM module was designed and characterized within this study in detail. It is a p-type sensor with p-stop isolation and 90 μm pitch at which the strips are 54 mm long. The thickness is about 270 μm. Hence, the input noise of each CBC channel is in the range of the future full size modules in which the sensors are about 10 cm long but with bisected strips. The frame of the module was constructed such that the separation of the sensors was about 2.75 mm. In order to emulate the CMS 3.8T magnetic field, one module (CNM) was mounted on a rotation stage (device under test, DUT) while the

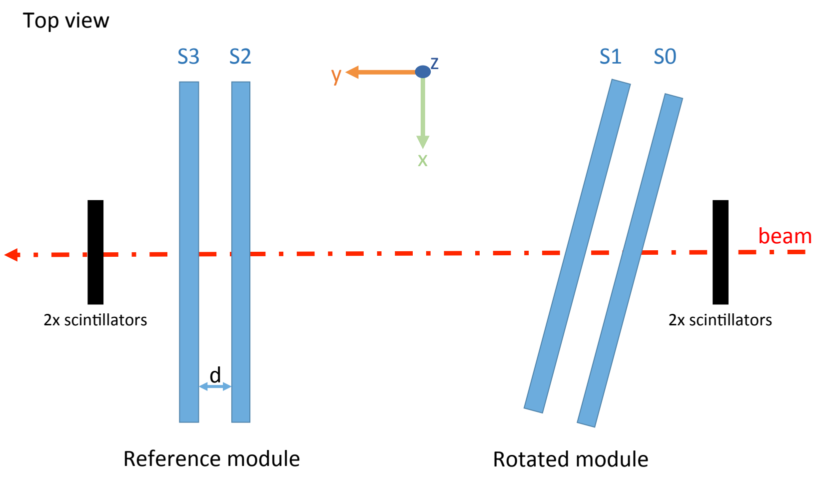

Figure 10.1: Schematic drawing of the DESY TB setup. S0 and S1 are the sensors of the DUT while the S2 and S3 are the sensors of the reference module. The x-y-plane of the coordinate system is horizontal, the z-axis is vertical.

other (Infineon) was placed downstream and perpendicular to the beam and used as a reference. A schematic overview of the module arrangement in the beam is shown in figure 10.1. The strips are oriented along the z axis. As a consequence, the rotation of the DUT module will result in an emulation of the magnetic field respectively the displacement of hits on the S0 and S1 sensor will increase with increasing rotation angle. The cluster width discrimination CWD was set to 3 strips and the correlation window for stubs was set to ±7 constantly.

The correlation of the particle $\mathrm{p_T}$ in GeV/c, the radial position of the module R in m in the tracker, the separation d in μm of the sensors and the stub direction ΔX in μm reads as follows [NÏ14]:

$$\Delta \mathrm{X} \approx \frac{0.6 \cdot R \cdot d}{\mathrm{p_T}}. \tag{10.1}$$

The angle α between the beam direction and the module rotation can be related to the particle $\mathrm{p_T}$ by:

$$\mathrm{p_T} \approx \frac{0.6 \cdot R}{\alpha}. \tag{10.2}$$

Unfortunately, the integration of the available telescope for track building was not successful. Therefore, efficiency studies were conducted by estimating tracks from hits on both DUT sensors as well as on both REF sensors. Basically, for each trigger event in which clusters on the REF planes and on S1 were present, hits within the correlation window of S0 were searched. An overview of the analysis including the DESY test beam facility, calibration of the modules, event reconstruction and analysis can be found in a CMS detector note [HhM14].

Using the event reconstruction mentioned above, the stub efficiency for unirradiated modules was calculated assuming a radial position of the module of 75 cm in the tracker barrel and is

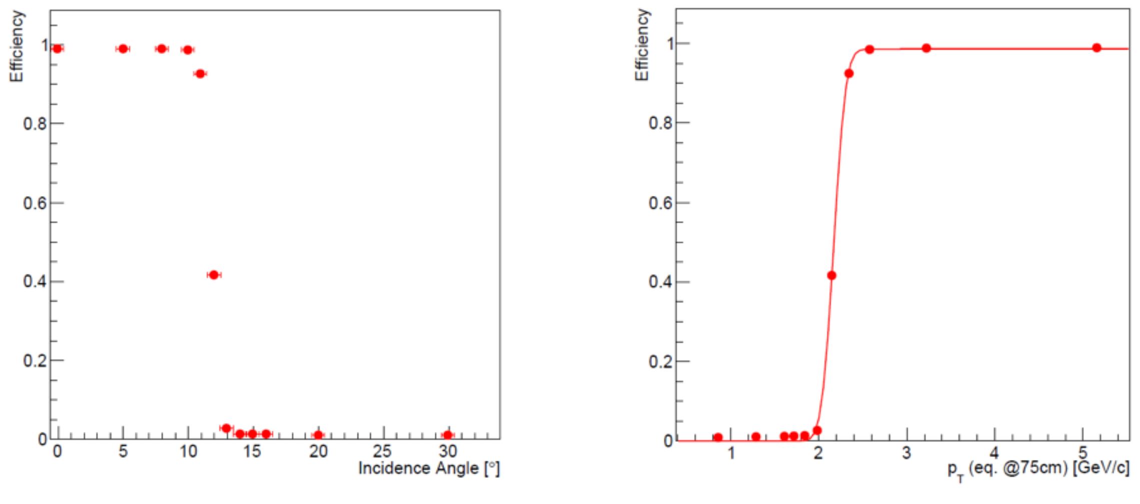

(a)

(b)

Figure 10.2: The stub efficiency of the 2S mini module as function of the beam incident angle (a) and for a calculated p_T at a radial distance of R=75 cm in (b). (With courtesy to M. Pesaresi)

shown in figure 10.2. For this module separation and strip pitch, the equation 10.2 predicts a p_T selection of 2.1 GeV/c with a 0.1 GeV/c resolution. Here, the efficiency was defined as the presence of stubs divided by the number of selected events. Below 10°, the module shows an efficiency of 99.5%. For angles higher than 12°, no stubs are produced by the CBC correlation logic because the displacement of hits between the bottom and the upper sensor is greater than 7 strips. From this point of view, the CBC stub finding logic seems to work efficiently, although an integration of straight telescope tracks would result in a more accurate analysis.
All information about the hardware, the DAQ and the analysis considering the first time test beam measurements of 2S mini modules were collected by the system working group and the publication is scheduled for early 2016.

10.2 SPS TB 2015 - irradiated mini module

A second test beam with 2S mini modules was executed as a collaborative effort within the system working group. The main aim was to study the performance of such p_T trigger modules after irradiation. Furthermore, a successful telescope integration in order to perform reliable efficiency studies was desired. In addition, gaining experience with the data aquisition system (DAQ) which was developed to be as close as possible to the future module readout was necessary in order to study the integration of the modules into the CMS readout system.
The tasks (module, DAQ) for the preparation of the test beam were distributed amongst the system test collaborators.
The SPS irradiation facility [SPS] at CERN was chosen due to the higher beam energies. In this

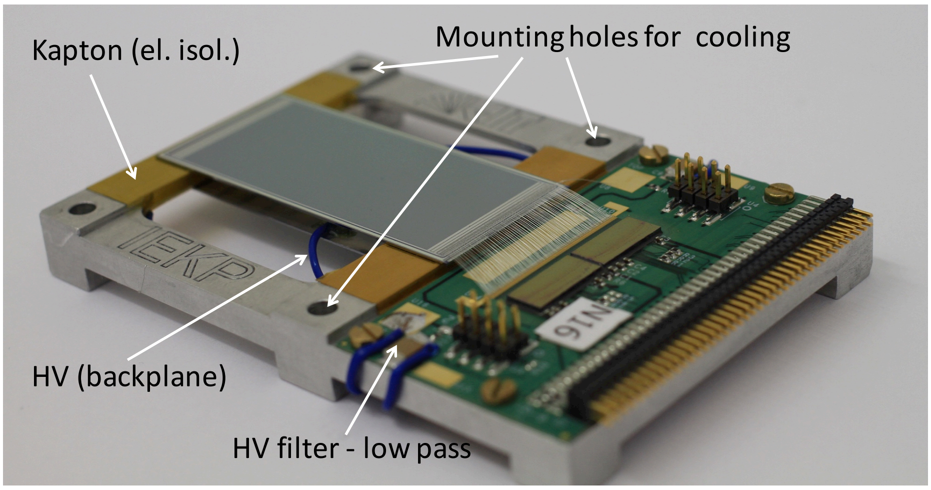

Figure 10.3: Picture of the irradiated 2S mini module for the SPS test beam. An aluminum frame was chosen to assure a good thermal conductivity. Kapton foil was used to isolate the sensors high voltage at the backplane from the aluminum frame.

test beam, a 120 GeV pion beam (compared to a 4 GeV electron beam at DESY) was available. Furthermore, the same EUDET/AIDA telescope [Rub12] as at the DESY test beam facility is present in the SPS beam area. Hence, lessons learned from the missed telescope integration during the DESY TB were used to successfully integrate the telescope this time.

10.2.1 Irradiated 2S mini module

At KIT, a modified design of the 2S mini module was developed. This was necessary due to the fact that the required cooling to about $T = -20°C$ of the existing mini modules which were studied in the DESY TB 2013 was not possible due to the module frame layout. This means that no opportunities of applying cooling contacts to the frame were given. As the modules are fragile, no subsequent frame modifications could be made. Before the assembly of the new mini modules, both the dual-CBC2 hybrid and the sensors were irradiated. The sensors were irradiated to the expected fluence (plus safety margin) of $\Phi = 5 \times 10^{14}$ $n_{eq}cm^{-2}$ protons. The dual-CBC2 hybrid was irradiated with protons at KIT as well to $\Phi = 2 \times 10^{14}$ $n_{eq}cm^{-2}$. This fluence using 23 MeV protons can be calculated to an equivalent dose of 30 Mrad, which is the expected dose after 3000 fb^{-1}.
A new aluminum frame was designed, which is mountable to a cooling plate flooded by C_6F_{14} fluid during the test beam. The separation of the sensors was chosen to be 2.5±0.05 mm. In figure 10.3, one of the new mini modules build at KIT is shown.
Preparatory test at KIT were performed in order to check whether the new frame design and the challenging wire-bonding of both sensors to one hybrid were successful. The channels of the CBCs are connected alternatingly in order to allow a correlation of hits on the two sensor layers. The mapping of the channels, which is important for the analysis, is shown in figure 10.4. For

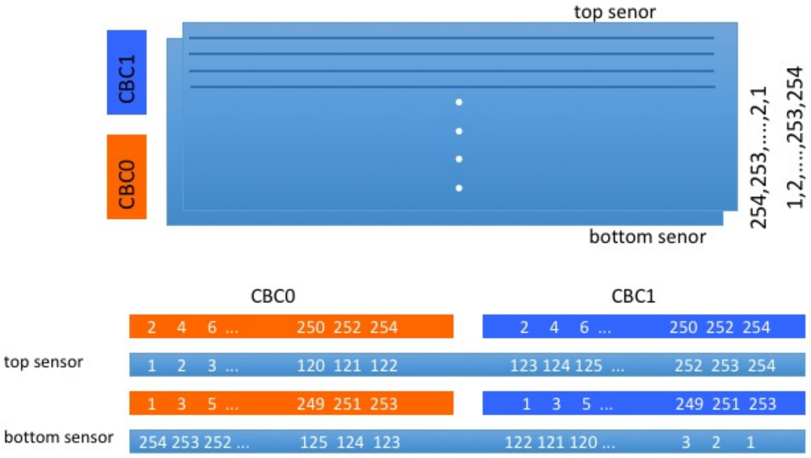

	CBC0	CBC1
	2 4 6 ... 250 252 254	2 4 6 ... 250 252 254
top sensor	1 2 3 ... 120 121 122	123 124 125 ... 252 253 254
	1 3 5 ... 249 251 253	1 3 5 ... 249 251 253
bottom sensor	254 253 252 ... 125 124 123	122 121 120 ... 3 2 1

Figure 10.4: Mapping of the channels of the 2S mini module.

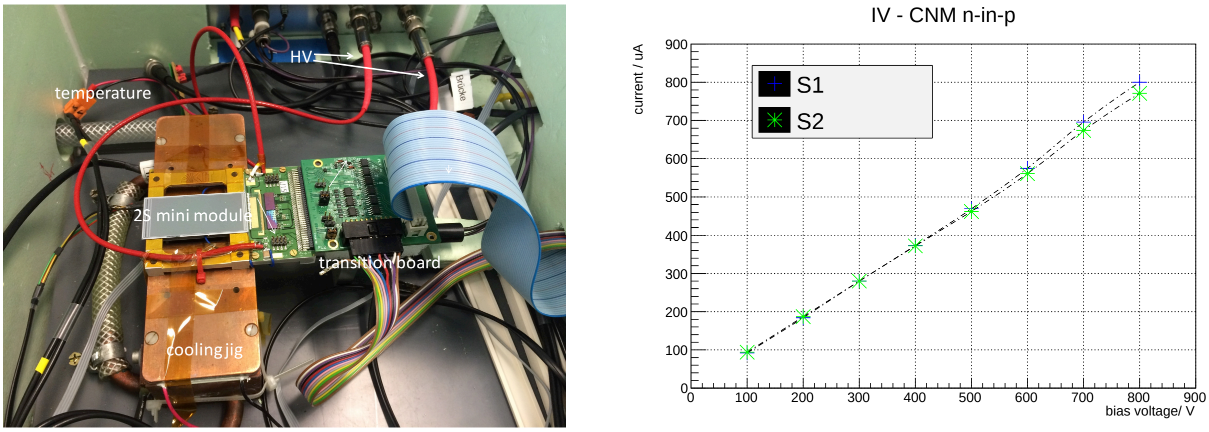

(a)

(b)

Figure 10.5: Cooling test of the 2S mini modules for the SPS TB. In (a) the test box with the module is shown and in (b) the results of the IV characteristics ($T_{\text{coolingjig}} = -20°C$).

preliminary tests in the lab, the module was placed into an aluminum box equipped with a cooling jig. The box was flooded with dry air in order to lower the dewing point below the measurement temperature of T= −20°C. The setup is shown in figure 10.5(a). The resulting IV curves of the sensors on the module after an irradiation of $\Phi = 5 \times 10^{14}$ $n_{eq}cm^{-2}$ is shown in figure 10.5(b). For a bias voltage of 600 V, the sensor power is about 350 mW each (S1 and S2) and about 640 mW at 800 V. These values are within the specifications on the maximum currents and the chiller capabilities during the test beam.

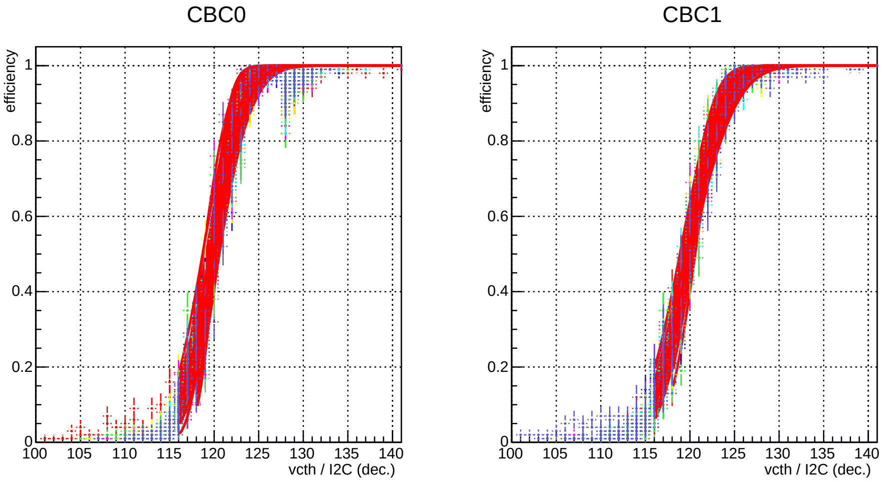

Figure 10.6: S-curves after calibration of the 2S mini module with irradiated sensors.

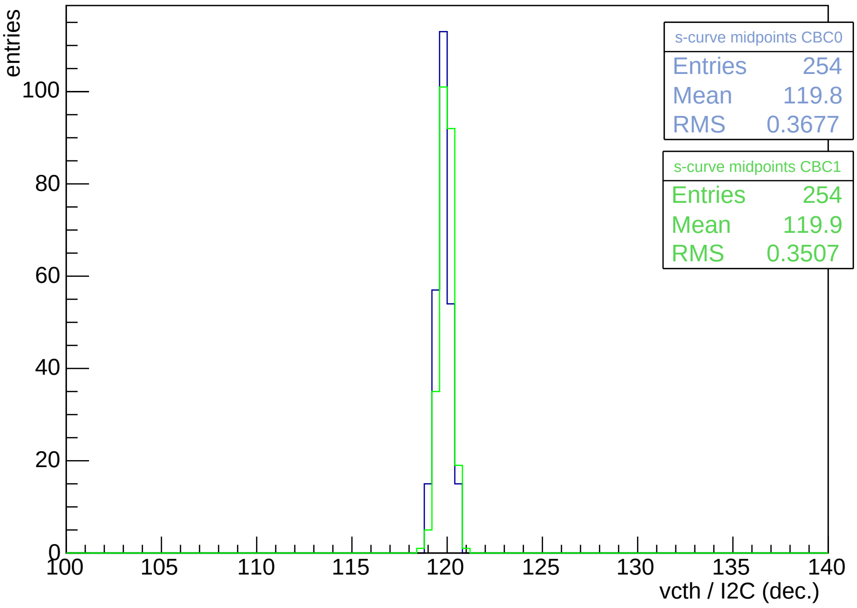

Figure 10.7: S-curves midpoint distribution after calibration of the 2S mini module with irradiated CNM sensors.

10.2.2 Calibration

The modules were calibrated with the CBC bench-top setup. The s-curves are plotted for all channels on both CBCs in figure 10.6 for the CNM module.

The shape of the s-curves shows that all channels on both CBCs and sensors were wire-bonded successfully and no bad channels on the sensor are present. The latter would be visible by a

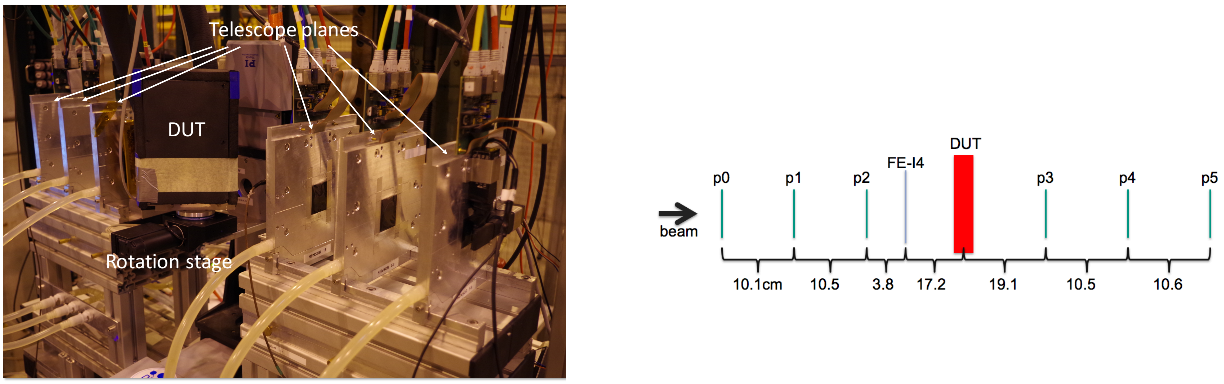

(a)

(b)

Figure 10.8: Test beam setup at SPS. In (a), the telescope with the mounted module on a rotation stage is shown. In (b), a schematic drawing of the telescope planes and the DUT arrangement is shown.

broadening of the s-curve due to increased noise. In figure 10.7, the midpoints or rather the inflection points of the fits to the s-curve were extracted and plotted. Also, after irradiation the calibration procedure works well and a calibration to Vcth=120 I^2C units resulted in a RMS of 118 electrons for the CBC0 and 113 electrons for the CBC1 (compared to about 80 electrons before irradiation).

10.2.3 Beam test setup

During the beam test, the DUT module was placed an a rotation stage equal to the one used during the DESY test beam inside a cooling box in the EUDET/AIDA telescope. The telescope consists of 6 Mimosa26 pixel chip planes with continous rolling shutter mode and is used to build tracks for a more sophisticated data analysis. A picture of the setup with the mounted module and a schematic drawing of the telescope planes and DUT arrangement is shown in figure 10.8. In addition, upstream to the DUT, an ATLAS FE-I4 trigger plane [OBH$^+$14] was placed as a reference due to the multiplicity of tracks in one telescope readout frame (up to 8 tracks). In order to match the correct track of the telescope to the corresponding hit on the DUT, a simultaneous hit on the FE-I4 within the CBC and the GLIB readout cycle respectively is required.

The hardware was comparable to the bench top setup. One GLIB was used to process the CBC data coming from the module via the Bristol FMC and handling the trigger signal distributed by the trigger logic unit (TLU) [Desa] in a simple handshake mode via the DIO5 FMC. The TLU is provided by the EUDET/AIDA telescope and distributes trigger signals and timestamps to all telescope planes and the DUT/FE-I4, if a coincidence on all 4 scintillators (2 upstream, 2 downstream, see figure 10.1) appears.

During the beam time of 4 days 158 runs were recorded. Here, also commissioning runs like

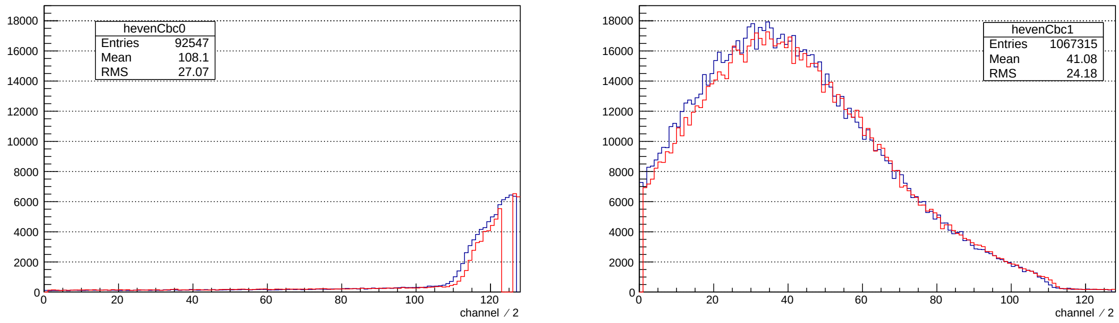

(a) (b)

Figure 10.9: The beam profile distribution on the DUT for (a) CBC0 and (b) CBC1.

data latency, stub latency and threshold scans are included. For the analysis, 75 physics runs are available, which cover threshold scans, angular scans and high statistics runs. The CBC raw data was converted after recording via a CMSSW-based unpacker into EDM [EDM] root files, which contain commissioning and event data.

10.2.4 Analysis

During the test beam, besides some basic data quality plots, no analysis was performed. A joint analysis working group within the system test working group formed after the test beam in order to analyze the test beam data.

Unfortunately, by simply plotting the occupancy of all channels for each CBC which reflects the beam profile in figure 10.9, one can see that the downstream sensor (red line in the figure) detects less hits than the upstream sensor. In the case of the shown figure, a threshold of 28 I^2C units corresponding to about 9000 electrons was set and the sensors were biased with 800 V and at 0 degree angle. Summing up all hits on both sensors, with respect to the number of triggers received, the upper sensor shows 4.3% fewer and the bottom sensor 8.9% fewer entries than expected. In figure 10.10, the hit efficiency for a run at the same conditions but fewer events is plotted. Det0 is the upstream sensor of the module and det1 the downstream sensor. Although the module was penetrated by the beam perpendicularly, only in 73% of the events hits on both sensor layers are detected. Also, the efficiency of the two sensor layers varies. This behavior was checked by several different group members who scripted individual codes in order to exclude any mistakes in the common analysis code developed by the working group with the same result. So far, there is no clear explanation for this issue. One possibility which is under investigation is the threshold set. The nominal comparator threshold of 6000 electrons for the 2S modules was not used but instead the lowest threshold was set to 9000 electrons (but a few additional runs towards the end of the TB). The reason for this choice are the random ghost hits of the CNM sensors after irradiation, see chapter 8.2. A threshold scan was performed in the lab and during

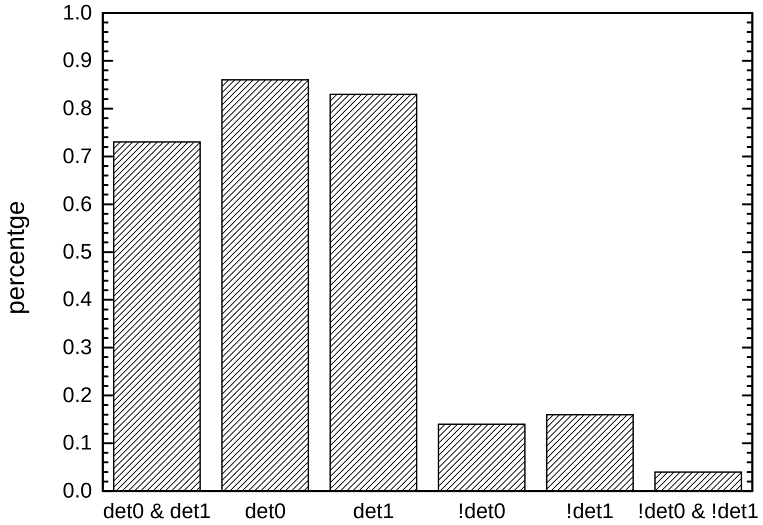

Figure 10.10: Hit efficiency of a 0 degree run at 800 V. Det0 marks the upstream sensor and det1 is the downstream sensor of the CNM module.

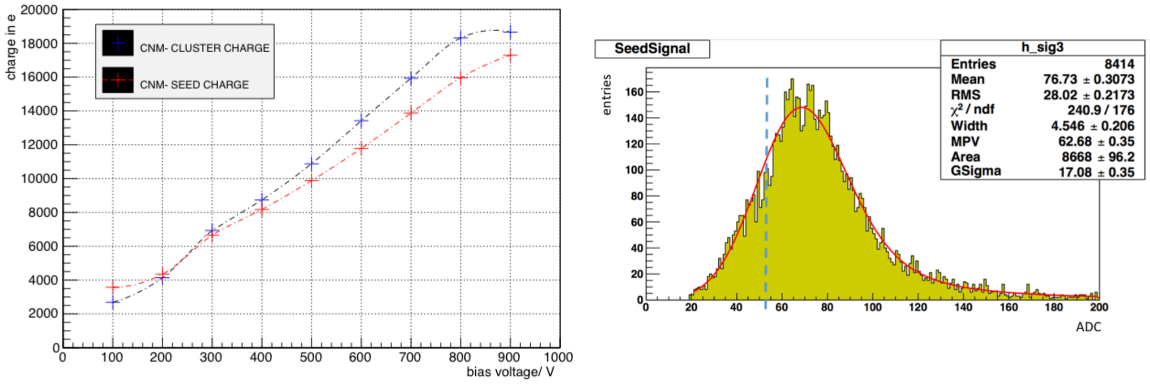

(a) (b)

Figure 10.11: Charge collection as a function of the bias voltage for an irradiated CNM sensors used for the 2S mini modules measured in the lab. $\Phi = 6 \times 10^{14}\ \mathrm{n_{eq}cm^{-2}}$ (20% higher than the fluence of the test beam sensors).

the test beam with the result that at the nominal threshold of 6000 electrons hits on the modules appeared, although no source/beam was on. By increasing the threshold to 9000 electrons, this effect was suppressed and a reliable distinction between real hits and no hits is possible during the analysis without taking the track reconstruction from the telescope into account.

The charge collection for these sensors measured with the analogue Beetle chip predicts the MPV

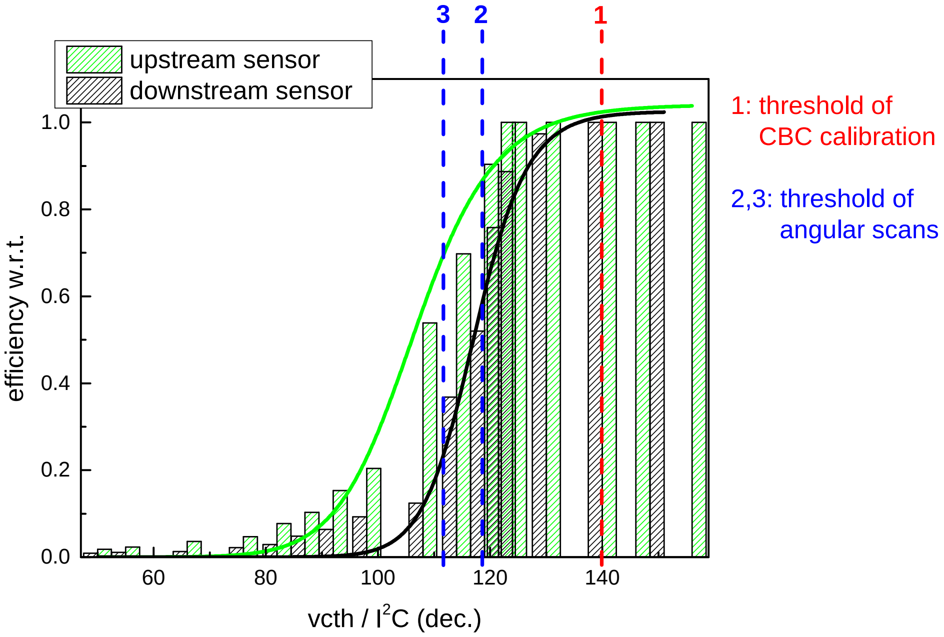

Figure 10.12: Hit efficiency as a function of the threshold of a 0 degree run at 600 V.

of the seed charge at 800 V to about 16000 and at 600 V about 12000, see figure 10.11(a). But on the other hand, the left part of the Landau signal distribution for low energy deposition is cut away by the threshold of 9000 electrons. This effect is indicated by the blue line in figure 10.11(b) for the CNM sensors at a bias voltage of 600 V.

The result on the hit efficiency as a function on the threshold set to the module is plotted in figure 10.12. The CBCs were calibrated to a value of 140. The measurements for the angular scans were performed either at a threshold of 112 corresponding to about 9000 electrons or for a few runs at 119 corresponding to 6800 electrons (accepting RGHs).

The resulting difference between the different efficiencies of the two sensors in one module still can not be explained. A possible reason might be a slightly different fluence for both the sensors during the irradiation. One of the CNM sensors broke during the gluing to the 2S mini module frame and as a consequence a third sensor had to be irradiated which might lead to a different fluence. A further hint on this assumption is that during the DESY BT with the unirradiated modules such behavior was not observed with such significance[1].

In order to check whether the correlation logic of the CBC works also after irradiation reliably, the stub bit generation was studied too. The stub analysis was reconstructed offline. The expectations were compared to the stub word. The stub word contains the stub bits for each CBC and in case of a stub also the information on the hit location (strip/channel number). Following

---

[1] There have been events with different efficiencies on both layers but in less than 1% of the recorded events.

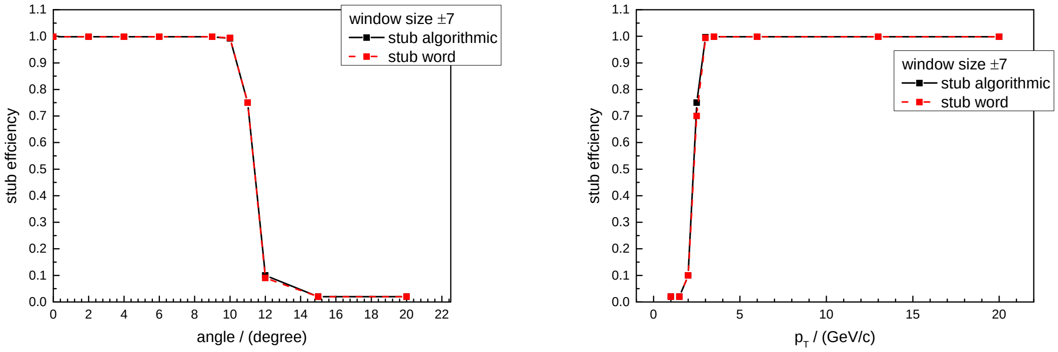

(a)

(b)

Figure 10.13: Stub efficiency as a function of the rotation angle (a) and the calculated p_T discrimination in (b) for a radial module position of R= 60 cm.

the stub reconstruction analysis of the DESY test beam data, several requirements have to be fulfilled:

- for the stub efficiency, at least one hit in each sensor layer must be present
- a cluster in the upstream sensor is matched with a cluster in the downstream sensor with the window size of ±7
- for several adjacent hits in one event, the cluster position is defined as $X = \left(\frac{strip_{first} - strip_{last}}{2}\right)$
- clusters >3 strips are rejected due to the CWD as this is related to low momentum particles (a change of the programmable CWD was not investigated during the BT)
- the window size of ±7 is in case of clusters on both sensors calculated from the location of the upstream cluster position $X_{upstream}$, hence $\Delta X = \pm 7 = X_{upstream} - X_{downstream}$
- the algorithmic stub efficiency is defined as the number of events with at least 1 stub, when there are clusters present on both sensor layers divided by the number of events with at least 1 cluster on both sensors

Taking these requirements into account, the stub efficiency was calculated as a function of the angle and compared to the stub word information. The result is shown in figure 10.13(a). By rotating the module, at an angle of 10 degrees the stub efficiency starts to drop for both the algorithmic definition as well as the stub word information. The latter means that no stub bits are recorded any more at angles higher than 12 degrees, hence the correlation logic seems to work well if the definitions and requirements listed above are obeyed during the offline reconstruction. Now assuming a magnetic field of 3.8 T and a radial distance of the module at 60 cm (the inner 2S

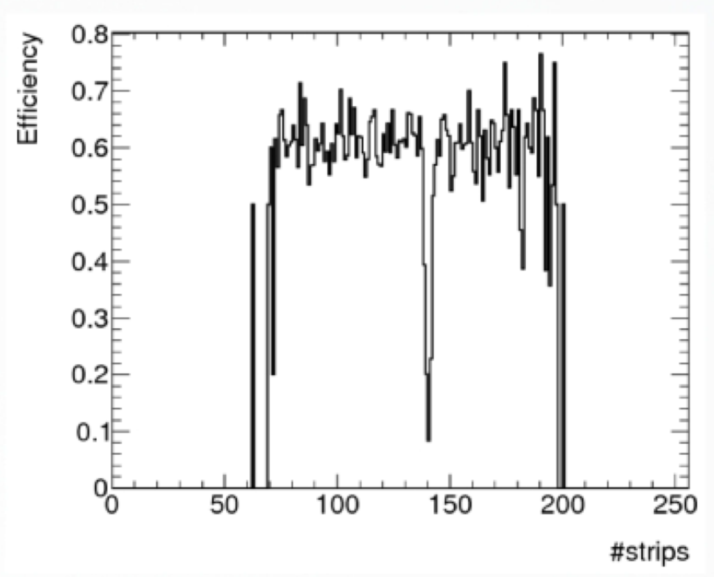

Figure 10.14: Stub efficiency with matched telescope tracks for an angular scan with a threshold of 9000 electrons at 600 V. (With courtesy to K. Skovpen and N. Chanon.)

module) and the sensor separation d, the angular scan can be translated into a p_T discrimination following the relation

$$\phi = arcsin\left(\frac{d}{2\cdot R}\right) \quad \text{with} \quad R = \frac{p_T}{0.3\cdot B}. \tag{10.3}$$

Under this assumption, from figure 10.13(b) one can see that the p_T discrimination rejects particles with a transverse momentum of about 2 GeV, leading to a significant data reduction, as simulated in 3.3.

As an example the real stub efficiency was analyzed by taking the track information of the telescope into account. The definition of the efficiency, in this case, is the presence of a stub matched to a telescope track divided by the presence of a track, and is shown in figure 10.14. The low efficiency of about 70% is directly related to the low efficiencies due to the chosen threshold of the comparator ($\approx$ 9000 electrons) for the angular scans.

Conclusion on the 2S mini module test beam results

The work presented in this chapter is the result of the efforts of the system test working group with several participating institutes. The first time test beam at DESY with unirradiated p_T discriminating mini modules proved the concept of the correlation logic of the CBC. Unfortunately, an integration of the telescope tracks due to synchronization problems was not possible, hence the efficiency studies have to be made purely algorithmicly. Nevertheless, the results are highly promising and it seems that the 2S module concept can lead to a successful trigger decision contribution after the Phase II Upgrade of the CMS Tracker.

The second test beam with irradiated mini modules (sensors and chips) at the SPS accelerator at CERN was a success, too. It was possible to synchronize the telescope and the DAQ, based on XDAQ. The readout chain was developed to be as close as possible to the final CMS Tracker DAQ and worked reliably during the data taking. Due to the characteristics of the silicon sensors which show random ghost hits after irradiation, the threshold was increased by 3000 electrons compared to the nominal threshold of 6000 electrons to 9000 electrons, in order to suppress the appearance of the RGHs. Although the fluence of $\Phi = 5 \times 10^{14}$ $n_{eq}cm^{-2}$ is not critically high, one can see how the comparator threshold affects the overall trigger module performance in particular the hit efficiency. As a direct consequence of this finding, the system test group decided to repeat the test beam with an irradiated module in 2016, in order to study in detail the performance as a function of the threshold at which the threshold has to be increased smoothly in 1 I^2C units which corresponds to approximately 300-350 electrons per unit. The analysis of the second test beam at SPS is still ongoing. This is necessary as, for instance, the mentioned software tkLayout relies on the recorded data from these test beams. The software is able amongst others to predict the perfomance of the whole future tracker in dependence on its layout. For this purpose, for instance the binary cluster widths have to be digitized and implemented in the software which will be provided by the test beam data analysis working group.

CHAPTER 11

SUMMARY AND OUTLOOK

Within this thesis, several studies with respect to the planned CMS Phase II Upgrade in 2024 were conducted. The future increased luminosity of the HL-LHC to about 5×10^{34} cm^{-2}s^{-1} with an energy of 7 TeV per proton beam ans 10 years of operation will lead to a challenging radiation environment for the experiments. Besides the increasing demands on radiation hardness of the silicon detectors and subdetectors, in particular the granularity of the CMS tracker has to be increased in order to cope with the higher expected particle track densities. Furthermore, in order to process the enormous data amount out of the tracker for further processing, a new binary readout of the new trigger module concept is the current baseline. The latter allows a contribution of the tracker to the Level-1 trigger decision by correlation of hits of two stacked sensors per module. For this purpose, a new binary chip is under development which has to fulfill the requirements of holding a correlation logic and radiation hardness.

In the first part of the analysis the radiation hardness of silicon strip and macro-pixel sensors was studied. Several silicon sensor irradiation and measurement campaigns were conducted within the CMS Tracker and the RD50 collaborations. Extensive studies on the radiation hardness for a fluence of up to $\Phi = 1.5 \times 10^{15}$ $\mathrm{n_{eq}cm^{-2}}$ for the inner modules at large pseudorapidity η equipped with strip sensors in the future tracker led to the decision to build the entire tracker with $\mathrm{n^{+}}$$-in-$p silicon sensors. The main reason is the fact that this type of silicon detectors retains a higher charge collection due to the higher mobility of electrons and as a consequence less trapping compared to the hole readout in n-type detectors.
Unfortunately, $\mathrm{n^{+}}$$-in-$p detectors have the disadvantage of a necessary additional isolation of the readout strips in order to avoid short circuits of the strips due the buildup of an accumulation layer as a consequence of the positive oxide charge at the sensor surface. The isolation is a

limiting factor of studied p-type detectors and has to be optimized in order to ensure a satisfactory strip isolation independent of the fluence and at the same time no negative influence on noise and break down characteristics. The pattern as well as the doping concentration and depth of the isolation dopants affect the overall sensor performance due to the the electric field strength and distribution. Measurements of silicon sensors produced with different isolation characteristics and vendors accompanied by T-CAD simulation studies were performed. In particular the latter was of great importance in order to understand and to describe the effects observed during the measurements. The isolation technique which seems to be most promising as a result of several investigations amongst different experiments is the p-stop atoll isolation, which is an individual boron implantation surrounding each individual strip. Simulations were conducted in order to optimize both the pattern as well as the doping characteristics which has not been studied in detail so far within the CMS Tracker collaboration. As a result of the simulations, the p-stops should be implanted in the center of adjacent strips while the p-stop doping concentration should not exceed the value of 2×10^{16} cm^{-3} and a depth of 2.5 μm. These values, assuming a gaussian shape of the p-stop implants, is equal to a surface projected charge of 1×10^{12} cm^{-2}, which is equal to the positive oxide charge. Three different wafers for submissions with three different vendors were designed by the author. On each wafer, the same test sensor designs were placed in order to guarantee the comparability of measurement results. The submissions basically differed in the doping characteristics which covered both the range expected to be radiation hard and the range which simulations would exclude. Experimentally obtained results before and after irradiation of the test sensors matched the predictions from simulations with remarkable precision. Also, the effect of random ghost hits, observed for the first time in p-type detectors, could be observed for sensors with p-stop doping concentration higher than 3×10^{16} cm^{-3} as predicted and understood with the help of T-CAD studies. Finally, the p-stop characteristics ensuring a good strip isolation and high breakdown voltages showing no random ghost hits were defined.

For the first time, macro-pixel prototype sensors for the PS trigger modules were designed with respect to the constraints on the bump pad layout provided by the CERN CMS electronics group. The experience from T-CAD simulations and measurements directly influenced the sensor layout. The sensors were qualified on their electrical properties and charge collection efficiencies before and after irradiation of up to $\Phi = 2 \times 10^{15}$ $\mathrm{n_{eq}cm^{-2}}$, which is two times the expected fluence after 3000 fb^{-1} at HL-LHC conditions for the most exposed modules. In spite of the high radiation level, the sensors behave well considering the breakdown voltage and charge collection and fulfill the ambitious requirements for the Phase II Upgrade. With respect to the strip isolation study, the p-stop isolation with a peak doping concentration of 1×10^{16} cm^{-3} and 1.5 respectively 2.5 μm was chosen for the submission and the results confirm both the simulation predictions and measurement outcomes of the silicon strip detectors investigated in the isolation study.

With respect to the demand for a higher granularity for a reliable reconstruction of tracks in a dense particle environment, the FOSTER (A Fourfold Strip Sensor with Readout at the Edges) with fourfold segmentation was developed within the IEKP CMS hardware group at KIT. The first prototypes of the FOSTER showed undesired signal coupling to the routing lines running between collecting electrodes. The effect was studied in detail with help of T-CAD simulations with the proposal to implant additional boron material below the routing lines in order to avoid the coupling. The boron implantation acts as a strip isolation and simultaneously redirects the electric field below the routing line. The latter repels drifting electrons towards the readout electrodes and no induced signals on the routing line are observed anymore. Though this type of sensor exceeds the demands of CMS with respect to the granularity, the FOSTER might be a promising candidate for future detectors present in high particle density experiments. Further simulation and measurement studies have to be performed.

Although the results from the simulations and measurements of the irradiation study for different sensor concepts match very well, the radiation damage model for T-CAD studies has to be improved. Especially the evolution of the surface damage as well as the annealing behavior of bulk and surface damage have to be parametrized and also the range of the fluence should be extended. The latter is particularly necessary in order to study the future pixel detector material and sensor layout, which will face a fluence beyond $\Phi = 1 \times 10^{16}\ \mathrm{n_{eq}cm^{-2}}$.
Furthermore, as mentioned, not only the p-stop technique but also the p-spray and a combination of both exist. Studies within the RD50 collaboration hint on the advantageous radiation hardness of the p-stop technique but no process variations of the p-spray comparable to the study discussed in this study were performed. Hence, submissions with known p-spray characteristics might be of interest in order to compare the different techniques, especially with respect to the Phase II pixel detector, which probably will also be built of p-type detectors but facing significantly higher radiations and less space for p-stop structures between pixels.

Not only the sensor material and layout for the Phase II Tracker changes but also the module concept. In the future, the tracker must contribute to the Level-1 trigger decision, therefore the trigger relevant data must be transmitted from the modules at 40 MHz. In order to cope with the huge data rate, particles with low transverse momentum which are attributed to non-interesting physics are rejected online, leading to significant data reduction. The rejection is achieved by correlation of hits on two stacked sensors which are both connected to one chip, the CBC. Depending on the track curvature and the resulting hit displacement on the second sensor with respect to the first sensor, the transverse momentum can be determined. A setup based on the CBC readout has built and measurements of silicon strip sensors before and after irradiation were done. The calibration and the response of the individual channels performs as expected. The gain of the bench top system was identified by measurements with known charge pulses. The setup is now ready and can be used in order to compare the signal detection of the binary chip with the expectations from measurements with analogue readout.

The trigger module concept was implemented in the smallest possible scale, consisting of two test sensors with 5 cm strip length and dual-CBC readout. After a first beam test experiment with unirradiated sensors and chips with confirming results of the low p_T particle discrimination, additional 2S mini modules were built. The hardware components (CBCs and sensors) were irradiated to the expected fluence and dose after 10 years of operation with 50% safety margin. The irradiated mini module was tested in a second beam test in order to check whether any discrepancy in comparison to the unirradiated module appears. The threshold had to be increased from the nominal 6000 electrons to approximately 9000 electrons due to the sensors which show random ghost hits after irradiation as a consequence of the high p-stop doping concentration. With this setting, the hit detection was not 100% efficient during the angular scan, hence an absolute module efficiency study could not be realized. By applying algorithmic boundary conditions to the data during the analysis, the stub finding logic was proven to work as expected. Nevertheless, a final conclusion on the module performance after irradiation cannot be drawn and a further beam test with the same physics program and irradiated 2S mini modules is scheduled for the year 2016.

Part III

Appendix

APPENDIX A

APPENDIX A

A.1 Particle identification in the CMS detector

Figure A.1 is a slice of the CMS detector showing a colorful cross-section of the different subdetectors. Depending on the charge, momentum and mass of the particles, they are bent more or less and absorbed by different subdetectors. The identification of the particles is determined by the tracks and energy deposition in the tracker, calorimeters and muon chambers.

By traversing the detector, charged particles leave ionization along their paths which are measured and reconstructed with the help of the tracking detector. By applying a strong magnetic field, it is additionally possible to easily determine the sign of the charge in dependence of the bent direction. The basic types for charged particles are $e^{\pm}$, $\mu^{\pm}$, $K^{\pm}$, $\pi^{\pm}$ and $p^{\pm}$ with typical momenta of 2-50 GeV.

Neutral particles like photons above 50 MeV, Neutrons and K_L^0 are detected by measuring the energy showers they deposit in the electromagnetic and hadronic calorimeters. Some neutral particles are detected by measuring their stable decay products. Te these belong the $K_S^0 \to \pi^+\pi^-$, $\Lambda \to p\pi^-$ and $\pi^0 \to \gamma\gamma$.

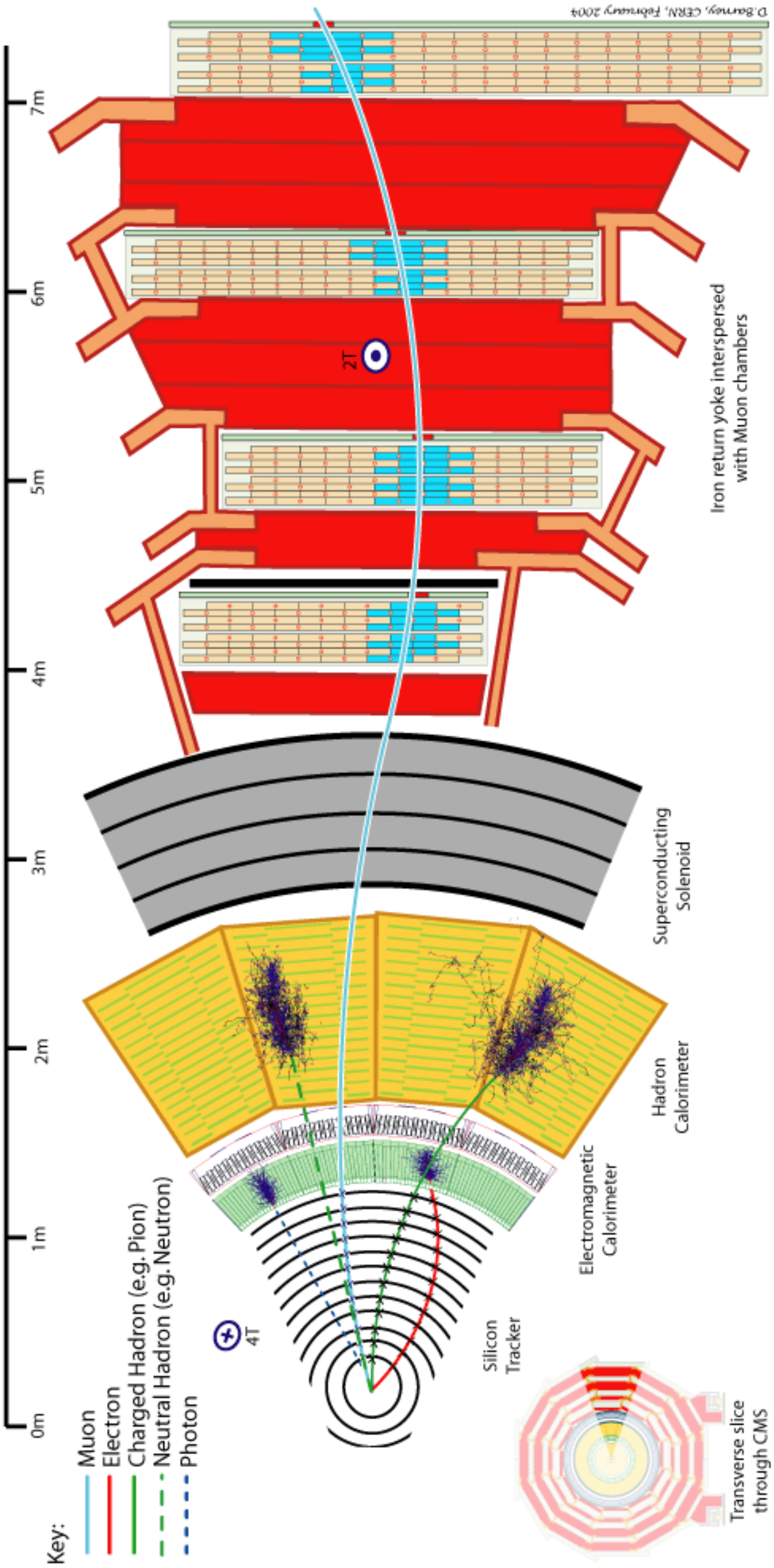

Figure A.1: Slice of the CMS detector with included tracks., [Lap10].

APPENDIX B

APPENDIX B

B.1 Wafer processing - exemplary at ITE Warsaw

The processing of silicon detectors for HEP applications is a complex operation with up to several hundreds of process steps. In the following chapter, a brief description of the process sequence is given with no claim on completeness but more to give the reader a feeling of the complexity. The summary is for a p-type sensor and was listed once in [gS12] and was extracted from [Mar05] from the ITE in Warsaw:

- Initially, the silicon wafer is oxidized in a quartz tube by heating in oxygen enriched atmosphere at temperatures of about 1000°C. In this case, the oxide is grown by wet oxidation method. Wet oxidation compared to dry oxidation is much faster and is used for thick oxides. The growing rate is about 400 nm/h, resulting in a density of about 2.18 g/cm^3 [Hil04]. Dry oxidation has a growing rate of about 50 nm/h with a density of 2.27 g/cm^3 and is hence of much higher quality. Growing in pure oxygen results in high densities and high breakthrough voltages, but it is time consuming and is only used for coupling oxides.

- Backside diffusion of boron to form an ohmic contact (p$^+$ highly doped). The diffusion depth depends on the technology. A common diffusion depth is about 6 to 7 μm, but also deep diffusion processes up to several hundreds of μm are possible (used, for instance, during the HPK campaign).

- After diffusion, the dopants have to be activated in the silicon lattice by temperatures above 1000°C.

- Oxide etching for the p^+ outer ring of the sensor, which is floating and avoids high electrical fields inside the crack region which is caused at the sensor edges during the cutting process. It is the first photolitographic step.
- Screen oxidation (dry, about 900°C, 20 nm). This screening oxide serves as a scattering layer for implantation. Thus, the channeling effect is suppressed, which constrains the path of a charged particle in a crystal lattice.
- Again oxidation to protect the wafer backside against doping performed later in processing.
- P+ implantation of the outer ring
- Oxide etching (removing of screening oxide)
- Oxidation wet
- Oxide etching for the p-stop region. Generally, p-stop and p-spray implantation is done before strip implantation. This is a consequence of the thermal budget. The achieved doping profiles of microstrips should be unchanged.
- Screening oxidation
- P-stop implantation
- Removing of the screening oxide
- Oxidation wet
- Oxide etching for the n^+ strips
- Screening oxidation
- N+ strip implantation
- Oxidation wet
- LPCVD[1] for polysilicon layer
- Wet etching to define the bias resistor shape
- Removing of the polysilicon layer from the backside with plasma etching
- Photolitography defining contacts to the resistors
- Annealing in nitrogen to tune the resistivity of bias resistors
- Photolitography defining contacts to the n^+ strips

---

[1] Low Pressure Chemical Vapor Deposition

- Al-Si-Cu sputter deposition on both sides of wafer
- Photolitography to define the pattern of metal layer on front side
- Metal sintering
- APCVD[2] or PECVD[3] (limited conformity and electrical quality) silicon dioxide deposition with D=600 nm to create a passivation layer at about 200°C, oxidation wet in two steps, 250 nm + 150 nm
- Photolitography for opening windows in the passivation layer

In addition, polishing and handling between the steps are done.

---

[2] Atmospehric Pressure CVD

[3] Plasma Enhanced CVD

B.2 ITE wafer

The ITE wafer - 4 inch, p-type substrate, $< 100 >$ lattice orientation, p-stop isolation

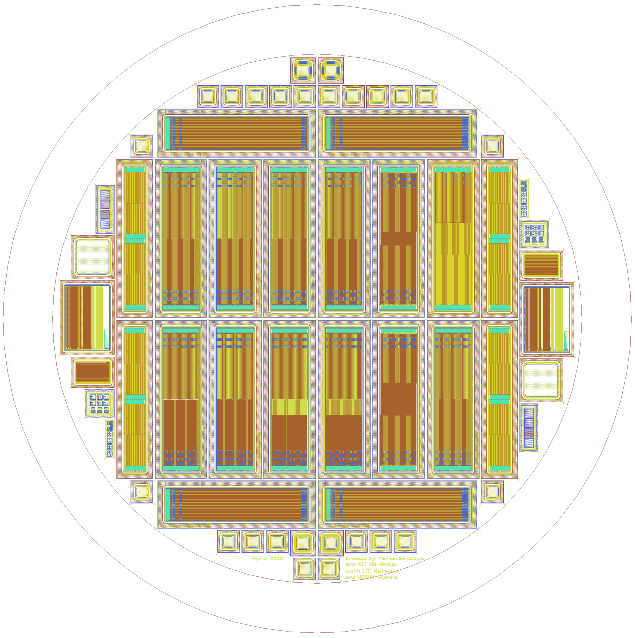

Figure B.1: Final ITE wafer layout

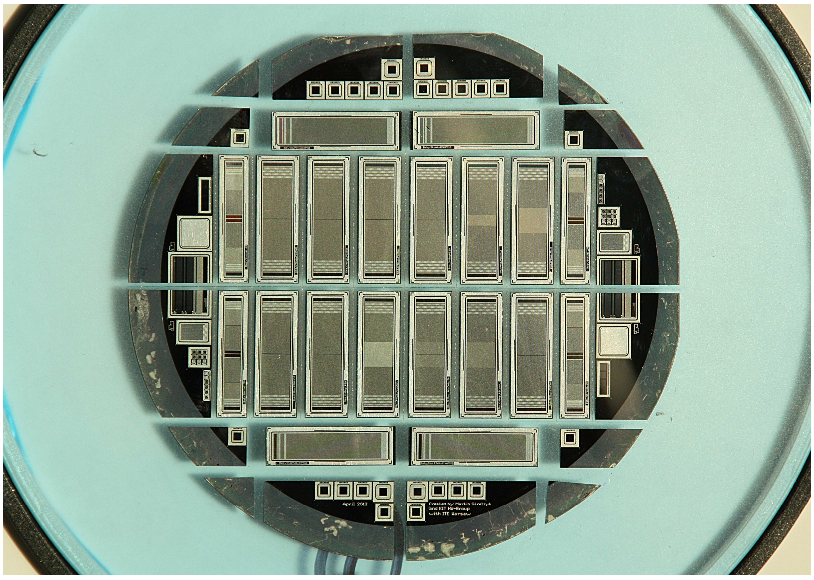

Figure B.2: Final ITE wafer after production and dicing

B.3 CiS wafer

The CiS wafer - 4 inch, p-type substrate, < 100 > lattice orientation, p-stop and p-spray isolation

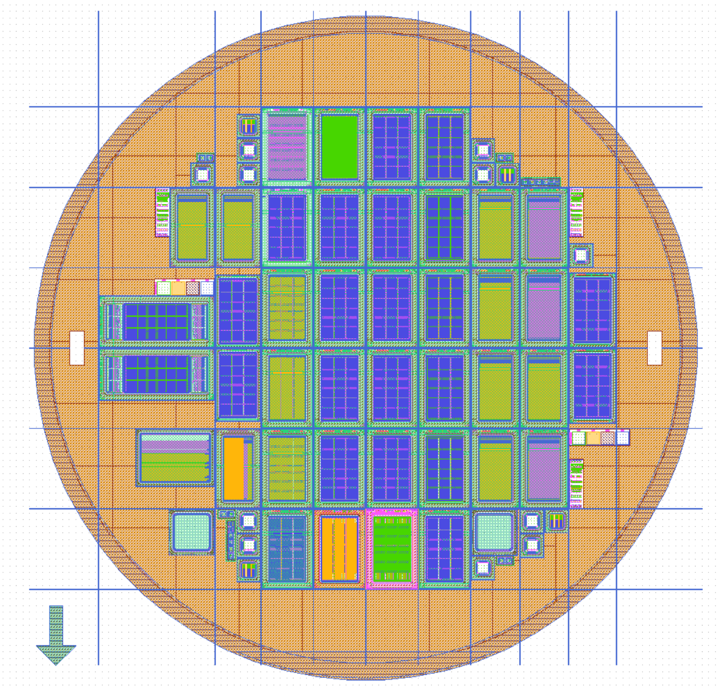

Figure B.3: Final CiS wafer layout

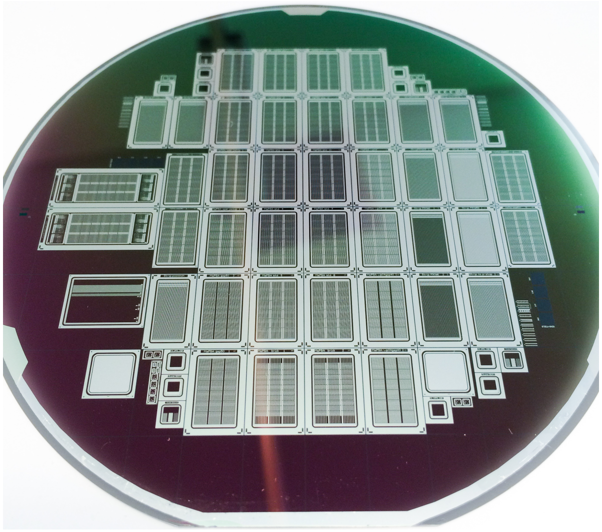

Figure B.4: Final CiS wafer after production and before dicing

B.4 CNM wafer

The CNM Barcelona wafer - 4 inch, p-type substrate, $< 100 >$ lattice orientation, p-stop isolation

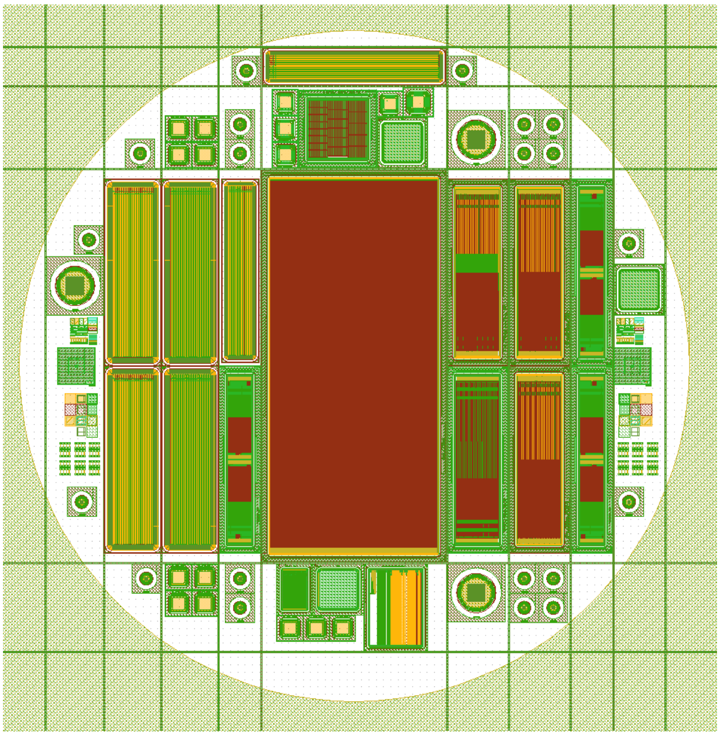

Figure B.5: Final CNM wafer layout

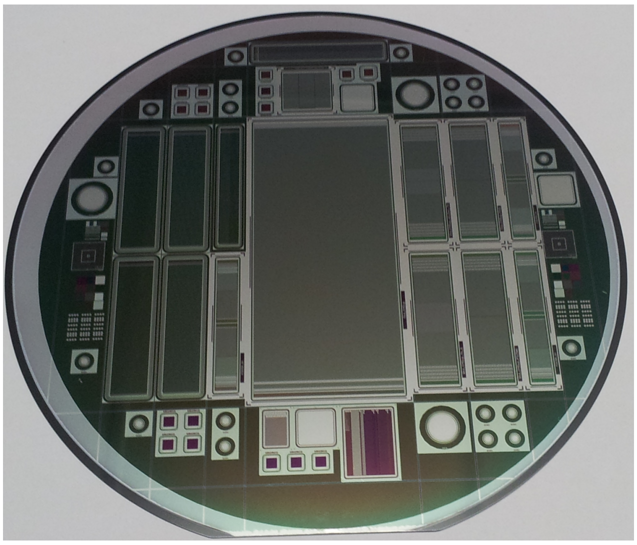

Figure B.6: Final CNM wafer layout after production and before dicing

APPENDIX C

APPENDIX C

C.1 Biasing option for silicon sensors in trigger modules

The p_T discriminating modules described in section 3.2.4 hold besides the functional challenge several mechanical challenges too. One of the latter is the application of the high voltage to the backplane of two stacked sensors in one module in which the backplanes of the sensors are facing each other. Figure C.1 shows an exploded CAD drawing of the current baseline concept of a 2S module (January 26th, 2016). The high voltage will be applied via wire-bonds to kapton foils which

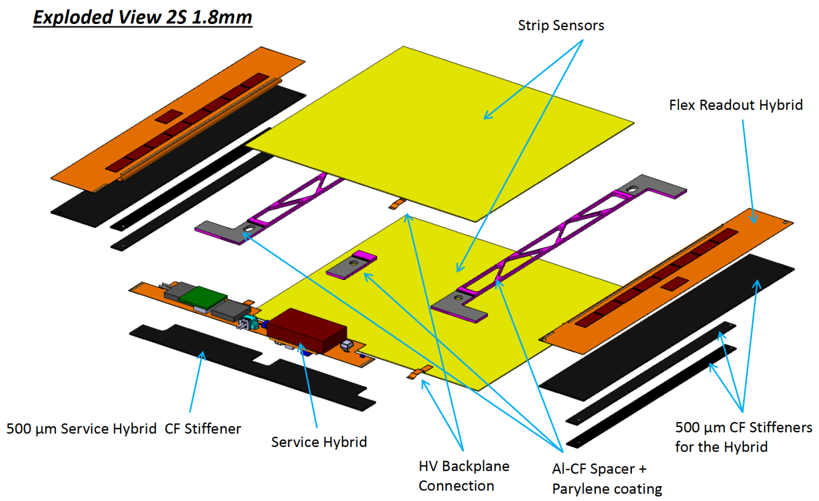

Figure C.1: Exploded view of the 2S trigger module baseline.

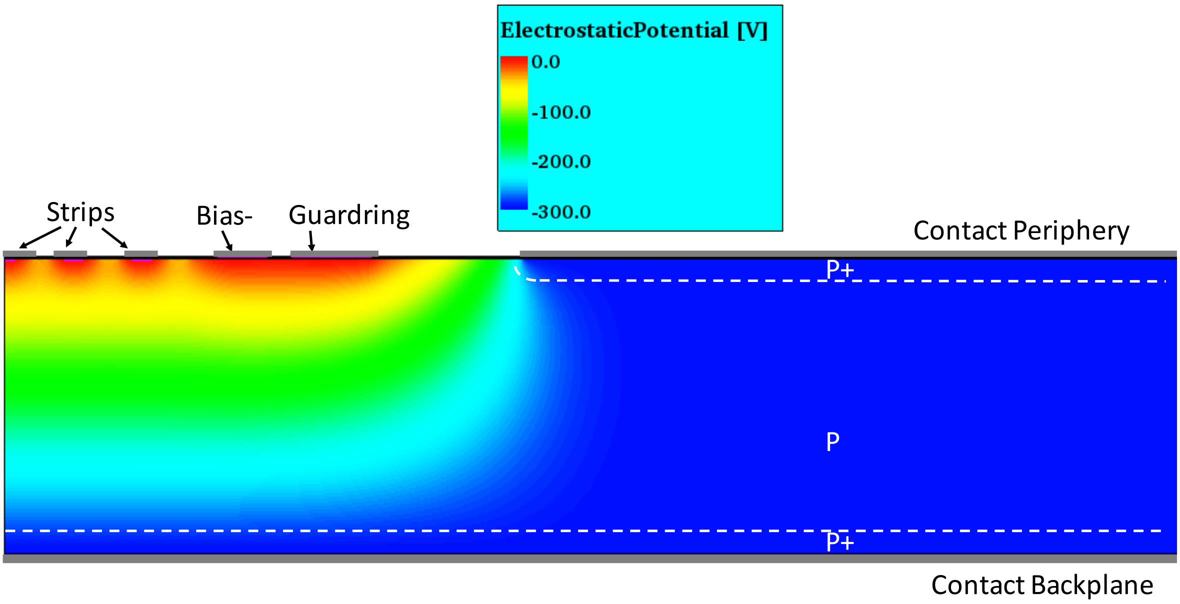

Figure C.2: Simulated potential at the sensor edge. Unirradiated at $V_{bias} = -300$ V and T= 20°C.

in contrary will be glued to the backplane. The tails of the kapton foils will be connected to a HV connector which will be placed on the service hybrid. However, this kind of mechanical solution holds risk of losing the backplane connection during operation besides additional challenges during the module assembly.

A possible alternative to apply the high voltage to the sensor is via its periphery which is on the same potential as the backplane. This is due to the fact that the periphery of a n-in-p type detector is p+ doped in order to avoid currents from the damaged silicon crystal at the sensor edges which is a consequence of the sawing. The potential at the sensor edge as a result from T-CAD simulations is shown in figure C.2. A conducting P+PP+ channel at the sensor edge is present. In order to check the connection of the high voltage via the periphery, additional passivation openings at the sensor surface for some of the productions presented earlier in this thesis have been placed. First samples before and after irradiation have been electrically qualified for their current characteristics and measured on their charge collection as function of the bias option (HV via backplane or via the periphery at the frontside).

One of the main parameter of a silicon sensor is its leakage current which has been measured in the ALiBaVa station for both bias options. Three samples have been measured exemplary so far. The sensors are from a huge measurement campaign and all of n-in-p type. For the first tests irradiated samples have been chosen with irradiation levels of $\Phi = 5 \times 10^{14}$ 1MeV $n_{eq}cm^{-2}$ protons, $\Phi = 7 \times 10^{14}$ 1MeV $n_{eq}cm^{-2}$ and $\Phi = 1.5 \times 10^{15}$ 1MeV $n_{eq}cm^{-2}$ mixed irradiation respectively. The result for this three sensors with different fluence is plotted in figure C.3. No significant changes for the different bias options have been observed. From this point of view, applying the bias voltage

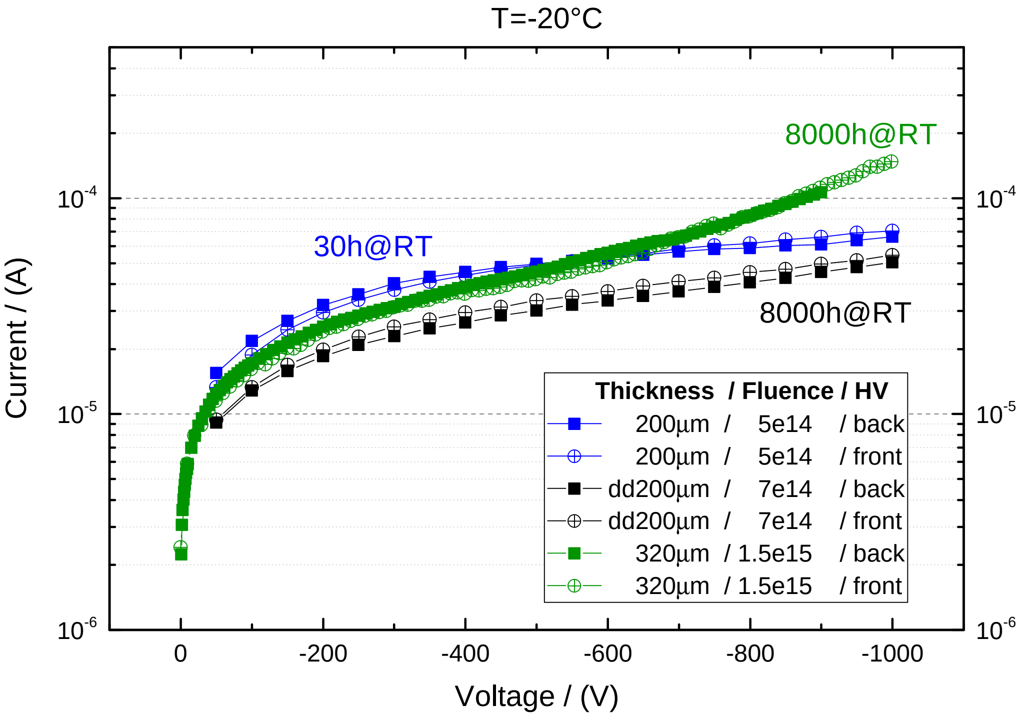

Figure C.3: Leakage current of three irradiated samples for the two bias options: back and front. Measurements have been performed at T= −20°C.

via the periphery in order to make the module production more comfortable looks promising. Furthermore, comparable leakage currents for the different bias connections hint on an equally depleted sensor bulk which is necessary for efficient charge generation.

Therefore, additional charge collection measurements have been performed with the ALiBaVa station using a Sr90 source for charge generation. Again, the bias voltage has been applied once to the backplane in the conventional way and once via the sensor periphery whereat the measurement conditions stayed constant. The charge collection of the samples as function of the bias voltage is shown in figure C.4.

Basically, the charge collection as function of the bias voltage is independent of bias technique. There is a slight difference for the 320 μm thick sensor after $\Phi = 1.5 \times 10^{15}$ 1MeV $n_{eq}cm^{-2}$ visible but might be related to the analysis or a slightly different sensor temperature.

The median noise of the strips measured in the KIT setup does not change too. This behavior is exemplary shown in figure C.5. But in some of the samples strips next to the periphery where the high voltage bond has been applied showed non negligible higher noise and had to be masked for the analysis. Hence, further investigations are necessary in order to prove the concept of front side biasing via the sensor periphery.

In June 2015 a new wafer submission with Hamamatsu Photonics Japan has been conducted.

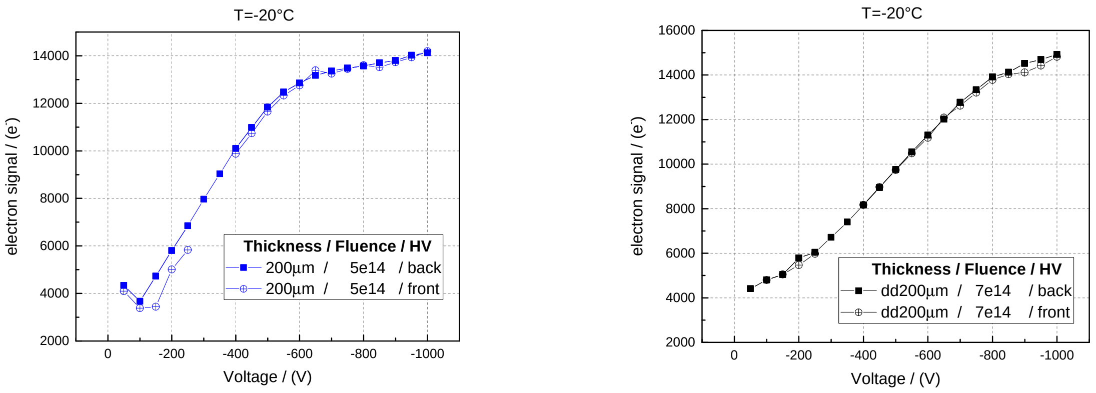

(a) 200 μm, p-spray

(b) deep diffused 200 μm, p-stop

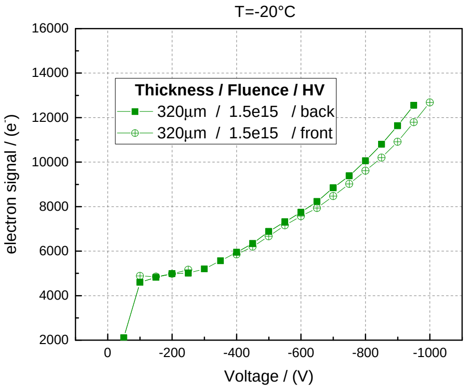

(c) 320 μm, p-spray

Figure C.4: Charge collection for back and front bias for different sensor thicknesses and irradiation levels.

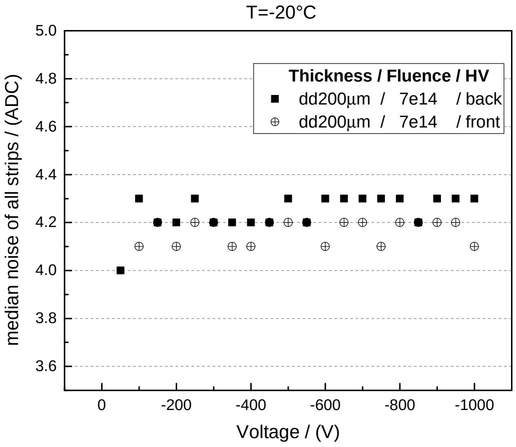

Figure C.5: Median noise for the dd200P sensor for back side and front side bias, T= −20°C.

The sensor layouts on the wafer all include the passivation opening in the periphery in order to study in more detail the front bias technique which might simplify the module construction for the CMS Phase II Outer Tracker Upgrade.

APPENDIX D

APPENDIX D

D.1 The ALiBaVa 2-end daughterboard

Board design with Autodesk Inventor for the measurement of the 2S test sensors. The board was designed such that the readout chips face each other. In this case, the sensor can be bonded on both sides and the segmentation region can be studied in more detail with laser measurements.

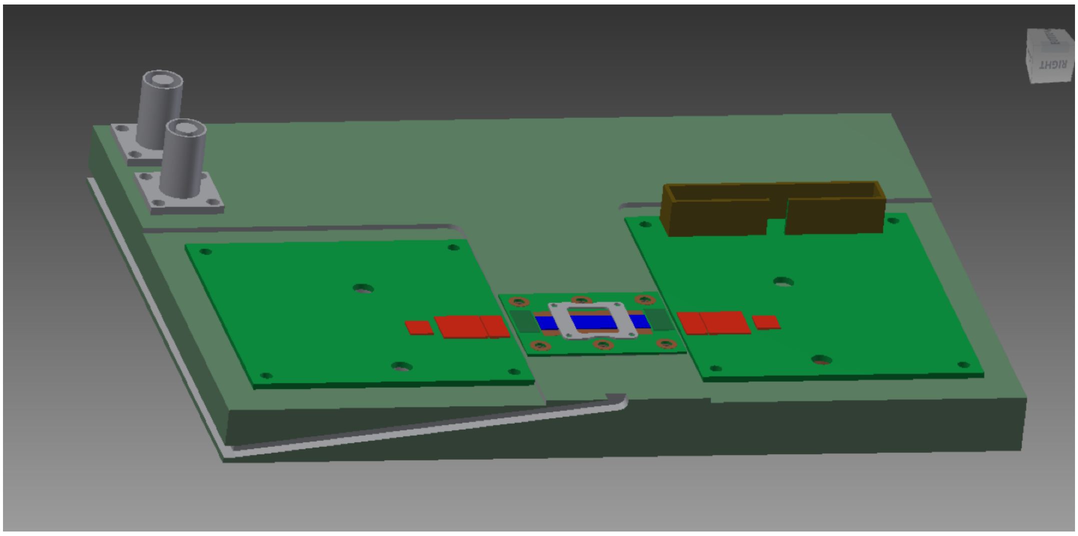

Figure D.1: Design of the 2-end daughterboard with Autodesk Inventor

PRODUCED BY AN AUTODESK EDUCATIONAL PRODUCT

Metrial:
Stückzahl: 1

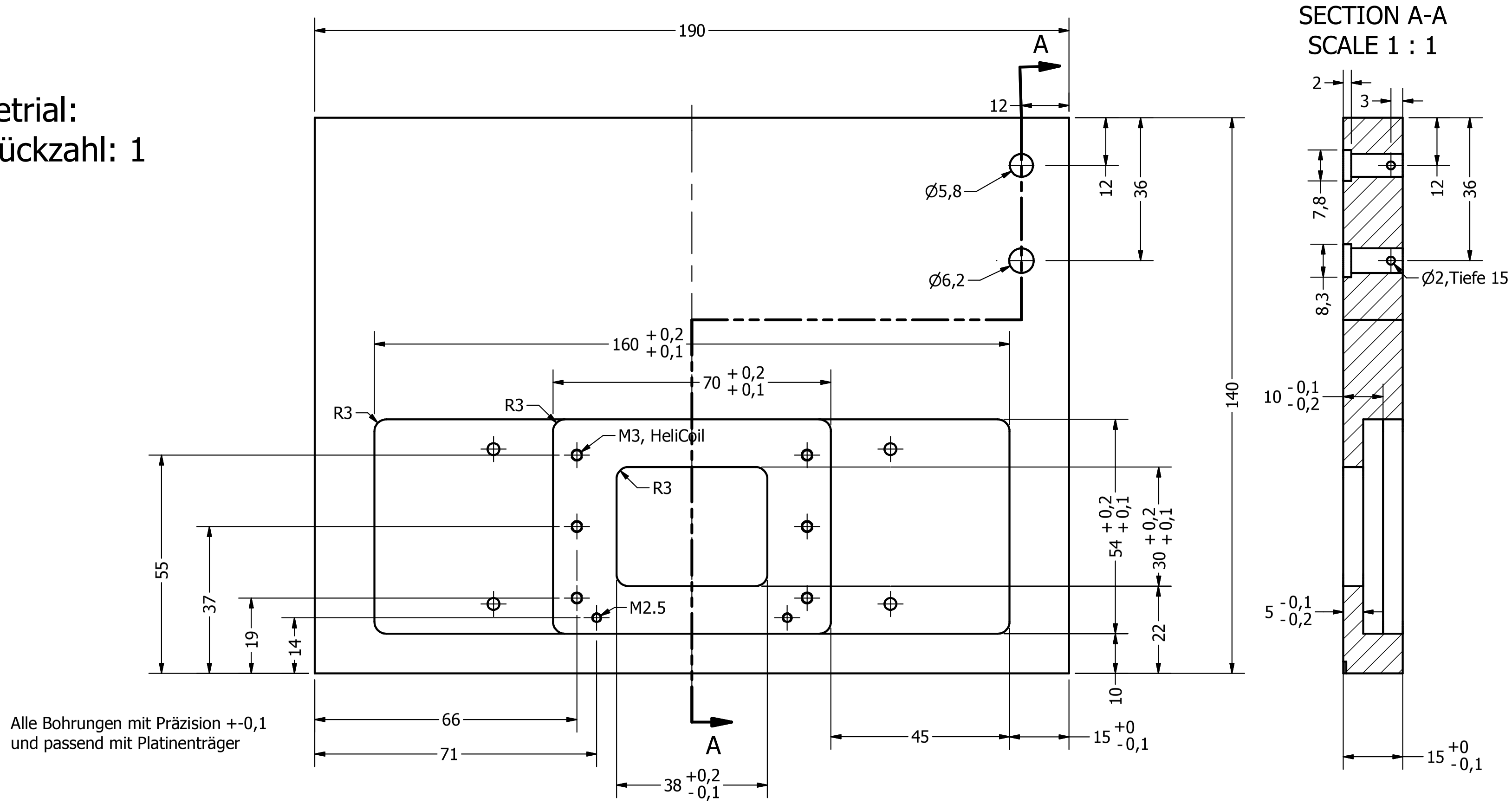

Alle Bohrungen mit Präzision +-0,1
und passend mit Platinenträger

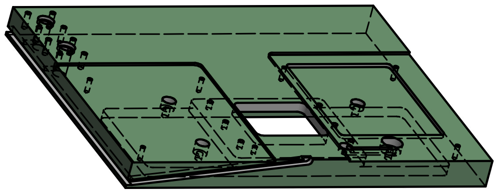

DRAWN
Martin Printz 06.06.2013
CHECKED
QA
MFG
APPROVED

KIT, IEKP

TITLE
2-end-daughterboard

SIZE A3
DWG NO board
REV
SCALE
SHEET 1 OF 3

PRODUCED BY AN AUTODESK EDUCATIONAL PRODUCT

PRODUCED BY AN AUTODESK EDUCATIONAL PRODUCT

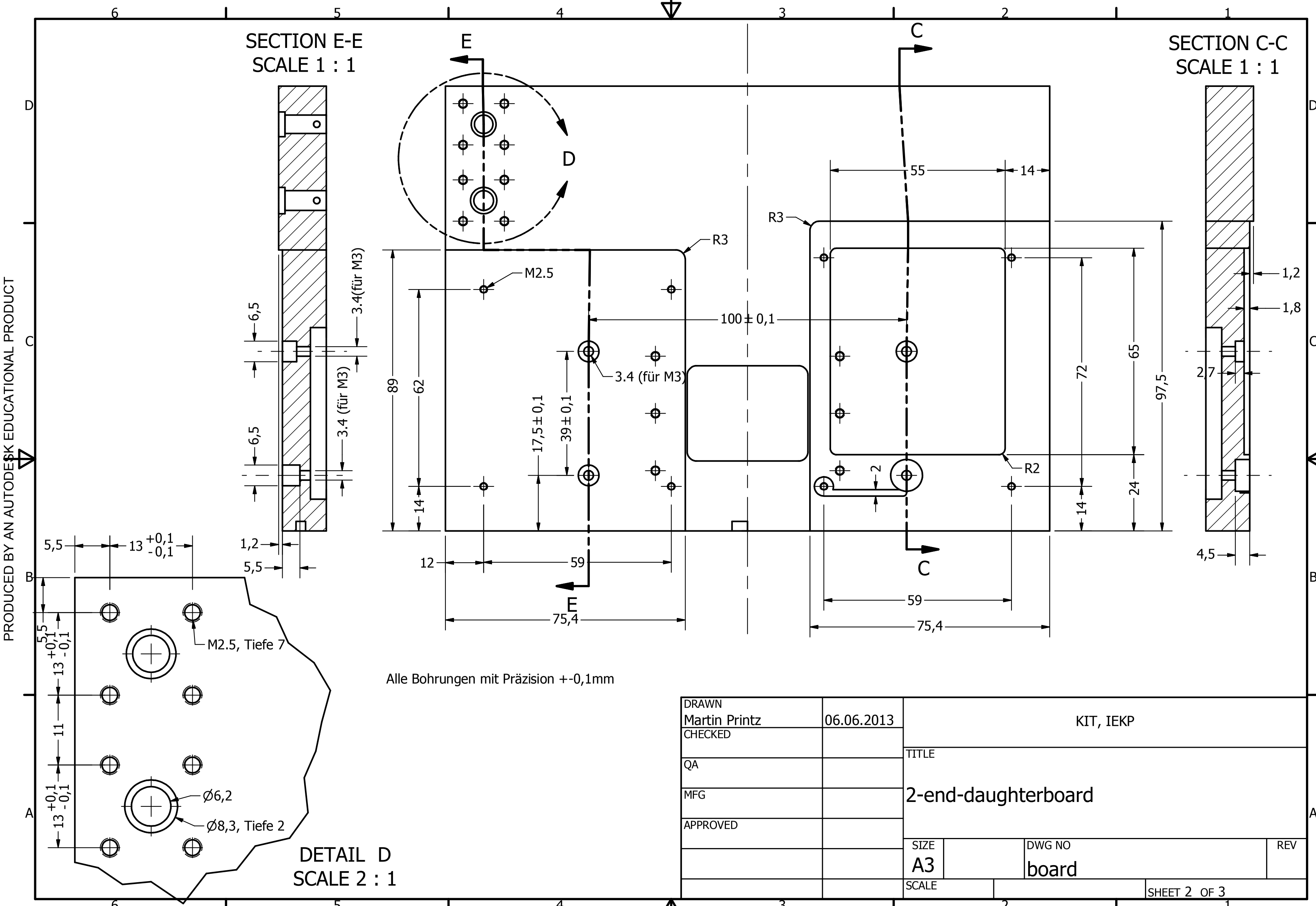

Alle Bohrungen mit Präzision +-0,1mm

DRAWN
Martin Printz
06.06.2013
CHECKED
QA
MFG
APPROVED

KIT, IEKP

TITLE
2-end-daughterboard

SIZE
A3
DWG NO
board
REV
SCALE
SHEET 2 OF 3

PRODUCED BY AN AUTODESK EDUCATIONAL PRODUCT

PRODUCED BY AN AUTODESK EDUCATIONAL PRODUCT

PRODUCED BY AN AUTODESK EDUCATIONAL PRODUCT

PRODUCED BY AN AUTODESK EDUCATIONAL PRODUCT

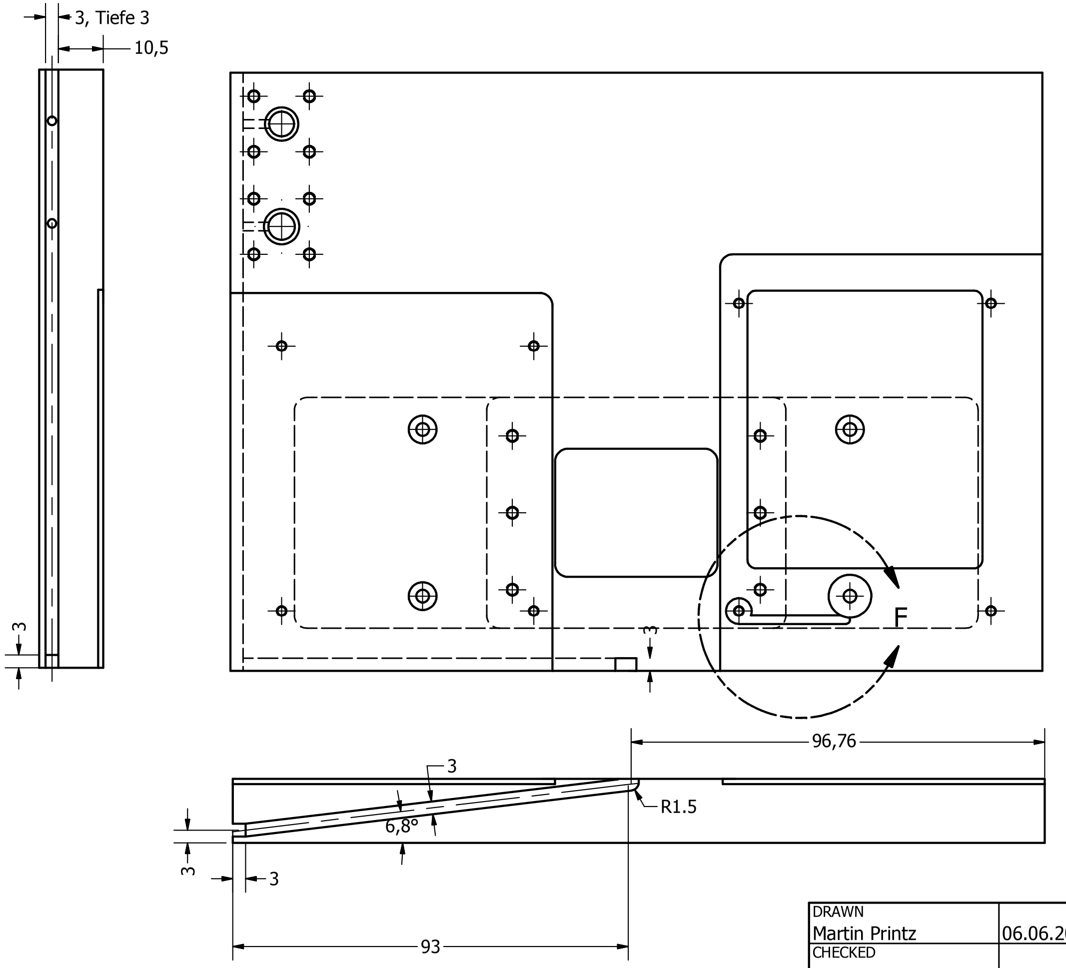

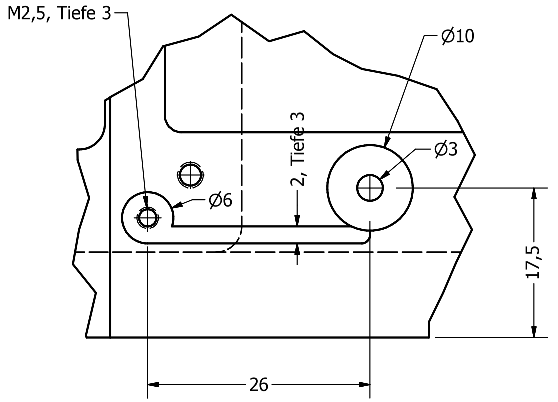

DETAIL F
SCALE 2 : 1

Massepunkt und Massepunkt_2 einpassen

DRAWN Martin Printz	06.06.2013	KIT, IEKP
CHECKED		TITLE
QA		2-end-daughterboard
MFG		
APPROVED		SIZE A3 · DWG NO board · REV
		SCALE · SHEET 3 OF 3

PRODUCED BY AN AUTODESK EDUCATIONAL PRODUCT

APPENDIX E

E.1 Pad layout of the MPA

The final layout of the MPA might slightly change but the bump pad pattern is fixed.

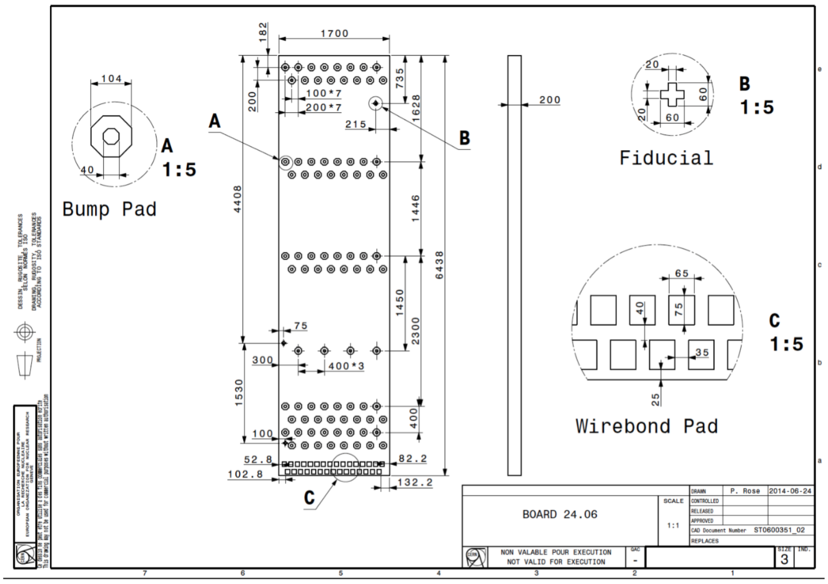

Figure E.1: MPA chip bump pad pattern.

E.2 Sensor layout combatible with MPA pad layout

The final layout of the macro pixel sensor might slightly change due to irradiation studies but the bump pad pattern is fixed.

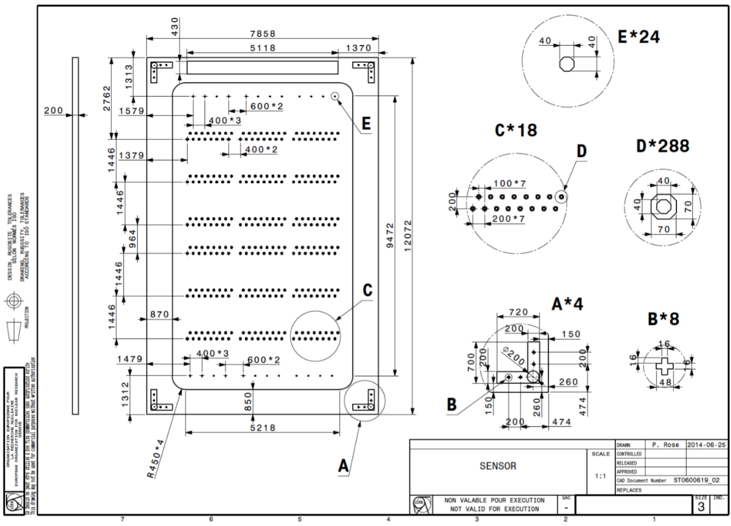

Figure E.2: Macro pixel sensor pad layout.

E.3 MaPSA light assembly

Drawing of the MaPSA light subassembly which was done with different suppliers by the electronics industry and at KIT.

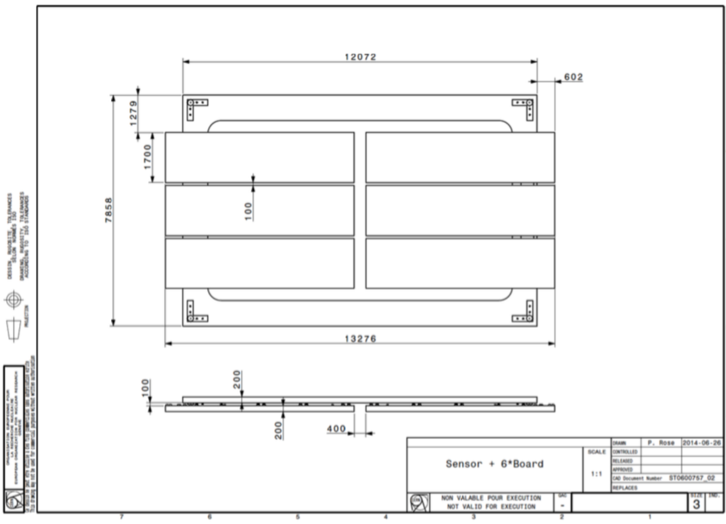

Figure E.3: Drawing of the MaPSA light subassembly.

APPENDIX F

APPENDIX F

F.1 Sentaurus Structure Editor input file

With the following config file, the structure for the simulation is built. Furthermore, the contacts as well as the doping materials and shapes are defined.
In addition, in the last section, the mesh is defined. This is particularly important. The mesh size should be small enough to allow a reliable calculation of the physics. On the other hand, if the mesh size is too dense, the simulator runs out of memory (depending on the machine).

```
;;# definition of variables for the Workbench input

(define Pitch 90)
(define Pitch_2 45)
(define Imp_width 20)
(define Imp_width_2 10)
(define Al_width 33)
(define Al_width_2 165e-1)
(define P-stop_conc @p_conc@)
(define p_d @p_d@)
(define Imp_conc 1e19)
(define n_d @n_d@)
(define bulk @bulk@)
(define depth @depth@)

;;#--------------------------------------------------------------------------------
---------------------------------------------
;;#----------Draw Structure----------
(sdegeo:create-rectangle (position 0 0 0)  (position Pitch 200 0) "Silicon"
"p-bulk" )
(sdegeo:create-rectangle (position 0 200 0)  (position Pitch 201 0) "SiO2" "oxide"
)
(sdegeo:create-rectangle (position 0 0 0)  (position Pitch 1 0) "Aluminum"
"backplane" )

(sdegeo:create-rectangle (position 0 2002e-1 0) (position Imp_width_2 201 0)
"Aluminum" "strip_alu1")
(sdegeo:create-triangle (position Imp_width_2 201 0) (position Imp_width_2 2002e-1
0) (position (+ Imp_width_2 8e-1) 201 0) "Aluminum" "strip_alu1")
(sdegeo:create-rectangle (position (- Pitch Imp_width_2) 2002e-1 0) (position
Pitch 201 0) "Aluminum" "strip_alu2")
(sdegeo:create-triangle (position (- Pitch Imp_width_2) 201 0) (position  (- Pitch
Imp_width_2) 2002e-1 0) (position (- (- Pitch Imp_width_2) 8e-1) 201 0) "Aluminum"
"strip_alu2")
(sdegeo:create-rectangle (position 0 201 0) (position Al_width_2 202 0) "Aluminum"
"strip_alu1_top")
(sdegeo:create-rectangle (position (- Pitch Al_width_2) 201 0) (position Pitch 202
0) "Aluminum" "strip_alu2_top")

(sdegeo:insert-vertex (position Imp_width_2 200.0 0.0))
(sdegeo:insert-vertex (position (- Pitch Imp_width_2) 200.0 0.0))


;;#--------------------------------------------------------------------------------
---------------------------------------------
;;#----------Define Contacts----------
(sdegeo:define-contact-set "contactbackplane" 4  (color:rgb 1 1 1 ) "##" )
(sdegeo:define-contact-set "contactstrip_1" 4  (color:rgb 1 0 0 ) "##" )
(sdegeo:define-contact-set "contactstrip_2" 4  (color:rgb 1 0 0 ) "##" )

(sdegeo:define-contact-set "contactn_1" 4  (color:rgb 1 1 0 ) "##" )
(sdegeo:define-contact-set "contactn_2" 4  (color:rgb 1 1 0 ) "##" )
```

```
;;#--------------------------------------------------------------------------------
---------------------------------------------
;;#----------Define Ref/Eval Window----------
(sdedr:define-refeval-window "dope_p++" "Line" (position 0 1 0) (position Pitch 1
0))
(sdedr:define-refeval-window "dope_n1" "Line" (position 0 200 0) (position
Imp_width_2 200 0))
(sdedr:define-refeval-window "dope_n2" "Line" (position (- Pitch Imp_width_2) 200
0) (position Pitch 200 0))

(sdedr:define-refeval-window "dope_pstop1" "Line" (position 35 200 0) (position 41
200 0))
(sdedr:define-refeval-window "dope_pstop2" "Line" (position 55 200 0) (position 49
200 0))




;;#--------------------------------------------------------------------------------
---------------------------------------------
;;#----------Set Contacts----------
(sdegeo:set-current-contact-set "contactbackplane")
(sdegeo:define-2d-contact (list (car (find-edge-id (position (/ Pitch 2) 0 0))))
"contactbackplane")
(sdegeo:set-current-contact-set "contactstrip_1")
(sdegeo:define-2d-contact (list (car (find-edge-id (position (/ Imp_width_2 2)
2002e-1 0)))) "contactstrip_1")
(sdegeo:set-current-contact-set "contactstrip_2")
(sdegeo:define-2d-contact (list (car (find-edge-id (position (- Pitch (/
Imp_width_2 2)) 2002e-1 0)))) "contactstrip_2")

(sdegeo:set-current-contact-set "contactn_1")
(sdegeo:define-2d-contact (list (car (find-edge-id (position (/ Imp_width_2 2) 200
0)))) "contactn_1")
(sdegeo:set-current-contact-set "contactn_2")
(sdegeo:define-2d-contact (list (car (find-edge-id (position (- Pitch (/
Imp_width_2 2)) 200 0)))) "contactn_2")


;;#--------------------------------------------------------------------------------
---------------------------------------------
;;#----------Define Dopingconcentrations----------
;;#----------Constant Doping Profile----------
(sdedr:define-constant-profile "ConstantProfileDefinition_1"
"BoronActiveConcentration" bulk)
(sdedr:define-constant-profile-region "ConstantProfilePlacement_1"
"ConstantProfileDefinition_1" "p-bulk")
;;#----------Analytic Doping Profile----------
(sdedr:define-analytical-profile-placement "AnalyticalProfilePlacement_1"
"AnalyticalProfileDefinition_1" "dope_p++" "Both" "NoReplace" "Eval")
(sdedr:define-erf-profile "AnalyticalProfileDefinition_1"
"BoronActiveConcentration" "Sympos" 2  "MaxVal" 5e18 "ValueAtDepth" bulk "Depth"
depth "Erf"  "Factor" 0)
```

```
(sdedr:define-analytical-profile-placement "AnalyticalProfilePlacement_2"
"AnalyticalProfileDefinition_2" "dope_n1" "Both" "NoReplace" "Eval")
(sdedr:define-gaussian-profile "AnalyticalProfileDefinition_2"
"PhosphorusActiveConcentration" "PeakPos" 3e-1  "PeakVal" Imp_conc "ValueAtDepth"
bulk "Depth" n_d "Erf"  "Factor" 8e-1)
(sdedr:define-analytical-profile-placement "AnalyticalProfilePlacement_3"
"AnalyticalProfileDefinition_3" "dope_n2" "Both" "NoReplace" "Eval")
(sdedr:define-gaussian-profile "AnalyticalProfileDefinition_3"
"PhosphorusActiveConcentration" "PeakPos" 3e-1 "PeakVal" Imp_conc "ValueAtDepth"
bulk "Depth" n_d "Erf"  "Factor" 8e-1)


(sdedr:define-analytical-profile-placement "AnalyticalProfilePlacement_4"
"AnalyticalProfileDefinition_4" "dope_pstop1" "Both" "NoReplace" "Eval")
(sdedr:define-gaussian-profile "AnalyticalProfileDefinition_4"
"BoronActiveConcentration" "PeakPos" 3e-1  "PeakVal" P-stop_conc "ValueAtDepth"
bulk "Depth" p_d "Erf"  "Factor" 8e-1)
(sdedr:define-analytical-profile-placement "AnalyticalProfilePlacement_5"
"AnalyticalProfileDefinition_5" "dope_pstop2" "Both" "NoReplace" "Eval")
(sdedr:define-gaussian-profile "AnalyticalProfileDefinition_5"
"BoronActiveConcentration" "PeakPos" 3e-1  "PeakVal" P-stop_conc "ValueAtDepth"
bulk "Depth" p_d "Erf"  "Factor" 8e-1)

;;#--------------------------------------------------------------------------------
---------------------------------------------
;;#----------Refinement Placement----------
(sdedr:define-refinement-size "RefinementDefinition_1" 10 20 5e-2 5e-2)
(sdedr:define-refinement-material "RefinementPlacement_1" "RefinementDefinition_1"
"Silicon" )
(sdedr:define-refinement-function "RefinementDefinition_1" "DopingConcentration"
"MaxTransDiff" 1)
(sdedr:define-refinement-size "RefinementDefinition_2" 5e-1 5e-1)
(sdedr:define-refinement-material "RefinementPlacement_2" "RefinementDefinition_2"
"SiO2" )
(sdedr:define-refinement-function "RefinementDefinition_2" "DopingConcentration"
"MaxTransDiff" 1)


(sde:build-mesh "snmesh" " " "n@node@_msh")
```

F.2 Sentaurus Device Simulator input file

The device config file contains all models which have to be included in the calculation of the physical properties and performance. The models are included via certain key words. All models are well described in the Sentaurus manual.
In addition, the SPICE network as well as the goal parameters (for instance the maximum bias voltage) of the simulation are defined.

```
# Simulation within Synopsis
# n-on-p strip detector
# PStop Investigation


Device n_on_p_strips {
;;#-----Initialize electrodes, start values--------------
    Electrode
    {
        {Name = "contactstrip_1" voltage=0.0 Area=10000}
        {Name = "contactstrip_2" voltage=0.0 Area=10000}


        {Name = "contactn_1" voltage=0.0 Area=10000}
        {Name = "contactn_2" voltage=0.0 Area=10000}


        {Name = "contactbackplane" voltage=0.0 Area=10000}
    }

    File
    {
            Grid    = "@tdr@"
            Current = "@plot@"
            Plot    = "@dat@"
    }

;;#-----------Physics section, apply models and radiation damage--------------
    Physics
    {
        Temperature = 253
        Mobility
        (
            DopingDep
            eHighFieldSaturation
            hHighFieldSaturation
            Enormal
            CarrierCarrierScattering (ConwellWeisskopf)
        )
        Recombination
        (
                SRH (DopingDep ElectricField(LifeTime=Hurkx))
                Auger
                eAvalanche (vanOverstraeten Eparallel)
                hAvalanche (vanOverstraeten Eparallel)
            CDL
        )
        EffectiveIntrinsicDensity(Slotboom)
        Fermi

;;#-------Generation of signal, MIP like energy deposition-------------
        HeavyIon
        (
```

```
            Direction=(0,1)
            Location=!(puts (@<Position>@,0))!
            Time=1e-9
            Length=[0 0.001 200 200.001]
            Wt_hi= [1.0 1.0 1.0 1.0]
            LET_f= [0 8.7176e-10 8.7176e-10 0]
            Gaussian
            PicoCoulomb
        )
    }

;;#------------radiation damage model------------------
    Physics ( material = "Silicon" )
    {
    Traps
      (

        (
        Acceptor Level
        fromCondBand
        Conc=!(puts [expr 1.189*@F@+6.454e13])!
        EnergyMid=0.525
        eXsection=1.0e-14
        hXsection=1.0e-14
        )

        (
        Donor Level
        fromValBand
        Conc=!(puts [expr 5.598*@F@*0.9-3.949e14])!
        EnergyMid=0.48
        eXsection=1.0e-14
        hXsection=1.0e-14
        )
    )
    }

    Physics (MaterialInterface = "Silicon/SiO2")
    {
        Traps( FixedCharge Conc=@<Q_Ox>@ )
    }


}
;;#-------------SPICE network--------------------
System {

       n_on_p_strips npp ( "contactn_1"=c1 "contactn_2"=c2 "contactbackplane"=bg
"contactstrip_1"=s1
                "contactstrip_2"=s2 )
       Vsource_pset v (bg 0) {dc = 0}
       Vsource_pset v1 (c1 0) {dc = 0}

       Resistor_pset r1c (c1 0) {resistance = 1800000}
```

```
       Resistor_pset r2c (c2 0) {resistance = 1800000}


       Resistor_pset r1s (s1 0) {resistance = 50}
       Resistor_pset r2s (s2 0) {resistance = 50}


}

File    {
    Output  = "@log@"
    ACExtract = "@acplot@"
    }

;;#-------------Plot section--------------------
Plot    {
        eCurrent/Vector hCurrent/Vector Current/vector
        eDensity hDensity
        ElectricField ElectricField/Vector
        eEparallel hEparallel
        Potential SpaceCharge
        Doping DonorConcentration AcceptorConcentration
        Auger eAvalanche hAvalanche AvalancheGeneration
        eMobility hMobility
        SRHRecombination
        #BeamGeneration
        eInterfaceTrappedCharge
        hInterfaceTrappedCharge
        eTrappedCharge
        hTrappedCharge
        HeavyIonCharge HeavyIonGeneration
    }

CurrentPlot   {

        ElectricField (Maximum(Material="Silicon"))
        eDensity((1 199.9))
        }

Math
{
    Method=pardiso
    Number_of_Threads = 8
    Extrapolate
    Derivatives
    RelErrControl
    Digits=4
    Notdamped=50
    Iterations=25
    RecBoxIntegr (5e-3 50 5000)
}

;;#-----------Solve section; calculation of equations-------------
Solve
```

```
{   Poisson
    Coupled (iterations=50 notdamped=0) { Poisson}
    Coupled (iterations=50 notdamped=0) { Poisson Electron Hole}


    QuasiStationary
    (
        InitialStep=1e-5
        Minstep   = 1e-8
        MaxStep   = 1e-2
        Increment = 1.5
        Decrement = 2
        Goal
        {
            Parameter = v.dc
            Voltage=-1000
        }

    )

    {Coupled {Poisson Electron Hole}}
        Save(FilePrefix="vg1")

    Load(FilePrefix="vg1")
    NewCurrentPrefix="vg1_"
    Quasistationary
        (InitialStep=0.01
        MaxStep=0.1
        MinStep=0.001
        Goal {Parameter =v1.dc voltage=2})
        {Coupled {Poisson Electron Hole}
        CurrentPlot (Time=
            (range = (0 0.2) intervals=20;
            range = (0.2 1.0)))
        }

    NewCurrentPrefix = "transient_"

;;#----------Transient section; plot MIP signal-----------------
        Transient
    (
                  InitialTime = 0.0
                  FinalTime=30.0E-9
                  InitialStep=0.5E-11
                  MaxStep=0.5E-9
        )
    {
        Coupled (iterations=8, notdamped=15){Poisson Electron Hole Circuit}
        Plot(Time=(0.5e-9;1e-9;2e-9;5e-9;10e-9;20e-9;30e-9) noOverwrite
FilePrefix="MIP_n@node@")
    }


}
```

LIST OF TABLES

TABLE **Page**

LIST OF FIGURES

FIGURE **Page**

BIBLIOGRAPHY

[ABC$^+$01] A. Akkermann, J. Barak, M.B. Chadwick, J. Levinson, M. Murat, and Y. Lifshitz. Updated NIEL calculations for estimating the damage induced by particles and gamma-rays in Si and GaAs. *Radiation Physics and Chemistry*, 62:301–310, 2001.

[ALI] Alice – A Large Collider Experiment. URL: http://aliceinfo.cern.ch.

[AM12] D. Abbaneo and A. Marchioro. A hybrid module architecture for a prompt momentum discriminating tracker at HL-LHC. *Journal of Instrumentation*, 7(C09001), 2012.

[ATL] ATLAS – The ATLAS Experiment. URL: http://atlas.web.cern.ch.

[B$^+$12] J. Beringer et al. Review of Particle Physics. *Physical Review D*, 86(01001.DOI:10.1103/PhysRevD.86.010001), 2012.

[BBH$^+$12] G. Blanchot, D. Braga, A. Honma, M. Kovacs, and M. Raymond. Hybrid circuit prototypes for the CMS Tracker upgrade frontend electronics. *Journal of Instrumentation*, 8(C12033), 2012.

[Bet30] H. Bethe. Zur Theorie des Durchgangs schneller Korpukularstrahlen durch Materie. *Annalen der Physik*, 397:325–400, 1930.

[BHJ$^+$12] D. Braga, G. Hall, L. Jones, P. Murray, M. Pesaresi, M. Prydderch, and M. Raymond. CBC2: a microstrip readout ASIC with coincidence logic for trigger primitives at HL-LHC. *Journal of Instrumentation*, 7(C10003), 2012.

[Blo33] F. Bloch. Zur Bremsung rasch bewegter Teilchen beim Durchgang durch Materie. *Annalen der Physik*, 403:285–320, 1933.

[BR] Davide Braga and Mark Raymond. CBC2: X-ray irradiation results. Tracker week talk, Nov. 6th 2014.

[Bra13] D. Braga. CBC2 (CMS Binary Chip 2) User Guide 1.1. URL: http://www.hep.ph.ic.ac.uk/ dmray/CBCdocumentation/, March 2013.

[CER] CERN – The European Organization for Nuclear Research. URL: http://www.cern.ch.

[CER09] CERN Communication Group. CERN LHC - the guide. February 2009.

[Chi11] A. Chilingarov. Generation current temperature scaling. *Technical Note RD50-2011-01*, 2011.

[CMK$^+$14] D. Ceresa, A. Marchioro, K. Kloukinas, J. Kaplon, W. Bialas, V. Re, G. Traversi, L. Gaioni, and L. Ratti. Macro Pixel ASIC (MPA): the readout ASIC for the pixel-strip (PS) module of the CMS outer tracker at HL-LHC. *Journal of Instrumentation*, 9(C11012), 2014.

[CMS] CMS Collaboration. CMS Physics Technical Design Report Volume 1: Detector Performance and Software. *J. Phys. G 34 (2006) 995*.

[CMS98] CMS Collaboration. Tracker technical design report. Technical report, CERN, 1998.

[CMS10a] CMS Collaboration. Performance and operation of the cms electromagnetic calorimeter. *Journal of Instrumentation*, 5(T03010), March 2010.

[CMS10b] CMS Collaboration. Performance of the CMS hadron calorimeter with cosmic ray muons and lhc beam data. *Journal of Instrumentation*, 5(T03012), 2010.

[CW00] T.F Ciszek and T.H. Wang. Silicon Float-Zone Crystal Growth as a Tool for the Study of Defects and Impurities. *NREL/CP-520-28569*, 2000.

[Czo17] J. Czochralski. Metalle. *Z. Phys. Chem.*, 92, 1917.

[dBDH$^+$15] Wim de Boer, Alexander Dierlamm, Frank Hartmann, Karl-Heinz Hoffmann, Andreas Kornmayer, Thomas Müller, Andreas Nuernberg, Giulio Pellegrini, Martin Printz, and David Quirion. A fourfold segmented silicon strip sensor with read-out at the edges. *Nucl. Instr. and Meth. A*, 788:154–160, 2015.

[Desa] Descrition on the JRA1 Trigger Logic Unit (TLU), v0.2c. URL:http://www.eudet.org/e26/.

[DESb] DESY test beam facility. Url:http://testbeam.desy.de.

[Die03] Alexander Dierlamm. *Studies on the Radiation Hardness of Silicon Sensors*. PhD thesis, Universität Karlsruhe, 2003.

[Die12] Alexander Dierlamm. Characterization of silicon sensor materials and designs for the CMS Tracker Upgrade. *Proceedings of Science*, (Vertex 2012)016, 2012.

[Die13] A. Dierlamm. Planar sensors for future vertex and tracking. *Proceedings of Science*, 027, 2013.

[ea00] M. Raymond et al. The CMS Tracker APV25 0.25μm CMOS Readout Chip. *Proceedings of the 6th workshop in Electronics for LHC Experiments, Crocow*, 2000.

[ea14a] D. Braga et al. Characterization of the CBC2 readout ASIC for the CMS strip-tracker high-luminosity upgrade. *Journal of Instrumentation*, 9(C03001), 2014.

[ea14b] G. Hall et al. CBC2: A CMS microstrip readout ASIC with logic for track-trigger modules at HL-LHC. *Nucl. Instr. and Meth. A*, 765:214–218, November 2014.

[EBD$^+$14a] Thomas Eichhorn, Ashutosh Bhardwaj, Ranjeet Dalal, Robert Eber, Kavita Lalwani, Alberto Messineo, Timo Peltola, Martin Printz, and Kirti Ranjan. Development of Radiation Damage Models for Irradiated Silicon Sensors Using TCAD Tools. *Journal of Instrumentation*, PoS(TIPP2014)(276), 2014.

[EBD$^+$14b] Thomas Eichhorn, Ashutosh Bhardwaj, Ranjeet Dalal, Robert Eber, Kavita Lalwani, Alberto Messineo, Timo Peltola, Martin Printz, and Kirti Ranjan. Simulation of Silicon Devices for the CMS Phase II Tracker Upgrade. *CMS Detetcor Note*, CMS DN-14-016, 2014.

[Ebe13] Robert Eber. *Investigations of new Sensor Designs and Development of an effective Radiation Damage Model for the Simulation of highly irradiated Silicon Particle Detectors*. PhD thesis, IEKP-KA/2013-27, KIT, 2013.

[EDM] CMSSW Application framework
https://twiki.cern.ch/twiki/bin/view/CMSPublic/WorkBookCMSSWFramework.

[Eic12] Thomas Eichhorn. Silicon Strip Sensor Simulations for the CMS Physe-II Tracker Upgrade. *IEEE Nucl. Sci. Symp. (NSS/MIC)*, 25(5):1664–1669, 2012.

[F$^+$13] V. Fadeyev et al. Scribe–cleave–passivate (scp) slim edge technology for silicon sensors. *Nucl. Instr. and Meth. A*, 731:260–265, 2013.

[FJM$^+$01] M.J. French, L.L. Jones, Q. Morrissey, A. Neviani, R. Turchetta, J. Fulcher, G. Hall, E. Noah, M. Raymond, G. Cervellic, P. Moreiracan, and G. Marseguerra. Design and results from the APV25, a deep sub-micron CMOS front-end chip for the CMS tracker. *Nucl. Instr. and Meth. A*, 466:359–365, 2001.

[FLU15] CMS Beam Radiation Monitoring
URL:https://twiki.cern.ch/twiki/bin/view/CMSPublic/BRILRadiationSimulation, October 2015.

[FMC] FMC projects-FMC DIO 5CH TTLA. Url:http://www.ohwr.org/projects/fmc-dio-5chttla/wiki.

[ftC14] Viktor Veszpremi for the CMS Collaboration. Operation and performance of the CMS tracker. *Journal of Instrumentation*, 9(C03005), 2014.

[G. 10] G. Lindström et al. Radiation hard silicon detectors - developments by the RD48 (ROSE) collaboration. *Nucl. Instr. and Meth. A*, 612(3):539–548, 2010.

[G. 14] G. Bianchi et al. tkLayout: a design tool for innovative silicon tracking detectors. *Journal of Instrumentation*, 9(C03054), 2014.

[Gia04] Fabiola Gianotti. Physics at the LHC. *Physics Reports*, 403–404(0):379 – 399, 2004. CERN - the second 25 years.

[gS12] Martin Printz (geb. Strelzyk). Design studies of n-in-p silicon strip sensors for the CMS tracker. Master's thesis, KIT, IEKP-KA/2012-22, 2012.

[Har09] Frank Hartmann. *Evolution of Silicon Sensor Technology in Particle Physics*. Springer, 2009.

[HhM14] Ali Harb, Johannes hauk, and Andreas Mussgiller. Test beam results of the first CMS double-sided strip module prototypes using the CBC2 read-out chip. *CMS Detetcor Note*, (DN-2014/025), 2014.

[Hil04] Ulrich Hilleringmann. *Silizium-Halbleitertechnologie*. Teubner B.G. GmbH, 2004.

[HM06] W. Herr and B. Muratori. Concept of the luminosity. *CERN school*, 2006.

[Hof11] K.-H. Hoffmann. Campaign to identify the future CMS tracker baseline. *Nucl. Instr. and Meth. A*, 658:30–35, 2011.

[Hof13] K.-H. Hoffmann. *Development of new Sensor Designs and Investigations on Radiation Hard Silicon Strip Sensors for CMS at the Large Hadron Collider during the High Luminosity Phase*. PhD thesis, IEKP-KA/2013-1, KIT, 2013.

[Huh02] M. Huhtinen. Simulation of non-ionizing energy loss and defect formation in silicon. *Nucl. Instr. and Meth. A*, 491:194–215, 2002.

[Hun07] Siegfried Hunklinger. *Festkörperphysik*. Oldenbourg, 2007.

[JBD$^+$15] G. Jain, A. Bhardwaj, R. Dalal, R. Eber, T. Eichorn, M. Fernandez, K. Lalwani, A. Messineo, F.R. Palomo, T. Peltola, M. Printz, K. Ranjan, I. Villa, and S. Hidalgo. Design optimization of pixel sensors using device simulations for the phase-II CMS tracker upgrade. *Nucl. Instr. and Meth. A*, in press, corrected proof, 2015.

[Jei14] M. Jeitler. The upgrade of the CMS trigger system. *Journal of Instrumentation*, C08002, 2014.

[Jun11] A. Junkes. *Influence of Radiation Induced Defect Clusters on Silicon Particle Detectors*. PhD thesis, DESY Hamburg, 2011.

[Kit96] Charles Kittel. *Introduction to Solid State Physics*. Wiley, 1996.

[Kor11] A. Kornmayer. Untersuchungen zur Signalkopplung an neuartigen Siliziumstreifensensorgeometrien. Master's thesis, IEKP-KA/2011-17, KIT, 2011.

[Lap10] Marzena Lapka. Interactive Slice of the CMS detector URL:https://cms-docdb.cern.ch/cgi-bin/PublicDocDB/ShowDocument?docid=4172 , July 2010.

[LE] Layout Editor, URL:http://www.layouteditor.net.

[LHC] Lhc-b – The Large Hadron Collider beauty experiment. URL: http://lhcb.web.cern.ch.

[LR09] Claude Leroy and Pier-Giorgio Rancoita. *Principles of Radiation Interaction in Matter and Detection*. World Scientific, 2009.

[Lut99] Gerhard Lutz. *Semiconductor Radiation Detectore: Device Physics*. Springer, 1999.

[Man13] I. Mandic. Silicon sensors for HL-LHC tracking detectors. *Nucl. Instr. and Meth. A*, 732:126–129, 2013.

[Mar05] Jacek Marczewski. *Bulk Silicon Detectors of Ionizing Radiation - The Role of the Depetion Layer*. Institute of Electron Technology Warsaw, 2005.

[MBB$^+$13] M. Barros Marin, S. Baron, V. Bobillier, M. Di Cosmo, S. Haas, M. Hansen, M. Joos, F. Vasey, and P. Vichoudis. A GLIB-based micro-TCA demonstration system for HEP experiments. *Journal of Instrumentation*, 8(C12011), 2013.

[Mer14] Stefano Mersi. Tracker layout studies https://espace.cern.ch/Tracker-Upgrade/Layout/SitePages/Home.aspx, November 2014.

[MH08] Ricardo Marco-Hernandez. A portable readout system for microstrip silicon sensors (ALIBAVA). *IEEE Nucl. Sci. Symp. (NSS/MIC)*, pages 3201–3208, 2008.

[Mol99] M. Moll. *Radiation Damage in Silicon Particle Detectors*. PhD thesis, Universität Hamburg, 1999.

[NÏ4] A. Nürnberg. *Studies in irradiated silicon sensors for the CS Tracker at the HL-LHC*. PhD thesis, IEKP-KA/2014-04, KIT, 2014.

[Neu13] Coralie Neubüser. Impact of Irradiations by Protons with different Energies on Silicon Sensors. Master's thesis, Universität Hamburg, 2013.

[OBH$^+$14] T. Obermann, M. Backhaus, F. Hügging, H. Krüger, F. Lütticke, C. Marinas, and N. Wermes. Implementation of a configurable FE-I4 trigger plane for the AIDA telescope. *Journal of Instrumentation*, 9(C03035), 2014.

[Pel14] Timo Peltola. Charge collection efficiency simulations of irradiated silicon strip detectors. *Journal of Instrumentation*, 9(C12010), 2014.

[PH10] M. Pesaresi and G. Hall. Simulating the performance of a p_T tracking trigger for CMS. *Journal of Instrumentation*, 5(C08003), 2010.

[Ram39] S. Ramo. Currents Induced by Electron Motion. *Proceedings of the IRE*, (27)9:584–585, 1939.

[RD5] Rd50 - radiation hard semiconductor devices for very high luminosity colliders. http://rd50.web.cern.ch.

[ROO] ROOT software framework. Url:http://root.cern.ch.

[Ros15] Pierre Rose. 2S module CAD drawing. URL: https://espace.cern.ch/Tracker-Upgrade/2S-Module/Shared, October 2015.

[RR14] P. La Rocca and F. Riggi. The upgrade programme of the major experiments at the large hadron collider. *Journal of Physics*, 515, 2014.

[Rub12] I. Rubinsky. An EUDET/AIDA pixel beam telescope for detector development. *Elsevier Physics Procedia*, 37:923–931, 2012.

[Sho38] W. Shockley. Currents to Conductors Induced by a Moving Point Charge. *Journal of Applied Physics*, (9)10:635–636, 1938.

[Sil] Silvaco software package. Url:http://www.silvaco.com.

[Spi05] Helmut Spieler. *Semiconductor Detector Systems*. Oxford Science Publication, 2005.

[SPS] SPS test beam facility. URL:https://sps-schedule.web.cern.ch/sps-schedule/.

[Syn] Synopsys Sentaurus T-CAD. Url:http://www.synopsys.com/tools/tcad/pages/default.aspx.

[Tey10] Daniel Teyssier. CMS muon system performance. *Nuclear Instruments and Methods in Physics Research Section A: Accelerators, Spectrometers, Detectors and Associated Equipment*, 623(1):88 – 90, 2010.

[The08] The CMS Collaboration. The CMS experiment at the CERN LHC. *Journal of Instrumentation*, 3(S08004):328, 2008.

[The10] The CMS Collaboration. Precise mapping of the magnetic field in the CMS barrel yoke using cosmic rays. *Journal of Instrumentation*, 5, March 2010.

[Tre12] W. Treberspurg. Enhanced measurement methods for sensor characterization. CMS Tracker Week, February 2012.

[TRI15] TRIGA Mark II. www.rcp.ijs.si/ric/description-a.html, November 2015.

[VBF$^+$12] M. Valentan, T. Bergauer, M. Fragicevic, M. Friedl, C. Irmler, E. Huemer, and W. Treberspurg. Optimization of Strip Isolation for Silicon Sensors. *Physics Procedia*, 37:891–898, 2012.

[vOdM70] R. van Overstraeten and H. de Man. Measurement of the Ionization Rates in Diffused Silicon p-n Junctions. *Solid-States Electronics*, 13(1):583–608, 1970.

[Wei13] P. Weigell. Recent results of the ATLAS upgrade planar pixel sensors R&D project. *Nucl. Instr. and Meth. A*, 731:177–182, 2013.

[Wun92] R. Wunstdorf. *Systematische Untersuchungen zur Strahlenresistenz von Silzium-Detektoren für die Verwendung in Hochenergiephysik-Experimenten*. PhD thesis, Universität Hamburg, 1992.

[Zha13] J. Zhang. *X-Ray Radiation Damage Studies and Design of a Silicon Pixel Sensro for Science at the XFEL*. PhD thesis, Universität Hamburg, 2013.

[Zon98] D. Zontar. *Study of radiation damage in silicon detectors for high luminosity experiments at LHC*. PhD thesis, University of Ljubljana, 1998.

[Zyk15] Zyklotron AG. http://www.zyklotron-ag.de, November 2015.

LIST OF PUBLICATIONS

Publications in refereed journals

I P-stop isolation study of irradiated n-in-p type silicon strip sensors for harsh radiation environment
Martin Printz on behalf of the CMS Tracker Collaboration;
Nucl. Instr. and Meth. A, in publication, submitted November 6th, 2015

II Design optimization of pixel sensors using device simulations for the Phase-II CMS Tracker Upgrade
G. Jain, A. Bhardwaj, R. Dalal, R. Eber, T. Eichorn, M. Fernandez, K. Lalwani, A. Messineo, F.R. Palomo, T. Peltola, M. Printz, K. Ranjan, I. Villa, S. Hidalgo;
Nucl. Instr. and Meth. A, http://doi:10.1016/j.nima.2015.08.053, September 8th, 2015

III A fourfold segmented silicon strip sensor with read-out at the edges
Wim deBoer, Alexander Dierlamm, Frank Hartmann, Karl-Heinz Hoffmann, Andreas Kornmeyer, Thomas Mueller, Andreas Nuernberg, Giulio Pellegrini, Martin Printz, David Quirion;
Nucl. Instr. and Meth. A, http://dx.doi.org/10.1016/j.nima.2015.03.082, April 8th, 2015

IV T-CAD analysis of electric fields in n-in-p silicon strip detectors in dependence on the p-stop pattern and doping concentration
Martin Printz on behalf of the CMS Tracker Collaboration;
Journal of Instrumentation, Vol.10, January 2015, http://dx.doi.org/10.1088/1748-0221/10/01/C01048, 2015

V A Method to Simulate the Observed Surface Properties of Proton Irradiated Silicon Strip Sensors
Thomas Eichhorn, Ashutosh Bhardwaj, Ranjeet Dalal, Robert Eber, Kavita Lalwani, Alberto Messineo, Timo Peltola, Martin Printz and Kirti Ranjan
Proceedings of Science, JINST, 16th International Workshop on Radiation Imaging Detectors, Trieste, Italy, 2014

VI Development of Radiation Damage Models for Irradiated Silicon Sensors Using TCAD Tools
Thomas Eichhorn, Ashutosh Bhardwaj, Ranjeet Dalal, Robert Eber, Kavita Lalwani, Alberto

Messineo, Timo Peltola, Martin Printz and Kirti Ranjan
Proceedings of Science, JINST, PoS(TIPP2014)276, 2014

VII Simulations of Inter-Strip Capacitance and Resistance for the Design of the CMS Tracker Upgrade
Thomas Eichhorn, Ashutosh Bhardwaj, Ranjeet Dalal, Robert Eber, Kavita Lalwani, Alberto Messineo, Timo Peltola, Martin Printz and Kirti Ranjan
Proceedings of Science, JINST, PoS(TIPP2014)279, 2014

VIII Radiation Hard Sensor Materials for the CMS Tracker Phase II Upgrade - Charge Collection of Different Bulk Polarities
Martin Printz on behalf of the CMS Tracker Collaboration;
Nucl. Instr. and Meth. A, ISSN 0168-9002, http://dx.doi.org/10.1016/j.nima.2014.04.042, April 26th, 2014

Other publications

IX Simulation of Silicon Devices for the CMS Phase II Tracker Upgrade
Thomas Eichhorn, Ashutosh Bhardwaj, Ranjeet Dalal, Robert Eber, Kavita Lalwani, Alberto Messineo, Timo Peltola, Martin Printz and Kirti Ranjan, 2015
CMS Detector Note DN-2014/016, 2015

DANKSAGUNG/ACKNOWLEDGEMENTS

Wie der Leser sich vorstellen kann, ist die Anfertigung dieser Arbeit nur mit Hilfe von vielen Menschen, ob Kollegen oder Familie, möglich gewesen. Dessen bin ich mir äußerst bewusst und werde dies auch niemals vergessen. Dankeschön!

Insbesondere danke ich Herrn Prof. Thomas Müller, dass er mir die Möglichkeit einer Doktorarbeit in diesem spannenden Gebiet an seinem Institut eröffnet hat. Ich kann mich genau erinnern, wie wir vor drei Jahren in Ihrem Büro saßen und Sie mich zu diesem Schritt ermutigt haben. Heute weiß ich, dass es die richtige Entscheidung war.

Herrn Prof. Willem de Boer danke ich für die Übernahme des Korreferats und viel mehr für die spontanen Besuche und Diskussionen am Institut. Die letzteren haben auch in schwierigen Phasen meine Motivation hoch gehalten.

Dr. Alexander Dierlamm danke ich für die unermüdlichen Diskussionen und Hilfestellungen trotz seiner umfangreichen Aufgaben als Gruppenleiter der CMS Hardware Gruppe. Vor allem sein Gespür für interessante Themen und Fragestellungen haben zu den vorgestellten Ergebnissen geführt. Außerdem gilt ihm mein großer Dank für das Korrekturlesen der Arbeit.

Die administrativen Aufgaben waren nur mit Hilfe von Frau Fellner, Frau Bräunling, Frau Gering und Herrn Dr. Simonis zu bewältigen. Vielen Dank hierfür.

Rege fachliche Diskussionen mit den Mitdoktoranden und Postdocs Dr. Robert Eber, Stefan Heindl und Dr. Andreas Nürnberg sowie Daniel Schell und Simon Kudella haben in vielen Phasen zum Verständnis bei Problemen geführt. Ihre Unterstützung bei Setup- und Analyseproblemen möchte ich besonders hervorheben.

I want to thank Dr. Alexander Dierlamm, Dr. Stefano Mersi and Dr. Mark Pesaresi for their confidence in me and the opportunity to take over the responsibility for the beam test at CERN. Furthermore, a big thank you to Dr. Georg Auzinger and Dr. Mark Raymond for the fruitful discussions about the CBC and the CBC setup.
Also to the test beam analysis working group a big thank you for the many and interesting discussions about the test beam data as well as taking over shifts during the beam test.

Jede Bestrahlung, jedes Setup sowie jeder gesetzte Bond haben zu den vorgestellten Resultaten geführt. Tobias Barvich, Felix Boegelspacher und Pia Steck, herzlichen Dank für Eure Unterstützung. Jegliche Studie wäre obsolet, wenn Ihr nicht gewesen wärt. Dankeschön!

I thank the CMS Upgrade Simulation Working Group for the many discussions and suggestions for the simulations.

Den vielen Bachelor- und Masterstudenten am IEKP danke ich für jede Messung, die sie unterstützend durchgeführt haben.

Bei der Anfertigung der Dissertation fielen viele Arbeitsstunden, Dienstreisen und arbeitsreiche Wochenenden an. Daher gebührt auch mein aufrichtiger Dank meiner Familie, sowohl für die Unterstützung als auch für die Ablenkung in schwierigen Phasen, insbesondere während der Niederschrift dieser Arbeit.

This work is supported by the Initiative and Networking Fund of the Helmholtz Association, contract HA-101 (Physics at the Terascale). The research leading to the results of this thesis has received funding from the European Commision under the FP7 Research Infrastructures project AIDA, grant agreement no 262025.

I acknowledge the support by the DFG-funded Doctoral School “Karlsruhe School of Elementary and Astroparticle Physics: Science and Technology (KSETA)“.